SYNTHESIS AND *IN VIVO* BIOMEDICAL APPLICATIONS OF ULTRASMALL METAL NANOPARTICLES

by

SHAHAB RANJBAR BAHADORI

DISSERTATION

Submitted in partial fullfilment of the requirements
for the degree of Doctor of Philosophy at
The University of Texas at Arlington
December, 2020
Arlington, Texas

Supervising Committee:

Yaowu Hao, Supervising Professor

Xiankai Sun

Efstathios Meletis

Jiechao Jiang

Yi Hong

Ye Cao

DEDICATION

This dissertation is dedicated to my parents for their unconditional support and endless love throughout my life, and my wife Fariba whose unyielding love and encouragement inspired me to complete this research.

ACKNOWLEDGEMENTS

I would like to express my sincere gratitude to my advisor Prof. Yaowu Hao for his continuous support, guidance, and motivation during my doctoral research without which I could not have completed this dissertation. I am very grateful to him for being very patient and for all his scientific advice, knowledge, and many insightful suggestions.

Besides my advisor, I have to thank my dissertation committee members Prof. Xiankai Sun, Prof. Efstathios Meletis, Prof. Jiechao Jiang, Prof. Yi Hong, and Prof. Ye Cao for their suggestions, feedbacks, and helpful career advice.

My sincere thanks go to Prof. Sun in Department of Radiology of UT Southwestern Medical Center who provided me an opportunity to join his team as an intern and gave me the access to the laboratories and research facilities. Also, I have to thank all his team members for their constant support. Without their precious help, it would not be possible to conduct this research.

I am immensely thankful to all the professors, staff, and friends in Characterization Center for Materials and Biology, Functional Applied Biomaterials Laboratory, Nano-Bio Physics Group, and Nanofab Research Center of University of Texas at Arlington.

Finally, I would especially like to thank my amazing parents, siblings, and wife. I am truly grateful for their love, support, and patience. Without them, I would not have been able to thrive in my doctoral program and finish my PhD journey.

December 10, 2020

ABSTRACT

SYNTHESIS AND *IN VIVO* BIOMEDICAL APPLICATIONS OF ULTRASMALL METAL NANOPARTICLES

Shahab Ranjbar Bahadori, Ph.D.
The University of Texas at Arlington, 2020

Supervising Professor: Yaowu Hao

Over the past decade, metal-based nanoparticles (MNPs) have gained much popularity in the field of nanomedicine owing to their exceptional physiochemical properties. Easy surface functionalization and conjugation with therapeutic moieties, stability, inertness, and inherent anticancer activities make MNPs promising diagnostic and therapeutic agents. Among different sizes of MNPs, which greatly affect their biodistribution and clearance, ultrasmall metal nanoparticles with the size less than 5 nm demonstrate unique pharmacokinetic properties, making them suitable for nanomedicinal applications. Therefore, many efforts have been made to synthesize various kinds of ultrasmall metal nanoparticles.

In this study, a revolutionary synthesis method, termed as liquid diffusion synthesis (LDS) was developed to produce ultrasmall metal nanoparticles. In this new approach, simply immersing a dialysis bag containing an aqueous solution of a metal salt mixed with citric acid in a NaOH solution reservoir for tens of minutes, few-nm sized nanoparticles form inside the dialysis bag. Not only is this process exceptionally simple and cost effective, conducting at room temperature using aqueous solution of metal salt, citric acid and NaOH, but also it can produce a wide range of colloidal nanocrystals, covering all possible ultrasmall metal nanocrystals used as nanomedicine. Using this method, the synthesis of ultrasmall metal nanocrystals of Co, Ni, Cu, Au, Ag, Pd, Pt, and Lu have been demonstrated. Also, ultrasmall metal oxide nanoparticles can be produced using the same method. Ultrasmall nanoparticles of MnO, RuO_2, Cu_2O, FeO, ZnO_2, and CeO_2 have been synthesized. A mechanistic study was conducted to reveal the nanoparticle formation mechanism. It was found that the gradual change of the solution pH caused by the diffusion of OH^- ions through the dialysis membrane played an essential role in the formation of these nanocrystals.

Synthesized ultrasmall Cu nanoparticles have preliminarily been tested for its *in vivo* biomedical applications. It shows that Cu nanoparticles are stable in phosphate-buffered saline and fatal bovine serum. *In vivo* studies shows the renal clearability of Cu nanoparticles; about 67% of nanoparticles is excreted via urine after 48 hours of injection.

TABLE OF CONTENTS

LIST OF ILLUSTRATIONS

LIST OF TABLES

LIST OF ABBREVIATIONS

BFCs: Bifunctional chelators
BSA: Bovine serum albumin
BT: Brachytherapy
CaBP: Calcium bisphosphonate
CL: Cerenkov luminescence
CPT: Chemo/photothermal therapy
CR: Cerenkov radiation
CRET: Cerenkov resonance energy transfer
CT: Chemotherapy
Cys: Cysteine
dBSA: Denatured bovine serum albumin
DFT: Density functional theory
DMAB: Dimethylamine borane
DP: Diphosphate
DPA: dipicolylamine
DTCBP: Dithiocarbamate bisphosphonate
EDX: Energy dispersive X-ray
FPLC: Fast protein liquid chromatography
FBS: Fatal bovine serum
FCC: Face-centered-cubic
FDA: Food and drug administration
FDG: Fluoro-2-deoxy-d-glucose
FGPNPs: Fe^{3+}/gallic acid/polyvinyl pyrrolidone NPs
FLI: Fluorescence imaging
FWHM: Full width at half maximum
GA: Gallic acid
GBM: Glomerular basement membrane
GFM: Glomerular filtration membrane

GHS: Glutathione
HA: Hydroxyapatite
HB: Hydrogen bond
HRTEM: High resolution transmission electron microscopy
HSA: Human serum albumin
HTT: Hyperthermia therapy
ICB: immune-checkpoint blockade
IG: Iron garnet
IO: Iron oxide
ICP-MS: Inductively coupled plasma mass spectrometry
LA: Lipoic acid
LDH: Layered double hydroxide
LDS: Liquid diffusion synthesis
LMCT: Ligand-to-metal charge transfer
LMMCT: Ligand-to-metal-metal charge transfer
MD: Molecular dynamics
MNPs: Metal-based nanoparticles
MnO_x-MS: Manganese oxide-based mesoporous silica
MRI: Magnetic resonance imaging
NHS: N-Hydroxysuccinimide
NIR: Near infrared
NIRF: Near infrared fluorescence
NIRFUCL: Near infrared upconversion luminescence
NPs: Nanoparticles
NRs: Nanorods
NSs: Nanosheets
OVA: ovalbumin
PAI: Photoacoustic imaging
PBS: Phosphate-buffered saline
PDT: Photodynamic therapy

PEG: Polyethylene glycol

PET: Positron emission tomography

PT: Proton transfer

PTT: Photothermal therapy

PVP: Polyvinylpyrrolidone

RGO: Reduced graphene oxide

RLI: Radioluminescence imaging

RT: Radiotherapy

SAED: Selected area electron diffraction

SAM: Self-assembled monolayer

SiFA: Silicon-fluoride acceptor

SERS: Surface-enhanced Raman scattering

SPECT: Single-photon emission computed tomography

SPR: Surface plasmonic resonance

TAT: Targeted-alpha therapy

TEM: Transmission electron microscopy

TT: Thermotherapy

UCF: Upconversion fluorescence

UCL: Upconversion luminescence

USMNPs: Ultrasamll metal nanoparticles

WGPNPs: Tungsten/gallic acid/polyethylene glycol nanoparticles

1. INTRODUCTION

With development of science and technology, nanotechnology has rapidly evolved in varied fields ranging from agriculture, food, to chemical and semiconductor industries, and more importantly in the healthcare field [1]. To date, many investigations have been done in the development of novel nano-formulations as therapeutic, diagnostic, or via a seamless combination of both as theranostic agents. A large subset of these efforts has been focused on inorganic nanoparticles including silica-based NPs [6], quantum dots [7], and metal-based nanoparticles (MNPs) [8, 1].

MNPs have drawn increasing attention due to their unique size-and material-dependent optical, electrical, magnetic, and biological properties, as well as metallic surfaces which enable chemical modifications to impart biocompatibility [9, 10]. As physicochemical properties of MNPs are noticeably affected by their size, MNPs are categorized into three classes [11]: (1) plasmonic nanoparticles with average size of greater than 2 nm, (2) nanoclusters which are smaller than 1 nm, and (3) ultrasmall metal nanoparticles (USMNPs) which are considered as a bridge between nanoclusters and large plasmonic nanoparticles, having the mean size of 1-2 nm.

As MNPs are injected into body, they experience various kinds of nano-bio interactions including interacting with serum proteins [12, 13], binding to macrophages in the liver [14, 15], entering tumor through blood vessels [16-18], being internalized by cancer cells [19, 20] and, finally, they are cleared via liver or kidney. These interactions define the targeting and clearance of MNPs, which determines the theranostic efficacy [21]. Through many investigations [22, 21] [22, 23][24, 25], mostly on Au nanoparticles, it has reached to a conclusion that nanoparticles with the mean size less than 6 nm can be cleared via kidney (renal clearance), and the highest renal clearance efficiency can be achieved with the size of 1-2 nm. For in vivo applications of nanoparticles, renal clearance is a highly desired property, which can minimize the accumulation of nanoparticles in normal organs, especially in reticuloendothelial system (RES) organs such as liver, spleen, and bone marrow. Hence, many attempts have been done to the synthesis of ultrasmall metal nanoparticles with size less than 6 nm [26, 27]. A comprehensive literature review about metal nanoparticles is presented in Chapter 2.

Here, we present a new simple and general technique, called liquid diffusion synthesis (LDS), to produce varieties of ultrasmall metal and metal oxide nanoparticles with the mean size ranging from 2 nm to 5 nm. This synthesis method is conducted at room temperature using citrate as reducing and capping agent, which makes it suitable for producing nanoparticles for biomedical application, since citrate coating can be easily replaced with other molecules to render favorable targeting and biodistribution properties. More importantly, this synthesis method is particularly suitable for embedding medical radioactive isotopes into these nanocrystals to make radioactive nanoparticles (nanoseeds) for cancer imaging and therapeutics, providing a new, chelate-free radiolabeling approach. The simplicity and short synthesis time of this method offers an efficient means to incorporate almost all medical metal radioisotopes (Cu-64, Cu-67, Pd-103, Lu-177, Y-90, Au-198, Au-199, Rh-105, Sm-153, Ho-166, Tb-161, Pm-149, Re-186, Re-188) into a renal clearable nanoparticle format, which would make them with a great *in vivo* stability, suitable for diagnostic imaging such as single photon emission computed tomography (SPET) or positron emission tomography (PET) and for internal radiotherapy. Comparing to traditional radiopharmacheuticals that are composed of radioisotopes bonded to organic molecules, these nano-radiopharmacheuticals (isotopes are carried by nanoparticles) possess every different pharmacokinetics after systematic injection into the blood stream: they are too large to rapidly extravasate across the endothelial barrier in blood vessels, so they will be restricted to the intravascular space, but the size is small enough to be filtered by the kidney and clear out through urine. For nano-radiopharmacheuticals, renal clearance is an essential requirement to avoid the radiation exposure of normal organs. Different radiolabeling methods for MNPs and biodistributions and pharmacokinetics of these nanoparticles are discussed in Chapter 3.

Using LDS, ultrasmall nanocrystals of Co, Ni, Cu, Au, Ag, Pd, Pt, Lu, MnO, RuO_2, Cu_2O, FeO, ZnO_2, and CeO_2 have been synthesized. Using the synthesis process of Cu and Cu_2O nanocrystals as a model system, a systematic study was conducted to obtain insight of the process. The results and discussions are presented in Chapter 4. Synthesized ultrasmall Cu nanoparticles have preliminarily been tested for its *in vivo* biomedical applications, and the results are discussed in Chapter 5.

2. ULTRASMALL METAL NANOPARTICLES

2.1. Introduction

Nanotechnology has gained huge attention since last century. Since nanotechnology was presented by Nobel laureate Richard P. Feynman [1] during his well famous 1959 lecture “There’s Plenty of Room at the Bottom”, there have been made various revolutionary developments in the field of nanotechnology [2]. The fundamental component of nanotechnology is nanoparticle. Nanoparticles are classified as materials in which at least one dimension (length, width, thickness) is within the range of 1-100 nm [3]. Nanoparticles are not new to the environment and occur naturally in the form of minerals, clays, and products of bacteria [4]. It has been used since ancient times as a colorant for metals, but the systematic design and engineering of nanoparticles for various uses has started only in the last few decades [5]. Engineered nanoparticles exhibit unique physical, chemical, and biological properties such as melting point, wettability, electrical and thermal conductivity, catalytic activity, light absorption and scattering resulting in enhanced performance over their bulk counterparts [6]. These properties of nanoparticles have led to their various applications (see Fig. 2.1).

Nanoparticles are broadly divided into various categories depending on their morphology, size, and chemical properties. Based on physical and chemical characteristics, some of the well-known classes of nanoparticles are including carbon-based nanoparticles, ceramic nanoparticles, semiconductor nanoparticles, polymeric nanoparticles, and metal-based nanoparticles (MNPs) [2]. Among them, MNPs have received much popularity due to the exclusive physiochemical properties such as high stability, easy synthesis, exceptional optical properties and catalytic activities, and tunable surface functionalization (see Fig. 2.2) [7-9].

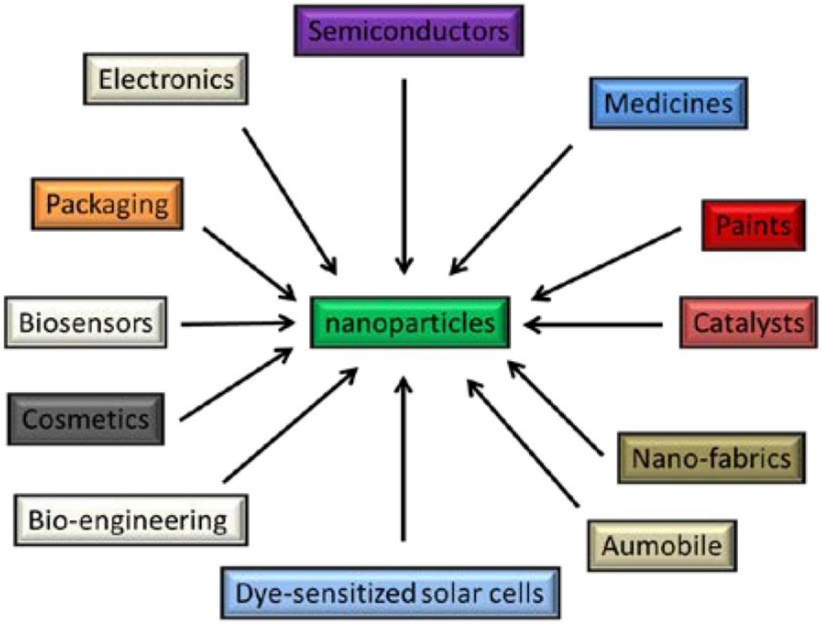

Fig. 2.1. Various applications of metal-based nanoparticles [10].

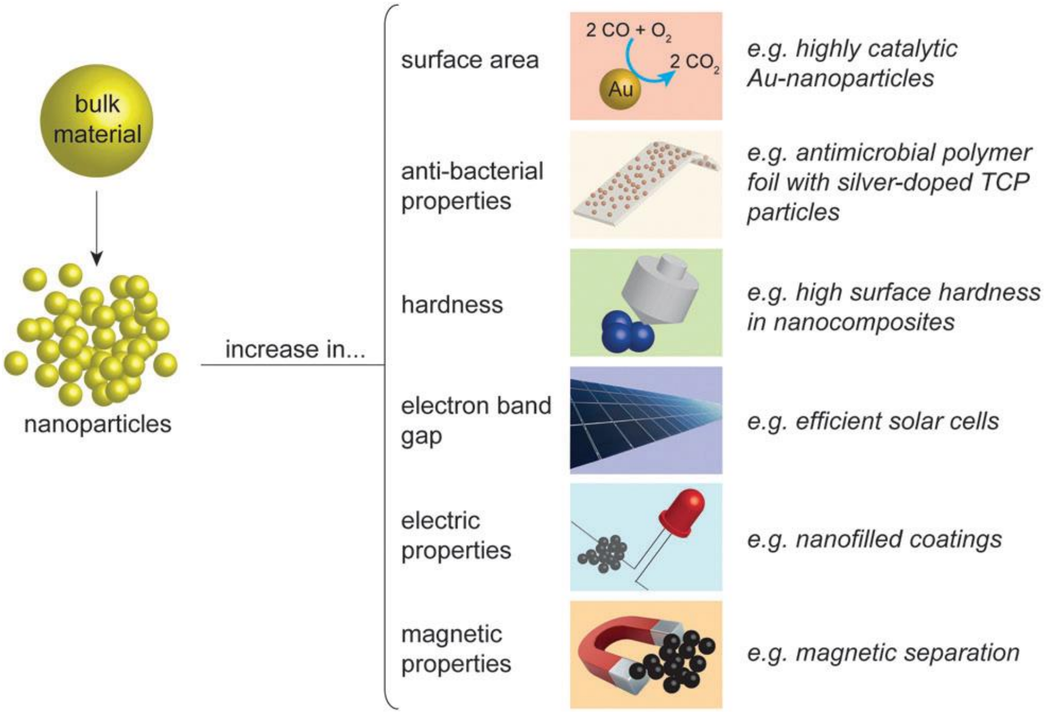

Fig. 2.2. Key examples of physiochemical and optoelectronic properties of metal-based nanoparticles [11].

2.2. Metal-based nanoparticles

Using MNPs dates back to the 14th and 13th century BC when Egyptians and Mesopotamians started making glass using metals, which can be cited as the beginning of the MNPs era [12, 6]. These materials may be the earliest examples of synthetic nanomaterials for a practical application. From the late Bronze Age (1200-1000 BC), red glass has been found in Frattesina di Rovigo (Italy) that is later found to be colored by surface plasmon excitation of copper nanoparticles (CuNPs) [12]. Similarly, the Celtic red enamels originating from the 400-100 BC period have been found to contain CuNPs and cuprous oxide [13]. Nevertheless, a Roman glass workpiece is the most famous example of ancient MNP usage. The Lycurgus Cups are a 4th-century Roman glass cup, made of a dichroic glass that displays different colors: red when a light passes from behind, and green when a light passes from the front (see Fig. 2.3) [14]. Recent studies showed that the Lycurgus Cups contain Ag-Au alloy nanoparticles, with a ratio of 7:3 in addition to about 10% Cu.

Fig. 2.3. Lycurgus Cup (British Museum; AD fourth century). This Roman cup is made of ruby glass and illustrates the myth of King Lycurgus [14].

Later, red and yellow colored stained glass found in medieval period churches was produced by incorporating colloidal gold nanoparticles (AuNPs) and silver nanoparticles (AgNPs), respectively [12]. During the 9th century, Mesopotamians started using glazed ceramics for metallic luster decorations [15]. These decorations showed amazing optical properties due to the existence of distinct AgNPs and/or CuNPs isolated within the outermost glaze layers. These decorations are an example of MNPs that display iridescent bright green and blue colors under particular reflection conditions. Transmission electron microscopy (TEM) analysis of these ceramics revealed a double layer of AgNPs (5-10 nm) in the outer layer and larger ones (5-20 nm) in the inner layer. The distance was observed to be constant at about 430 nm in between two layers, giving rise to interference effects. The scattered light from the second layer leads to the phase shift due to the scattering of light by the first layer. This incoming light wavelength dependent phase shift leads to a different wavelength while scattering. Later, the red glass was manufactured using this process all over the world. In the mid-19th century, a similar technique was used to produce the famous Satsuma glass in Japan (see Fig. 2.4). The absorption properties of CuNPs were helpful in brightening the Satsuma glass with ruby color [16].

In 1857, Michael Faraday reported the synthesis of a colloidal AuNPs, which is the first scientific description to report nanoparticle preparation and initiated the history of nanomaterials in the scientific arena [6]. He also revealed that the optical characteristics of Au colloids are dissimilar compared to their respective bulk counterpart. This was probably one of the earlier reports where quantum size effects were observed and described. Later, Mie [17] explained the reason behind the specific colors of metal colloids.

Fig. 2.4. Stained glass window from the Sainte-Chapelle in Paris [12].

2.2.1. Classification of metal nanoparticles

When size of metals reduces to become metal nanoparticles, the motion of electrons becomes limited by the size of nanoparticle and interactions are expected to be mostly with the surface. In fact, much of the interest in nanoscale materials arises from both an understanding of the physical, chemical, and size-dependent phenomena on the nanometer length scale. Fig. 2.5 shows some of the important physicochemical properties of nanoparticles that dictate their microscopic as well as their macroscopic behaviors [18]. These properties include size, shape, surface composition, aggregation, concentration, and their ability to be active, i.e., to have changing properties as a function of time or some other variables. These properties impact and dictate the most fundamental characteristics of nanomaterials including their ability to get into cells.

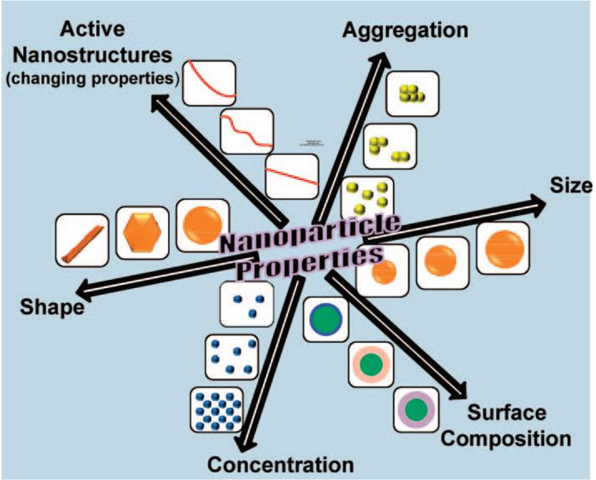

Fig. 2.5. Microscopic and macroscopic behavior of nanoparticles which is dependent on a number of important characteristics and properties [18].

Among the mentioned parameters, the size factor has the greatest effect on the physical and chemical properties of metals. With the varying size, their behaviors go through several noticeable transitions [19-25]. Bulk metals are good optical reflectors and electrical conductors. The electronic situation in bulk metals is characterized by the existence of energy bands. They result from the combination of infinite numbers of energetically very similar orbitals. The valence band contains the relevant valence electrons. The conduction band overlaps to some extent with the valence band and so becomes partially occupied with electrons. These electrons are finally responsible for the electric conductivity of metals. In contrast to the electrons in a filled band, those in the conduction band are fully mobile and make conductivity possible. In bulk metals, the energy levels of the electrons are continuous. Hence, in view of freely moving delocalized electrons in the conduction band, metals in a bulk state are good optical reflectors and electrically conducting (see Fig. 2.6).

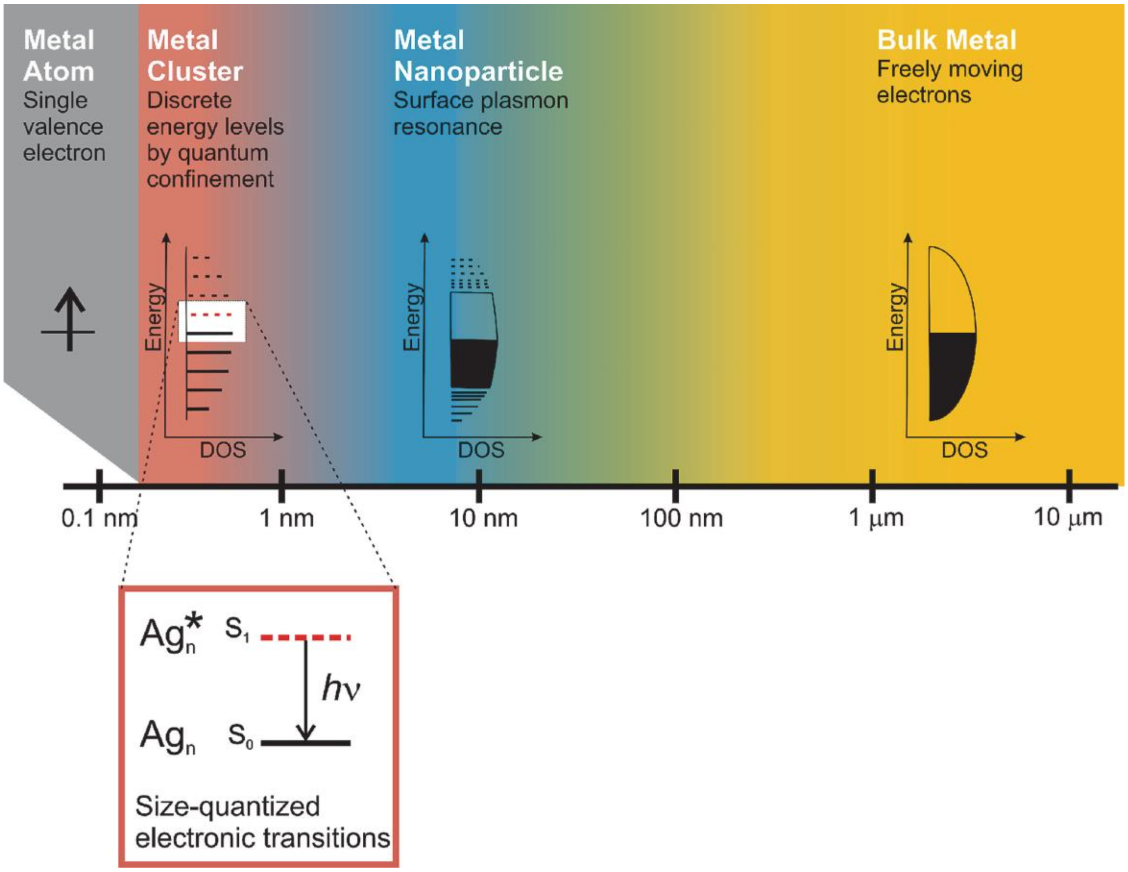

Fig. 2.6. The effect of size on behavior of metals due to the electron band structure change [19].

Physicochemical properties of metal nanoparticles including optical properties, catalytic activity, and biological properties of MNPs are considerably influenced by their size because the electron band structure changes as the size varies [9]. Accordingly, MNPs are divided into three classes as shown in Fig. 2.7:

(1) Plasmonic nanoparticles having size greater than 2 nm.

(2) Nanoclusters which are made of only a few to tens of atoms and are smaller than 1 nm,

(3) Ultrasmall nanoparticles with size ranging from 1 nm to 2 nm, which are considered as a bridge between nanoclusters and large plasmonic nanoparticles.

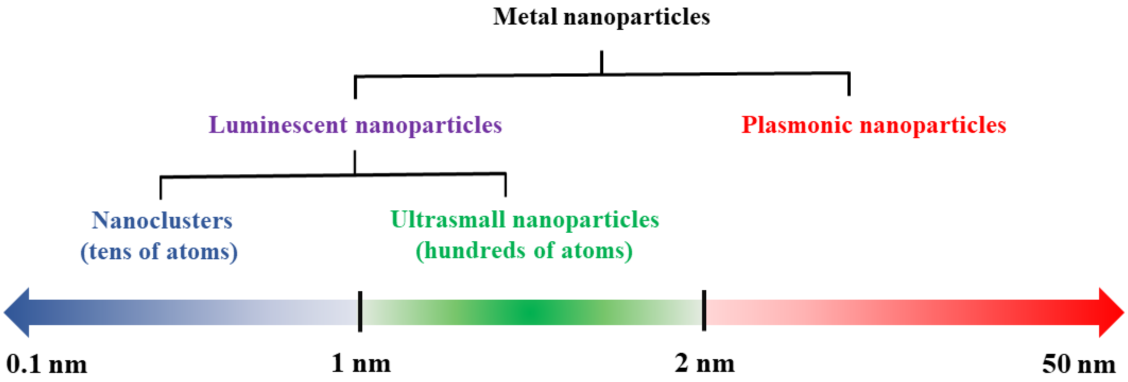

Fig. 2.7. Classification of metal nanoparticles based on size variation.

2.2.1.1. Plasmonic nanoparticles

If MNPs are irradiated by light, strong optical absorption and/or scattering phenomenon will happen forcefully and it relies on their size, morphology, and dielectric environment, which is recognized as surface plasmon resonance (SPR) [26]. Consequently, MNPs show intense colors owing to the collective oscillation of conduction electrons upon interaction with light and this particular property has been widely developed in catalysis, optoelectronics, sensing, and surface-enhanced resonance Raman scattering (SERS) [27-29]. Metal can be considered as positively charged atomic nuclei surrounded by a plasma of free electrons from the conduction band. As for MNPs, a specific size-dependent plasma absorption will be presented when the size is smaller than the average free path length of conduction electrons (i.e., < 50 nm) based on Mie's theory [17, 30]. The wavelength dependence of SPR can be modeled using Mie theory and is given by [31]:

$$E(\lambda) = \frac{24 N_A a^3 \varepsilon_m^{\frac{3}{2}}}{(\lambda \ln(10))\left(\frac{\varepsilon_i}{(\varepsilon_r + 2\varepsilon_m)^2 + \varepsilon_i^2}\right)} \qquad \text{Eq. (2.1)}$$

where N_A is the density of nanoparticles, a is the radius of the nanoparticle, ε_m is the dielectric of the medium, λ is the wavelength, and ε_r and ε_i are the real and imaginary parts of the metal dielectric constant.

SPR is a collective oscillation of electron plasma near nanoparticles surface when the nanoparticle is irradiated (see Fig. 2.8) [32, 33]. Thus, the exact analysis of SPR implies solving the Maxwell equations with the appropriate boundary conditions [34]. However, a simplified classical picture can be more useful to understand the physical meaning of SPR [35].

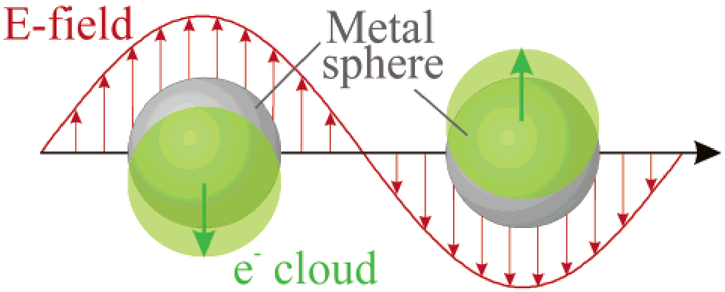

Fig. 2.8. Schematic of plasmon oscillation for a sphere, showing the displacement of the conduction electron charge cloud relative to the nuclei [33].

A MNP can be described as a lattice of ionic cores with conduction electron moving almost freely inside the nanoparticle (the Fermi sea) as illustrated in Fig. 2.9. When the particle is illuminated, the electromagnetic field of the light exerts a force on these conduction electrons moving them towards the nanoparticle surface. As these electrons are confined inside the nanoparticle, negative charge will be accumulated on one side and positive charge in the opposite side, creating an electric dipole. This dipole generates an electric field inside the nanoparticle opposite to that of the light that will force the electrons to return to the equilibrium position. The larger the electron displacement, the larger the electric dipole and consequently the restoring force. The situation is similar to a linear oscillator with a restoring force proportional to the displacement from the equilibrium position. If the electrons are displaced from the equilibrium position and the field is removed later, they will oscillate with a certain frequency that is called the resonant frequency; in the case of SPR, it is named the plasmonic frequency. The electron movement inside the nanoparticle exhibits some degree of damping. The ionic cores and the nanoparticle surface partially damp the electron oscillations. Thus, the system is similar to a linear oscillator with some damping.

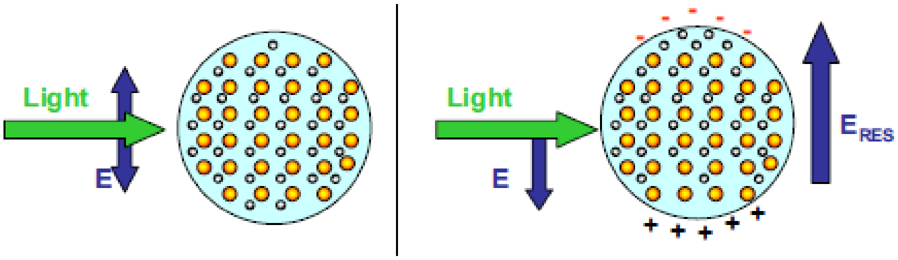

Fig. 2.9. Scheme of the light interaction with a MNP. The electric field of the light induces the movement of conduction electrons which accumulate at the NP surface creating an electric dipole. This charge accumulation creates an electric field opposite to that of the light [35].

When an alternating force is applied to a linear oscillator, the system oscillates with the same frequency as the external force, but the amplitude and phase will depend on both the force and the intrinsic parameters of the oscillator. In particular, the oscillating amplitude will be maxima for the resonant frequency (Fig. 2.10). It is quite straightforward to understand that, if the frequency of the external force is the same as the plasmonic frequency of the nanoparticle, it will be easy to make the electrons oscillate, but as we move far away from this frequency the movement of electrons will be more difficult, i.e. with reduced amplitude.

It is not possible to directly observe the movement of electrons to determine their oscillating amplitude. However, we can determine this amplitude indirectly. The electronic oscillation implies an increase in kinetic and electrostatic energies associated with the electric fields of the dipole. As energy must be conserved, this increase in energy must be provided by the illuminating light. Therefore, the light extinguishes partially when exciting SPR inside the nanoparticle. The larger the electron oscillations, the larger the light extinction, so the optical absorption spectrum allows one to detect the excitation of SPR. The resonant frequency for these oscillations in metallic nanoparticles corresponds typically to UV-Vis light and as Fig. 2.10 illustrates [36].

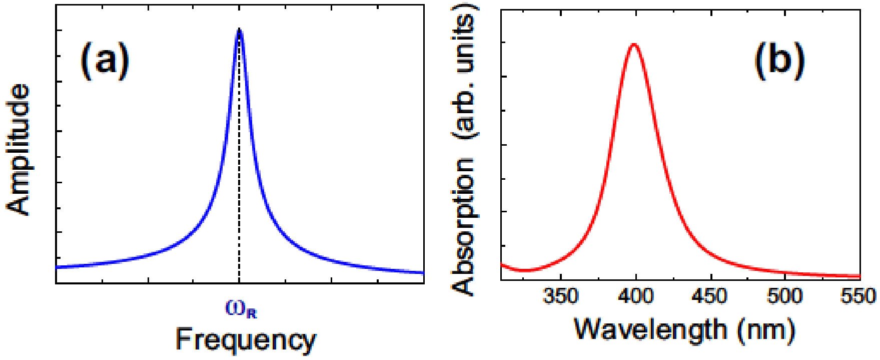

Fig. 2.10. Oscillation amplitude for a linear oscillator as a function of the external force frequency. (b) Optical absorption spectrum corresponding to 10 nm AgNPs embedded in a silica glass [35].

SPR frequencies of MNPs depend on composition, size, aspect ratio, and the morphology of the particles. A 20-nm AuNP, PtNP, AgNP, and PdNP has characteristic wine red color, yellowish gray, black, and dark black color, respectively [2]. Fig. 2.11 shows an example of this illustration for AuNPs synthesized with different sizes. These nanoparticles demonstrate characteristic colors and properties with the variation of size and shape, which can be utilized in bioimaging applications [37].

Fig. 2.11. AuNPs commonly applied in biomedical applications. (a) Gold nanorods, (b) silica-gold core-shell nanoparticles, and (c) gold nanocages. The intense color of these nanoparticles arises from the collective excitation of their conduction electrons, or SPR modes, which results in photon absorption at wavelengths which varies with (a) aspect ratio, (b) shell thickness, and/or (c) galvanic displacement by gold [37].

According to Fig. 2.11, the color of the solution changes due to variation in aspect ratio, nanoshell thickness, and gold concentration. The alteration of any of the above discussed factor influences the absorption properties of the nanoparticles, so different absorption colors are observed. Fig. 2.12 illustrates that AgNPs exhibit a sharp extinction peak at 393 nm, 394 nm, 398 nm, 401 nm, 406 nm, 411 nm, 420 nm, 429 nm, 449 nm, and 462 nm wavelength for silver nanoparticles with the average size of 5 nm, 7 nm, 10 nm, 15 nm, 20 nm, 30 nm, 50 nm, 63 nm, 85 nm, and 100 nm, respectively [38]. As predicted, the absorption maxima of AgNPs shifted to longer wavelength with increase in AgNP size. The full width at half maximum (FWHM) of the corresponding peaks determines dispersity of the nanoparticles, where a large FWHM is attributed to peak broadening and hence, polydispersity. As the size of AgNPs increased from 5 nm to 30 nm, FWHM values increased from 55 nm to 85 nm. Further increase in nanoparticle size from 50 nm to 100 nm yielded significant peak broadening with an increase in FWHM from 138 nm to 162 nm, respectively.

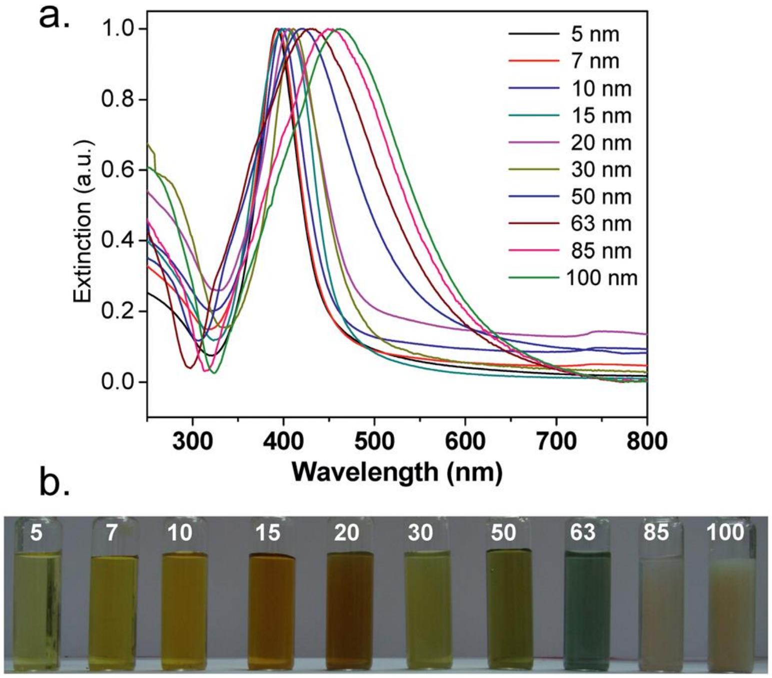

Fig. 2.12. (a) UV-Vis extinction spectra and (b) the distinctive color of different-sized AgNPs [38].

According to Gan's theory [39], when shape of AuNPs changes from spheres to rods (Fig. 2.13(A)), the SPR band is split into two bands: a strong band in near-infrared (NIR) region corresponding to electron oscillations along the long axis, referred to longitudinal band, and a weak band in the visible region at a wavelength similar to that of gold nanospheres, referred to transverse bands. While the transverse band is insensitive to the size changes, the longitudinal band is red shifted largely from the visible to NIR region with increasing aspect ratios (length/width), causing the color change from blue to red (Figs. 2.13(B) and (C)) [40].

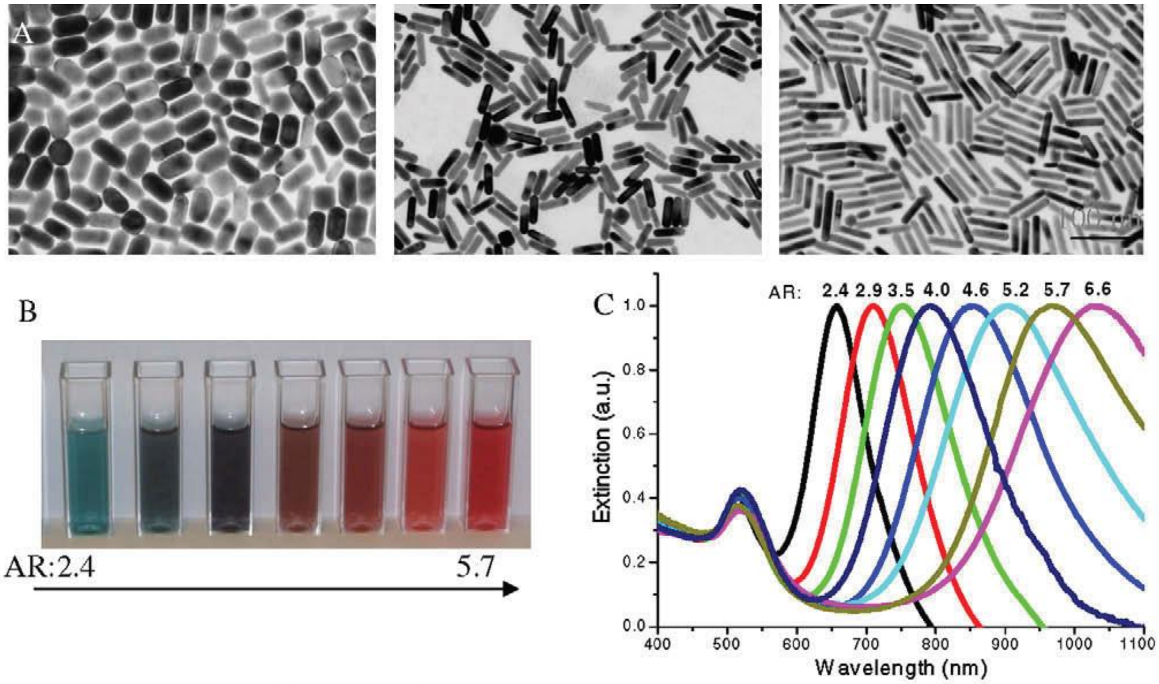

Fig. 2.13. Tunable optical properties of gold nanorods by changing the aspect ratios. (A) Gold nanorods of different aspect ratios exhibit different dimensions as seen by TEM, (B) in different color and (C) different SPR wavelength [40].

Besides the shape factor for optical tuning into NIR region, structure variation can result in similar phenomenon [40]. Two examples are the gold nanoshells and nanocages. Developed by Halas and co-workers [41], gold nanoshell is composed of a silica core around 100 nm and a thin shell of gold about few nanometers. The shell is formed by aging the gold clusters attached on the silicon core. The red shift has been explained as the results of the hybridization of the plasmons of the inner sphere and outer cavity [42]. The SPR wavelength of gold nanoshells can be controlled by changing the shell thickness. Decreasing the thickness of the gold shell from 20 nm to 5 nm leads to SPR red shift about 300 nm, which is attributed to the increased coupling between the inner and outer shell surface plasmons for thinner shell particles [42].

2.2.1.2. Metal nanoclusters

Nanoclusters are made of only a few to tens of atoms and the size of their cores is usually below 1 nm [43]. On this length scale, the properties of particles disappear, and the electronic band structure of metal nanocluster is broken down into discrete energy levels under the condition of free electrons' size near Fermi wavelength (i.e., < 1 nm), resulting in the acquisition of molecule-like behaviors like the discrete electronic state (see Fig. 2.14) [44, 45]. Metal nanoclusters are not conductors any more as the energy levels are too far separated. Thus, the collective oscillation of electrons is obstructed, and nanoclusters do not give rise to SPR effect. However, they will follow quantum mechanical rules for interaction with light and electronic transitions between the energy levels; they will show luminescence. The production of luminescence in metal nanoclusters is believed to comes from the electronic transitions caused by energy splitting, including intraband transition (sp ← sp) and interband transition (sp ← d) [46-48].

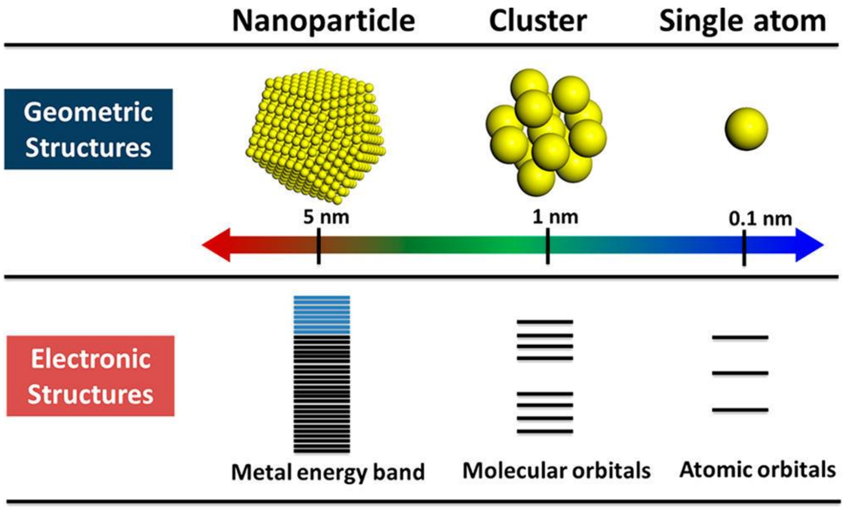

Fig. 2.14. Geometric and electronic structures of single atom, clusters, and nanoparticles [49].

Fig. 2.15 (A) shows that the emissions at 3.22 eV, 2.72 eV, 2.43 eV, 1.65 eV, and 1.41 eV correspond to Au_5, Au_8, Au_{13}, Au_{23}, and Au_{31}, respectively. That is, the excitation and emission maxima shift to longer wavelength with increasing initial Au concentration [50]. For the Au nanoclusters, the dependence of emission energy on the number of gold atoms (N) in each nanocluster, demonstrated in Fig. 2.15(B), can be quantitatively fit with a simple scaling relation of $E_{Fermi} = N^{\frac{1}{3}}$, in which E_{Fermi} is the Fermi energy of bulk gold (5.53 eV), similar to the scaling law observed from electronic absorptions of alkali metal nanoclusters in gas matrices [51, 50]. These results indicate that the electronic structure of dendrimer coated few-atom gold lusters is determined by the number of free electrons in Au nanoclusters, following a free-electron (Jellium) model [52, 53].

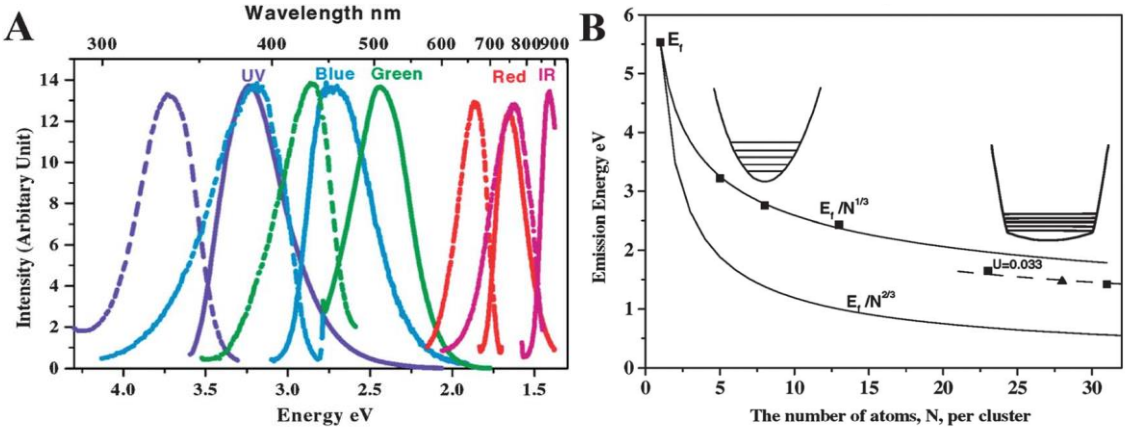

Fig. 2.15. (A) Excitation (dashed) and emission (solid) spectra of different gold nanoclusters, (B) correlation of the number of gold atoms (N) per cluster with emission energy [51].

Luminescence observed from few-atom gold cluster follows the free electron model, suggesting that emission fundamentally arises from intraband (sp-sp) rather than interband (sp-d) transitions. Fig. 2.16 shows the evolution of the energy level spacing of the sp band with the cluster size number [54]. With the increase of the gold atom number, the energy level spacing becomes smaller and smaller and eventually becomes comparable to thermal energy (kT), resulting in disappearance of luminescence. Conventional local electrical field enhancement was not involved in the emission from few-atom gold clusters, in contrast to emission observed from large gold nanorods and bulk gold films. For the smallest Au clusters (Au_3 to Au_{13}), cluster-emission energies can be well fit with the energy-scaling law $E_{Fermi} = N^{\frac{1}{3}}$, indicating that electronic structure transitions of these small Au clusters are well-described by a spherical harmonic potential. With increasing size, small anharmonicities distort the potential well, which at larger sizes gradually distorts into a Woods-Saxon potential surface, and eventually becomes a square-well potential characteristic of electrons in large metal nanoparticles [50].

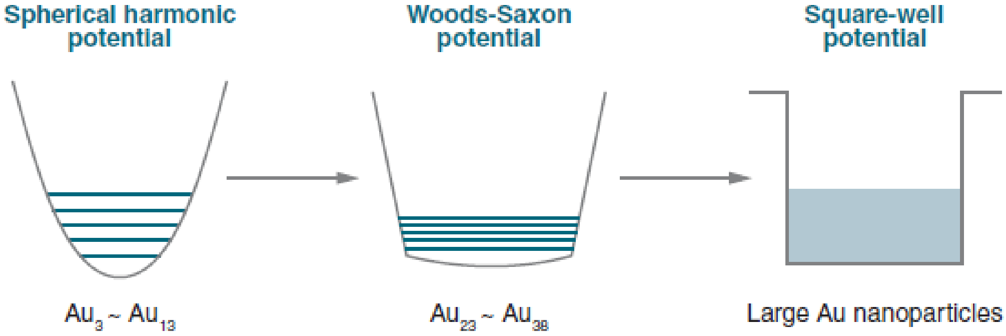

Fig. 2.16. Schematic of size-dependent surface potentials of Au clusters on different size scales [50].

2.2.1.3. *Ultrasmall metal nanoparticles (USMNPs)*

USMNPs with the core size of 1 nm to 2 nm lie in between metal nanoclusters and larger-sized nanoparticles and, consequently, exhibit intermediate structural, optical, electrical, catalytic, and magnetic properties [55]. Some of these unique properties are summarized in Fig. 2.17.

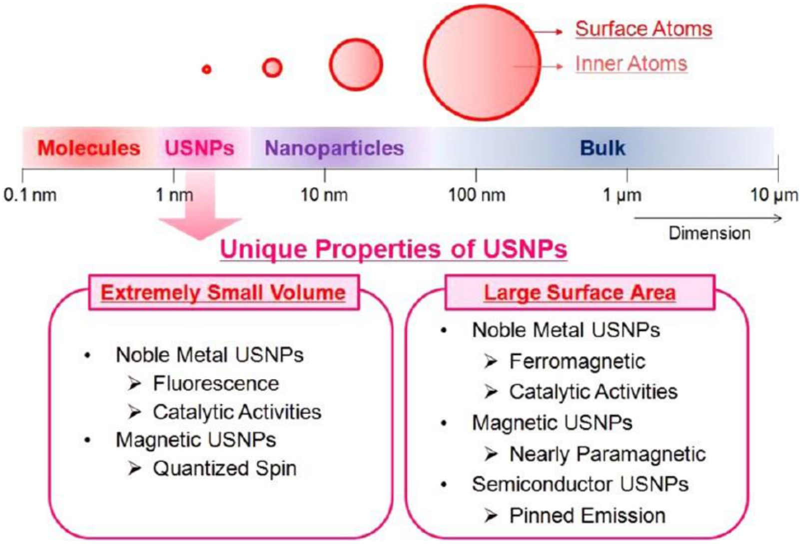

Fig. 2.17. Schematic diagram juxtaposing the differences in size of particles and their resultant properties [55].

When the size of a material decreases to 1-2 nm, the number of atoms constituting the material falls to less than 500. Consequently, USMNPs can be regarded as large molecules in which the majority of the component atoms are located at the interface with the solvent [56]. This means that a greater number of the constituent atoms of USMNPs are exposed to the outer environment. This tendency is shown in Fig. 2.18, where the smallest USMNPs are almost entirely exposed to the solvent and thus have essentially no true core. The percentage of atoms on the surface of a 1.2 nm particle is 76%, while a 2.5 nm particle exposes 45% of its atoms [57]. Below 1 nm, the particles are almost complete molecular dispersions, which is a partial reason for the differences in the macroscopic properties of USMNPs compared with clusters. Additionally, as many properties are derived from interfacial interactions of the surface atoms with the solvent, it is easy to see why USMNPs accentuate these properties compared with their bulk counterparts. Dominant surface states and the surrounding environment in USMNPs can also lead to unique physical properties [55].

The electronic structure of the USMNPs is similar to the large size nanoparticles but optically, they are luminescent. Due to the large density of states and extremely small electron Fermi wavelength (~ 0.5 nm) of metals, their luminescence is much more sensitive to the size than that of semiconductor quantum dots (exciton Bohr radius: ~10 nm) [58]. For example, once the number of Au atoms in a gold cluster reaches 55 atoms (about 1.2 nm in diameter), $Au_{55}(PPh_3)_{12}Cl_6$ no longer fluoresces [59]. Recently, Qian et al. [60] reported that $Au_{333}(SR)_{79}$ clusters (about 2.2 nm in diameter) start to give surface plasmons at 520 nm because the energy level spacing in the cluster is so small that collective oscillation of free electrons can occur.

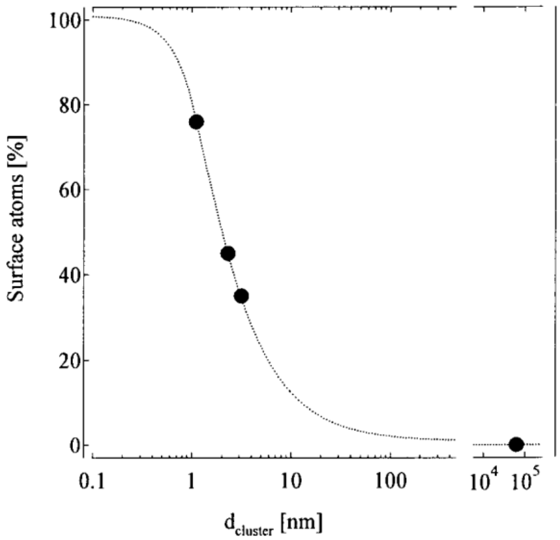

Fig. 2.18. The percentage of surface atoms changes with the cluster diameter [57].

These studies suggest that quantized states can rapidly diminish with the increase of the particle size from a few atoms to a few nanometers; therefore, in theory, the few-nanometer nanoparticles should no longer give fluorescence. However, in the past decade, a large number of luminescent few-nanomater AuNPs (1.5–3 nm) has been synthesized, suggesting that additional emission mechanisms exist in AuNPs [61-65]. Based on the emission wavelength, they are divided into NIR emitting and visible emitting USMNPs [50]. Emission can be tuned through changing the particle size, surface ligands, and valence states of metal atoms and the grain size. While there is significant progress in the understanding of emission mechanisms, most of these mechanisms are not completely clear.

2.3. Luminescence of ultrasmall metal nanoparticles

Researchers have made great efforts to explore the luminescence mechanism in metal nanoclusters. Although no complete mechanism has been mapped out, there has been important progress in identifying some important factors.

2.3.1. Size effect

As previously stated, when the size of nanoparticles decreases to the Fermi wavelength of conduction electrons, the number of electrons reaches a critical value (e.g. < 200), and the continuous band (for nanoparticles) becomes discontinuous (for nanoclusters) [66]. The luminescence characteristics of nanoclusters are critically depended on the energy gap (E_g). The relationship between E_g of metal cluster and the Fermi level (E_f) of bulk metal can be described as:

$$E_g = E_f N^{\frac{1}{3}} \qquad \text{Eq. (2.2)}$$

where N is the number of metal atoms [54]. When the luminescence of metal cluster is from the electronic transition in the metal core, the size increase (i.e., the N value) will lead to a red shift of the emission wavelength of luminescence. For gold clusters, when $N > 30$, luminescence will shift out of the visible light range (see Fig. 2.19) [50].

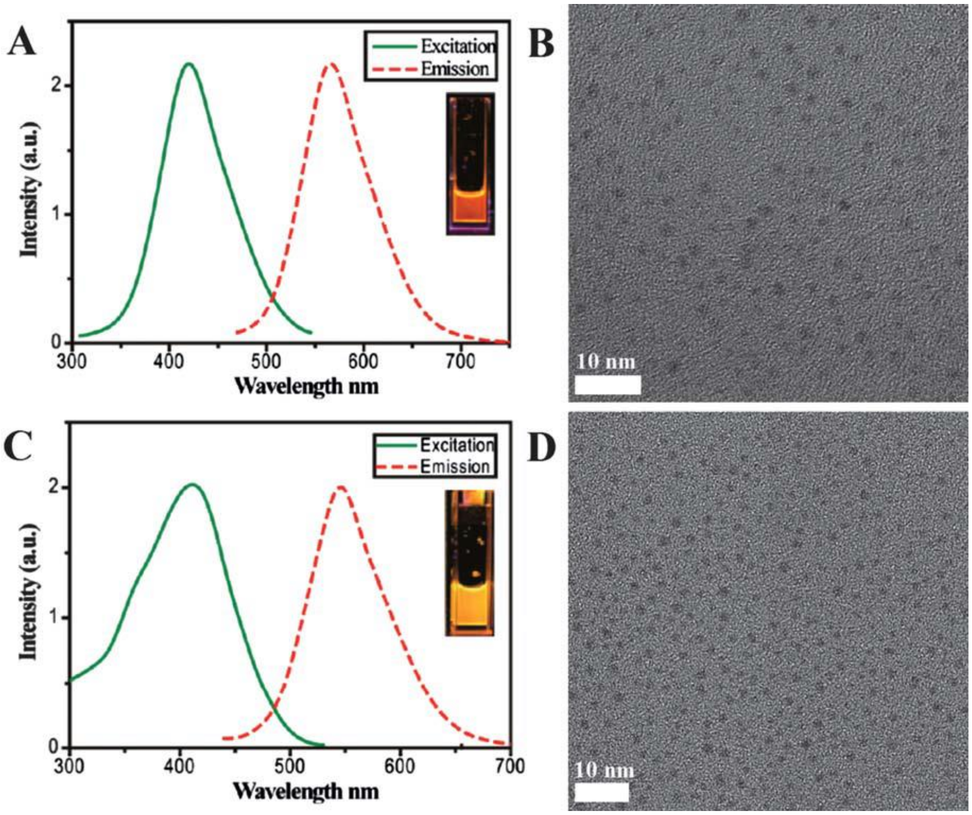

Fig. 2.19. (A) The excitation and emission spectra of orange emitting GS–AuNPs , (B) a typical TEM image of OGS-AuNPs with the average size of 1.7 nm, (C) the excitation and emission spectra of YGS–AuNPs, and (D) a typical TEM image of GS-AuNPs with the average size of 2.1 nm [50].

2.3.2. Ligand effect

The complexes of metal and ligands can also produce luminescence due to the ligand-to-metal charge transfer (LMCT) and ligand-to-metal-metal charge transfer (LMMCT) [67]. Compared with the luminescence being from the electronic transition in the metal core, the luminescence from LMCT or LMMCT usually has a much longer lifetime [68]. The electron-donating ability of the ligands will affect the luminescence quantum yield, as the charge transfer in LMCT and LMMCT comes from S atom to Au (or to Au-Au).

Wu et al. [68] found that the luminescence quantum yields of $[Au_{25}(SC_2H_4Ph)_{18}]^-$, $[Au_{25}(SC_{12}H_{25})_{18}]^-$, and $[Au_{25}(SC_6H_{13})_{18}]^-$ were ~ 1×10^{-4}, 5×10^{-5}, and 2×10^{-5}, and correspondingly the order of emission intensity is $[Au_{25}(SC_2H_4Ph)_{18}]^- > [Au_{25}(SC_{12}H_{25})_{18}]^- > [Au_{25}(SC_6H_{13})_{18}]^-$. Fig. 2.20 demonstrates that the emission intensity of metal nanoclusters is consistent with the electron-donating ability of ligand; in other words, the increase of electron-donating ability leads to the increase of emission intensity. In addition, the emission intensity can be effectively enhanced by adopting ligand with electron-rich groups or increasing the ligand ratio [69].

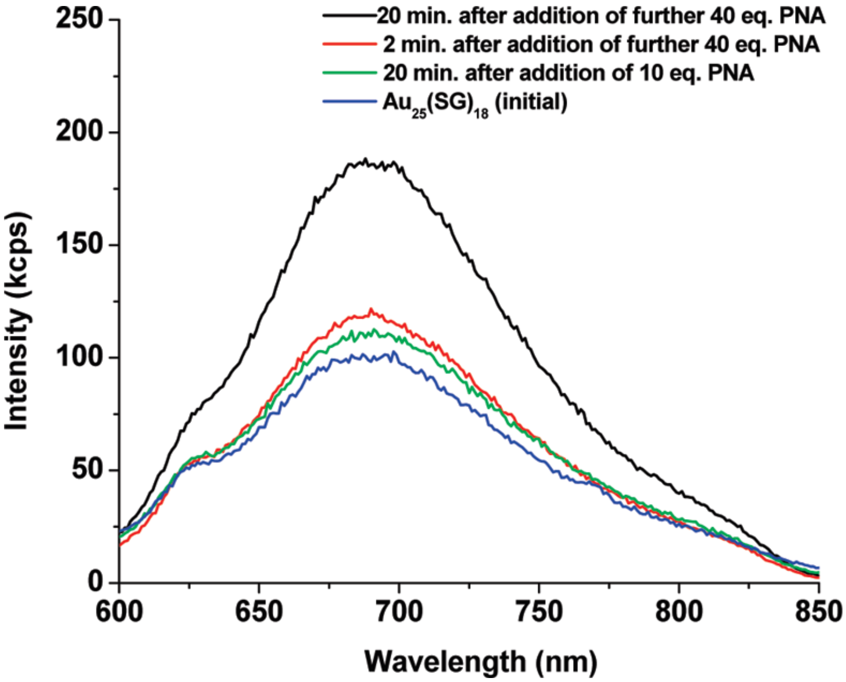

Fig. 2.20. PNA-affected fluorescence enhancement of $[Au_{25}(SG)_{18}]^-$. (the initial concentration of $[Au_{25}(SG)_{18}]^-$ was 1.1 μM, excited at 514 nm) [68].

2.3.3. *Structure effect*

The optical properties of USMNPs are also found to be related to their geometrical structure. Wang et al. [70, 71] synthesized Ag_{62} through a two-phase ligand exchange method (NC-I) and a one-pot method (NC-II), respectively. Both nanoclusters were similar in morphology, as both had a face-centered-cubic (FCC) core and an $Ag_{48}(StBu)_{32}$ shell. However, these nanoclusters had different structures, as NC-II had a central S atom, which was not existent in NC-I, resulting in differences of structure and free electron number. Therefore, NC-II exhibited strong red fluorescence, while NC-I had complete fluorescence quenching (see Fig. 2.21). The oxidation state of the core also affects the optical properties of metal nanoclusters. Duan et al. [72] found that after reduction with $NaBH_4$, the luminescence color of polyethylenimine (PEI) stable AuNCs turned from green to blue [73]. According to Fig. 2.22, the luminescence of metal nanocluster has a close relationship with the charge transfer from S to metal atom. Thus, the core with a reduced state will enhance the efficiency of charge transfer, resulting in stronger luminescence intensity.

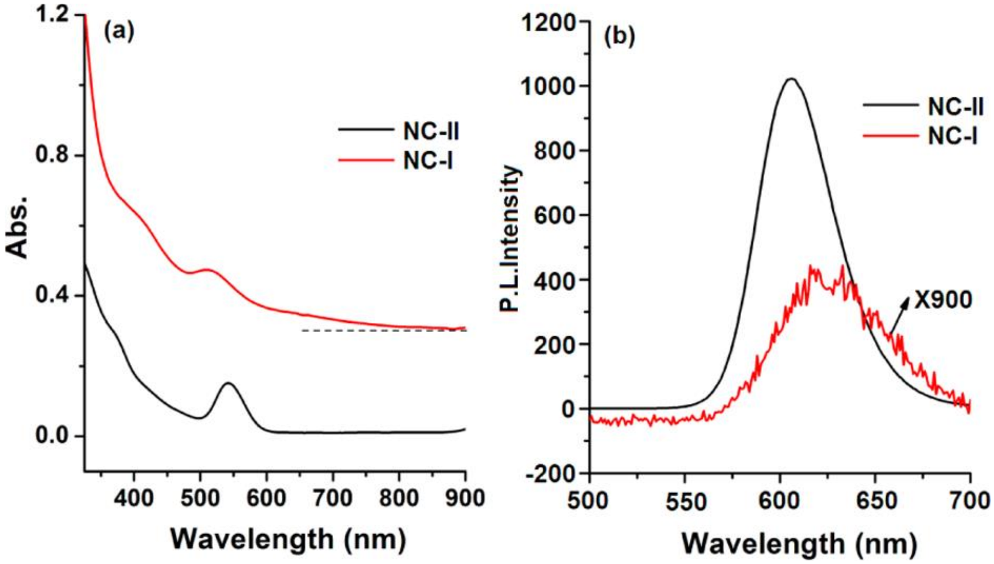

Fig. 2.21. (a) UV-Vis absorption spectra and (b) photoluminescence spectra of NC-I and NC-II [71].

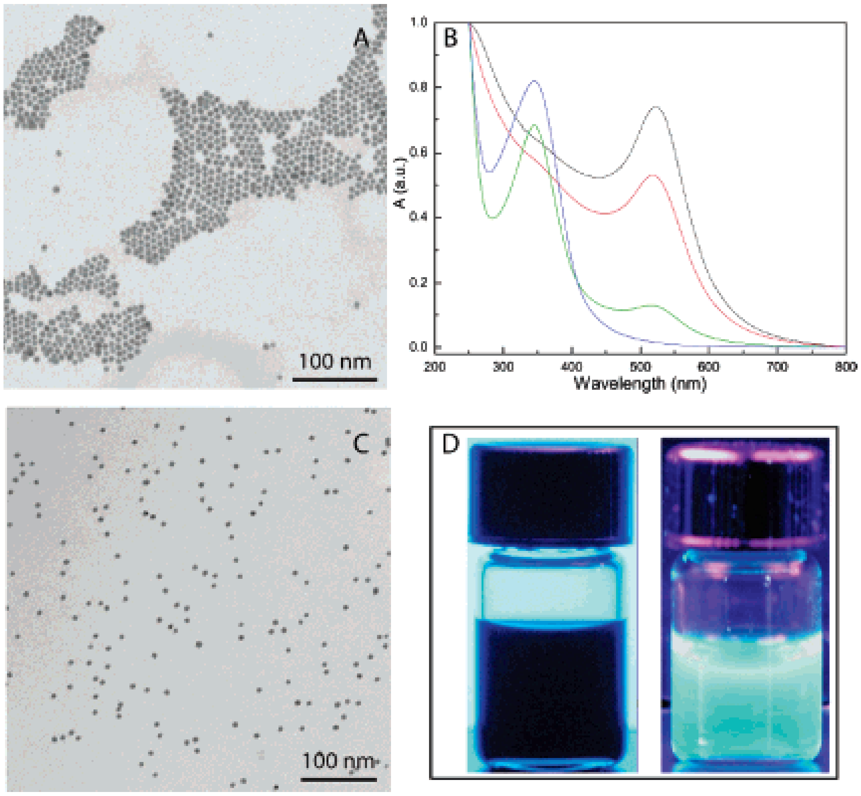

Fig. 2.22. (A, C) TEM micrographs of Au nanocrystals before and after ligand-induced etching. (B) Optical absorption spectra of the original Au nanocrystals (black curve), the solution mixture after etching (green curve), the etched nanocrystals after separation (red curve), and the pure supernatant after separation (blue curve). (D) Color photographs of the original Au nanocrystals in chloroform (left) and the supernatant nanocluster in water after etching and separation (right). Both were illuminated with a UV lamp (365 nm) [72].

2.3.4. Effect of composition

Recent studies have shown that the metal composition in the core is also an important factor for the luminescence of USMNPs due to the synergetic effect of different metals. Bootharaju et al. [74] conducted a comparative study of the fluorescence for Ag_{25}, Pd_1Ag_{24}, and Au_1Ag_{24}, and found that the fluorescence emission intensity of Au_1Ag_{24} was ~25 times higher than that of Ag_{25}. Kang et al. [75] synthesized trimetal nanoclusters, $Pt_1Au_{6.4}Ag_{17.6}$ (of note, the fractions are statistical averages of 25-metal atoms) and $Pt_2Au_{10}Ag_{13}$, based on the template of Au_1Ag_{24}. Compared with Au_1Ag_{24}, the emission intensity of rod-like $Pt_2Au_{10}Ag_{13}$ increased by 15 times, while fluorescence quenching occurred in $Pt_1Au_{6.4}Ag$ (see Fig. 2.23).

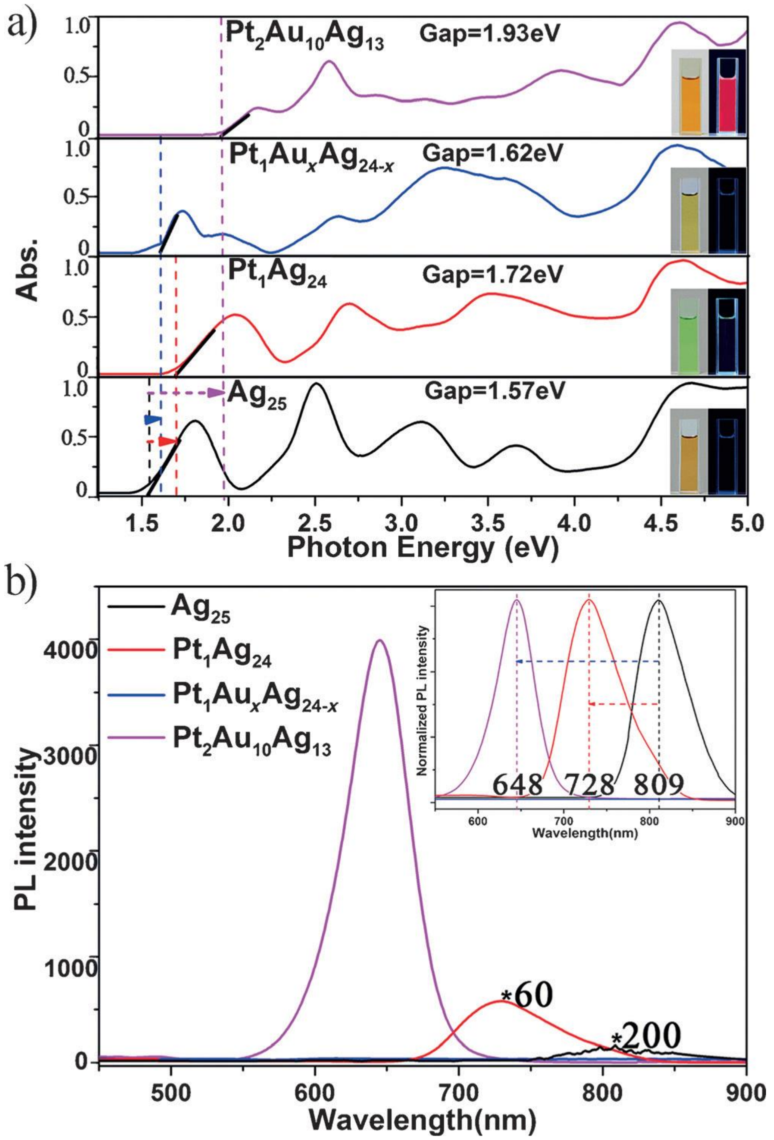

Fig. 2.23. The optical properties of the trimetallic nanoclusters and digital photo of each cluster in CH_2Cl_2 under visible and UV light; (a) energy scale optical absorption spectra of the different nanoclusters, (b) photoluminescence intensity of the Ag_{25}, Pt_1Ag_{24}, $Pt_1Au_xAg_{24-x}$, and $Pt_2Au_{10}Ag_{13}$ nanoclusters [74].

2.3.5. Effect of pH

Feng at al. [76] invented a simple protocol to prepare water-soluble fluorescent copper nanoclusters using trypsin as a stabilizer and hydrazine hydrate as a reducing agent. They found out that pH of the reaction solution was critical in determining the fluorescence of copper nanoparticles. According to Fig. 2.24, copper clusters with blue and yellow fluorescent emission were obtained under basic and acidic conditions, respectively [76].

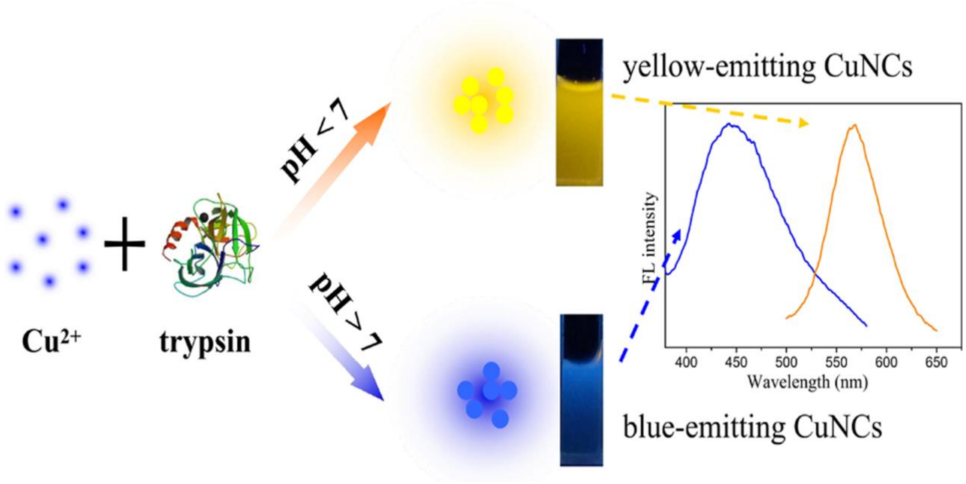

Fig. 2.24. Effect of synthesis pH of copper nanoclusters on fluorescence emission [76].

Fig. 2.25 demonstrates that copper nanoclusters were highly uniform and monodisperse. The average diameters of clusters for blue and yellow emission were about 1.8 nm and 2.5 nm, respectively. These results were highly in accordance with the phenomenon of fluorescence wavelength dependence on the size of copper nanoclusters. That is, the larger size of clusters corresponded to the red-shifted fluorescence emission wavelength, similar to that for other fluorescent nanostructures such as gold clusters [77].

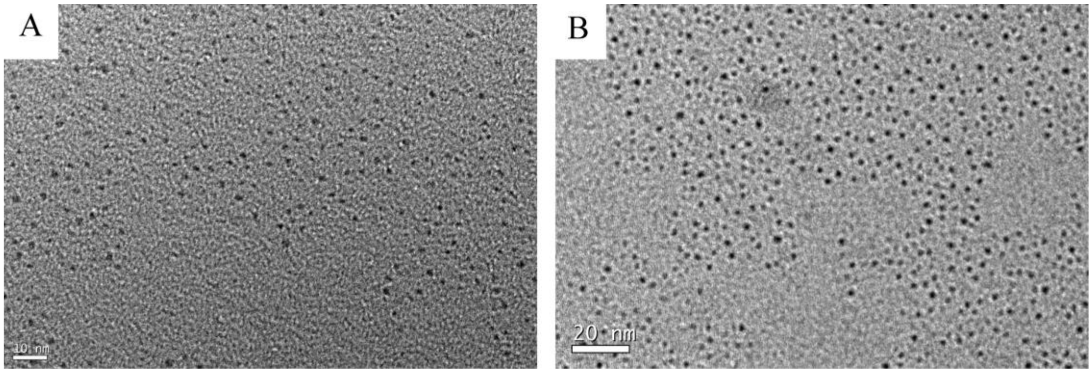

Fig. 2.25. TEM images of (A) the blue-emitting and (B) yellow-emitting copper clusters [76].

2.4. Synthesis of ultrasmall metal nanoparticles

In general, there are two strategies to produce USMNPs [78, 79]:

(1) Bottom-up method: In this technique, nanoclusters are synthesized from metal ion precursors by reducing them in the presence of suitable ligands. It is the most efficient way to nucleate clusters, and most importantly, nucleation can be controlled by varying the quantities of the ligands and reducing agents or by varying the solvents (see Fig. 2.26). Aqueous and organic soluble clusters can be produced using this approach [80-82, 79].

(2) Top-down method: In this approach, the nanoclusters are synthesized from bigger nanoparticles by either core etching or size reduction. Initially, a metal nanoparticle is synthesized which is then treated with extra ligands or metal ions to form nanoclusters [73, 83-89]. Fig. 2.26 summarized some of the most common techniques which are used for USMNPs synthesis.

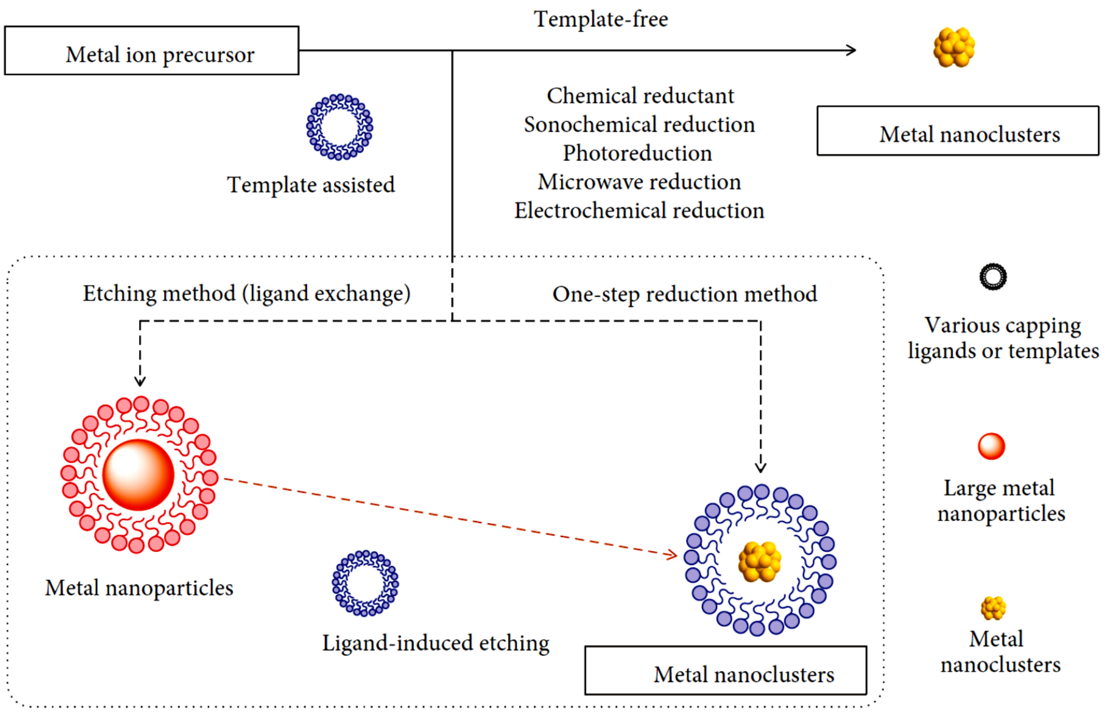

Fig. 2.26. Schematic of various techniques used for synthesis of USMNPs [90].

2.4.1. Microwave-assisted method

Microwave-assisted techniques have attracted considerable attention in enhancing nanomaterial preparations due to their distinct, fascinating advantages of uniform heating, low energy consumption, cost effectiveness, and environment-friendly features [91, 92]. The driving force for speeding up chemical reactions comes from the electromagnetic field, resulting in the oscillating friction between polarized molecules, which heat up the entire solution. Homogeneous and rapid heating in a solution induced by the microwave irradiation can offer homogeneous nucleation and shorter crystallization times. Hence, microwave energy is frequently utilized to shorten the reaction time and to produce uniform nanocrystals in terms of size and composition.

Obviously, microwave irradiation is also very suitable for the synthesis of uniform and monodisperse metal nanoclusters. Zhu and coworkers [93] prepared highly fluorescent water-soluble silver nanoclusters in by means of microwave irradiation using polymethacrylic acid sodium salt as templates. The reaction was fast, and the reaction time was reduced to seconds. The resultant gold clusters are highly stable, monodisperse, highly fluorescent under visible light as illustrated in Fig. 2.27. Moreover, Yue et al. [94] prepared highly fluorescent gold cluster with 16 gold atoms under microwave irradiation for 6 h with power of 700 W using BSA as the reducing agent and the stabilizer.

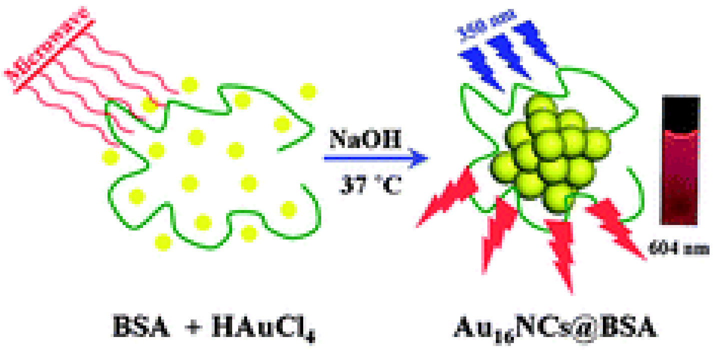

Fig. 2.27. Schematic of an one-step microwave-assisted method used for the synthesis of small gold nanoclusters, Au_{16}NCs@BSA [94].

2.4.2. Sonochemical method

Sonochemical synthesis is another effective strategy for preparing nanomaterials, and its advantages include being non-hazardous, rapid reaction rate, controllable reaction conditions and the ability to form nanoparticles with uniform shapes, narrow size distribution and high purity [95, 96]. As it is shown in Fig. 2.28, ultrasound is irradiated into a liquid and triggers the nucleation, growth, and implosive collapse of bubbles (acoustic cavitation) in liquid [97]. During treatment, very high temperature, pressure, and extremely rapid cooling rates can be achieved, so providing a unique platform for the growth of nanomaterials [98, 99]. Consequently, highly reactive species, such as radical HO_2●, H●, OH●, and possibly free electrons are generated during the irradiation of ultrasound [100, 101]. These highly reactive species can reduce metal ions into metal atoms.

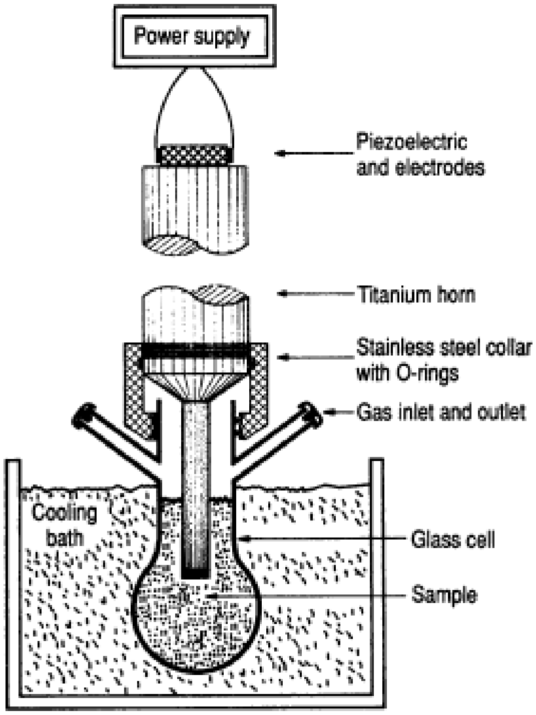

Fig. 2.28. A typical sonochemical apparatus. Ultrasound can be easily introduced into a chemical reaction with good control of temperature and ambient atmosphere [95].

Suslick et al. [102] prepared light-emitting, stable, and water-soluble Ag clusters by a handy sonochemical process with polymethy-lacrylic acid as a ligand. The properties of the Ag clusters could be regulated by varying the time of sonication, ratio between two species (carboxylate groups and Ag ions), and the molecular weight of polymer. Liu and co-workers [103, 104] reported an easy, one-pot, sonochemical route for the preparation of BSA-AuNCs for the selective and sensitive detection of nitrite (see Fig. 2.29). Compared with other methods of synthesis, microwave-assisted synthesis and sonochemical synthesis require short reaction times, and the particle sizes are relatively uniform due to the even distribution of heat and energy supply. However, the major limitations of sonochemical synthesis are that byproduct formation and noise pollution are inevitable in many circumstances [105].

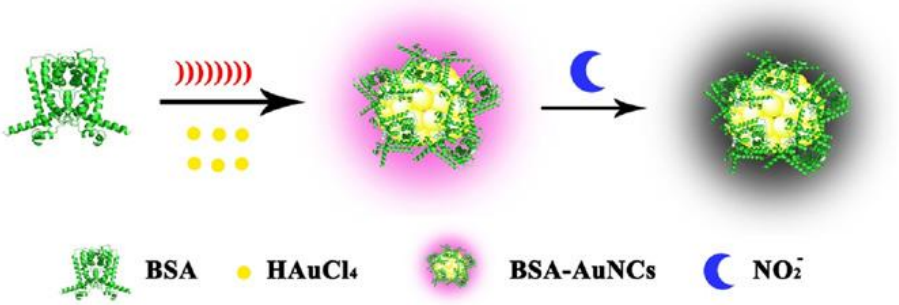

Fig. 2.29. Schematic of the synthetic strategy for BSA-AuNCs and the principle of nitrite sensing [104].

2.4.3. *Photoreduction method*

In 2001, Dickson et al. [106] first demonstrated that nanoclusters could be produced by photoreduction without the addition of reduction agents. Metal ions encapsulated in microgel could efficiently and spontaneously form nanoclusters under sunlight. Aqueous microgel dispersions can produce H●, OH●, and perhaps organic radicals by the irradiation of UV, which can reduce metal ions into metal atoms [107]. Soejima et al. [108] synthesized gold nanoclusters with a mean particle size less than 3 nm by the photoreduction of a Au complex at a UV-irradiated TiO_2 surface. The preparation process consisted of two steps: chemisorption and subsequent photoreduction. $[\mathrm{Au(OH)_3 - Cl}]^-$ was adsorbed on the TiO_2 surface via the ligand-exchange mechanism, and then it was reduced to Au^0 on the TiO_2 surface under light irradiation. The chemisorbed and physiosorbed H_2O acted as the reductant in the photoreduction of the Au complex to Au^0.

Banerjee et al. [109] prepared a stable hydrogel with Ag ions encapsulated using N-terminally Fmoc-protected dipeptide and then formed Ag clusters upon the sunlight irradiation at a physiological pH value of about 7.46. Later, the same group used an amino acid that was Fmoc-protected at the N-terminal to form a hydrogel and then prepare Ag clusters under a similar condition [110]. In addition to hydrogels, polymer is the other excellent template when the photoreduction method is used to synthesize nanoclusters. Ras et al. [111] mixed polystyrene-block-poly (methacrylic acid) block copolymer (PS-b-PMAA) and Ag salts in selected organic solvents to prepare nanoclusters with the irradiation of a visible light. Furthermore, Sun et al. [112] synthesized Ag nanoclusters through a photoreduction process using small molecules like D-penicillium and L-penicillium.

Solid templates can also be used to facilitate the formation of nanoclusters by photoreduction. Takagi et al. [113] reported a photosensitized template reduction method to prepare gold cluster presented in Fig. 2.30. Porphyrin molecules were assembled on the clay surface and formed a unique pattern. Then gold clusters were deposited on its surface via the UV photoreduction of Au precursors.

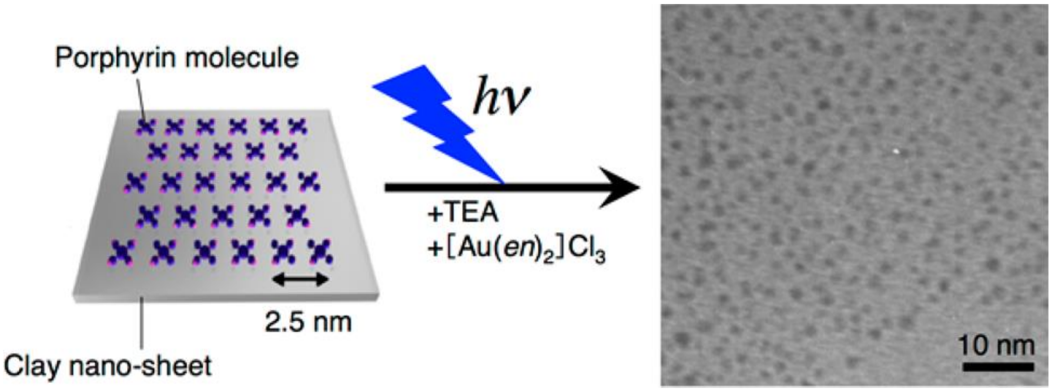

Fig. 2.30. Schematic of synthesis of gold nanoclusters through the assembling of porphyrin molecules on a clay surface and the subsequent deposition of gold nanoclusters via UV photoreduction of gold precursors [113].

The Au nanoclusters were assembled into a pattern defined by the pattern of porphyrin molecules. The deposition density and aggregation of nanoclusters could be precisely controlled by this method without protective agents. Compared with the use of reducing agents, photoreductive synthesis is a low cost, non-toxic, less time-consuming and more environment-friendly method for preparing Au nanoclusters [105].

2.4.4. Chemical etching

The etching-based strategy has been used to synthesize metal nanoclusters in the presence of excess ligands. Accordingly, two possible routes are proposed by researchers: ligand-induced etching and core etching. In the first perspective, atoms are detached from the nanoparticles surface by the ligand and then form nanoclusters through strong atom-atom interactions [114]. For the case of gold nanoclusters, in the presence of excess thiol, the surface-Au atoms of AuNPs are removed leading to the formation of Au(I)-thiolate complexes and these complexes can then undergo strong Au(I)–Au(I) interactions to form gold nanoclusters [115].

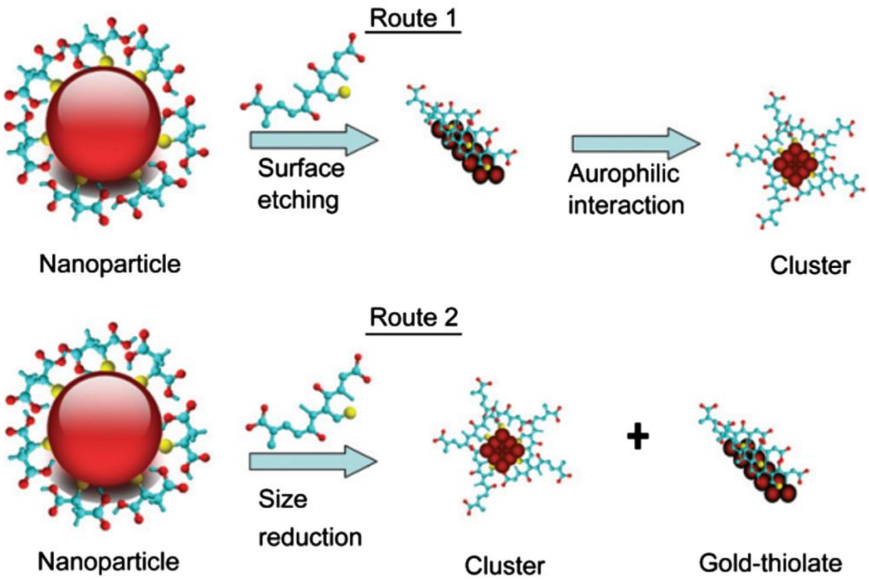

Fig. 2.31. Two possible routes for forming gold nanoclusters (AuNCs) via etching MSA-protected gold nanoparticles (AuNPs) [105].

Ligand-induced etching may also be regarded as a ligand-exchange or complete mechanism of synthesis. In the second approach, the nanoparticles are etched by the ligand and their sizes are reduced in steps till proper NCs have formed [116]. The etching process usually occurs at the interface between water and oil [117, 118]. These two possible routes for etching are shown in Fig. 2.31. Muhammed et al. [116] prepared two kinds of AuNCs from a single MSA (Methanesulfonic) acid-protected AuNPs precursor by pH-dependent glutathione etching, yielding Au_{25} and Au_8, respectively at pH 3 and 7-8.

2.4.5. Electrochemical method

This synthesis technique was first developed by Reetz et al. [119] in 1994. During the progress of electrochemical synthesis, metal ions are produced from a sacrificial anode and reduced into metal atoms at the cathode. These metal atoms further aggregated into nanoclusters in the presence of surfactants or ligands. It is easy to manipulate the nanocluster size through controlling the current, voltage, concentration of stabilizers, and electrolyte etc. Also, solid template can be used in an electrochemical reduction to prepare metal atomic clusters. Gösele et al. [120] introduced the metal deposition method on ordered alumina pores with pulsed electrodeposition. Gonzalez et al. [121] later modified this process and used porous alumina to produce nanoclusters (see Fig. 2.32). Briefly, a hexagonally ordered porous alumina substrate was generated. The diameter, depth and interpore spacing of the nanoporous structure were 10 nm, 1 μm and 35 nm, respectively. After being immersed into a metal plating bath, the system was subjected to a pulsed electrodeposition program. Gold and nickel nanoclusters were generated at the bottom of pore in nanoporous alumina. This strategy showed many advantages including simplicity, high stability against aggregation, and cluster size control. In addition, the metal nanoclusters provide a non-blocked active surface because of the absence of stabilizers.

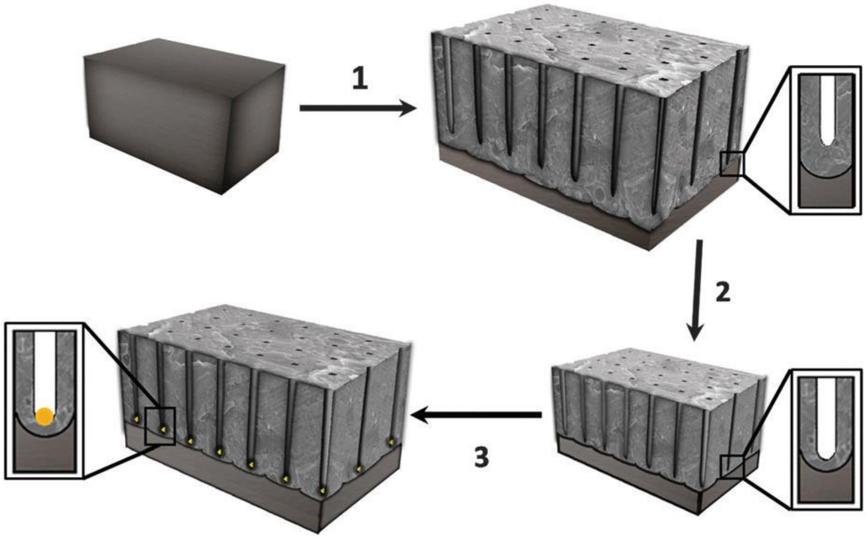

Fig. 2.32. Cluster synthesis scheme: (1) aluminum anodizing, (2) etching of the oxide barrier, (3) metal pulsed electrodeposition [121].

2.4.6. Chemical reduction method

This approach is the most widely used method in preparing nanoclusters. Different from the other methods described above, reducing agents are needed in chemical reduction process. Brust-Schiffrin method and their variants are the representative chemical reduction synthetic strategies. Whyman et al. [122] first developed the Brust-Shiffrin method in 1994. They synthesized gold nanoclusters by using BH_4^- as a reducing agent and $C_{12}H_{25}SH$ as a protecting ligand. This synthesis can be described by the phase transfer of metal precursors (Eq. (2.3)) followed by the reduction of metal ions (Eq. (2.4)):

$$AuCl_4^- \text{ (aq)} + N(C_8H_{17})_4^+ \text{ (toluene)} \rightarrow N(C_8H_{17})_4^+AuCl_4^- \text{ (toluene)} \qquad \text{Eq. (2.3)}$$

$$mAuCl_4^- \text{ (toluene)} + nC_{12}H_{25}SH \text{ (toluene)} + 3me^- \rightarrow 4mCl^- \text{ (aq)} + (Au_m)(C_{12}H_{25}SH)_n \text{ (toluene)} \qquad \text{Eq. (2.4)}$$

A modified Brust-Schiffrin method directly reduced metal ions in solution by using one-phase system without the phase transfer of metal precursors. There are many elements that can affect the core size and the surface properties of metal nanoclusters, such as the ratio of ligand to metal, reducing agents, the stabilizing ligands, time and temperature of reaction, and the pH value.

The nature of the protecting ligands is very important for the application of nanoclusters in biomedical applications. Phosphine, thiols, polymers, proteins, and DNA have been widely used as templates and/or protecting ligands in the chemical reduction process (see Fig. 2.33).

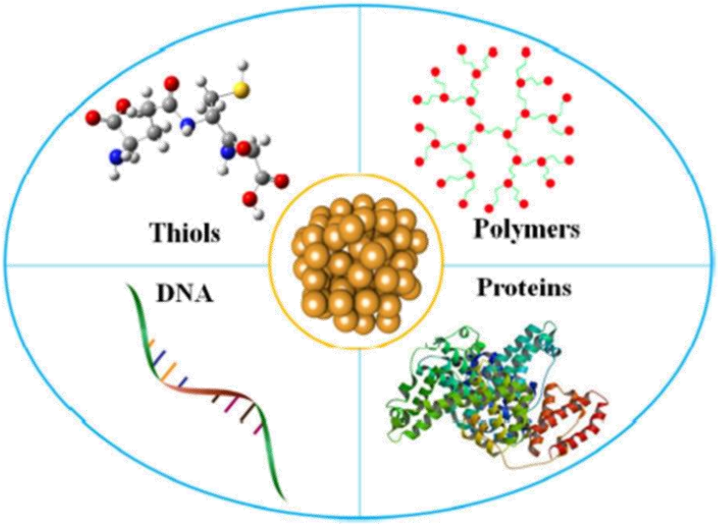

Fig. 2.33. Various types of stabilizers for metal nanoclusters synthesis [67].

2.4.6.1. *Thiols*

Thiols are often used as self-assembled monolayer (SAM) agents to modify the nanocluster surface [78]. They have been mostly employed to synthesize Au clusters. The interaction between the thiolate ion and gold atom is similar to that between two Au atoms, making it possible for thiolate ligands to break Au-Au bond and consequently form S-Au bond. Thus, thiols as protecting ligands are widely used to prepare and functionalize Au clusters. For instance, Xie et al. [123] developed a two-step reduction approach using carbon monoxide as a reducing agent to synthesize highly luminescent Au clusters $\left(Au_{22}(\mathrm{SR})\right)_{18}$, where SR represents a thiolate ligand. First, Au-glutathione complexes were reduced into $\left(Au_{18}(\mathrm{SR})\right)_{14}$ by CO. Then the final production of $\left(Au_{22}(\mathrm{SR})\right)_{18}$ was achieved by a pH-induced aggregation of small Au-glutathione complexes onto $\left(Au_{18}(\mathrm{SR})\right)_{14}$. To date, a number of thiolate-protected Au clusters (e.g. Au_{18} [124], Au_{30} [125], Au_{133} [126], etc) have been prepared and their structures have been confirmed.

2.4.6.2. *Small molecules*

Inspired by the success of the thiolate-stabilized nanoclusters preparation, other small molecules such as phosphines and alkynyl were applied to protect nanoclusters. Wang and coworkers [127] prepared a novel Au_{19} NCs composition: $[\mathrm{Au_{19}(PhC \equiv C)_9\ (Hdppa)_3](SbF_6)_2}$. They were composed of a centered icosahedral Au_{13} core and coated by three V-shaped PhC≡C−Au− C≡C(ph)−Au−C≡CPh motifs (Fig. 2.34). More recently, Zheng et al. [128] prepared an intermetallic $Au_{24}Au_{20}$ superatom nanocluster $\mathrm{Au_{24}Au_{20}(2-Spy)_4(PhC \equiv C)_{20}Cl_2}$ which displayed three kinds of anionic ligands, including phenylalkynyl, 2-pyridylthiolate, and chloride, on its surface at the same time as a concentric three-shell (see Fig. 2.35).

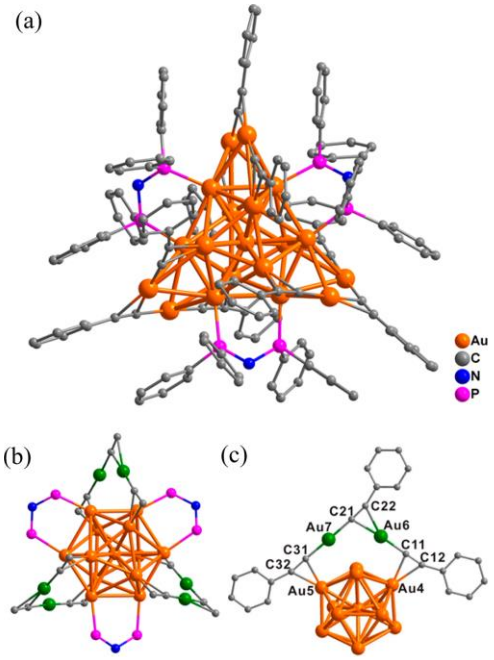

Fig. 2.34. (a) Structure of the dicationic $[\mathrm{Au19(PhC \equiv C)9(Hdppa)3}]^{2+}$ cluster. (b) Three V-shape $\mathrm{PhC{\equiv}C{-}Au{-}\ C{\equiv}C(ph){-}Au{-}C{\equiv}CPh}$ “staple” motifs with six surrounding gold atoms highlighted in green. Phenyl groups omitted for clarity. (c) The $\mathrm{PhC_2{-}Au{-}C_2Ph{-}Au{-}C_2Ph}$ motif [127].

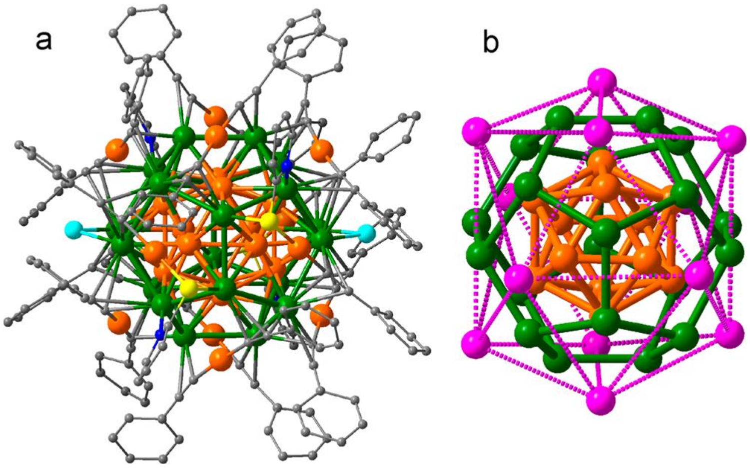

Fig. 2.35. Crystal structure of the $\mathrm{Au_{24}Ag_{20}(SP_y)_4(PA)_{20}Cl_2}$ cluster, (a) Overall structure of the cluster, and (b) concentric three-shell $\mathrm{Au_{12}@Ag_{20}@Au_{12}}$ framework of the 44 metal atoms in the cluster. Color legend: orange and pink spheres, Au; green sphere, Ag; yellow sphere, S; blue sphere, N; cyan sphere, Cl; gray sphere, C. All hydrogen atoms are omitted for clarity [128].

2.4.6.3. Proteins

Proteins are biological macromolecules and are widely used to produce nanoclusters with improved biocompatibility. Xie et al. [82] first applied bovine serum albumin (BSA) as both a protecting agent and a reducing reagent and prepared fluorescent Au clusters. Motivated by Xie’s research, Irudayaraj et al. [129] used denatured bovine serum albumin (dBSA) and synthesized highly stable fluorescent Ag clusters shown in Fig. 2.36. So far, numbers of proteins have been successfully adopted to prepare nanoclusters such as lysozyme [130], insulin [131], trypsin [132], ovalbumin [133].

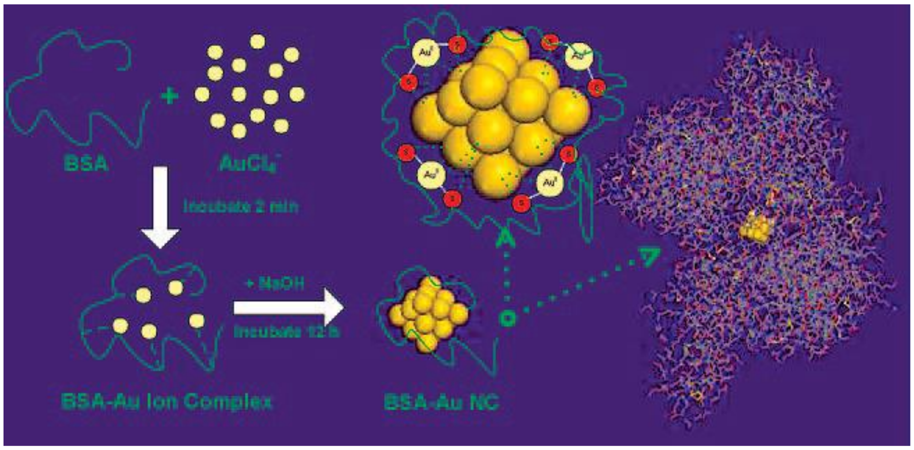

Fig. 2.36. Schematic of the formation of Au nanoclusters in BSA solution [82].

It was found that the eggshell membrane, a solid protein, could serve as a unique platform to generate fluorescent Ag and Au clusters [134]. Moreover, peptides and amino acids are excellent templates and/or reducing agents. Ogawa et al. [135] designed and synthesized α-helical coiled coils in the forms of peptide trimers, tetramers, and hexamers; these peptide polymers could be specifically combined with 6, 8, and 12 Ag^+ ions (see Fig. 2.37).

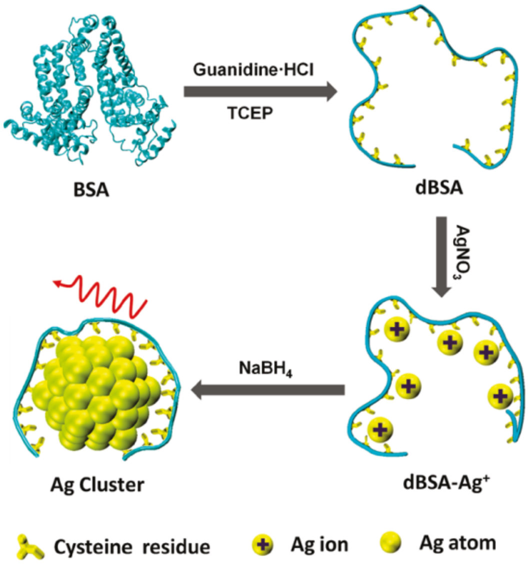

Fig. 2.37. Schematic of the denatured protein directed synthesis of fluorescent Ag clusters [129].

When treated by the $NaBH_4$, a set of peptide-capped Ag clusters were produced. They further demonstrated that these nanoclusters exhibited a strong visible fluorescence, and that their emission energies were associated with the number of metal atoms included by the nanoclusters. Glutathione (GSH) includes a γ-amido bond and a thiol and can serve as a ligand and reducing agent. Luo et al. [136] mixed aqueous solutions of $HAuCl_4$ and GSH to synthesize strongly orange-emitting Au clusters.

2.4.6.4. Polymers

The other categorized ligands for preparing nanoclusters are polymers, such as dendrimers and polyelectrolytes. Mattoussi et al. [137] synthesized bidentate ligands by conjugating a poly (ethylene glycol) short chain or a zwitterion group on a lipoic acid (LA), i.e. LA-PEG and LA-Zwitterin. Then they successfully prepared a series of intense fluorescent Au clusters employing these ligands in the presence of $NaBH_4$. Dispersions of these Au clusters showed excellent long-term stability and fluorescent lifetimes. In addition, due to the functionalization with reactive radicals (for instance, carboxylic acid or amine), these nanoclusters were suitable for common coupling strategies. More recently, Pal et al. [138] reported a convenient and eco-friendly approach for the preparation of Ag clusters. In this process, a poly(N-vinylpyrrolidone) homopolymer acted as a stabilizer and acetonitrile or N,N-dimethylformamide (DMF) was used as both a solvent and a reducing agent. On the other hand, polymers can also form micelles which can assemble metal atoms into nanoclusters. Zhang et al. [139] prepared an interfacially cross-linked reverse micelle by cross-linking a cationic surfactant with a hydrophilic dithiol. The cationic surfactant was capped with a triallylammonium headgroup. The interfacially cross-linked reverse micelle could extract AuCl_4^- into the hydrophilic core, followed by the reduction of the captured AuCl_4^- into gold clusters without the presence of extra reducing agent (see Fig. 2.38).

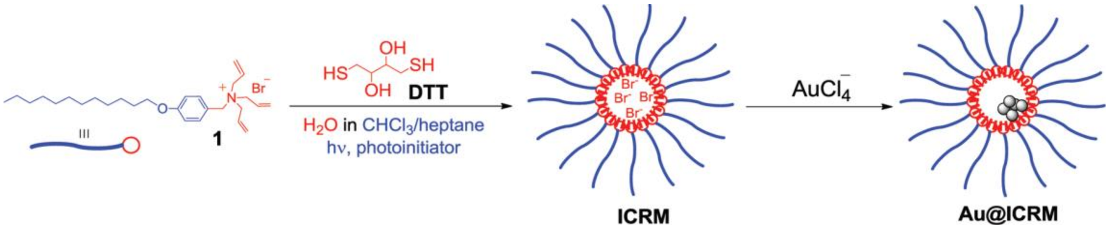

Fig. 2.38. Preparation of interfacially cross-linked reverse micelles and template synthesis of subnanometer gold clusters [139].

2.4.6.5. DNA

DNA oligonucleotides have also been used in the synthesis of nanoclusters. In 2004, Dickson et al. [140] used DNA as a template and synthesized DNA-capped Ag clusters. Thereafter, various DNA sequences have been applied to synthesize nanoclusters, and to reveal the mechanism based on which DNA interacts with nanoclusters [141, 142]. Han et al. [141] reported that duplex, hairpin, i-motif and G-quadruples DNA could stabilize nanoclusters. Fluorescence stability of Ag clusters capped by these polymorphic DNA is related to their binding affinities and the C-rich strand could stabilize Ag clusters for over 300 h. Wang et al. [142] used DNA monomers (deoxycytidine, deoxyadenosine, de-oxythymidine and deoxyguanosine monomers) as the scaffolds to synthesize Ag nanoclusters. As it is illustrated in Fig. 2.39, Martinez et al. [79] synthesized Au nanoclusters of ~1 nm in diameter using a hybrid DNA and a dimethylamine borane (DMAB), which functioned as a template and a reducing agent, respectively.

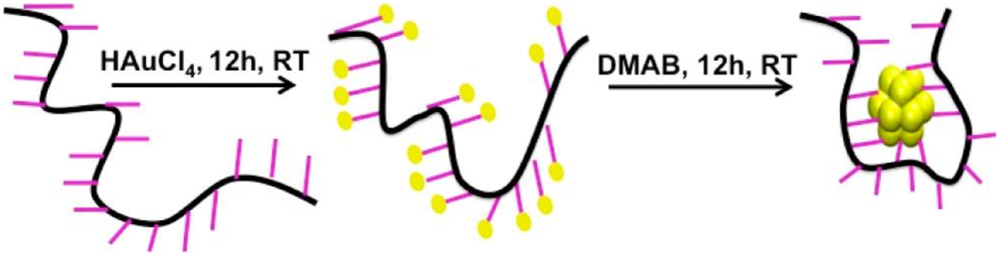

Fig. 2.39. Synthetic scheme of the gold clusters. Black curves represent DNA backbone, pink lines represent DNA bases, individual yellow spheres represent Au, while gold cluster is shown as the cluster of yellow spheres [79].

Fig. 2.40 illustrates that formation and stabilization of Ag nanoclusters in solution could be accomplished in various ways [21]. Fig. 2.40(a) shows polymers such as poly(methacrylic acid) can act as an excellent scaffold for the preparation of Ag nanocluster in water solution, by photoreduction with visible light [143], UV-light [144] or sonochemistry [102, 145]. Furthermore, Fig. 2.40(b) demonstrates Ag nanoclusters could be produced by etching large nanoparticles and stabilized with small molecules such as mercaptosuccinic acid [118, 117]. Fig. 2.40(c) also shows that DNA oligonucleotides, mainly consisting of 12 bases, were found to be excellent scaffolds for the formation of emissive Ag nanoclusters by sodium borohydride reduction of solutions with molar ratio of 2 : 1 [146, 140].

(a) Stabilized with polymers

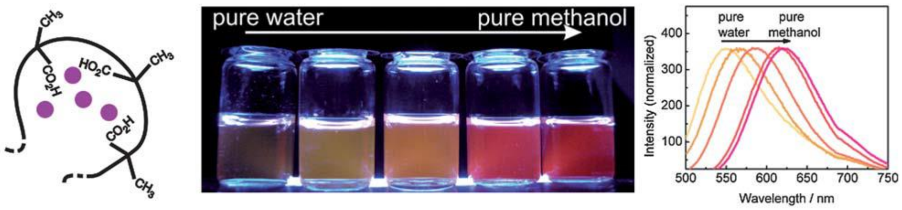

(b) Stabilized with short molecules

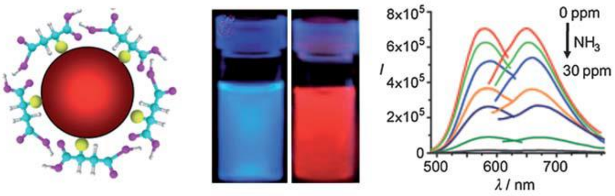

(c) Stabilized with DNA oligonucleotides

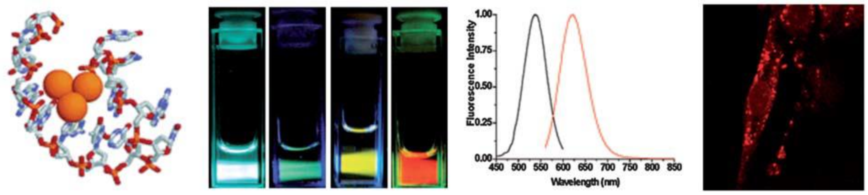

Fig. 2.40. (a) Schematic drawing of silver nanoclusters protected by carboxyl groups of poly(methacrylic acid). Photograph under UV-light of samples in water/methanol mixtures, from pure water on the left to pure methanol on the right [143, 145]. (b) Silver nanoclusters prepared by interfacial etching from silver nanoparticles and stabilized with small molecules (i.e. mercaptosuccinic acid). Fluorescence quenching by addition of NH_3 [117]. (c) Representation of silver nanoclusters encapsulated in DNA oligonucleotides. Photographs under UV light of samples with different oligonucleotides and hence different emitters. Emission spectra of the last sample, showing red emitters. Confocal fluorescence microscopic image shows the live cells incubated with (anti-heparin sulfate)-(DNA oligonucleotides)-(silver nanoclusters) [146, 140].

3. RADIOACTIVE METAL NANOPARTICLES

3.1. Radiolabeling of metal-based nanoparticles

Designing a successful radioactive MNP theranostic platform is based upon the amalgamation of three major components including MNP selection, radionuclide selection, and radiolabeling strategy. MNP selection is dependent upon the intended *in vivo* pharmacokinetics in order to attain desirable targeting efficiency with minimal toxicity. AuNPs [147-149] and iron oxide nanoparticles (IONPs) [150, 151] are extensively employed as core-particles for incorporating/attaching radionuclides in radiotherapy (RT) and nano-diagnostics due to their low toxicity, superior biocompatibility, and ease of functionalization, as well as MRI capabilities of IONPs. Other MNPs have also been reported, including Ag, Gd_2O_3, TiO_2, Co, Ce, CeO_2, Mn_3O_4, and ZrO_2 among many others. The exploration of these nanoparticles has generally been limited to a very few research groups that have developed special nanoparticle synthesis methods. Due to the lack of comprehensive *in vitro* and *in vivo* evaluation of these nanoparticles, the prospect of using them for real clinical applications remains to be tested. However, these studies still provide valuable information about radiolabeling and pharmacokinetics of MNPs.

While the radionuclide selection depends on the physical characteristics of the isotope such as emission mode, decay half-life, as well as chemical properties, availability, and cost, the radiolabeling reaction is chosen based on the maximum attainable yield within a reasonable timeframe set by the radionuclide’s half-life, which affords a stable product without significantly altering their physical, chemical, and biological properties with minimal radiation exposure [152, 153]. The radiolabeling strategy of MNPs is in turn dependent on the selected radionuclide and the ultimate theranostic goal (imaging and/or therapy) [154, 152]. To date, several strategies have been established for radiolabeling of MNPs [155], which can be categorized as direct or indirect methods.

3.2. Indirect radiolabeling

In the methods of indirect radiolabeling, exogenous coordination chemistry moieties, namely bifunctional chelators (BFCs) and prosthetic groups, are employed to conjugate an MNP for labeling with a radionuclide through chemical linkers [156, 157]. By selecting a proper BFC or prosthetic group, indirect radiolabeling is a simple approach that has been commonly used. However, appending bifunctional groups to the surface of MNPs can negatively impact their particle size, charge, and solubility [158]. Furthermore, enzymatic interactions *in vivo* can cause probable dissociation of the radionuclide from the MNP, resulting in false imaging readout [153]. Hence, for indirect radiolabeling to be successful, selection of a BFC with high *in vivo* stability with the radionuclide has the highest priority. Summarized in Table 3.1 are the main indirect radiolabeling methodologies that have been reported for radiolabeling of MNPs.

Table 3.1. Indirect MNPs radiolabeling techniques.

Metal nanoparticle	**Radionuclide**	**Therapeutic and/or imaging function**	**Reference**
DOTA-based bifunctional chelators			
IONPs	^{64}Cu	PET, MRI	[159]
IONPs	^{64}Cu	PET, MRI	[160]
IONPs	^{64}Cu	PET, MRI	[161]
AuNPs	^{177}Lu	PTT, RT	[162]
AuNPs	^{177}Lu	RT	[163]
IONPs	^{68}Ga	PET, MRI	[164]
ZrO_2 NPs	^{68}Ga	PET	[165]
IONPs	^{111}In	---	[166]
IONPs	^{111}In	---	[167]
AuNPs	^{177}Lu	---	[168]
AuNPs	^{177}Lu	RT	[169]
AuNPs	^{177}Lu	PTT, RT	[170]
AuNPs	^{177}Lu	RT	[171]
AuNPs	^{177}Lu	---	[172]
Au nanoseeds	^{177}Lu	---	[173]
AuNPs	^{177}Lu	RT	[174]
AuNSs	^{64}Cu	---	[175]
AuNSs	^{64}Cu	PET	[176]
AuNPs	^{64}Cu	PET	[177]
AuNPs	^{64}Cu	PET	[178]
AuNCs	^{64}Cu	PET	[179]
IONPs	^{64}Cu	PET, MRI	[180]
$GdVO_4$:Eu nanoshells	^{64}Cu	PET, MRI, FLI	[181]
Hollow gold nanospheres	^{64}Cu	PET, PAI	[182]
NOTA-based bifunctional chelators			
RGO-IONPs	^{64}Cu	PET	[183]
IONPs	^{68}Ga	PET, MRI	[184]
IONPs	^{64}Cu	PET, MRI	[185]
Au/Fe_3O_4 heterostructure	^{64}Cu	PET, MRI	[186]

Au tripods	^{64}Cu	PET, PAI	[187]
Mn_3O_4 NPs	^{64}Cu	PET, MRI	[188]
Mn_3O_4 NPs	^{64}Cu	PET, MRI	[189]
IONPs	^{68}Ga	PET, MRI	[190]
AuNPs	^{68}Ga	PET	[191]
IONPs	^{18}F	PET, MRI	[192]
DTPA-based bifunctional chelators			
USIONPs	^{99m}Tc	SPECT, MRI	[193]
MnO_x-MS NPs	^{99m}Tc	SPECT, MRI	[194]
AuNPs	^{111}In	---	[195]
IONPs	^{99m}Tc ^{68}Ga	PET, MRI or SPECT, MRI	[196]
IONPs	^{67}Ga	---	[197]
IONPs	^{166}Ho	---	[198]
AuNPs	^{67}Ga	---	[199]
AuNPs	^{99m}Tc	SPECT	[200]
AuNPs	^{99m}Tc	SPECT	[201]
AuNPs	^{111}In	RT	[202]
IO nanocapsules	^{111}In	SPECT, MRI	[203]
Other bifunctional chelators			
IONPs	^{188}Re	RT	[204]
AuNPs	^{177}Lu	---	[205]
IONPs	^{99m}Tc	SPECT, MRI	[206]
IONPs	^{90}Y	RT	[207, 208]
$Mn_xZn_{1-x}Fe_2O_4$ NPs	^{188}Re	RT	[209]
Bi_2S_3 NPs	^{99m}Tc	SPECT, PAI, PTT, RT	[210]
AuNPs	^{99m}Tc	SPECT	[211]
AuNPs	^{99m}Tc	SPECT	[212]
AuNPs	^{99m}Tc	---	[150]
AgNPs	^{99m}Tc	SPECT	[213]
IONPs	^{99m}Tc	SPECT, MRI	[214]

$NaGdF_4$:Yb,Tm,Ca@$NaLuF_4$ core@shell upconversion	^{99m}Tc	SPECT, NIRFUCL	[215]
Endorem/Feridex	^{64}Cu	PET, MRI	[216]
USIONPs	^{99m}Tc	SPECT, MRI	[217]
Endorem/Feridex	^{99m}Tc	SPECT, MRI	[218]
Ferucarbotran/Perimag-COOH	^{89}Zr ^{99m}Tc	---	[219]
IONPs	^{89}Zr ^{68}Ga	PET, MRI	[220]
Ferumoxytol	^{89}Zr	PET, MRI	[221]
AuNPs	^{99m}Tc	SPECT	[222]
Gd_2O_3 NPs	^{99m}Tc	SPECT, MRI, NIRF	[223]
Strategies using prosthetic groups			
IONPs	^{11}C	PET, MRI	[224]
IONPs	^{14}C	---	[225]
CeNPs	^{18}F	PET	[226]
$NaGdF_4:Yb^{3+}/Er^{3+}$	^{124}I	NIRFUCL , PET, MRI	[227]
Au nanorods	^{125}I	SPECT, PTT	[228]
IONPs	^{125}I	SPECT, MRI	[229]
SiO_4@IO NPs	^{125}I	SPECT, MRI, FLI	[230]
CoNTs	^{131}I	---	[231]
AuNPs	^{18}F	PET	[232]
AuNPs	^{18}F	PET	[233]
AuNPs	^{18}F	PET	[234]
IONPs	^{18}F	PET	[235]
USIONPs	^{125}I	SPECT, MRI	[236]
AuNPs	^{125}I	SPECT	[237]
Fe@Fe_3O_4 NPs	^{125}I	SPECT, MRI, PTT	[238]
AuNPs	^{111}In or ^{64}Cu/^{125}I	SPECT	[239]
Fe^{3+}/GA/PVP (FGP) complex	^{125}I	SPECT, MRI, PAI	[240]

3.2.1. Indirect radiolabeling via BFCs

Indirect radiolabeling via a proper BFC is based on the coordination chemistry between the metal radionuclide and the BFC conjugated to the MNP surface. BFCs are molecules consisting of a metal chelating unit and a reactive functionality [241]. While the former binds to metallic radionuclides, the latter has been covalently conjugated to the surface of MNPs [156]. Conjugation of BFCs to the MNP usually requires surface modification by attaching carboxyl, thiol, or amino groups to the MNP surface. As the BFCs can be designed to be reactive to the aforementioned functionalities, their conjugation with MNPs are often straightforward and can be carried out by standard operating procedures [151].

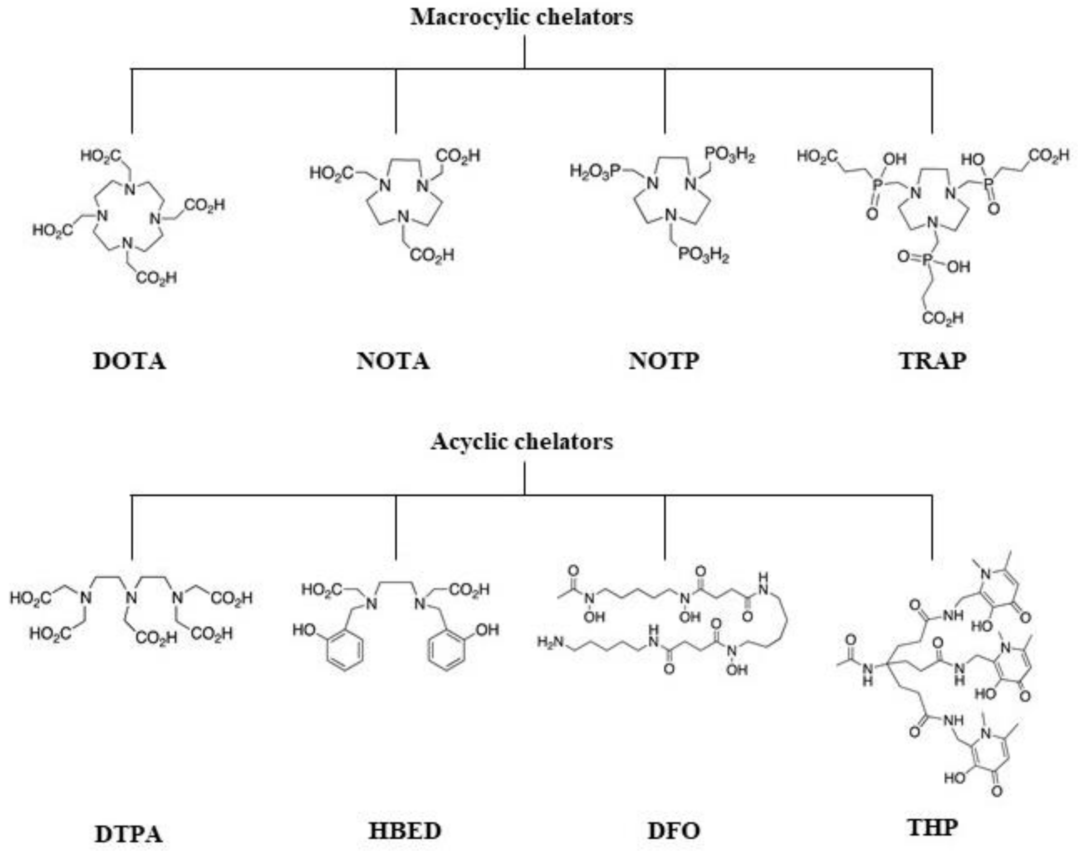

Fig. 3.1. Macrocyclic (upper) and acyclic (lower) bifunctional chelators for radiometal labeling of MNPs.

The chelator selection is dependent upon the radionuclide of choice and the desired physicochemical properties of the radiolabeled MNPs, by which the intended pharmacokinetics will be determined. Nevertheless, the guiding principle of BFC selection is to ensure the *in vivo* inertness of the resulting radiometal complex [242]. Based on their structures, BFCs are categorized into two groups: (1) Macrocyclics, such as 1,4,7,10-tetraazacyclododecane-1,4,7,10-tetraacetic acid (DOTA), 1,4,7-triazacyclononane-1,4,7-triacetic acid (NOTA), 1,4,7-triazacyclononane macrocycles substituted with phosphonic acid (NOTP), and 3,3′,3”-(((1,4,7-triazonane-1,4,7-triyl)tris(methylene))tris(hydroxyphosphoryl)) tripropanoic acid (TRAP), and (2) Acyclic chelators such as diethylenetriaminepentaacetic acid (DTPA), bis(2-hydroxybenzyl)ethylenediaminediacetic acid (HBED), desferrioxamine-B (DFO), and tris(hydroxypyridinone) (THP), and their derivatives (Fig. 3.1) [243].

3.2.1.1. Radiolabeling via DOTA-based chelators

A multidentate chelator, DOTA is one of the most commonly used BFCs, which exhibits high affinity to most metal radionuclides, including ^{64}Cu [159-161], ^{177}Lu [163, 162], ^{68}Ga [165, 164], and ^{111}In [166, 167] [244]. Among them, ^{177}Lu ($t_{1/2}$ = 6.734 days), that decays by both β emissions and γ rays, is of particular interest to the development of theranostics. To date, AuNPs have been radiolabeled with ^{177}Lu via conjugation with a Gly-Gly-Cys (GGC) peptide chain containing DOTA [169, 168] or modification by a multi-thiol functional group including a copolymer with a polyethylene glycol (PEG)-block, a polyglutamide-block with 8 pendant DOTA, and 4 terminal lipoic acid groups [PEG-pGlu(DOTA)$_8$-LA$_4$]. Such co-polymer functionalization was reported with capabilities to increase the desired biological stability, facilitate a desirable curvature formation on the MNP surface for multifunctional presentation and easy accessibility by the surrounding molecules [245], and reduction in the *in vivo* hepatic uptake [172, 173, 171, 174]. Another interesting approach to label AuNPs with ^{177}Lu was recently reported by trapping AuNPs inside the dendritic cavity of a generation 4 (G4) polyamidoamine (PAMAM) dendrimer, which had been pre-conjugated with p-SCN-benzyl-DOTA as well as folate/bombesin for cancer targeting [170].

By using the same DOTA chelating moiety, Xie et al. [176, 175] reported methods of labeling Au nanoshells (AuNSs) with ^{64}Cu, which were then evaluated for photothermal therapy (PTT). As illustrated in Fig. 3.2, the anchoring of DOTA at the surface of AuNSs was through the Au-S linkage rendered by bifunctional O-pyridyl disulfide-polyethylene glycol 2000-DOTA (OPSS-PEG$_{2k}$-DOTA). The labeling of resultant DOTA-PEG$_{2k}$-OPSS-AuNSs with ^{64}Cu was straightforward. Similar approaches have also been reported for ^{64}Cu-labeling of AuNPs with PEG$_{2k}$ linker [177, 178], Au nanoclusters (AuNCs) with PEG$_{5k}$ linker [179], and IONPs with a linker containing 1,2-distearoyl-sn-glycero-3-phosphoethanolamine-N-[amino(polyethylene glycol)2000] (DSPE-PEG$_{2k}$) [180]. To further enhance the stability of the coating of MNPs, reduced lipoic acid with two free thiol groups has been used to construct a bifunctional linker. While the disulfide linkage provides a strong anchoring of the linker onto the MNP surface, a DOTA chelator is conjugated to the other side of linker for labeling with radiometals. Employing such an approach, Tian et al. [182] first reported ^{64}Cu-labeling of gold nanospheres to enable PET imaging. However, the labeling efficiency of this approach was lower because of the existence of metal impurities (e.g., Co^{2+}) from the gold nanospheres synthesis, which were in competition with ^{64}Cu^{2+} for the DOTA moiety.

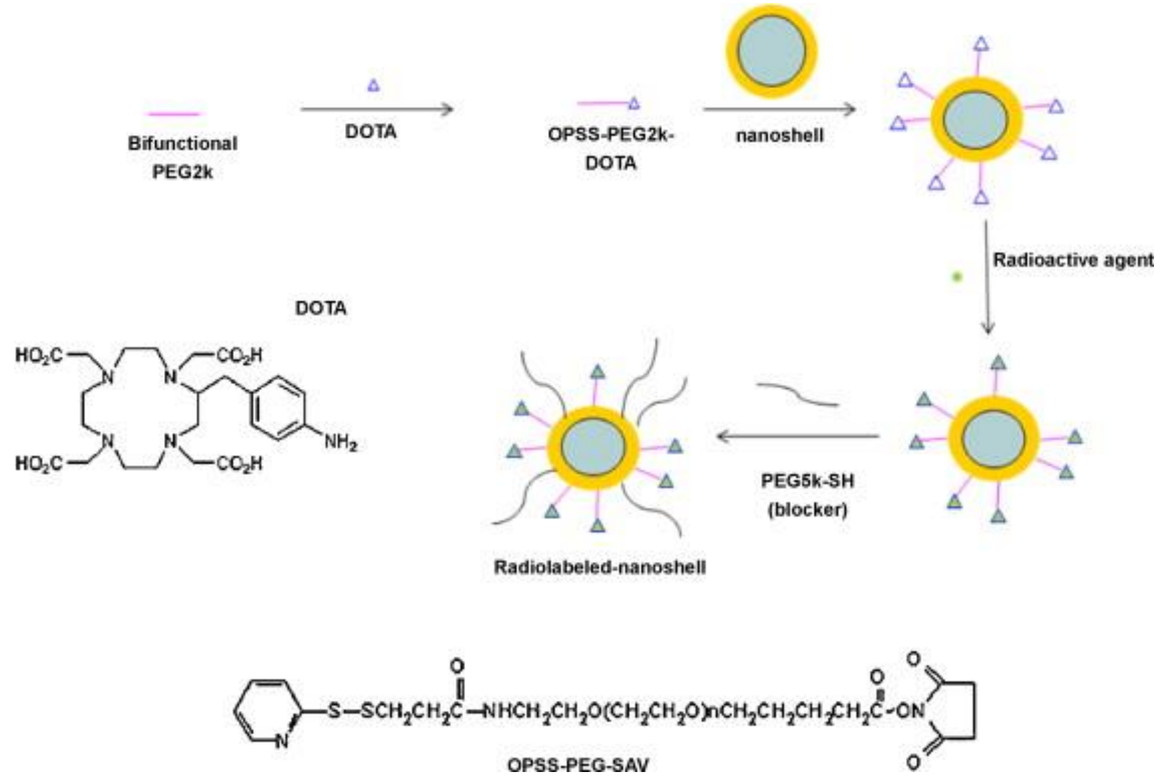

Fig. 3.2. Schematic step-wise synthesis of ^{64}Cu-labeled AuNSs: 1) conjugating p-NH$_2$-Bn-DOTA to OPSS-PEG$_{2k}$-NHS, 2) coating the surface of AuNSs with OPSS-PEG$_{2k}$-DOTA , 3) ^{64}Cu labeling of AuNS-OPSS-PEG$_{2k}$-DOTA, and 4) further pegylation with longer PEG$_{5k}$-thiol to shield the ^{64}Cu-labeled AuNSs from external attacks [176].

3.2.1.2. Radiolabeling via NOTA-based chelators

A hexadentate N$_3$O$_3$ chelator, NOTA and its derivative are commonly used for gallium and copper radiopharmaceuticals. To date, they have been used for labeling of MNPs with ^{67}Ga/^{68}Ga and ^{64}Cu [184, 183]. It is noteworthy that NOTA and its derivatives exhibit similar radiolabeling efficiency and kinetic stability with ^{64}Cu comparable to, if not higher than, other BFCs including DOTA, DTPA, ethylenediaminetetraacetic acid (EDTA), and triethylenetetramine (TETA) [246, 247]. To conjugate MNPs with a NOTA moiety for $^{68/67}$Ga or ^{64}Cu labeling, the general approach is to functionalize NOTA with a thiol group (NOTA-SH) for radiolabeling and conjugation with

MNPs, respectively. The thiol-functionalized NOTA (NOTA-SH) can be readily synthesized by reacting p-SCN-Bn-NOTA with 2-aminoethanethiol hydrochloride in the presence of triethanolamine [185]. If necessary, NOTA-SH can be further conjugated with a PEG chain to optimize the *in vivo* kinetics of the resultant MNPs. To date, this approach has been reported for ^{64}Cu labeling of Au/Fe_3O_4 hybrids [186], Au tripods [187], and Mn_3O_4 NPs [248].

In addition to the commonly used PEG chains, many other linkers or spacers have also been seen in the surface modification of MNPs. For instance, polyethyleneimine (PEI) was reported to functionalize Mn_3O_4 NPs for ^{64}Cu labeling through NOTA conjugation [189]. The ^{64}Cu labeling yield of the resultant Mn_3O_4 nanoprobe was high (> 85% yield) due to the exceptional characteristics of PEI, such as branched internal cavity and multiple terminal amines [249]. Stearylamine (SA), an amphiphile, was also seen in the construction of IONPs for highly efficient radiolabeling with ^{68}Ga through NOTA conjugation [190].

It has been well-documented that the linker lengths play an essential role in the *in vivo* kinetics of resultant MNPs [250, 251]. For instance, two thiol-functionalized NOTA-SH constructs, one built from an 11-carbon atom aliphatic chain (C11) and the other lipoic acid (Lip), can result in very different biodistribution profiles when presented onto a common AuNP platform [191]: the AuNPs with the shorter Lip linker exhibited lower accumulation in the liver than the ones with the longer C11 linker. Recently, NOTA has also been commonly used for ^{18}F labeling after loaded with Al^{3+}, which has high affinity to ^{18}F fluoride [252-254]. As such, the NOTA-SH methods described above can also be used for ^{18}F labeling of MNPs. As illustrated in Fig. 3.3, IONPs were labeled with ^{18}F through an Al-NOTA moiety for PET/MR imaging [192].

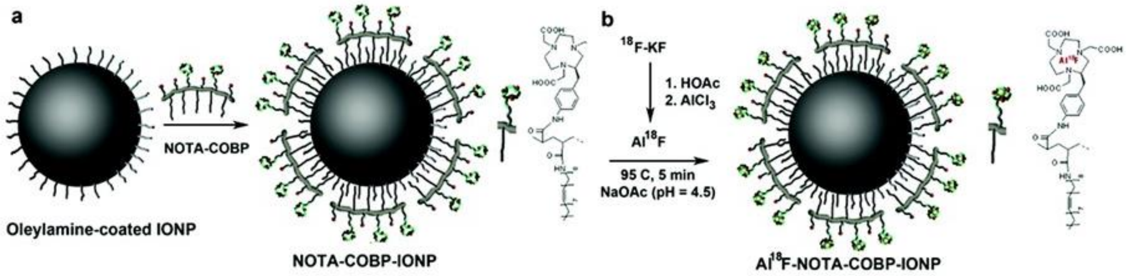

Fig. 3.3. (a) Coating the IONPs with a layer of comb-like oleylamine-branched polyacrylic acid (COBP)-NOTA, and (b) chelating ^{18}F-aluminum fluoride ions with NOTA on COBP-NOTA functionalization of IONPs [192].

3.2.1.3. Radiolabeling via DTPA-based chelators

A polydentate acyclic chelator, DTPA is commonly used in the construction of MRI and nuclear imaging agents [255, 256, 244]. For radiopharmaceuticals, it has been used for labeling with many radiometal ions such as ^{99m}Tc [193, 194], ^{111}In [195], ^{67}Ga/^{68}Ga [197, 196], and ^{166}Ho [198]. Given its acyclic nature, DTPA and its derivatives can be readily labeled with metal radionuclides (matter of minutes) [244]. However, the resultant complexes demonstrate low *in vivo* kinetic stability. In a comparative study [199] using a thiolated DOTA (trimethyl2,2´,2´´(10 2(3-(tritylthio)-propamido)ethyl)-1,4,7,10 tetraazacyclododecane-1,4,7-trityl)triacetate) and a thiolated DTPA (2-[bis[2-[carboxymethyl-[2-oxo-2 (2sulfanylethylamino)ethyl] amino] ethyl] amino]acetic acid) to label a common AuNP nanoplatform with ^{67}Ga, it was found that the *in vivo* stability of ^{67}Ga-AuNPs was unequivocally higher if constructed with the thiolated DOTA than with the thiolated DTPA. Nevertheless, DTPA chelation complexes showed reasonable stability when used for ^{99m}Tc labeling of generation 2 (G2) PAMAM-functionalized AuNPs [200] and PEI-modified AuNPs [201], which was evidenced by the high quality of SPECT/CT imaging. In addition, because DTPA is a good chelator for indium-111 radiopharmaceuticals, radiolabeling of MNPs with ^{111}In has been reported through conjugation with thiolated DTPA, such as an AuNP nanoplatform functionalized with epidermal growth factor (EGF) [202]. Similarly, a multi-modality (fluorescence/MR/SPECT) imaging nanoprobe was so constructed on an IONP nanoplatform, which was coated by poly lactic-co-glycollic acid and conjugated with DTPA for ^{111}In-labeling [203].

3.2.1.4. Other chelators

In addition to DOTA, NOTA, DTPA, and their derivatives, there are other BFCs that have been used, though less commonly, for radiolabeling of MNPs [209, 207, 208, 205, 210, 204, 206]. Among them, 6-hydrazinonicotinamide (HYNIC) plays an important role if ^{99m}Tc is the radionuclide of choice. Although DTPA can be used for ^{99m}Tc-labeling of MNPs as described above, HYNIC is of particular importance as it is commonly used in the design and synthesis of ^{99m}Tc radiopharmaceuticals [257-259]. Not surprisingly, HYNIC has been reported for ^{99m}Tc-labeling of AuNPs via a short peptide linkage, HYNIC-Gly-Gly-Cys-NH_2 (HYNIC-GGC), where the thiol group is incorporated for its attachment to the surface of AuNPs [211]. Due to the high radiochemical stability, the AuNPs were evaluated for sentinel lymph node (SLN) detection via SPECT imaging. Similarly constructed ^{99m}Tc-labeled AuNPs were also reported for cancer imaging via SPECT when conjugated with specific ligands to target gastrin-releasing peptide receptors (GRP-r) and alpha-v-beta-3 integrin ($\alpha_v\beta_3$) [212, 150]. Recently, the first silver-based SPECT imaging nanoprobe was reported using this HYNIC approach for ^{99m}Tc-labeling of AgNPs [213].

Besides HYNIC, diphosphate can also be used for ^{99m}Tc labeling of MNPs, given that ^{99m}Tc-labeled methylene diphosphate (^{99m}Tc-MDP) is an FDA approved bone scan agent. To do so, a methylene diphosphate moiety needs to be incorporated into the surface coating of MNPs or other linkages. For instance, ^{99m}Tc-labeling of IONPs can be readily realized by replacing the oleate ligand on IONPs with an asymmetric PEG containing the diphosphate functionality [214]. Such an approach was also reported for ^{99m}Tc labeling of $NaGdF_4$:Yb,Tm,Ca@$NaLuF_4$ core@shell upconversion NPs [215]. Other bisphosphonate functionalities can also be exploited for ^{99m}Tc labeling of MNPs. For instance, dipicolylamine-alendronate (DPA-ale) has been used to coat ultrasmall IONPs (USIONPs) [217], super paramagnetic IONPs (SPIOs) namely Endorem/Feridex [218], and Ferucarbotran/perimag-COOH [219] for ^{99m}Tc labeling to enable SPECT imaging. Indeed, the methylene diphosphate (or 1,1-bisphosphonate) moiety and its derivative can find applications in the functionalization and surface modification of metal oxide NPs because of their high affinity to metal oxide in addition to facilitating ^{99m}Tc labeling of MNPs.

Currently most of FDA-approved nuclear medicine agents are ^{99m}Tc-based [260, 261]. Therefore, the chelating moieties that have been used in ^{99m}Tc radiopharmaceuticals can technically all be used to design and construct MNPs for ^{99m}Tc labeling. MAG3 is an FDA approved agent for renography. As such, it has been used as a chelating agent to label AuNPs with ^{99m}Tc [222] for SPECT imaging of atherosclerotic plaques containing apoptotic macrophages (AuNPs conjugated with Annexin V).

It is noteworthy that a common acyclic chelator, dithiocarbamate (DTC), can also be used to label metal oxide NPs, as DTC binds to virtually all transition metals. For instance, DTC was reported for ^{64}Cu labeling of IONPs [216]. However, the long-term stability of ^{64}Cu-DTC could be a potential issue. A polydentate acyclic chelator, DFO natively binds Fe^{3+} [262]. As such, this acyclic chelator has been employed for ^{68}Ga- and ^{89}Zr-labeling of IONPs [221, 220]. Of note, the complex moiety of ^{68}Ga-DFO or ^{89}Zr-DFO is highly stable *in vivo*, and as such, they have been employed in FDA-approved clinical trials [263-266].

3.2.2. Indirect radiolabeling through prosthetic groups

An important consideration about indirect radiolabeling via chelators is that the radiolabel can potentially suffer from issues of radiometal trans-chelation *in vivo* upon interaction with a large number of native biological chelators and ions including transport proteins, storage proteins, and metal-containing enzymes inside the body [267, 244]. A technique to minimize this problem is by employing non-metallic radionuclides instead of metallic radionuclides [242]. The most common non-metallic radioisotopes which are covalently bound to MNPs through prosthetic groups are ^{11}C [224], ^{14}C [225], ^{18}F [226], ^{123}I [156], ^{124}I [227], ^{125}I [229, 228, 230], and ^{131}I [231].

[^{18}F]-fluoro-2-deoxy-D-glucose (^{18}F-FDG) is the most commonly used PET imaging agent for non-invasive assessment of glycolysis. It has been used for radiolabeling AuNPs [232]. For this purpose, cysteamine was first conjugated to mannose triflate (Man-CA) before ^{18}F labeling, leading to a cysteamine linked radiotracer (^{18}F-FDG-CA) after ^{18}F labeling. Then, ^{18}F-FDG-CA was mixed with gold chloride ($HAuCl_4$) to obtain AuNPs. In addition, silicon-fluorine (SiFA-SH) [233] and N-succinimidyl-4-fluorobenzoate (SFB) [234] prosthetic groups were also used for ^{18}F-labeling of AuNPs. Dextran-coated IONPs have also been radiolabeled with ^{18}F. In a study by Nahrendorf et al. [235], dextran-coated IONP surface was first functionalized with amines and then reacted with hydroxysuccinimide-derivatized fluorochromes and azides for click-reacting short ^{18}F-labeled PEGs to the MNPs. Comprised of ^{18}F and a far-red fluorochrome, these IONP-based nanoprobes were capable of dual-modality imaging of fluorescence-mediated tomography (FMT) and PET, which could enable parallel interrogation of up to five molecular targets for imaging cancers in mouse models. Recently, arginyl-glycyl-aspartic acid (RGD) peptides have attracted much attention as a potent targeting ligand due to their low immunogenicity, high stability, and ease of synthesis [236]. Additionally, cyclic RGD (c-RGD) peptides provide 30-

times higher stability and integrin $\alpha_v\beta_3$ binding affinity compared to their linear counterparts. They have been used for ^{125}I-labeling of Fe@Fe_3O_4 NPs (see Fig. 3.4) [237, 238] after incorporating a tyrosine moiety for radioiodination. Replacing ^{125}I with ^{123}I/^{124}I, or ^{131}I could enable SPECT/MR, PET/MR, or radiotherapy, respectively [268].

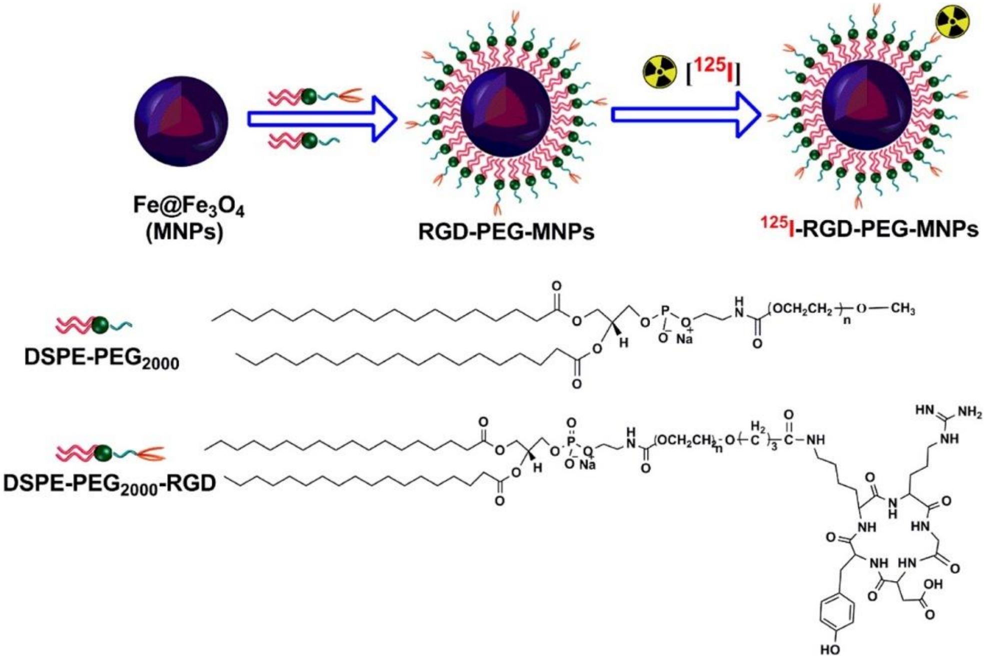

Fig. 3.4. Schematic presentation of Fe@Fe_3O_4 NPs conjugation with DSPE-PEG_{2k}-RGD and subsequent addition of Na^{125}I to synthesize the ^{125}I-RGD-PEG-MNPs [238].

The same radioiodination approach can be applied to label other MNPs. For instance, Black et al. [239] radiolabeled AuNPs with ^{125}I through a tyrosine moiety, in addition to ^{111}In or ^{64}Cu via a DTPA BFC. The ^{125}I-labeled AuNPs were used for multispectral SPECT imaging of the expression level of matrix metalloproteinase-9 (MMP9) in tumors after conjugation with an MMP9-cleavable peptide. Recently, an interesting multifunctional ultrasmall MNP system was reported through simple coordination reactions between ferric ions and gallic acid (GA) in presence of polyvinylpyrrolidone (PVP) in aqueous solution [240]. The resulting Fe^{3+}/GA/PVP complex NPs (FGPNs) were stable due to the surface capping with PVP. The radiolabeling of FGPNs with ^{125}I or other iodine radionuclides is straightforward due to the presence of GA. As such, the ^{125}I labeled FGPNs were evaluated for their *in vivo* pharmacokinetics by SPECT imaging. The results indicated that the ultrasmall multifunctional FGPNs might be of potential to be developed as theranostic agents capable of SPECT/photoacoustic (PAI)/MR imaging and photothermal therapy (PTT) because of their colloidal stability, low toxicity, intrinsic photothermal conversion ability, and paramagnetic characteristics of Fe/GA complexes.

3.3. Direct radiolabeling

For indirect radiolabeling, it is important to consider whether or not the addition of a BFC or a prosthetic group might negatively impact the biological behaviors of the resulted MNPs, because the modification may change the particle's size, surface charge, and hydrophilicity [267, 269]. Besides, the probable detachment of radionuclide *in vivo* may result in erroneous interpretations of the particles' distribution, which is the main determinant of MNP's potential biomedical applications [267]. Hence, chelator-free radiolabeling strategies have gained attention in the field to overcome the potential issues [152]. Through direct and chelator-free radiolabeling, MNPs were incorporated with proper radionuclides via surface interactions, while maintaining their native pharmacokinetic characteristics [269]. Furthermore, the range of radionuclides for radiolabeling MNPs can be broadened because the limitation of chelator selection does not exist in order to achieve stable radiolabeled nanoformulations *in vivo* [270]. Summarized in Table 3.2 are recently reported direct radiolabeling methods for MNPs.

Table 3.2. Direct MNPs radiolabeling techniques.

Metal nanoparticle	Radionuclide	Therapeutic and/or imaging function	Reference
Chemisorption			
$Al(OH)_3$ HA (hydroxyapatite)	^{18}F	PET	[271]
Gd-UC ($NaYF_4$ (co-doped with Yb, Er, Tm, Gd)	^{18}F	PET, MRI, RLI	[272]
$Gd^{3+}/Yb^{3+}/Er^{3+}$ co-doped $NaYF_4$	^{18}F	PET, MRI, UCL	[273]
USPd nanosheets	^{125}I	SPECT, PTT	[274]
AgNPs	^{125}I	SPECT	[275]
AuNPs	^{125}I	RT	[276]
AgNPs	^{125}I	---	[277]
Au nanorods	^{125}I	---	[278]
$KGdF_4$	^{18}F	PET, MRI	[279]
Fe_3O_4-Ag heterodimer	^{125}I	SPECT, MRI	[280]
TiO_2-Ag NPs	^{211}At	RT	[281]
AuNPs	^{211}At	RT	[282]
AuNPs	^{211}At	RT	[283]
AgNPs	^{211}At	---	[284]
CuNCs	^{64}Cu	---	[285]
Fe-GA-PEG CPNs	^{64}Cu	PET, MRI, PAI, NIRF, PTT	[286]
W-coordination polymer NDs (W-GA-PEG-CPNs)	^{64}Cu	PET, RT	[287]
Au nanorods	^{64}Cu	---	[288]
CDPGMNPs	^{64}Cu	PET, MRI, PAI, PTT	[289]
Silica-coated IO nanorods	^{68}Ga	---	[290]
SiO_2-coated IONPs	^{68}Ga	PET, MRI	[291]
IONPs	^{67}Ga ^{68}Ga	PET or SPECT	[292]
SiO_2-coated AuNPs	^{68}Ga	PET, SERS	[293]
USIONPs	^{89}Zr	PET	[294]
M_xO_y	^{89}Zr	PET, MRI	[295]

M : Gd, Ti, Te, Eu, Ta, Er, Y, Yb, Ce, and Mo, x : 1-2, y = 2-5			
MNPs (($Zn_{0.4}Mn_{0.6}$)Fe_2O_4)	^{89}Zr	PDT	[296]
Feraheme	^{89}Zr	PET	[297]
Gd_2O_2S:Eu NPs	^{89}Zr	PET, RLI	[248]
Mn_3O_4 NPs	^{89}Zr	PET, MRI	[298]
Iron-doped hydroxyapatite (FeHA)	^{99m}Tc	PET, MRI or SPECT, MRI	[299]
Cu-Fe-Se (CFS) NSs	^{99m}Tc	SPECT, PAI, PTT	[300]
$ZnFe(CN)_5NO$ NSs	^{32}P	CL, FLI, RT-ICB	[301]
AuNPs	^{99m}Tc	---	[302]
CaBP NPs	^{99m}Tc ^{32}P	RT	[303]
AuNPs	^{125}ln	SPECT	[304]
IONPs	^{111}In	SPECT, MRI	[305]
IONPs	^{71}As ^{72}As ^{74}As ^{76}As	PET, MRI	[306]
IONPs	^{69}Ge	PET, MRI	[307]
IONPs	^{223}Ra	---	[308]
$Co_xFe_{3-x}O_4$@$NaYF_4$ core-shell	^{18}F ^{64}Cu ^{99m}Tc	PET, SPECT, MRI, UCF	[309]
Feraheme	^{89}Zr or ^{64}Cu for PET ^{111}In for SPECT	PET, MRI or SPECT, MRI	[310]
CuS	^{64}Cu	PET, PTT, NIRF	[311]
Radiochemical doping			
AuNPs	^{64}Cu	PET	[312]
AuNPs	^{64}Cu	PET, CRET, NIRF	[313]

AuNPs	^{64}Cu	PET	[314]
AuNPs	^{64}Cu	PET	[315]
AuNPs	^{111}In	---	[316]
AgNPs	^{131}I	---	[317]
IONPs	^{68}Ga	PET, MRI	[318]
GdF_3 NPs	^{90}Y	---	[319]
CuS NPs	^{64}Cu	PET, NIRF	[83]
CuS NPs	^{64}Cu	PET, NIRF, RT, PTT	[320]
CuS NPs	^{64}Cu	---	[321]
CuS NPs	^{64}Cu	PET	[322]
AuNCs	^{64}Cu	PET	[323]
Au nanocages	^{64}Cu	PET	[324]
IONPs	^{111}In ^{125}I	SPECT	[325]
IONPs	^{59}Fe ^{14}C ^{111}In	SPECT, MRI	[326]
AuNPs	^{198}Au	PET, PAI, RLI	[327]
AuNPs	^{198}Au	---	[328]
AuNPs	^{198}Au	---	[329]
Au nanocages	^{198}Au	CL	[330]
AuNPs	^{199}Au	SPECT	[331]
AgNPs	^{110m}Ag	---	[332]
CeO_2 NPs	$^{141}CeO_2$	---	[333]
AuNPs	^{199}Au	---	[334]
PdCu@Au tripods	^{64}Cu	PET, MRI	[335]
$LaPO_4$ NPs	^{225}Ac	RT	[336]
Multilayered $LaPO_4$	^{225}Ac	RT	[337]
Au/$LaPO_4$	^{225}Ac	RT	[338]
$LaPO_4$ core, $LaPO_4$ core + 1 $LaPO_4$ shell, and $LaPO_4$ core + 2 $LaPO_4$ shells	^{223}Ra ^{225}Ra/^{225}Ac	TAT	[339]
Hadronic bombardment			

HA-Gd NRs	^{159}Gd ^{32}P	RT	[340]
AuNPs	^{198}Au	---	[341]
HoIG-Pt	^{166}Ho	---	[342]
CeO_2 NPs	^{141}Ce	---	[343]
TiO_2 NPs	^{48}V ^{7}Be	---	[344]
CeO_2 NPs	^{139g}Ce, ^{141}Ce, and ^{143}Ce	---	[345]
AuNPs	^{111}Ln ^{198}Au	---	[346]
AuNPs	^{198}Au/^{14}C	PET or SPECT	[347]
AuNPs	^{198}Au	---	[348]
AuNPs	^{195}Au	---	[349]
AuNPs	^{198}Au	---	[350]
AgNPs	^{110m}Ag	---	[351]
Co/Co_3O_4 Ag CeO_2	^{60}Co ^{110m}Ag ^{141}Ce	---	[352]
CeO_2 ZnO SiO_2-coated CeO_2 SiO_2-coated ZnO	^{141}Ce ^{65}Zn	---	[353]
CeO_2 NPs	^{141}Ce	---	[354]
CeO_2 NPs	^{141}Ce	---	[355]
ZnO $Zn(NO_3)_2$	^{65}Zn	---	[356]
Al_2O_3 NPs	^{13}N	PET	[357]
TiO_2 NPs	^{18}F	PET	[358]
Isotope exchange			
AgNPs	^{110m}Ag	---	[359]
TiO_2 NPs	^{44}Ti ^{45}Ti	---	[344]

IONPs	^{59}Fe	PET, MRI or SPECT, MRI	[360]
IONPs	^{59}Fe	---	[361]
IONPs	^{59}Fe	---	[362]
Ion exchange			
HA:Gd NRs	^{153}Sa	SPECT, MRI	[363]
Mg_2Al-based Layered double hydroxide (LDH)	^{64}Cu ^{44}Sc	PET	[364]
TiO_2 NPs	^{225}Ac	RT	[365]
AuNPs	^{124}I ^{125}I	---	[366]
AuNPs	^{124}I ^{125}I	---	[367]
IO/MoS_2 nanocomposite	^{64}Cu	PET, MRI, PAT, PTT	[368]
rGO-MnO_2 nanocomposites	^{131}I	MRI, FLI, RT	[369]
$FeSe_2$-decorated Bi_2Se_3 NSs	^{64}Cu	PET, MRI, PAI, PTT	[270]

3.3.1. Chemisorption

Chemisorption involves a direct chemical bond formation between the radionuclide and the MNP surface. For radiolabeling of MNPs, chemisorption synthesis is carried out in solution by mixing the radionuclides with MNPs that have high affinity towards the radionuclides. There are several non-metallic radionuclides adsorbed onto MNPs by this method, such as ^{18}F [271, 273, 272, 279], ^{125}I [278, 276, 275, 277, 280, 274], and ^{211}At [284, 281-283]. These radionuclides are attached to the surface of MNPs based on the strong affinity between halogen and metal surface [370-372]. For instance, Au nanorods were radiolabeled with ^{125}I by leveraging the strong interaction of the radionuclide with AuNPs and its capability to replace citrate functionalization on the surface of AuNPs (Clanton et al., 2018 [276]. The synthesized AuNPs could be stabilized rapidly upon the addition of sodium citrate and thus further addition of ^{125}I did not cause any aggregation. Another study proposed a solution for binding of ^{211}At to MNPs, which consists of

TiO_2 NPs modified with Ag atoms acting as carriers for ^{211}At [281]. Silver cations were adsorbed onto the TiO_2 NPs through ion exchange and then reduced by Tollens' reaction. The obtained TiO_2-Ag NPs could be readily radiolabeled with ^{211}At based on the high affinity of astatine towards the metallic silver.

Based on the Pearson acid-base concept, in which soft and hard Lewis acids react faster and form stronger bonds with soft and hard Lewis bases, respectively [373], various MNPs can be directly radiolabeled with metal radionuclides such as ^{64}Cu [285, 288, 287, 286, 289], ^{67}Ga and ^{68}Ga [290-293], ^{89}Zr [294, 297, 248, 296, 298, 295], ^{99m}Tc [302, 300, 303, 299], *In (* = 111 and 125) [304, 305], *As (* = 71, 72, 74, and 76) [306], ^{69}Ge [307], and ^{223}Ra [308].

Of particular interest is using hard Lewis radiometal ions (e.g., $^{67/68}$Ga, ^{64}Cu, ^{111}In, ^{99m}Tc, and ^{89}Zr, etc.) to directly label MNPs that present electron-rich atoms such as nitrogen, oxygen, and sulphur through chemisorption. For instance, Feraheme (FH) NPs, which can be used for treating anemia, have been radiolabeled with $^{89}Zr^{4+}$ or $^{64}Cu^{2+}$ for PET, $^{111}In^{3+}$ for SPECT [310] for non-invasive monitoring of the MNP's tissue distribution profiles. Similarly, CuS NPs, which possess consistent NIR absorbance and are cheaper comparing the other photothermal probes such as AuNPs [374], have been radiolabeled with $^{64}Cu^{2+}$ for both PET imaging and PTT [311]. Of note, for such direct radiolabeling via chemisorption, temperature may be increased to facilitate the labeling as necessary under the condition that the high temperature would not be detrimental to the MNP's physicochemical properties.

Recently, MNPs have been reported for targeted delivery of toll-like receptor 9 (TLR-9) agonists (CpGs). Shown in Fig. 3.5 is an MNP system that consists of an IONP nanoplatform directly labeled with ^{67}Ga or ^{68}Ga to enable imaging (SPECT or PET, respectively), whose surface was coated with both ovalbumin and toll-like receptor 9 agonists (CpGs) through lipid micelles

[292]. The magnetite-filled PEGylated phospholipid (PEG-PLs) micelles are thought to promote direct attachment of $^{67}Ga^{3+}$ (or $^{68}Ga^{3+}$) ions and protect the radiolabel from *in vivo* dissociation. Impressively, the ovalbumin coated IONP micelles were able to improve the magnitude of immunoglobulin G1 (IgG1) and immunoglobulin G2a (IgG2a) ovalbumin specific antibody responses by more than 2 times in the test animal model. Together with loaded toll-like receptor 9 agonists, ovalbumin-coated IONPs triggered strong immunostimulatory response in targeted organs (spleen and lymph nodes) and stopped the systemic release of proinflammatory cytokines, as compared to viral nucleic acids which lead to a widespread systemic immune activation.

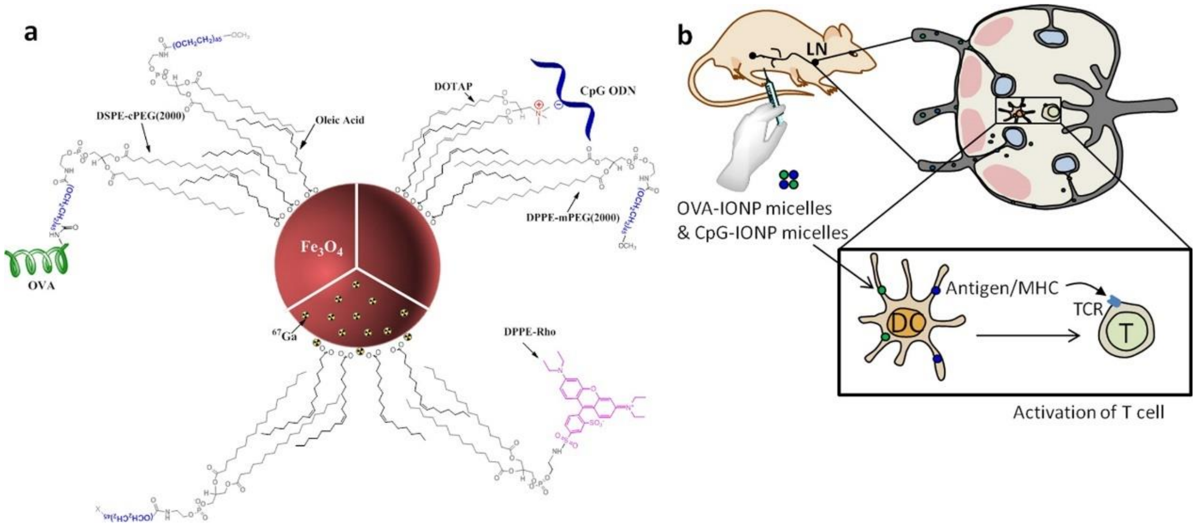

Fig. 3.5. (a) Schematic OVA and CpG lipid micelles presented on an IONP core directly labeled with 67Ga and (b) Microdosing of the nanosystem developed to deliver vaccine components to secondary lymphoid organs such as the lymph nodes [292].

In addition to electron-rich nitrogen, oxygen, and sulphur, ^{99m}Tc also exhibits high affinity towards phosphorus and selenium atoms. When these electron-rich atoms presented in an MNP system, direct ^{99m}Tc labeling of the MNPs can be considered. Two-dimensional (2D) nanomaterials are another type of MNPs which exhibit superior physiochemical properties, making them attractive for biomedical applications [375]. Jiang et al. [300] reported the synthesis of Cu-Fe-Se nanosheets (CFSNSs), a 2D MNP system, using a sequential co-precipitation approach, followed by surface functionalization with doxorubicin (DOX) anticancer drug via a PEG linker (NH_2-PEG_{2k}-NH_2). Because of the presence of selenium, the 2D MNPs were directly labeled with ^{99m}Tc through surface adsorption. The drug loaded (CFSNs@DOX) exhibited excellent enhanced antitumor efficiency by combining chemo/photothermal therapy. Tian et al. [301] synthesized ZnNO 2D nanosheets including zinc ions and sodium nitroprusside as a clinical drug. By ^{32}P-labeling of this 2D structure, CL emission causes persistent release of NO which can be used to modulate hypoxic immunosuppressive tumor microenvironment (TME), resulting in complete destruction of tumor by combined RT- immune-checkpoint blockade (ICB) therapy. For sequestration of the alpha emitter ^{225}Ac and its decay products, Cędrowska et al. [365] proposed the use of TiO_2 NPs which exhibit high affinity for $^{225}Ac^{3+}$ and its daughter radionuclides $^{211}Fr^{+}$ and $^{213}Bi^{3+}$. The radiolabeled MNPs could retain ^{225}Ac in phosphate-buffered saline (PBS), physiological salt, and cerebrospinal fluid (CSF) for up to 10 days. Regarding the daughter radionuclides, about 30% leaching of ^{221}Fr radioisotope, which is the first decay daughter of ^{225}Ac, was detected only in CSF after 10 days.

Hybrid MNPs can be designed as multimodal imaging agents with a well-organized core-shell structure to facilitate MNP core and surface modifications. Cui et al. synthesized $Co_xFe_{3-x}O_4$@$NaYF_4$ core-shell-based NPs, in which the shell was co-doped with lanthanide cations providing optical imaging capabilities [309]. Because of the presence of the YF_4^- moieties and electron-rich oxygen atoms in these core-shell NPs, direct radiolabeling of the core-shell NPs can be done with [^{18}F]-fluoride and hard Lewis radiometal ions, such as $^{67/68}$Ga, ^{64}Cu, ^{99m}Tc, and

^{89}Zr, respectively. Indeed, the authors labeled the NPs with ^{18}F, ^{64}Cu, and ^{99m}Tc (though its labeling could be through DTCBP and DPA-ale conjugates as well) in the report.

3.3.2. Radiochemical doping

Radiochemical doping refers to a direct radiolabeling process that the radionuclide is incorporated into its cold counterpart or surrogate of the reagents for the synthesis of MNPs, which results in intrinsically radioactive MNPs with high radiolabeling yield and stability [156, 267, 151]. Although this method forms highly stable radioactive MNPs, the increased radiation exposure during their production is a significant working hazard [376]. Therefore, automation of the synthesis in a lead-shielded unit should be considered if a large amount of radioactivity is to be used. Based on similarities between radioactive and non-radioactive isotope cations, this technique can be divided into two subcategories of hetero-radionuclide and homo-radionuclide. In case of hetero-radionuclides, the MNP core cation and the radionuclide are different, such as doping AuNPs with ^{64}Cu [315, 313, 314, 312], AuNPs with ^{111}In [316], AgNPs with ^{131}I [317], IONPs with ^{68}Ga [318], AuNCs with ^{64}Cu [323], GdF_3 NPs with ^{90}Y [319], and CuS NPs with ^{64}Cu [320, 377, 321, 322]. A typical example of such radiochemical doping methods is illustrated in Fig. 3.6 [324]. For radiolabeling, a trace amount of $^{64}CuCl_2$ was added to the mixture of $HAuCl_4$ and $CuCl_2$, which was reduced onto the AuNCs by ascorbic acid in presence of NaOH and PVP for surface-coating, that was then replaced with methoxy-PEG_{2k}-SH.

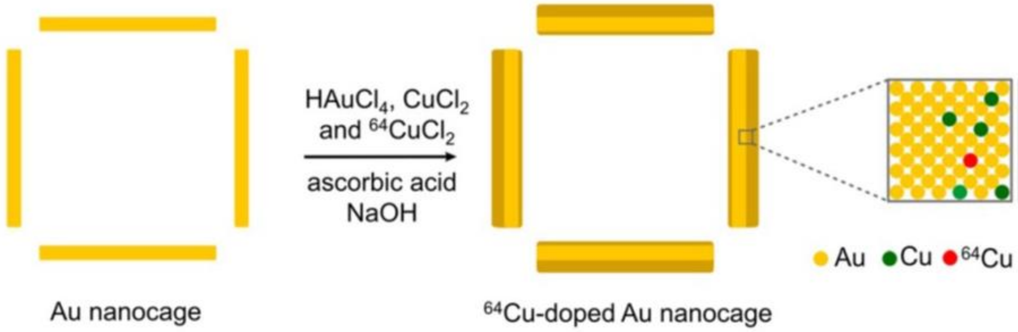

Fig. 3.6. Schematic synthesis of ^{64}Cu-doped Au nanocages via co-deposition of Au and Cu atoms on the pre-synthesized Au nanocages and subsequent ^{64}Cu-labeling through radiochemical doping technique [324].

Multifunctional MNPs feature multiple functionalities presented on a single nanoplatform. As such, the integrity of the nanosystem is essentially important. Radiolabeling of different components of a multifunctional MNP system with different radionuclides emitting γ-rays with distinct energies enables non-invasive imaging evaluation of the *in vivo* integrity of the nanosystem. Llop et al. [325] assessed the *in vivo* stability and degradation of PLGA-IONPs that were dual-labeled with ^{111}In and ^{125}I. During IONP formation, ^{111}In was co-precipitated into the core, followed by NP surface-coating with PLGA, and surface-adsorption of bovine serum albumin (BSA), which was then radiolabeled with ^{125}I. The biodistribution results illustrated that the MNP core and coating behaved differently *in vivo*, with slow dissociation of ^{125}I from the NPs into the thyroid. While the ^{111}In-core was retained in the liver until 6 days post-injection (p.i.), the ^{125}I activity was almost completely cleared indicating that *in vivo* deiodination is a serious issue to be considered. A similar observation was reported with IONPs radiolabeled with ^{59}Fe, ^{14}C, and ^{111}In via radiochemical doping, chemisorption, and chelation techniques, respectively [326]. The radiolabeling was performed sequentially. To radiolabel with ^{59}Fe, a small volume of ^{59}Fe^{3+} chloride solution was added to the mixture of ferrous and ferric chloride solution before ammonia addition. Next, IONPs were coated by ^{14}C-oleic acid in solution. Finally, ^{111}ln-labeling was conducted by attaching 1,2-dimyristoyl-sn-glycero-3-phosphoethanolamine-N-diethylenetriaminepentaacetic acid (DMPE-DTPA) to the IONPs and subsequent incubation with ^{111}In citrate at room temperature for 1 hour. The biodistribution studies enabled by the three distinct radiolabels demonstrated that the dissociation of the surface components from the core was not a negligible issue.

The main problem of hetero-radionuclide approach is the potential dissociation of the metallic radionuclide from the MNPs or the add-on radiolabel component may change the physicochemical properties of the radiolabeled-MNPs. Some of the changes may be detrimental to the biomedical applications of MNPs. An alternative is to employ the homo-radionuclide doping, in which a radioisotope of the metal element to form the MNP core is used. Given the identical chemical properties of the radioisotope to the cold element, the MNP synthesis and more importantly the MNP's properties would stay the same. This approach has been exploited extensively as well for radiolabeling of MNPs, such as making homo-radionuclide labeled AuNPs by adding $H^{198}AuCl_4$ to $HAuCl_4$ [328, 330, 327, 331, 329], AgNPs from $^{110m}AgNO_3$ and $AgNO_3$ [332], and CeO_2 NPs from $^{141}Ce(NO_3)_3$ and $Ce(NO_3)_3$ [333]. Displayed in Fig. 3.7 is a typical homo-radionuclide doping method for radiolabeling of AuNPs with ^{199}Au [334], whose surface was conjugated with a cyclic-RGDfK peptide as a cancer targeting molecule. Biodistribution studies of the ^{199}Au-labeled AuNPs in relevant mouse xenograft models confirmed the tumor targeting specificity of the AuNPs. Further experiments indicated that this AuNP system might find applications in neoadjuvant brachytherapy for $\alpha_v\beta_3$-overexpressing cancers.

If the core of an MNP system is formed by more than one metal elements, the radioisotope of any of the elements if available can be used for direct radiochemical doping labeling of the

MNP system. For instance, ^{103}Pd, ^{64}Cu, or $^{198/199}$Au can be used for direct radiochemical doping/labeling of a PdCu@Au core-shell tripod nanosystem. Indeed, ^{64}Cu-labeled PdCu@Au core-shell tripods were reported [335], in which ^{64}Cu was directly incorporated into the crystal lattice of Pd-Cu core and a conformal Au shell was formed on it to prevent Cu and Pd atoms from being leached out.

Recently, targeted radiotherapies with α-emitters have gained a tremendous momentum partially powered by the availability of the radionuclides made by the National Isotope Development Center (https://www.isotopes.gov/catalog), such as $^{223/225}$Ra and ^{225}Ac. Radiolabeling of MNPs with these α-emitters through BFCs suffers from the fact that their daughter isotopes are often also radioactive, but do not have good binding affinity towards the BFCs. Consequently, the hazardous daughter radioisotope engenders a severe concern for the further advancement of the MNPs to translational or clinical use. Direct labeling of MNPs with α-emitters may potentially overcome this problem if they are doped into the core of MNPs or shielded components so that their daughter radioisotopes can be locked *in situ* as well. For instance, Woodward et al. [336] incorporated ^{225}Ac into lanthanum phosphate ($LaPO_4$) NPs via radiochemical doping, followed by surface-modification with 6-aminohexanoic acid, which enabled conjugation with the monoclonal antibody 201B targeting thrombomodulin in the lung endothelium of mice. While the MNPs showed high lung uptake (e.g., ~30% of the injected dose at one hour post-intravenous (IV) injection), it was found that more than 80% of the daughter radionuclide (^{213}Bi) stayed together with the MNPs even after 120 hours p.i. The target retention of ^{213}Bi can be further increased by employing a multi-layered approach as in $(Gd_{0.5}La_{0.5})(^{225}Ac)PO_4@4GdPO_4$ shell@AuNPs. Later, the desirable targeted alpha therapy (TAT) was achieved by similar MNP nanosystems [338, 337]. Moreover, it was confirmed that the core

$LaPO_4$ and core-shell (with up to two shells) MNPs [339] can be used as effective nanocarriers for TAT with $^{223/225}$Ra and ^{225}Ac, as they successfully retained both, the α-emitters and their daughter radioisotopes, within the MNP matrix over an extended period longer than 35 days.

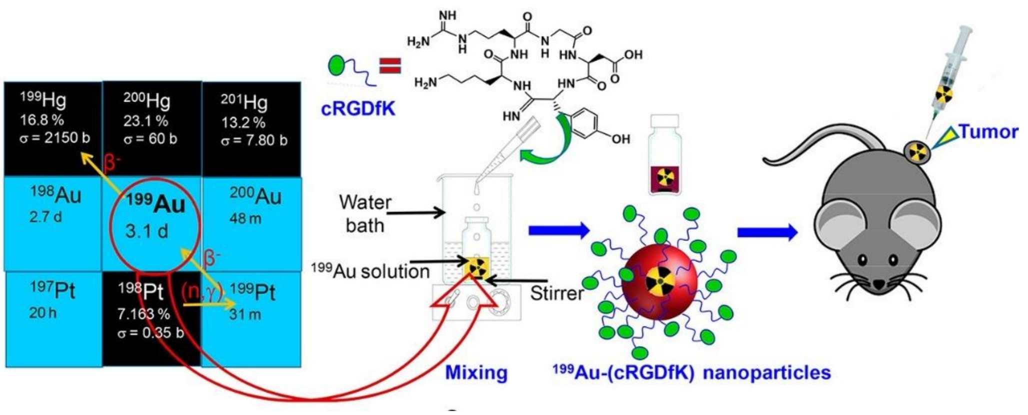

Fig. 3.7. A schematic illustration of direct radiolabeling of AuNPs via homo-radionuclide doping with ^{199}Au [334].

3.3.3. Hadronic bombardment

Hadronic bombardment is performed by irradiating the pre-fabricated MNPs via accelerated particles, such as neutrons [341-343, 340], protons [344, 359], or deuterons [345], to induce nuclear reactions converting the stable isotopes in MNP lattice to radioisotopes, thus resulting in radiolabeled MNPs [154]. Since the induced nuclear reactions occur at the level of nuclei, whose yields are determined by the cross sectional area of the corresponding nuclei [378], the radiolabeling of the MNPs by this approach can be technically controlled by the beam-line energy, current, and bombardment time. However, because the beam-line energies (often > 10 MeV) are orders of magnitude higher than chemical bonding energies (< 10 eV), most MNPs are not able to survive the heat generated by the bombardment if no effective heat dissipation techniques are employed for the process. In other words, as a prerequisite for this method to be used for radiolabeling of MNPs, the integrity of the MNPs must be maintained, as issues such as structural damages caused by high energy beam bombardment may often occur and are still not so controllable. Because the damages have to be identified during characterization after the bombardment, along with the induced radioactivity the defective MNPs may become of no use to *in vivo* applications [379]. No need to mention, this method is highly resource demanding and costly as a high energy particle accelerator or nuclear reactor is required for the hadronic bombardment.

In cases that an MNP can sustain the hadronic bombardment, this method possesses advantages for consideration. For instance, because the MNPs are already fully synthesized and characterized, they can be bombarded for radiolabeling as needed [152] and therefore very short-lived radionuclides can be exploited for imaging applications as long as a sufficient amount of radioactivity can be produced by a short bombardment. If the induced element conversion is deep within the MNP matrix, the resultant radioactive signals would faithfully reflect the distribution of the MNPs. However, this can hardly be realized in reality, because all the nuclei presented in the MNPs facing the beam-line are bombarded, which often generates radioisotopes outside the matrix as well as unwanted radioactive impurities that are detrimental to further biomedical applications. To date, many MNP nanosystems have been reported with reasonable suitability for hadronic bombardment radiolabeling in order to enable non-invasive and quantitative tracking of their *in vivo* distribution, such as AuNPs [348, 350, 349], AgNPs [351, 352], CeO_2 NPs [354, 355, 352, 353], ZnO and $Zn(NO_3)_2$ NPs [356, 353], and Co and Co_3O_4 NPs [352].

An interesting example of using very short-lived radionuclides induced by hadronic bombardment for imaging was presented in a report by Pérez-Campaña et al. [357]. Shown in Fig. 3.8, under the bombardment of a 16 MeV proton beam (current = 5 μA, irradiation time = 6 min), the ^{16}O nuclei in Al_2O_3-NPs that were placed in a solid aluminium target capsule were transformed into ^{13}N ($t_{1/2}$ = 9.97 min) *via* ^{16}O(p,α)^{13}N nuclear reaction. Because of the strong chemical bonding of Al-O and Al-N, the resultant [^{13}N]Al_2O_3-NPs remain stable as long as they can sustain the proton bombardment. Followed by characterization and resuspension in saline, the [^{13}N]Al_2O_3-NPs were injected into rats for PET imaging up to an hour p.i. despite the short half-life of ^{13}N.

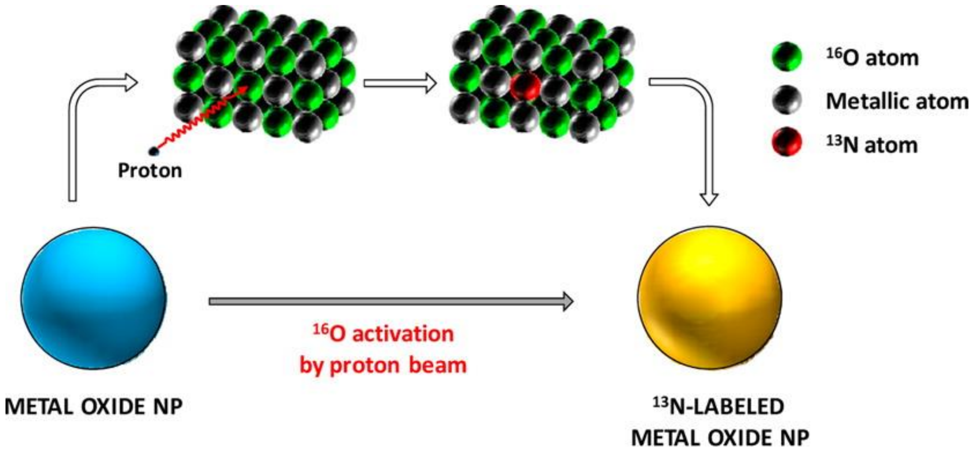

Fig. 3.8. Schematic production of [^{13}N]Al_2O_3 NPs by proton irradiation of Al_2O_3 NPs via the ^{16}O(p,α)$_{13}$N nuclear reaction [357].

The same group went further to apply this approach to make [^{18}F]TiO_2 NPs (^{18}F: $t_{1/2}$ = 110 min) via the ^{18}O(p,n)^{18}F nuclear reaction [358], by irradiating ^{18}O-enriched TiO_2 NPs using a 12.8 MeV proton beam (current = 5 μA, irradiation time = 6 min). As mentioned above, radioisotope impurities were also produced, such as short-lived ^{13}N and ^{47}V ($t_{1/2}$ = 32.7 min), and long-lived ^{44g}Sc ($t_{1/2}$ = 3.97 h) and ^{48}V ($t_{1/2}$ = 16 d), because all Ti isotopes and ^{16}O in the ^{18}O-enriched TiO_2 NPs along with other chemical impurities were irradiated by the proton beam as well. As these radioisotopes are all positron-emitters, factors that affect the quality of PET imaging with [^{18}F]TiO_2 NPs have to be considered judiciously. Thanks to the low positron-decay probabilities of ^{44g}Sc and ^{48}V, a delayed imaging that allows the complete decay of ^{13}N and ^{47}V can afford reasonable images of quality from [^{18}F]TiO_2 NPs. In addition, the authors performed the biodistribution studies of [^{18}F]TiO_2 NPs out to 7.7 hours p.i. and PET imaging after the short-lived radionuclides had decayed. Given its low abundancy and positron-emitting probability, ^{48}V did not interfere with the biodistribution quantifications. On the other hand, because of its long half-life, ^{48}V also facilitated the long-term quantification of *ex-vivo* measurements by γ-counting.

3.3.4. Isotope exchange

Isotope exchange is a radiolabeling process through chemical equivalent exchange between the stable and radioactive isotopes of an element in different chemical states [242]. Since the exchange is proportional to their molar ratio, this technique results in lower specific activity. In other words, when high specific activity is required for imaging or therapy, this method is not an option [156]. To date, a few MNP systems have been radiolabeled by this approach [359, 344, 360]. For instance, ^{59}Fe-labeled IONPs can be prepared by the isotope exchange method [361]. Functionalized with oleic acid, IONPs are soluble in chloroform. A simple incubation of IONPs with $^{59}FeCl_3$ could lead to 0.01-0.5% of the Fe^{3+} in the IONPs exchanged with ^{59}Fe. The resulting ^{59}Fe-labeled IONPs were stable. Recently, Pospisilova et al. [362] compared the radiolabeling methods of radiochemical doping and isotope exchange using the same ^{59}Fe-labeled IONP system. Shown in Fig. 3.9, radiochemical doping and isotope exchange afforded ^{59}Fe radiolabeled IONPs with 90% and 83% of ^{59}Fe-incorporation efficacy, respectively. Interestingly, the methods showed no impact on the size and morphology of IONPs. However, further assessment of radiochemical stability of the ^{59}Fe-IONPs revealed that ^{59}Fe incorporated via radiochemical doping was more stable than that via isotope exchange. This is likely due to the fact that the isotope exchange of

^{59}Fe/Fe only occurs on the surface of the IONPs but the ^{59}Fe atoms doped inside the core are more evenly distributed throughout the core.

We would like to note that the isotope exchange method presented in this section is similar or even identical to chemisorption described earlier unless the ferric ions displaced by ^{59}Fe are quantified to confirm the isotope exchange. Since ferric ions are a hard Lewis acid, they can be tightly bound to the hard Lewis base, namely the electron-rich oxygen atoms on the surface of IONPs.

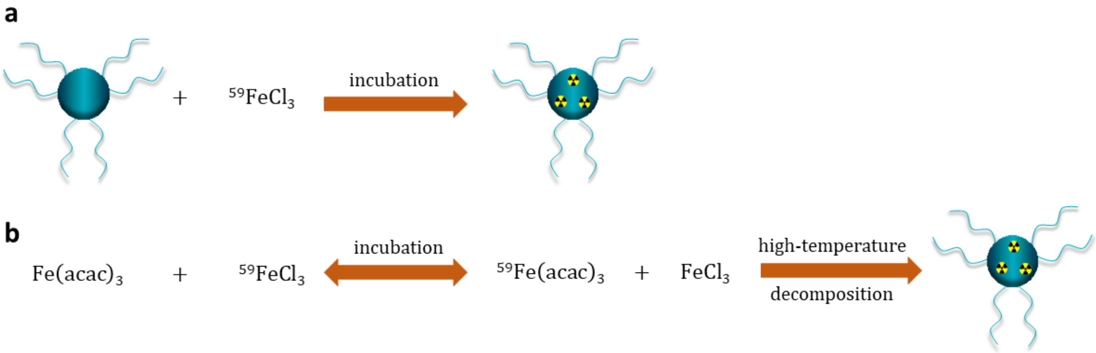

Fig. 3.9. Comparative preparation of ^{59}Fe-IONPs through (a) isotope exchange and (b) radiochemical doping techniques [362].

3.3.5. *Cation exchange*

Cation exchange is a cost effective and fast method developed recently. It is similar to the isotope exchange approach, but the process happens between a cation within an MNP and a different cationic radionuclide. The relative thermodynamic stability of the reactants compared to the products is the driving force for this mechanism [242, 151]. Because this new method still requires much improvement regarding the stability and the yield of resulting radioactive MNPs, its application is currently limited to only a few MNPs [153]. For instance, through the cation exchange of Ca^{2+} with $^{153}Sm^{3+}$, ^{153}Sm was rapidly labeled onto gadolinium-doped hydroxyapatite nanorods ($[Ca_{10}(PO_4)_6(OH)_2$; Gd]-NRs) [363] in quantitative yield (100%). Impressively the ^{153}Sm-labeled nanorods stayed intact in fetal bovine serum after 48 hours of incubation, indicating the effectiveness of this technique for radiolabeling of MNPs with radiotherapeutic lanthanides. Understandably, the valency of metal ions involved in the radiolabeling process of cation exchange plays a critical role. Indeed, it was found that the valency of radioisotope cations was a major determinant in the radiolabeling of Mg_2Al-based layered double hydroxide (LDH) MNPs [364]. While bivalent ($^{64}Cu^{2+}$) and trivalent ($^{44}Sc^{3+}$) cations exhibited superior cation exchange efficiencies with Mg^{2+} in the MNPs, tetravalent cation $^{89}Zr^{4+}$ failed to label the LDH-MNPs as it did not fit into the LDH crystal structure.

Apparently, the cation exchange is also similar or even identical to chemisorption unless the cations displaced by radiometal ions are quantified to confirm the exchange, because the radiometal ions are all hard Lewis acids with a strong tendency to bind with the electron-rich oxygen atoms on the surface of the NPs.

3.3.6. Encapsulation

Encapsulation is achieved by physically trapping the radionuclide of choice, or one of its chemical entities inside the native cavities or defects within MNPs [158], or the core-shell/layered structures of MNPs. Most of the time, it refers to the latter cases. As shown in Fig. 3.10, Lee et al. [366] synthesized radionuclide-embedded AuNPs (RIe-AuNPs) via encapsulation approach. They first modified the amine groups of the adenine-rich oligonucleotides pre-anchored on the surface of AuNPs (A10-AuNPs) with sulfosuccimidyl-3-[4-hydroxyphenyl]propionate (sulfo-SHPP) for radiolabeling with ^{125}I or ^{124}I, followed by reacting the MNPs with $HAuCl_4$ to create an Au shell to shield the dissociation of ^{125}I or ^{124}I from the resultant RIe-AuNPs with excellent *in vivo* stability. Later, the same group further applied this radiolabeling approach to produce ^{124}I-labeled tannic acid gold core-shell NPs (^{124}I-TA-Au@AuNPs) [367].

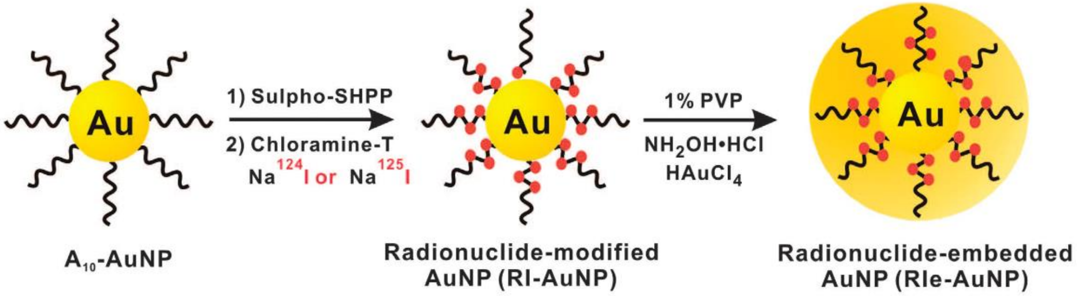

Fig. 3.10. Schematic synthesis of ^{125}I or ^{124}I-encapsulated AuNPs [366].

Nanocomposites with 2D layered structures can be readily radiolabeled by encasing a radionuclide of choice or one of its chemical forms in layered spaces. Shown in Fig. 3.11, Liu et al. [368] reported a novel 2D nanocomposite by self-assembly of IONPs on MoS_2 nanosheets that were sandwiched by PEGylation, into which ^{64}Cu ions were stably adsorbed onto the surface of MoS_2 through doping into the Mo structural defects. These double PEGylated MoS_2-IONPs (^{64}Cu-MoS_2-IO-(d)PEG), which simultaneously exhibit high NIR absorbance and strong T2-MR contrast, potentiate tri-modality imaging of PET/PA/MR. The authors performed such multi-modality imaging in a mouse model bearing 4T1 tumors. Tao et al. [369] employed encapsulation technique to label PEG modified reduced nano-graphene oxide-manganese dioxide (rGO-MnO_2-PEG) nanocomposites with ^{131}I radioisotope to reduce hypoxic tumor microenvironments. Furthermore, released MN^{2+} ions from MNO_2 NPs in the presence of H_2O_2 act as MR contrast agents, improving the efficiency of imaging guided RT. Similarly, other 2D nanocomposites, such as $FeSe_2/Bi_2Se_3$, can be radiolabeled via cation exchange, followed by surface PEGylation to encapsulate the radiolabels [270].

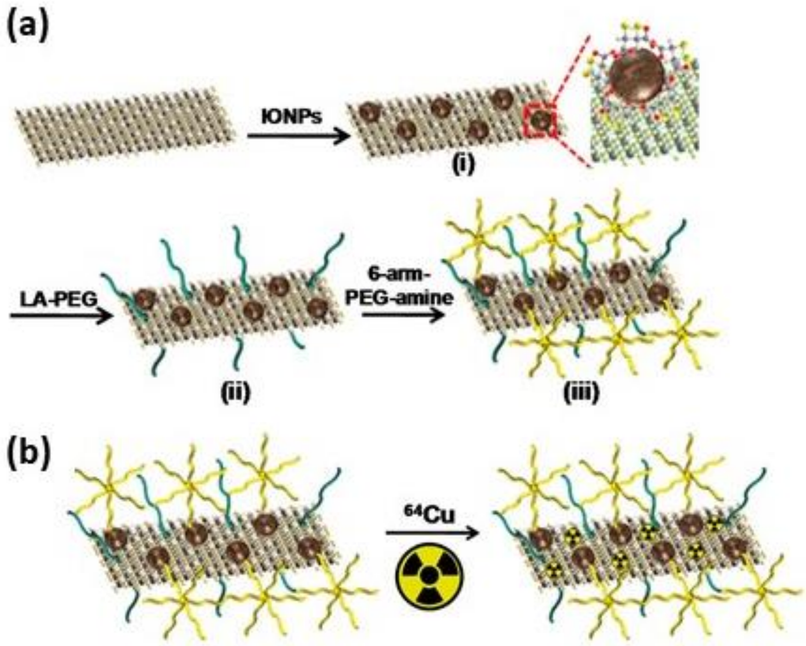

Fig. 3.11. (a) Schematic synthesis of MoS_2-IO 2D nanocomposites by self-assembly of meso-2,3-dimercaptosuccinnic acid (DMSA)-modified IONPs on the MoS_2 nanosheets followed by PEGylation; (b) Radiolabeling of MoS_2-IO-(d)PEG with ^{64}Cu within the PEG layers [368].

3.4. PHARMACOKINETICS OF RADIOLABELED MNPs

While the use of radiolabeled MNPs for nanotheranostics has surged with the recently reported advances and promises, many factors regarding their *in vivo* pharmacokinetics and toxicity remain to be elucidated [380]. The "fallout" presented by the nanoscale X-ray contrast agent *"Thorotrast"* in the 1960's exemplifies the hazards that can be presented by nanoscale radiopharmaceuticals [381]: while possessing a desirable property for biomedical application (thorium's high opacity to X-ray), "*Thorotrast"* is highly, but not acutely (thus not immediately observable) toxic when disintegrated, and its emission of α particles is extremely carcinogenic. Thus, the interactions of MNPs with all potential biological compartments for absorption, distribution, and elimination must be evaluated, to ensure their safety prior to their application to human subjects. This section discusses the factors associated with MNP design that may affect the overall pharmacokinetics of the MNPs, including their translocation through the bloodstream, subsequent uptake in organs, and their ultimate elimination through renal and/or non-renal pathways.

3.4.1. Blood circulation and absorption of radiolabeled MNPs

Upon entry into the bloodstream, MNPs are known to interact with varied biomolecules, including proteins, liposomes and ions present in the physiological microenvironment. Such interactions of MNPs with *in vivo* proteins can result in formation of a surface coating on the MNPs, known as the “protein corona”[382, 383]. This resultant surface modification may possess physicochemical characteristics independent of the original MNP design, and as a result, it may significantly dominate the pharmacokinetic properties of the resultant “*in vivo* modified” MNPs [384, 385]. Additional factors that have implications to influence this formation of protein coronas include MNP size [386, 387], morphology [388], surface charge [389], and hydrophobicity [390].

In order to improve the biocompatibility of MNPs, many biopolymers and synthetic polymers have been used to coat the surface of MNPs, by not only preventing or delaying *in vivo* protein interactions but also providing secondary functions (e.g., improving the MNP’s dispersion in media, and preventing aggregation) [391]. One of the well-documented and most extensively used surface modification polymers for MNPs is PEG. Surface modification of MNPs using linear and branched PEG and their derivatives is widely used to promote their retention in the blood circulation, while reducing their clearance through the mononuclear phagocytic system (MPS) [392-394]. Moreover, varying the molecular weights, chain lengths and densities of such PEG polymers may significantly impact the *in vivo* pharmacokinetics of the resultant nanoformulations.

One such study by Zhang et al. [195] investigated the impact of PEG chain lengths on the pharmacokinetics of an AuNP system, which was ^{111}In-labeled via DTPA incorporated into the PEG chains that were built on thiotic acid (TA) for attachment to the AuNP surface. It was found that the PEG chain lengths determined the size variations of the modified AuNPs. At the fixed PEG chain length using TA-PEG$_{5k}$, the blood retention of the MNPs was highly dependent on their core sizes. For instance, the MNPs with core diameters of 20, 40, and 80 nm showed substantial variations in the blood retention of ~55.2%, ~39.1%, and ~5.2% ID/mL, respectively, after 8 hours p.i. This significant difference observed could be attributed to the result of increased PEG surface density in the smaller (20 and 40 nm) MNPs, which essentially protected them from the non-specific protein and opsonin interactions *in vivo*, thus reducing their uptake by the MPS system, and clearance organs like the liver and spleen.

As a surface modification strategy for MNPs, introduction of target specific moieties (vectors such as proteins, peptides, aptamers, small molecules, etc.) in conjunction with the surface modification polymers, can synergistically act to facilitate biocompatibility as well as accumulation of the MNPs in their intended targets, thus potentially improving their imaging/therapeutic efficacy. One such example is a study by Zhao et al. [331], in which methoxy-PEG$_{5k}$-SH modified [^{199}Au]AuNPs were surface-conjugated with a specific ligand, D-Ala1-peptide T-amide (DAPTA), for C-C chemokine type 5 receptor (CCR5) targeted SPECT imaging in 4T1 breast cancer models. Impressively, these DAPTA-conjugated AuNPs exhibited significantly higher bloodstream retention (~4.77% ID/g) than their non-targeted counterparts (~0.5% ID/g) at 24 hours p.i., in addition to the much desired ~60% reduction in hepatic uptake.

The observed favorable *in vivo* kinetics could be attributed to the surface functionalization with DAPTA, which along with active-targeting had been reported to optimize the surface properties thus resulting in favourable biodistribution profiles of other polymeric NPs [395]. Similarly, Wang et al. [238] reported that the biodistribution profiles of a nanotheranostic IONP platform coated with DSPE-PEG$_{2k}$ were further improved after functionalized with ^{125}I radiolabeled cyclic-RGDyK for imaging and PTT in xenograft models bearing $\alpha_v\beta_3$-expressing glioblastomas. The cyclic-RGDyK functionalized MNPs demonstrated a prolonged blood circulation time as compared to their non-targeted counterparts, which in turn facilitated the designed theranostic application by enabling more effective active-targeting as well as the enhanced permeability and retention (EPR) effect for increased tumor accumulation [396].

With surface modification of MNPs using PEG-derived polymers comes a consequential increase in the size of the PEGylated MNPs, which is often measured by their hydrodynamic diameters (HDs) *in situ*, due to the inherent length of the polymer chains and the added hydrophilic chemical interactions with the surrounding media [397]. This can become an issue, in particular for renal clearable NPs, where the HDs must be maintained below the glomerular filtration threshold of 6-8 nm. However, PEGylation significantly increases the MNP's HDs, thus significantly reducing or even blocking their renal clearance [195]. To address this issue, tuning of the PEG-derived polymer chain-lengths and/or modifications is necessary to render the MNPs with sufficient surface PEG coverage density, while keeping the MNPs renal clearable. Illustrated in Fig. 3.12, Zhao et al. [398] synthesized renal clearable AuNCs coated with TA-PEG$_{750}$ and AMD3100, an antagonist for the chemokine receptor CXCR4 that is highly expressed in tumor cells.

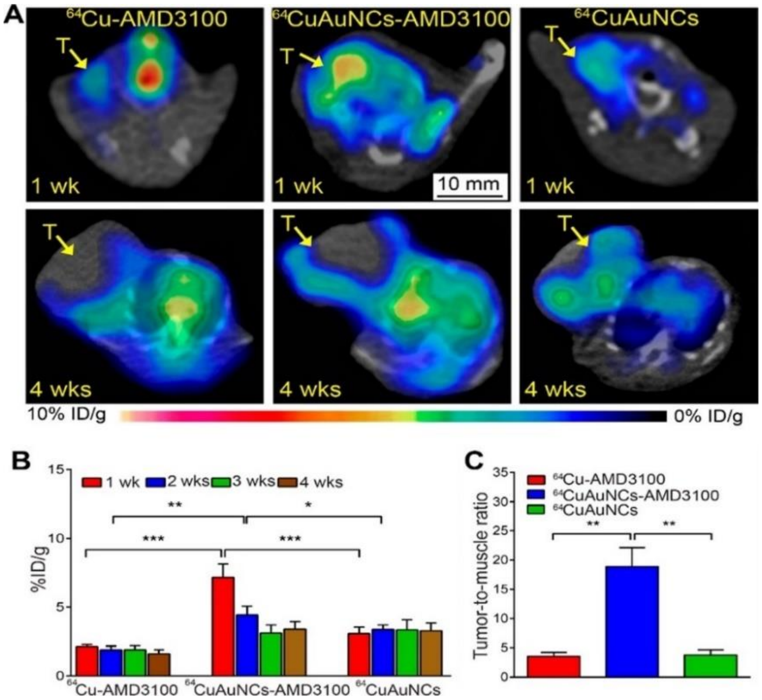

Fig. 3.12. Tumor targeting capability of MNPs was achieved while retaining their renal clearance by tuning surface modification strategies. (a) PET/CT axial images depicting the accumulation of ^{64}Cu-AMD3100, ^{64}Cu-AuNCs-AMD3100, and ^{64}Cu-AuNCs radiotracers in 4T1 breast cancer tumor models after 1 week and 4 weeks of tumor implantation in mice, (b) Quantitative 4T1 tumor uptake of the three treatments after 1, 2, 3, and 4 weeks of tumor implantation, and (c) Tumor-to-muscle uptake ratios of the mentioned treatments after 1 week of tumor implantation (*$p < 0.05$, **$p < 0.005$ and ***$p < 0.001$) [398].

To enable PET imaging, the core of AuNCs was labeled with ^{64}Cu. It was found that a shorter PEG chain (~750 Da) coupled with a bidentate di-sulfide TA linker for attachment to the MNP surface resulted in a closely packed design with reduced HD and increased surface polymer density, thus promoting active targeting capability *in vivo*. Consequently, the resultant ^{64}Cu-AuNC-AMD3100 (HD ~4.5 nm) showed a shorter blood circulation half-life than its control ^{64}Cu-AuNCs (HD ~4.2 nm), namely, 0.57 hours vs. 1.22 hours. Nevertheless, they exhibited comparable blood activity retention after 4 hours p.i., namely ~3% for ^{64}Cu-AuNC-AMD3100 vs. ~2% ID/g for ^{64}Cu-AuNCs. Similar observations were reported by Heo et al. for a renal clearable CuNC nanosystem (HD: ~5.5 nm; core ^{64}Cu-labeled) coated with TA-PEG$_{12}$ and targeted with CXCR4 receptor specific peptide FC131 for imaging triple negative breast cancer xenografts [399].

Another group of molecules that has been increasingly employed for surface coating of MNPs is zwitterionic ligands such as glutathione [400], cysteine [389], and carboxybetaine [401]. Owing to their ionic nature these ligands form strong electrostatic interactions with water molecules, and as a result provide a physical and thermodynamic barrier for the MNPs for protein interactions *in vivo,* thus avoiding corona formation [402, 403]. Moreover, due to their low molecular weights, zwitterionic ligands result in negligible size changes when used for MNP functionalization, in sharp contrast to large polymers such as PEG chains [404]. Zhou et al. first reported using glutathione to coat renal clearable ultrasmall [^{198}Au]AuNPs (HD ~3 nm), which were synthesized by a one-pot synthesis method [400]. The resultant glutathione-coated AuNPs (GS-[^{198}Au]AuNPs) were fluorescent thus enabling dual-modality imaging (SPECT and fluorescence), and the bloodstream activity retention of GS-[^{198}Au]AuNPs was determined to be ~7.06% and ~6.13% ID/g at 1 and 4 hours p.i., respectively, comparable to those observed with MNPs modified with other known polymers, such as TA-PEG$_{750}$-coated ultrasmall ^{64}Cu-AuNCs (HD ~4.2 nm) described above [314]. Shown in Fig. 3.13, GS-[^{198}Au]AuNPs were effectively cleared from kidneys and the NP integrity was demonstrated by the strong fluorescence of the excreted GS-[^{198}Au]AuNPs in the urine. The result shows the effectiveness of using glutathione as a coating agent to prepare renal clearable MNPs. Further pharmacokinetic analysis revealed that the rapid *in vivo* distribution and clearance of these ultrasmall GS-[^{198}Au]AuNPs followed a two-compartment model with distribution and elimination half-lives of ~5 minutes and ~12.7 hours, respectively, similar to small molecular imaging probes [405]. Similar *in vivo* kinetics were also observed for luminescent ultrasmall [^{64}Cu]CuNPs coated with glutathione (GS-^{64}Cu-CuNPs, HD ~2.7 nm) [406].

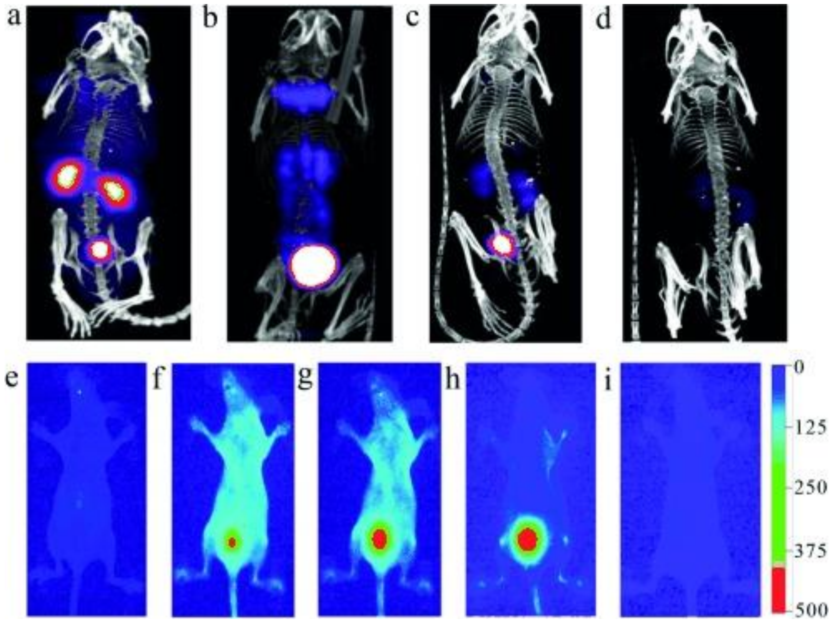

Fig. 3.13. SPECT and fluorescence imaging evaluation of renal clearable ultrasmall glutathione-coated-[^{198}Au]AuNPs. SPECT images of Balb/c mice after (a) 10 min, (b) 1 h, (c) 4 h, and (d) 24 h of injection with GS-[^{198}Au]AuNPs and *in vivo* fluorescence imaging of (e) pre-injection, (f) 5 min, (g) 20 min, (h) 1 h, and (i) 24 h GS-[^{198}Au]AuNPs post-injection [400].

3.4.2. Distribution of radiolabeled MNPs in normal organs and target sites

After administered into the bloodstream, the translocation and accumulation of radiolabeled MNPs in the unintended organs or tissues can result in unwanted acute and/or chronic side-effects and toxicities. The physicochemical parameters in MNP design, such as size, surface charge, and surface modification, would largely determine the organ distribution and retention as well as the clearance profiles of the MNPs. As described earlier, MNPs with the same surface coating may display very different *in vivo* distribution and clearance if the core size varies. For instance, the TA-PEG$_{5k}$ coated AuNPs [195] showed substantially higher hepatic and splenic uptake (53.16% and 62.75% ID/g, respectively) if the core size led to large MNPs (HD 80 nm), than to small ones (HD 20 nm) (30.31% and 15.15% ID/g, respectively). Consequentially, this would result in a decreased elimination rate of the larger MNPs from the circulation as compared to the smaller ones, which is not a favourable feature of pharmacokinetics for the design of targeted nanotheranostics that requires reasonable blood circulation half-lives for both active targeting and passive retention at the intended site of action.

It has been well-documented that pre-coating the MNP surface with physiological proteins such as albumin may render the MNPs with desired stealthiness to evade the MPS sequestration by minimizing protein corona formation, thus enhancing the intended target delivery [407, 408]. However, the protein coatings have to be judiciously selected, as their interactions with physiological proteins/pathways can cause accumulation of the MNPs in unintended organs. A study by Schaffler et al. [409] utilized [^{198}Au]AuNPs coated with two different physiological proteins, human serum albumin (HSA) and apolipoprotein E (APOE), to investigate their effects on the overall biodistribution of the MNPs. Interestingly, the HSA-coated [^{198}Au]AuNPs (HD ~112 nm) showed significantly higher accumulation in the brain (5.53×10^{-3} accumulated fraction/g) than the citrate-stabilized [^{198}Au]AuNPs (HD: ~21 nm) (1.98×10^{-5} accumulated fraction/g) and the APOE-coated ones (HD: ~115 nm) (1.64×10^{-3} accumulated fraction/g). The group attributed the result to HSA's modulation of MNPs’ transport across the blood brain barrier.

Most research studies employ the intravenous route for preliminary testing of investigational formulations to circumvent the challenges associated with other conventional routes of dose administration, such as gastrointestinal absorption issues and first pass metabolism encountered for oral formulations, skin permeation and skin irritation issues for transdermal formulations [410, 411]. However, depending on their intended application, non-conventional routes of administration may hold more relevance for testing. Depending on the size of the MNPs, the route of MNP administration may be an important factor affecting their overall biodistribution and organ retention patterns. For instance, Moeendarbari et al. [412] tested naked ^{103}Pd/Pd coated hollow Au nanoshells (^{103}Pd/Pd-HAuNPs) as neoadjuvant brachytherapy agents, by performing intratumoral injections of the nanoseeds in prostate cancer subcutaneous xenograft mouse models (see Fig. 3.14).

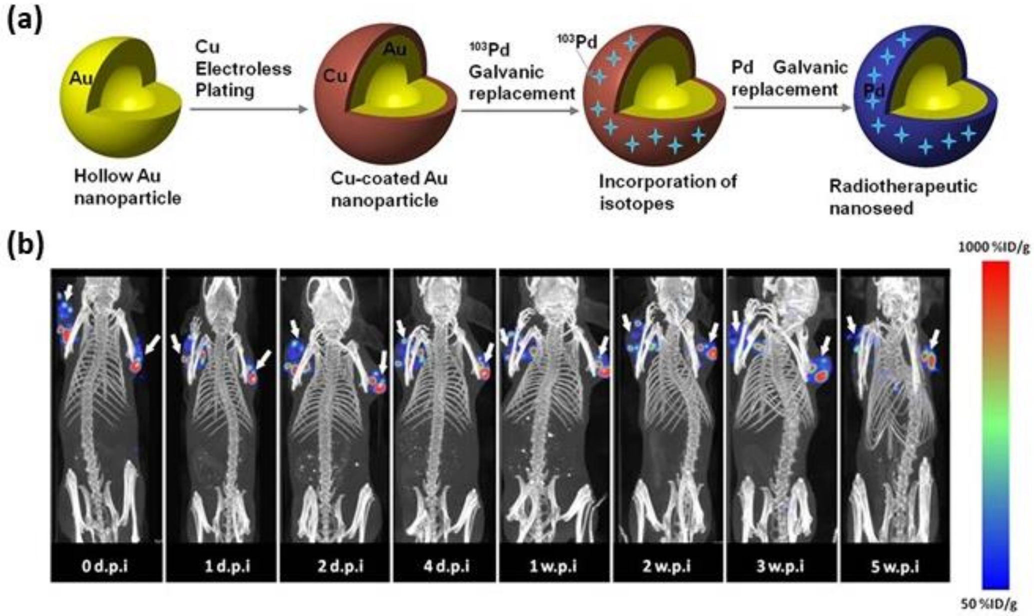

Fig. 3.14. Substantially high tumoral retention was observed for the large sized ^{103}Pd/Pd-coated hollow gold nanoshells (^{103}Pd/Pd-HAuNPs) after intratumoral injection for brachytherapy application (a) Simple schematic of ^{103}Pd/Pd-HAuNPs synthesis through a Cu layer electrodeposition and subsequent Pd galvanic replacement and (b) SPECT/CT images of PC3-tumor bearing SCID mice after 0, 1, 2, 4, 7, 14, 21, and 35 days of 1.51 mCi ^{103}Pd/Pd-HAuNPs injection [412].

Notably, even after 5 weeks post-administration, these large ^{103}Pd/Pd-HAuNPs showed nearly perfect tumor retention and minimal leakage to the liver (~3.31% ID/g) and spleen (~0.39%

ID/g), which was visualized and quantified by SPECT/CT imaging. This high tumor retention of ^{103}Pd/Pd-HAuNPs was attributed to the injection route (intratumoral) combined with their large size (HD: ~140.5 nm), which retained high concentrations of ^{103}Pd/Pd-HAuNP deposits at the injection sites in the tumors with minimal to no diffusion into the surrounding vasculature. However, it should be noted that this is largely a size dependent feature, and such intratumoral administration of smaller sized MNPs, may result in their diffusion from the tumor microenvironment into the blood circulation and surrounding organs.

3.4.2.1. Accumulation in target site

Functionalization of radiolabeled MNPs using target-specific vectors allows increased accumulation of the NPs at the desired diseased site, with the intent to accentuate their therapeutic and/or diagnostic action, while limiting spread to other sites post-administration. Although the application of radiolabeled MNPs has been investigated for varied disease conditions such as respiratory diseases, neurological conditions, etc. [413, 414], most studies have focused on MNPs targeting cancers. Thus, for better clarification, tumors will be highlighted as the target site for discussion. Target accumulation strategies for MNP design can be implemented by two main approaches, passive accumulation, and active targeting.

Passive accumulation includes both, passive diffusion of ultrasmall MNPs (< 1 nm) [415, 416] and a preferential accumulation of large (> 30 nm) MNPs in tumors, known as the EPR effect [417, 396]. A study found that proteins > 30 kDa would preferentially distribute in the interstitium of tumor tissues and accumulate there for an extended time [418]. While initially attributed to the fenestration in tumor blood vessels and poor drainage, further research determined that several interwoven biological processes undergoing in tumors contribute towards EPR, including angiogenesis and vascular permeability [417]. The degree of passive accumulation by EPR is determined by the MNP size and their blood retention [419, 417, 420, 421]. Several factors limit the distribution and effectiveness of passive accumulation for MNPs in tumors, such as compromised tumor vasculature and irregular blood pressure, that limit the flow of MNPs to the tumor core, thus leading to their distribution in the peripheral edges, commonly called as the "rim effect" [422]. One such example is a study by Frellsen et al. [312] wherein PET imaging in mice xenograft models showed that the ^{64}Cu-AuNPs-PEG$_{5k}$-OMe were heterogeneously distributed in the tumors, with higher concentrations of the injected MNPs accumulating in the tumor's periphery owing to EPR effect and insufficient tumor perfusion. Similar observations were also reported in other studies using the EPR effect-based strategy for tumor accumulation of MNPs [203, 335].

However, there is a caveat to this approach, despite promising preliminary results. The MNP accumulation levels in tumors by EPR may be highly exaggerated in animal models when considering translational applications, as the tumor-grafts represent a much larger fraction of body mass in the animal models than they do in humans [423]. Also, clearance mechanisms and tumor microenvironment differ substantially between the most commonly used rodent animal models (mice and rats) and humans. This has to be taken into account when considering translational applications of an MNP nanotheranostic agent that has shown promising results in rodent models [417].

One widely exploited strategy in the field of oncology is to target the cell membrane proteins that are known to be over-expressed by cancer cells in comparison to the normal cells [424, 425]. This has led to the design of numerous high-affinity vectors (including proteins, peptides, aptamers, or even small molecules) targeting specific cancer cells for theranostic applications. Surface functionalization of the MNPs with such vectors (*e.g.,* the monoclonal antibody trastuzumab for targeting human epidermal growth factor receptor 2 over-expressed in breast cancers [171, 391]) can significantly improve their tumor targeting specificity and accumulation level. Moreover, due to the substantially higher surface-to-volume ratios in nano-sized particles, in general, the density of these targeting vectors upon MNP surface functionalization can be high as compared to the individual vectors by themselves or in a small molecular combination [426]. Such features can potentially translate into the much-desired high tumor targeting capability for nanotheranostics, and thus significantly accentuating their theranostic efficacies. Gao et al. [285] reported that the tumor uptake of BSA-coated [^{64}Cu]CuNCs was substantially (~4 times) higher after functionalization with luteinizing hormone releasing hormone (LHRH) peptide, known to target receptors over-expressed by various cancers including lung cancers, as the non-targeted [^{64}Cu]CuNCs only had the EPR mediated tumor accumulation. This difference was further confirmed by the tumor-to-background PET imaging contrast enabled by ^{64}Cu owing to their high renal clearance and reduced MPS uptake caused by their ultrasmall size (< 5 nm).

However, it should be noted that functionalizing MNPs with the receptor/protein-specific ligands may also enhance their uptake in other organs that express the targeted receptor, which is undesirable. For example, Zhao et al. [314] reported renal clearable ^{64}Cu-AuNCs targeted with AMD3100 (a CXCR4 antagonist) as PET imaging agents for primary breast cancer tumors and metastases in mouse models. To their surprise, the targeted ^{64}Cu-AuNCs were found with significantly ($p < 0.001$) higher accumulation in the liver, spleen, and bone marrow than the control ^{64}Cu-AuNCs after 24 hours p.i. This likely reflects the fact that CXCR4 receptors are also expressed on the immune and inflammatory cells harbored in these organs. Moreover, due to CXCR4 receptor-mediated (rather than non-specific) endocytosis in the hepatocytes, which led to increased retention and then delayed hepatobiliary elimination, a delayed but substantial (6-fold higher) increase in fecal elimination was observed for the targeted ^{64}Cu-AuNCs, as compared to their non-targeting controls after 48 hours p.i. This demonstrates that an effective targeting strategy must be judiciously considered.

As discussed earlier, there exist many other disease conditions wherein the applications of MNP theranostics are gaining more attention. By using a common MNP nanoplatform, active targeting strategies could be game changers towards the desired applications. Active targeting relies on the interaction among targeting moieties conjugated on the surface of MNPs and antigen or receptor on cell target and increase the drug delivery efficiency compared to passive targeting mechanism [427-429]. Li et al. [430] showed that antibody conjugated AuNPs improved the contrast of *in vivo* PA imaging of xenograft squamous tumor (Cal27) in mice improved for 3.5 dB. In another research, Au nanocages, conjugated with (Nle4,D-Phe7]-melanocyte-stimulating hormone as the targeting molecule, exhibited 3.5-time higher accumulation than the untargeted Au nanocages [431].

In one such study evaluating *in vivo* PET imaging of lung inflammation, Pellico et. al. reported that [^{68}Ga]-labeled IONPs (~14.5 nm HD) functionalized with N-cinnamoyl-F-(D)L-F-(D)L-F (cFLFLF) peptide were able to specifically target neutrophils in acute lung inflammation in mouse models [318, 432] because the cFLFLF ligand avidly binds to the formyl peptide receptor-1 expressed by neutrophils. This approach was further developed to detect atherosclerosis with bio-orthogonal click reactions between trans- cyclooctene (TCO) and tetrazine (Tz) [433]. The monoclonal antibody E-06, which targets lipoproteins integral to athesclerotic progression, was functionalized with TCO and injected into ApoE$^{-/-}$ mice, followed by an injection of [^{68}Ga]-labeled IONPs functionalized with Tz. The bioorthogonal click-reaction between TCO and Tz resulted in much higher accumulation of IONPs in pre-targeted mice with atherosclerosis (14.7 ± 2.7 %ID/g) compared to control models (1.5 ± 0.5 – 3.4 ± 1.5 %ID/g).

3.4.2.2. Distribution in normal organs/tissues

The most notable unintended uptake for MNPs injected intravenously is their accumulation in the organs governed by the MPS, specifically the liver, spleen, lymph nodes, and bone marrow (H. S. Choi et al., 2010). The non-specific uptake of MNPs is primarily determined by their size, shape, and surface charge and chemistry (Q. Huang et al., 2020; Kettler et al., 2014; Panzarini et al., 2018). Particles larger than ~10 nm can be easily taken up by the macrophages and endothelial cells (Nam et al., 2013), whereas particles larger than 100 - 200 nm can be trapped in the red pulp of the spleen (Cataldi, Vigliotti, Mosca, Cammarota, & Capone, 2017). In another research, Geertsma et al. (Wim H De Jong et al., 2008) confirmed broad distribution of 10 nm AuNPs throughout the body, which the larger nanoparticles were just confined in liver, blood, and spleen.

Xie et al. (X. Xie, Liao, Shao, Li, & Lin, 2017) synthesized AuNPs with the same size and coating (mPEG) but different shapes of stars, triangles and rods to evaluate their cellular uptake by RAW 264.7 macrophages. The results demonstrated that triangular and stars AuNPs have the highest and lowest uptake, respectively, with various internalization mechanism. In fact, Yu et al. (S. S. Yu et al., 2012) reported that the size was a much stronger factor than the charge in determining the non-specific uptake of IONPs. Compared to their counterparts with negative or neutral surfaces (Wilhelm et al., 2016), positively charged NPs are taken up more easily by macrophages and even normal cells, due to their stronger interactions with cell membranes that have a net negative charge potential (Ma, Poole, Goyette, & Gaus, 2017). In another research, Saha et al. (Saha et al., 2013) demonstrated that the uptake of cationic AuNPs in normal (MCF10A) cells is dependent on the AuNPs surface monolayer. Also, various endocytic pathways and relevant specific cell surface receptors such as scavenger receptors are involved through this process.

3.4.3. Disposition of radiolabeled MNPs

Given the fact that only a small fraction of MNPs would be delivered to and retained in the target organs to elicit the intended theranostic actions after administration, understanding the metabolic and clearance pathways that govern the disposition of MNPs in the body is critically important to the rational design of an efficacious and safe MNP nanoplatform towards a nanotheranostic. In general, NPs are cleared from the body by renal and/or biliary excretion pathways, which are largely dependent on the size and surface properties of the NPs.

3.4.3.1. Renal clearance

In order to be renal clearable, the HD of MNPs must stay below the size threshold for renal glomerular filtration, which refers to either the physical size (6-8 nm) under the physiological condition or the molecular weight (30-50 kDa) of the nanoplatform [434, 435]. In addition, a net positive surface charge [436, 437] with minimal interactions with proteins facilitates the desired renal clearance. When the size of MNPs falls below the threshold, surface modification with hydrophilic polymers that shield the MNPs from interacting with proteins, such as PEG or zwitterionic-molecules, tends to increase the excretion of MNPs from the renal pathway [438]. Further, functionalization of MNPs may also alter the balance of the two excretion pathways. For instance, 61.4% ID of ultrasmall ^{64}Cu-CuNCs (HD < 6 nm) were cleared via the renal pathway at 24 hours p.i. After functionalization with a CXCR4 targeting peptide, FC131, the degree of their renal clearance dropped to 40.4% ID [399]. The decreased renal clearance of FC131-functionalized ^{64}Cu-CuNCs could be attributed to the significantly elevated hepatic uptake (from

~7.5% to ~15% ID/g 24 hours p.i.; $p < 0.05$) due to the CXCR4 expression in the inflammatory cells that might result in elevated fecal excretion (biliary clearance, from 13.5% to 22.8% ID), and the significantly increased tumor uptake (from ~2.44% ID/g to ~6.08% 24 hours p.i.; $p < 0.005$).

An optimal renal clearable MNP nanoplatform should have high *in vivo* stability, in addition to the desired high renal excretion within a reasonable timeframe. However, many MNPs may undergo *in vivo* surface degradation or even some forms of metabolism under the physiological conditions, prior to their disposition from the body. For example, in a study reported by Lin et al., the HD of neutron-activated ^{198}Au-AuNPs nanocomposites increased from 2 nm to 60 nm after coating with gum arabic [439]. The ^{198}Au-Au/gum arabic nanocomposites were not expected to be seen upon urinary excretion because of their size being well above the renal clearance threshold. However, a significant amount of ^{198}Au activity (~5%) was found in the urine over the course of 2 weeks after their injection, likely because of the disintegration of the gum arabic coating from the ^{198}Au-Au/gum arabic nanocomposites, which resulted in the observed renal clearance of the core ^{198}Au-AuNPs (diameter: 2 nm).

3.4.3.2. Metabolism and clearance through the MPS organs

Previously called the "reticuloendothelial system (RES)", the MPS, which mainly involves the liver, spleen, and lymph nodes, where phagocytic cells (e.g., macrophages) reside, is the first line of defence in the body against foreign pathogens or substances [440-442]. Regarded by the body as foreign substances, most of all NPs including MNPs after injection are sequestered by the MPS and/or eliminated by the renal excretion pathway if their sizes are below the renal clearance threshold. As the matter of fact, the MPS sequestration of NPs is the main determinant of the *in vivo* distribution of NPs, which results in high off-target deposition and thus gives rise to the main safety concern with respect to the nanomedicine [443-445]. To date, the desired "stealthiness" to the MPS sequestration is still an unmet need in the field of nanomedicine. As discussed earlier, immediately upon their entry into the bloodstream, NPs interact with serum proteins to form a protein corona on their surface, which elicits their uptake by the MPS organs. As such, the common strategy of evading the MPS sequestration is to coat the NP surface with non-immunogenic and hydrophilic polymers, such as varieties of PEGs [446-448], to minimize the protein corona formation. Once ingested by the phagocytes in the MPS organs, NPs are transported to the endosomes for metabolism and degradation, which often takes much longer than renal clearance [449].

While the specific degradation mechanism is highly dependent on the material composition of the MNPs, their size, and surface charge, intracellular metabolic pathways relevant to the MNPs also play an important role [450], in particular when the metal components are bioinorganic elements in the body as in IONPs, where iron is a life essential metal. For instance, in a study reported by Pospisilova et al. [362], it was found that the iron readout by ^{59}Fe, which was incorporated into the IONPs by radiochemical doping (HD: ~82.7 nm), could be used as a measure of the *in vivo* degradation of IONPs, because the iron (read by ^{59}Fe) from the lysosome-degraded IONPs was identical to the endogenous iron for iron metabolism within the MPS organs, where IONPs were sequestered. Of course, the iron (read by ^{59}Fe) can further incorporate into the overall iron pool in the body. Consequently, only $< 2\%$ of the injected ^{59}Fe dose was excreted in feces or urine over a 7-day period.

Copper is also a life-essential element. As such, similar observations were found with [^{64}Cu]CuNPs. For instance, copper ions catalyse oxidation of biomolecules including glutathione, a thiol antioxidant found in high concentrations in the liver, which results in the trapping of copper (read by ^{64}Cu) decomposed from the CuNPs in the form of Cu(II) glutathione disulphide complexes (Cu(II)-GSSG) in the liver, thus delaying the clearance of injected ^{64}Cu activity [451]. Yang et al. [406] evaluated this degradation process using ultrasmall renal clearable luminescent glutathione-coated [^{64}Cu]CuNPs (HD: ~2.7 nm) by a comparative study with ^{64}Cu[Cu](II)-GSSG complexes in mouse models. Despite the size difference, the glutathione-coated [^{64}Cu]CuNPs showed much higher renal clearance and lower hepatic uptake than the small molecule ^{64}Cu[Cu](II)-GSSG complexes due to the fact that the ultrasmall glutathione-coated [^{64}Cu]CuNPs were processed by the body as a single entity, which was reasonably stable during the period of study without copper being translocated to participate in copper metabolism as measured by the small ^{64}Cu[Cu](II)-GSSG complexes.

For MNPs made from life essential metals, such as iron and copper described above, their metabolic fate, either by excretion or metabolism for entry into the endogenous metal pool in the body, would not raise a severe safety concern if the nano-entities themselves are non-toxic, because the metal absorption and homeostasis is tightly regulated in healthy individuals [452-455]. However, the administration of the MNPs indeed would raise the concentration level of the corresponding metal in the body if the metal gets into the endogenous pool. Therefore, the use of MNPs for clinical trials has to take into consideration some rare genetic disorders [456-459], such as hemochromatosis and Wilson’s Disease that prevent the body from removing extra iron and copper, respectively. For MNPs made from or comprised of non-life essential metals, such as heavy metals, an extra safety measure will have to be factored into the overall design and development of the MNPs-based nanotheranostics, because the leakage of toxic metal ions from the MNPs may implicate a severe hazard to the body, sometimes irreversible or even fatal, similar to the nephrogenic systemic fibrosis caused by breakdown of gadolinium(III) from MRI contrast agents accumulated in individuals with kidney failure or reduced kidney function [460-462]. In other words, the metabolic fate of MNPs along with their *in vivo* stability is of paramount importance to their potential use as nanotheranostics in humans.

4. LIQUID DIFFUSION SYNTHESIS

4.1. Introduction

The last two decades have seen an exponential growth of research on the synthesis of colloidal metal and metal oxide nanocrystals, and it has become one of the most active research fields in chemistry. This was initially driven by the potential usage of colloidal nanocrystals as a building block for heterogeneous catalysts for chemical industry and as a model system to study the catalytic mechanisms [463, 464]. Later, their potential applications as nanomedicine [403, 465] and artificial enzymes (nanozymes) [466, 467] further fuel the enthusiasm in this research field. Myriad methods have been developed and optimized to synthesize a variety of nanocrystals [468, 469]. Among them, wet chemical methods [470] such as the reduction of metal salts [471-477] and the decomposition of organometallic precursors [478-481] are the most popular synthesis methods. The synthesis is usually conducted at an elevated temperature, and often using expensive or dangerous reducing agent such as inorganic or organic hydrides and organic solvent. Here, we report a simple process, called liquid diffusion synthesis (LDS), using aqueous solution at room temperature to produce a variety of ultrasmall metal and metal oxide nanocrystals.

4.2. Materials and methods

The chemicals including cobalt(II) chloride hexahydrate ($CoCl_2.6H_2O$, 98%), nickel(II) chloride hexahydrate ($NiCl_2.6H_2O$, 98%), silver nitrate ($AgNO_3$, 99%), gold(III) chloride trihydrate ($HAuCl_4.3H_2O$, 99.9%), platinum(II) chloride ($PtCl_2$, 98%), palladium(II) chloride ($PdCl_2$, 99%), iron(III) chloride hexahydrate ($FeCl_3$.6H2O, 98%), cerium(II) chloride heptahydrate ($CeCl_2.7H_2O$, 99.9%), ruthenium(III) chloride hydrate ($RuCl_3.xH_2O$), zinc chloride ($ZnCl_2$), lutetium(III) chloride hexahydrate ($LuCl_3.6H_2O$), manganese(II) chloride tetrahydrate

($MnCl_2.4H_2O$), sodium citrate dihydrate ($HOC(COONa)(CH_2COONa)_2{\cdot}2H_2O$), citric acid ($C_6H_8O_7$, 99.5%), and dialysis tubing cellulose membrane (MWCO 14000) were purchased from Sigma-Aldrich (St. Louis, MO). Copper(II) chloride dihydrate ($CuCl_2.2H_2O$, 99%) was obtained from Alfa Aesar (Ward Hill, MA). Furthermore, sodium hydroxide (NaOH, 97%) were purchased from Thermo Fisher Scientific (Waltham, MA) and L-ascorbic acid ($C_6H_8O_6$) was provided from Serva. All aqueous solutions were prepared in Millipore Milli-Q DI water (18 MΩ-cm) which was provided from a Millipore Gradient Milli-Q water system (Billerica, MA).

High resolution transmission electron microscopy (HRTEM) micrographs, selected area electron diffraction (SAED) patterns, and energy dispersive X-ray (EDX) analysis were achieved using a Hitachi H-9500 HRTEM operated at an accelerating voltage of 300 kV. The suspension of nanoparticles in DI water was sonicated for about 20 minutes, and then spread on 300-mesh copper TEM grid covered with a lacey carbon film and dried overnight. The magnetic measurements were conducted at room temperature using a MicroSense EV7 vibrating sample magnetometer (VSM). Ni or Co nanoparticle water suspension (very high concentration) was dropped on a piece of silicon wafer, and then dried. This silicon wafer was measured. The diamagnetic signal from silicon wafer and quartz sample holder was subtracted to obtain ferromagnetic signal from Ni or Co.

UV-Vis absorbance spectra of Cu, Au, and Ag nanoparticle suspension was measured using a Perkin Elmer Lambda 35 UV-Visible Spectrometer. The samples were prepared by re-suspending the washed metal nanoparticles in about 1.5 ml of DI water, followed by transferring the suspension into 1.5 ml polystyrene semi-micro cuvettes. The slit width was 1 nm and the scanning speed was 120 nm/min. Fluorescence spectra of colloidal Cu nanoparticles were recorded on a PerkinElmer LS 55 Luminescence Spectrometer using 3.5 ml four-sided fused quartz cuvettes. The slit width was 10 nm and the scanning speed was 100 nm/min.

4.3. Synthesis process of ultrasmall metal nanoparticles

Fig. 4.1 depicts the setup used in LDS, in which a dialysis bag containing a mixture of a metal salt and citric acid solution is immersed in a NaOH solution reservoir. After the immersion for a certain period of time, ultrasmall metal nanoparticles form in the solution inside the dialysis bag.

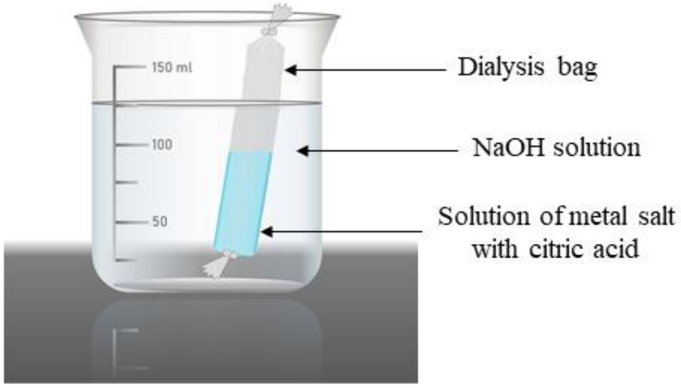

Fig. 4.1. Simple schematic of liquid diffusion synthesis setup.

The entire synthesis process for making metal Cu nanoparticles is illustrated in Fig. 4.2. First, a mixture of 1.5 mM of citric acid and 1.5 mM of $CuCl_2$ is stir-mixed for 30 mins. Next, the mixture is transferred to a dialysis bag, followed by immersing the dialysis bag into a 0.5 M NaOH solution for 2 hours at room temperature. The pH variation was monitored during the synthesis using a Mettler Toledo SevenEasy S20 pH meter (Columbus, OH). At the end of the fixed time period, the solution inside the membrane is collected, followed by centrifugation using an Eppendorf Centrifuge 5418 at 14000 rpm for about 20 min to precipitate the large precipitates. Then, the resultant supernatant is mixed with acetone at a 4:1 (acetone: supernatant) ratio. Such mixture is centrifuged at 14000 rpm for 20 mins. The precipitation is collected and diluted with DI water, and then transferred to a new dialysis bag to be washed inside DI water. Simply replacing

$CuCl_2$ with $CoCl_2$, $NiCl_2$, $HAuCl_4$, $AgNO_3$, $PdCl_2$, $PtCl_2$, and $LuCl_3$, the same process is used to produce ultrasmall Co, Ni, Au, Ag, Pd, Pt, and Lu nanoparticles. For Cu, Ag, Au, Pd, Pt, and Lu the washing process lasted 12 hours with replacing DI water every two hours. For Co and Ni, the washing process lasted 3 hours. After washing, the nanoparticle suspension was frozen and lyophilized using a Labconco FreeZone freeze-dryer (Kansas City, MO) to attain the final particle powder.

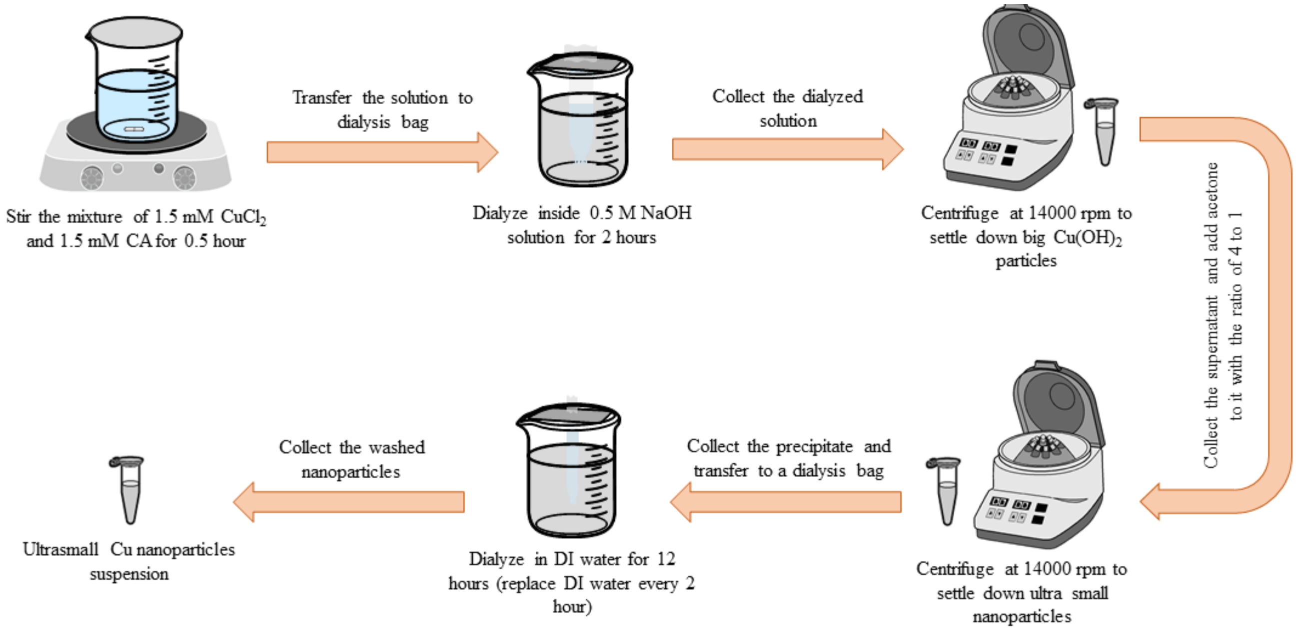

Fig. 4.2. Schematic of LDS steps to produce colloidal Cu nanocrystals.

Fig. 4.3(a) shows the TEM images of resultant CuNPs, having the average size of 3 nm to 5 nm. The absorption peak at wavelength of about 614 nm, illustrated in Fig. 4.4(b) as a main characteristic of metal nanoparticles, verifying the existence of metal copper nanoparticles. Fig. 4.4(c) exhibits the copper oxides precipitated accompanied the formation of ultrasmall copper nanoparticles (which will be examined in the following section).

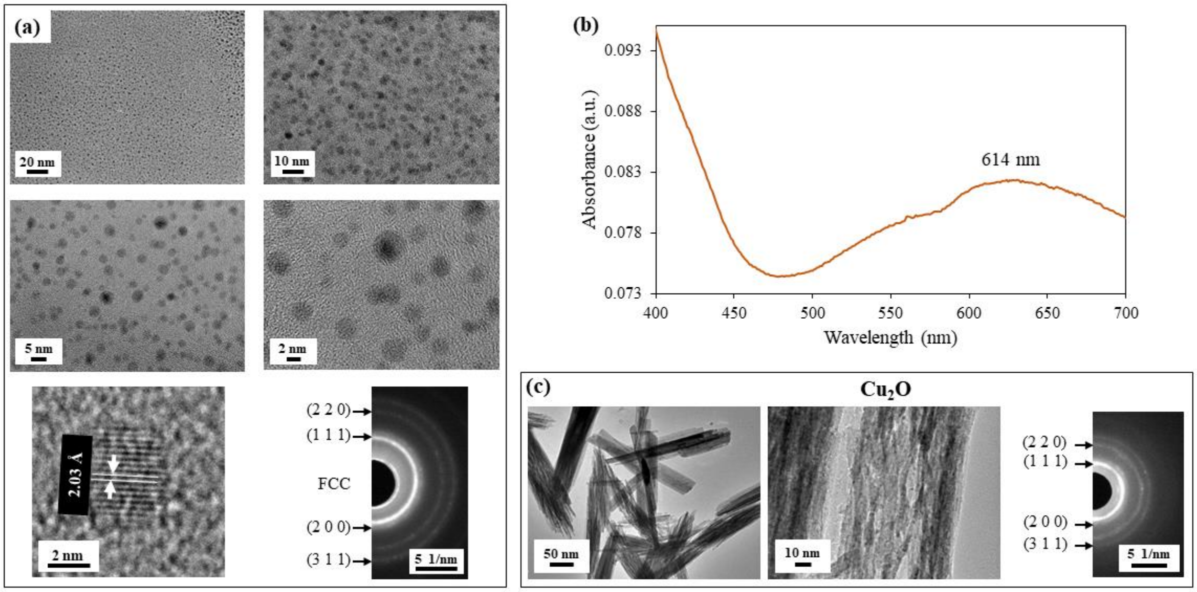

Fig. 4.3. (a) HRTEM images, corresponding SAED pattern, and (1 1 1) lattice fringes of Cu nanocrystals synthesized through LDS, (b) UV-Vis absorption spectra of Cu nanocrystals, and (c) TEM micrographs and SAED patterns of large particles formed during the synthesis process.

4.4. Formation mechanism of ultrasmall metal nanoparticles

The formation mechanism of ultrasmall metal nanocrystals is illustrated in Fig. 4.4. We chose Cu nanocrystal synthesis process as a model system for more detailed investigations, aiming to gain insight into this method. The dialysis membrane forms a diffusion barrier for OH^- ions to gradually diffuse from the reservoir into the solution inside the dialysis bag, so that a pH gradient (decreasing from the pH of the NaOH reservoir to the initial pH) is generated in the solution (see Fig. 4.4(b)). Based on the Fig. 4.4(c), considered as an element at LSD setup, different parts of the solution experience a certain pH at different time points, and the entire volume of the solution experiences a gradual pH change from the initial pH (typically about 2) to the pH of the NaOH reservoir.

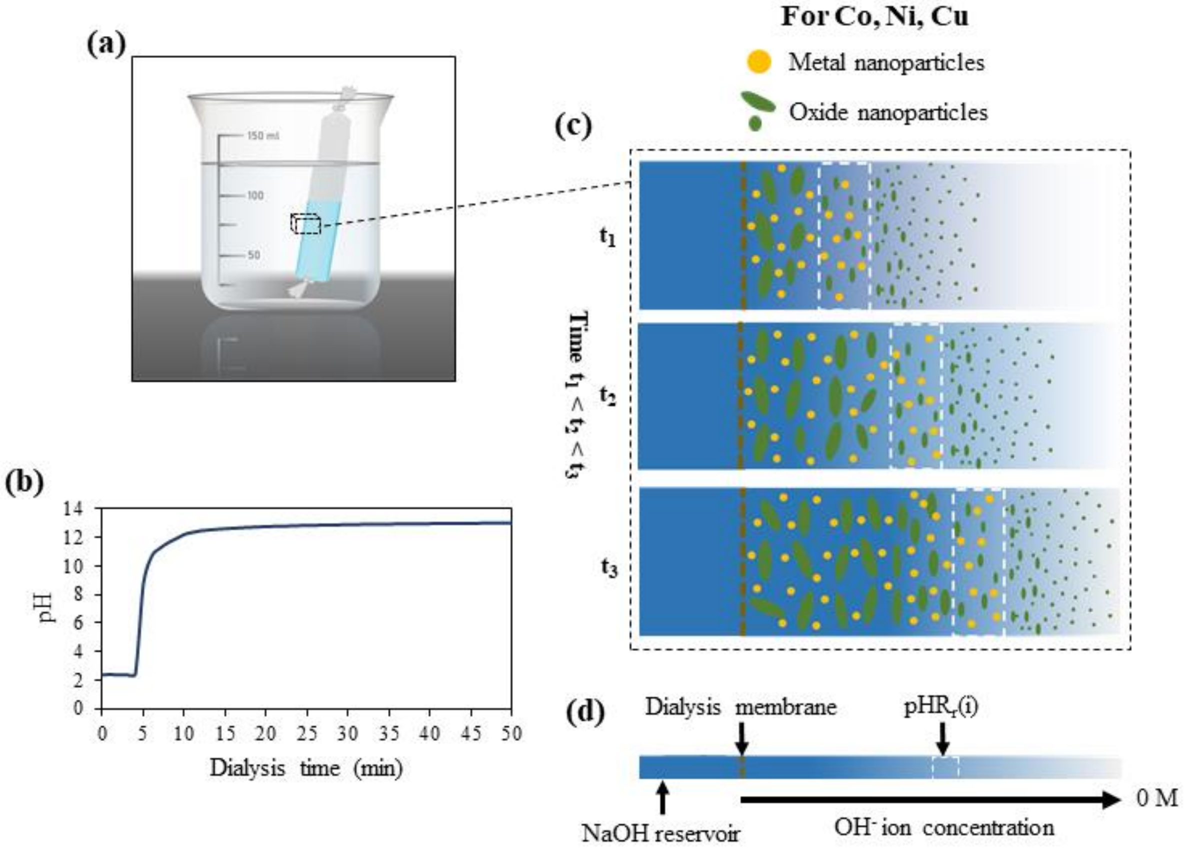

Fig. 4.4. (a) Simple schematic of LDS setup, (b) pH gradient created in the solution inside the dialysis bag, and (c) schematics of the formation mechanisms of Cu, Co, and Ni nanocrystals in LDS process.

Here citric acid plays a key role as a chelating agent inside the dialysis membrane. To understand the functionality of chelating agent, we should define the complexation concept. Complexation happens when two simple independent species are associated and form a new species [482, 483]. When one of the initial species is a metal ion, the resulting species is called a metal complex where the central metal atom is bound to coordinating atoms (or donor atoms) of ligands. A ligand which binds to a metal ion through one atom is called a monodentate ligand. If a ligand coordinates the metal atom by more than one donor atom, it is called a multidentate or chelating agent and, consequently, the metal complex that is formed is a metal chelate [484]. Chelation is originated from a Greek word called “Chela” which means claw of a lobster. The term of chelate was first used by Sir Gilbert T. Morgan and H. D. K. Drew in 1920 [485]. They employed it for the caliper-like groups functioning as two associating units which fasten on a central atom, so creating heterocyclic rings [486].

Chelating agents can possess ligand binding atoms which create either two covalent bindings or one covalent and one co-ordinate or two co-ordinate linkages in the case of bidentate chelates. Mainly atoms like S, N and O performs as ligand atoms in the form of chemical groups like -SH, -S-S, -NH_2, =NH, -OH, -OPO_3H, etc. Bidenate or multidentate ligands create ring-like structures which contain the metal ion and the two-ligand atoms attached to the core metal [487].

Generally, the metal-ligand complex is formed according to the equation mentioned below [488, 484]:

$$xM^{m+} + yH^{+} + zL^{n-} \overset{K_{xyz}}{\longleftrightarrow} M_xH_yL_z{}^{(mx+y-zn)} \qquad \text{(Eq. 4.1)}$$

the equilibrium constant, K_{xyz}, can be expressed as follows:

$$K_{xyz} = \frac{[M_xH_yL_z{}^{(mx+y-zn)}]}{[M^{m+}]^x[H^+]^y[L^{n-}]^z} \qquad \text{(Eq. 4.2)}$$

where *x*, *y*, and *z* are stoichiometric coefficients, $[M^{m+}]$ is the concentration of metal ion, $[H^+]$ is the concentration of hydrogen ion, $[L^{n-}]$ is the concentration of ligand, and $[M_xH_yL_z{}^{(mx+y-zn)}]$ is the concentration of metal-ligand complex at equilibrium conditions. Accordingly, the logarithm of equilibrium constant (log K_{xyz}) is considered as the stability constant of the mentioned complex.

The strength of the metal-ligand complexation is different for various kinds of metal ions [489]. Besides, various factors affect stability constant. For example, size of chelating agent, number of chelate rings, strength of chelating molecules, and nature and the number of donor atoms influence the stability constant [490]. Also, radius of metal atom affects the stability constant where smaller ions are complexed more strongly, referring to higher electrostatic interactions. Other parameters such as temperature, ionic strength of chelating agent, and concentration of hydrogen ions can change stability of complex [491].

Citric acid is considered as a weak chelating agent, binding metal ions in solution to form highly stable chelate complex, slowing down the outbound diffusion of metal ions. It, furthermore, decelerates the formation of copper oxide particles. According to the data summarized in Table 4.1, for the case of Cu^{2+} the stability constant of citrate complexes is less than those formed by EDTA and salicylic acid. The mentioned characteristic is exactly what is required inside the dialysis bag to form ultrasmall Cu nanoparticles. If a stronger chelating agent is used instead of citric acid, the binding between copper ions will be strong, so they will not be reduced to copper atoms. On the other hand, if we employ a weaker chelating agent, the binding between ions will be dissociated easily, so copper ions will diffuse out the membrane or form oxide particles.

Table 4.1. Stability constant of chelates (log K) [489, 491, 490].

Chelating agent	**Ca^{2+}**	**Mg^{2+}**	**Mn^{2+}**	**Fe^{2+}**	**Fe^{3+}**	**Zn^{2+}**	**Cu^{2+}**
EDTA	10.70	8.69	13.56	14.30	25.70	16.50	18.80
Citric acid	3.50	2.80	3.20	3.20	11.85	4.50	6.10
Salicylic acid	N/A	4.70	2.70	6.55	16.35	6.85	10.60

As pH increases, such chelates become unstable; citric acid dissociates with metal ions, and further dissociates into citrate ions. Citrate has long been used as both the mild reductant and stabilizer to synthesize precious metal nanoparticles such as Au, Ag and Pd, which is referred as the Turkivech method [471-476], and has extensively been investigated [492-496]. The citrate reduction reaction can be expressed as:

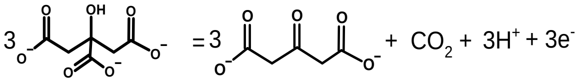

Eq. (4.3)

The solution pH can be tuned to control the overall reaction rate; the higher pH, the higher the reaction rate. There exists a pH range for each of these metal ions in which metal ions are reduced by citrate ions into metal atoms that nucleate and form ultrasmall nanocrystals. For convenience of latter discussion, we refer to this pH range as $pHR_r(i)$ where i represents different metal elements. As the pH gradually increases from the edge towards the center, the solution sequentially experiences $pHR_r(i)$, and the amount of ultrasmall metal nanocrystals gradually increases. When a part of solution experiences pH outside $pHR_r(i)$, other precipitation reactions or particle formation processes occur. For the cases of Co, Ni, and Cu, when pH is lower than $pHR_r(i)$ but higher than a certain value, termed as $pH_o(i)$, citrate is not capable of reducing metal ions into metal atoms, but oxide precipitation reactions can take place to produce oxide nanoparticles. As pH increases to a value above $pHR_r(i)$, oxide precipitation proceeds at a much higher rate than citrate reduction, which leads to a product primarily consisting of large oxide nanoparticles.

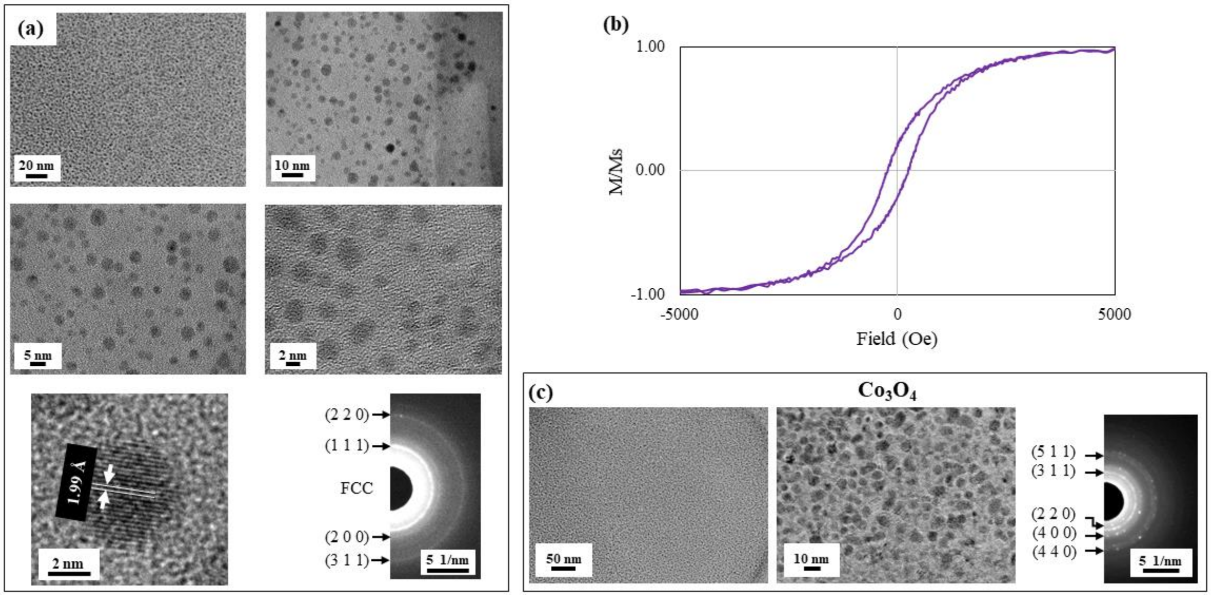

Fig. 4.5. (a) HRTEM images, corresponding SAED pattern, and (1 1 1) lattice fringes of Co nanocrystals synthesized through LDS, (b) Magnetic hysteresis loop of Co nanocrystals, and (c) TEM micrographs and SAED patterns of large particles formed during the synthesis process.

Similarly, Figs. 4.5 and 4.6 show the TEM micrographs of cobalt and nickel nanocrystals synthesized via LDS, respectively. Measurements of the magnetic properties of Co and Ni nanocrystals (shown in Figs. 4.5(b) and 4.6(b)) confirm that they exist as metallic nanoparticles in solution (not as byproducts of high energy electron beam reduction in HRTEM, since these properties can only result from metal nanocrystals). It should be noted that synthesized Co and Ni nanoparticles are not stable at a pH below 9, dissolving back into ions.

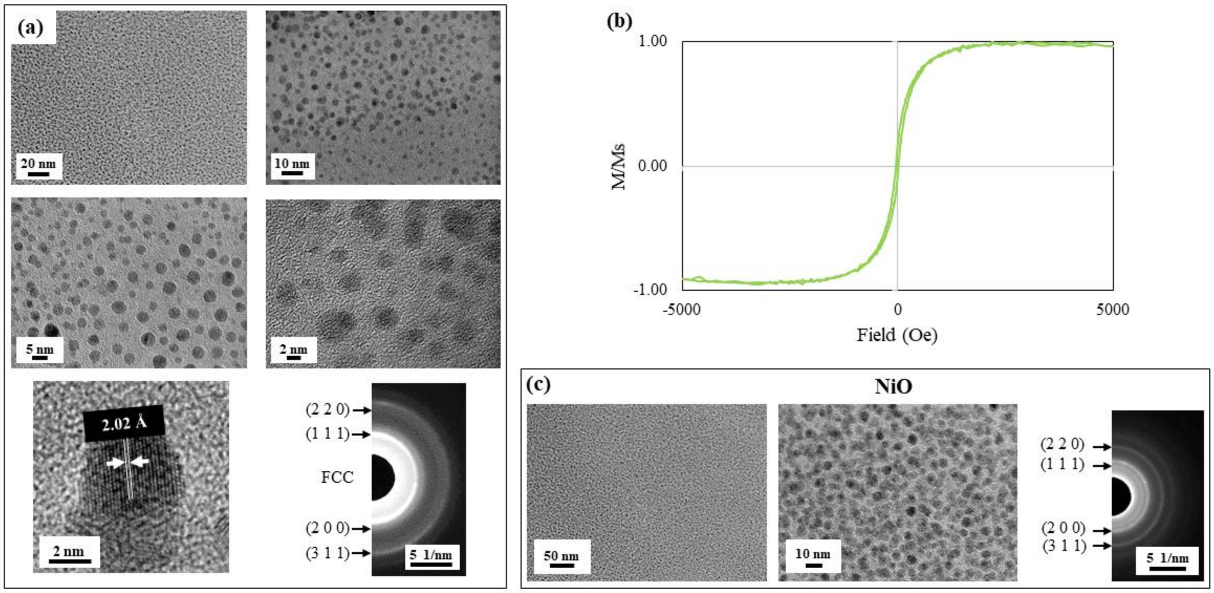

Fig. 4.6. (a) HRTEM images, corresponding SAED pattern, and (1 1 1) lattice fringes of Ni nanocrystals synthesized through LDS, (b) magnetic hysteresis loop of Ni nanocrystals, and (c) TEM micrographs and SAED patterns of large particles formed during the synthesis process.

For Ag, Au, Pd, and Pt the whole formation mechanism of metal nanocrystals is similar to the case of Co, Ni, and Cu nanoparticles, but based on the difference in their reactivities, the reactions inside the dialysis bag varies. When pH is lower than $pHR_r(i)$, metal ions are more stable comparing less reactive metals like Co, Ni, and Cu, so no reaction occurs. As pH approaches $pHR_r(i)$, the citrate reduction reaction takes place. However, if pH is higher than $pHR_r(i)$, the citrate reduction reaction rate is too high, which makes nuclei quickly grow into large particles before they are fully capped by citrate ions. Only at $pHR_r(i)$, the nucleated ultrasmall nanoparticles can be sufficiently capped by citrate ions to prevent them from growing larger.

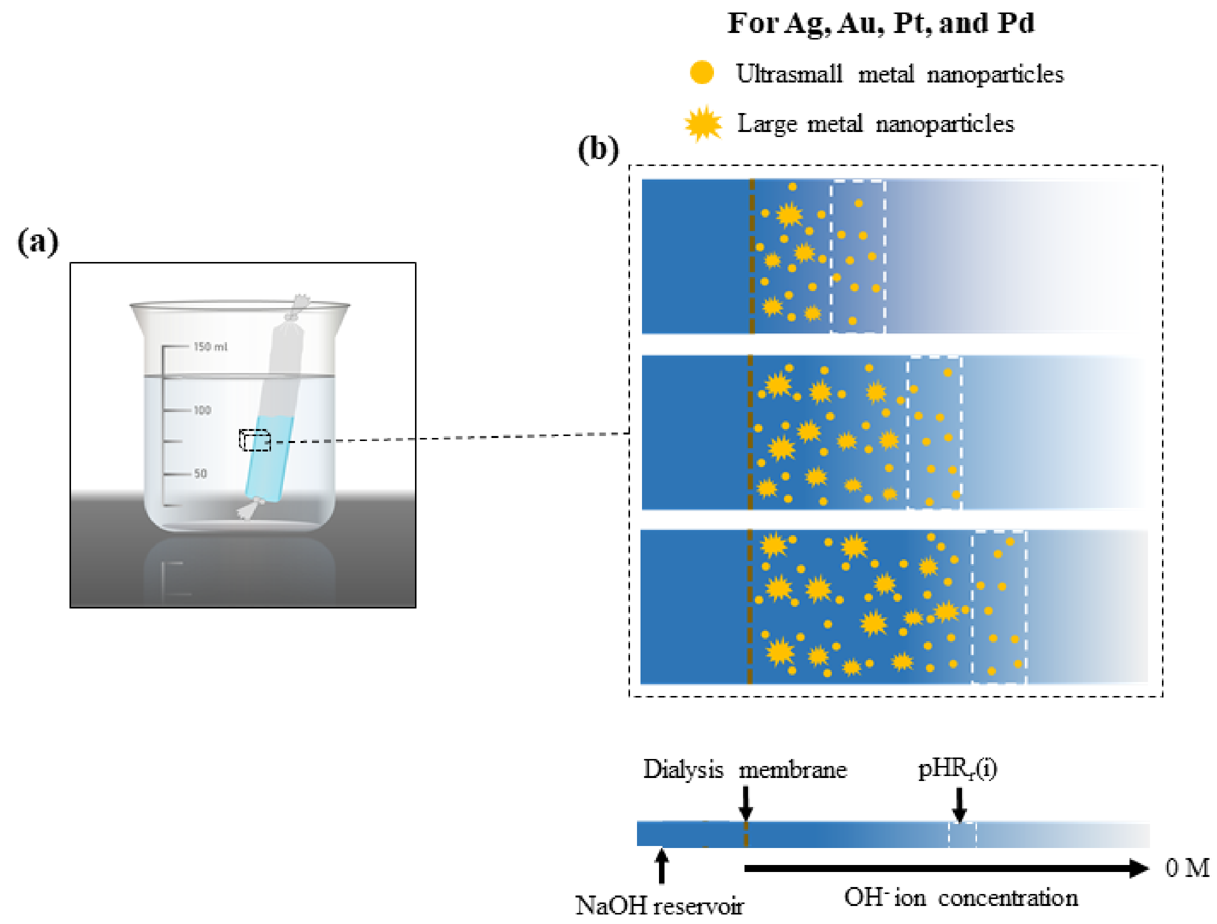

Fig. 4.7. (a) Simple schematic of LDS setup, and (b) schematics of the formation mechanisms of Au, Ag, Pt, and Pd nanocrystals in LDS process.

The formation of ultrasmall metallic nanoparticles of Au, Ag, Pd, and Pt, is accompanied by large particles of Ag, Au, Pt, and Pd, respectively (Figs. 4.8-4.11). These large particles generated outside pHR$_r$(i) can be readily separated from the ultrasmall metal nanocrystals formed in pHR$_r$(i) by a simple centrifugation step at 14000 rpm for 20 minutes which is performed by the end of dialysis step.

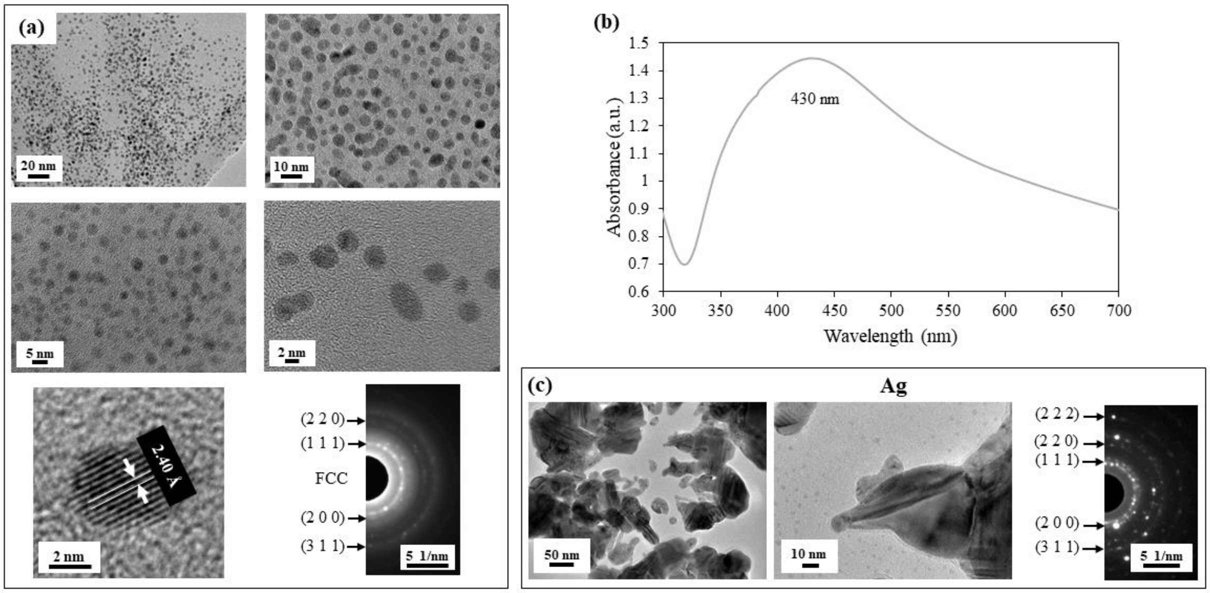

Fig. 4.8. (a) HRTEM images, corresponding SAED pattern, and (1 1 1) lattice fringes of Ag nanocrystals synthesized through LDS, (b) UV-Vis absorption spectra of Ag nanocrystals, and (c) TEM micrographs and SAED patterns of large particles formed during the synthesis process.

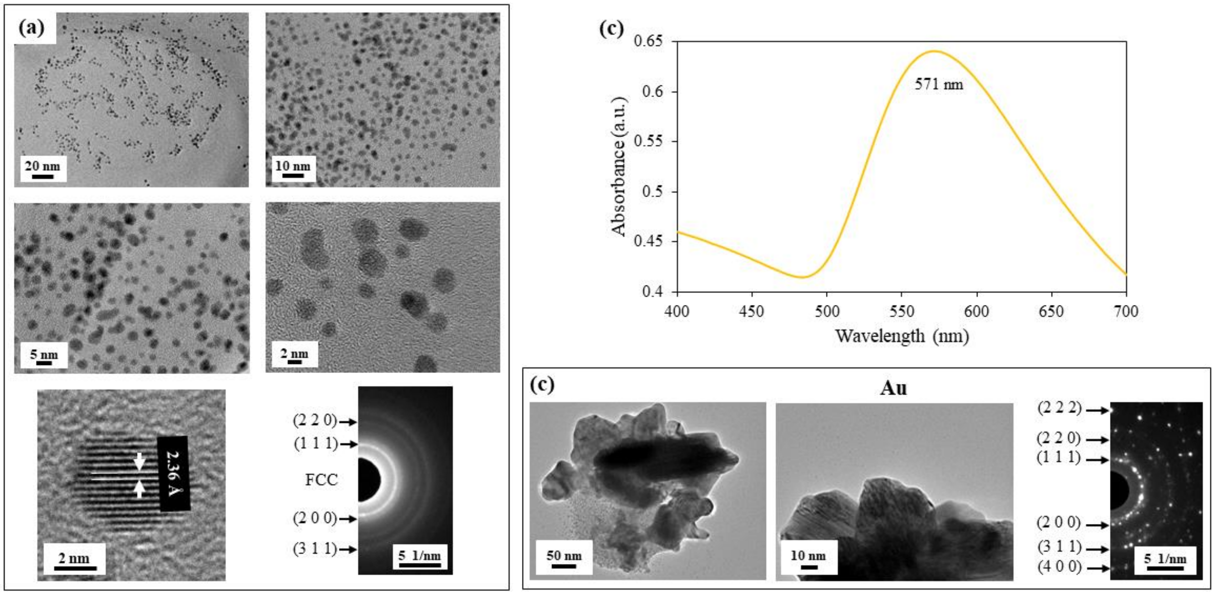

Fig. 4.9. (a) HRTEM images, corresponding SAED pattern, and (1 1 1) lattice fringes of Au nanocrystals synthesized through LDS, (b) UV-Vis absorption spectra of Au nanocrystals, and (c) TEM micrographs and SAED patterns of large particles formed during the synthesis process.

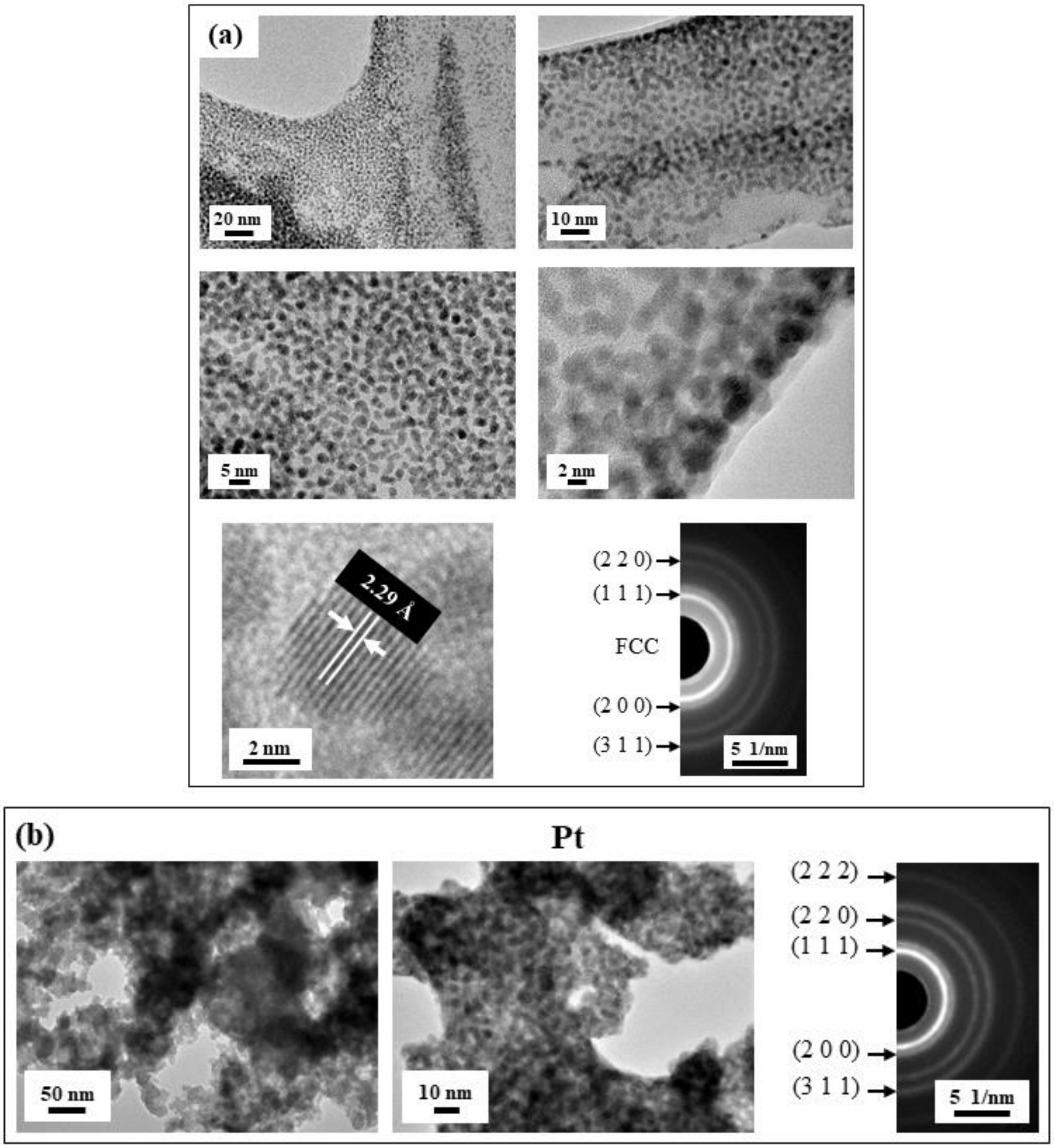

Fig. 4.10. (a) HRTEM images, corresponding SAED pattern, and (1 1 1) lattice fringes of Pt nanocrystals synthesized through LDS and (b) TEM micrographs and SAED pattern of large particles formed during the synthesis process.

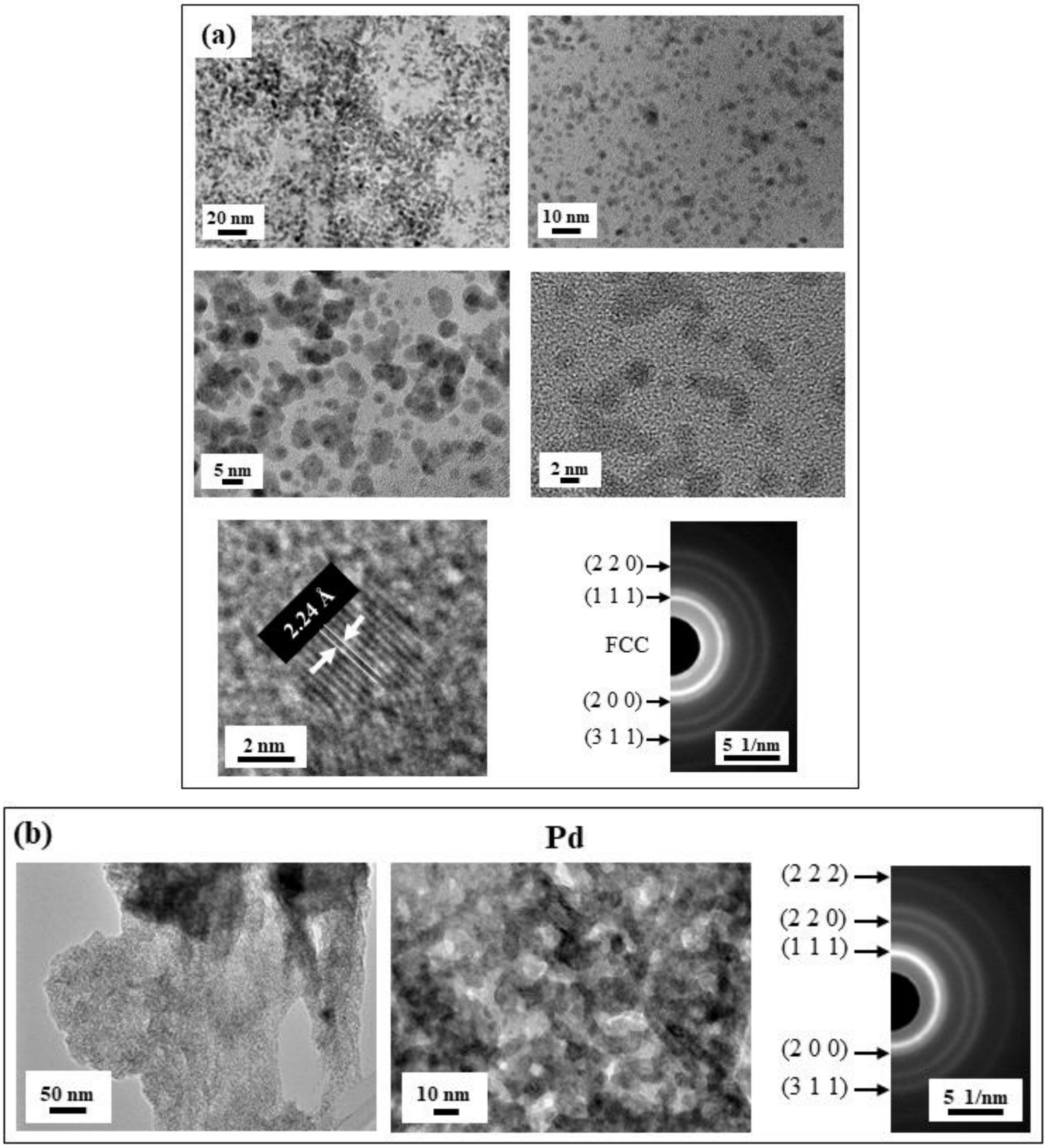

Fig. 4.11. (a) HRTEM images, corresponding SAED pattern, and (1 1 1) lattice fringes of Pd nanocrystals synthesized through LDS and (b) TEM micrographs and SAED pattern of large particles formed during the synthesis process.

In case of Ru, we obtained a set of interesting data. Based on the standard reduction potential data summarized in Table 4.2, Ru has a reduction potential similar to Ag and Pd, so it was expected to follow the same formation mechanism and form metal ruthenium nanoparticles.

However, TEM micrographs and SAED data presented in Fig. 4.12 demonstrate the formation of ruthenium oxide nanoparticles. The reason is most probably because the reduction potential of citrate complex differs significantly from metal ions. Hence, due to a decrease in reduction potential, instead of metal ruthenium nanoparticles, ruthenium oxide nanocrystals are formed.

Table 4.2. Standard reduction potentials of metals employed in DLS process [497-499].

Element	**Half reaction**	**Reduction potential (V)**
Ce	$Ce^{3+} + 3e^- \leftrightarrows Ce_{(s)}$	-2.34
Lu	$Lu^{3+} + 3e^- \leftrightarrows Lu_{(s)}$	-2.28
Mn	$Mn^{2+} + 2e^- \leftrightarrows Mn_{(s)}$	-1.18
Zn	$Zn^{2+} + 2e^- \leftrightarrows Zn_{(s)}$	-0.76
Fe	$Fe^{2+} + 2e^- \leftrightarrows Fe_{(s)}$	-0.44
Co	$Co^{2+} + 2e^- \leftrightarrows Co_{(s)}$	-0.28
Ni	$Ni^{2+} + 2e^- \leftrightarrows Ni_{(s)}$	-0.25
H	$2H^{2+} + 2e^- \leftrightarrows H_{2(g)}$	0.00
Cu	$Cu^{2+} + 2e^- \leftrightarrows Cu_{(s)}$	+0.34
Ru	$Ru^{3+} + 3e^- \leftrightarrows Ru_{(s)}$	+0.60
Ag	$Ag^{+} + e^- \leftrightarrows Ag_{(s)}$	+0.80
Pd	$Pd^{2+} + 2e^- \leftrightarrows Pd_{(s)}$	+0.92
Pt	$Pt^{2+} + 2e^- \leftrightarrows Pt_{(s)}$	+1.19
Au	$Au^{3+} + 3e^- \leftrightarrows Au_{(s)}$	+1.52

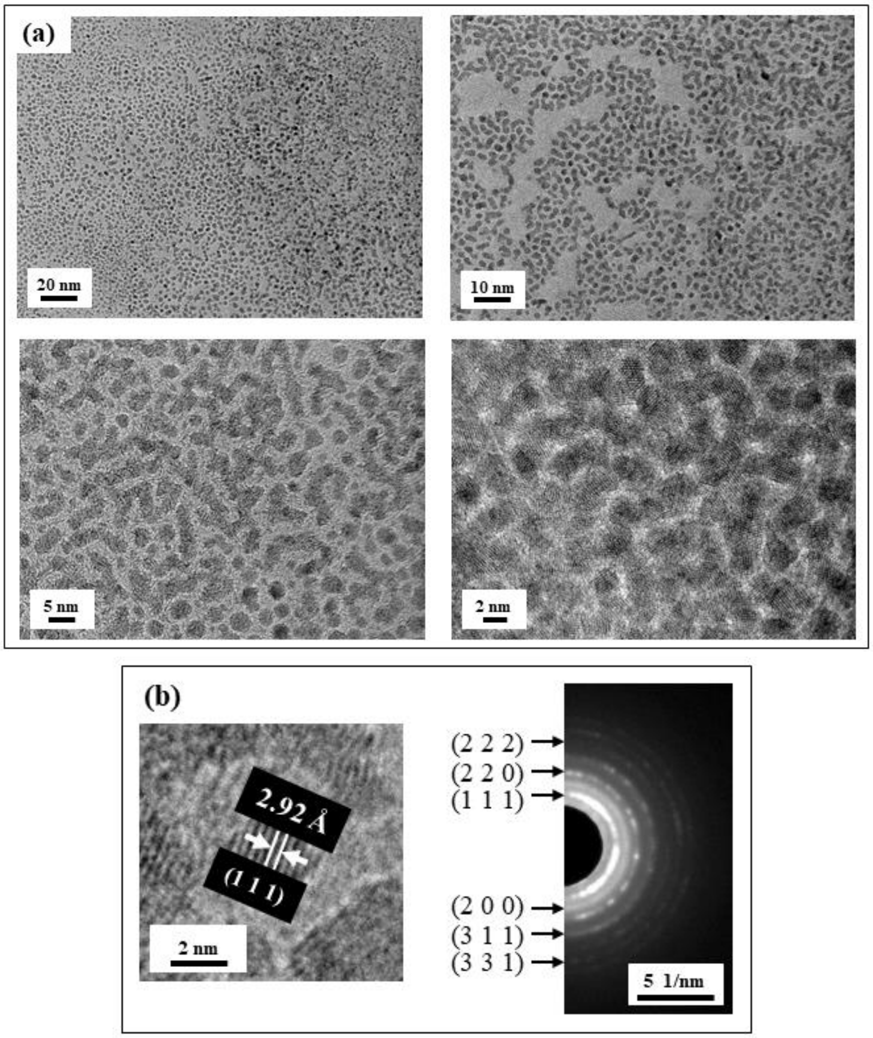

Fig. 4.12. (a) HRTEM images and (b) corresponding SAED pattern and (1 1 1) lattice fringes of ruthenium oxide (RuO_2) nanocrystals synthesized via LDS.

4.5. Synthesis parameters of LDS

4.5.1. Concentration of $CuCl_2$

To examine the effect of $CuCl_2$ concentration on the efficiency of Cu nanocrystals production, the LDS of copper was conducted using 1.0 mM, 1.5 mM, 6.0 mM, and 60.0 mM of $CuCl_2$. The other process parameters including the volume of solution inside the dialysis bag (10 ml), the NaOH concentration of 0.5 M, and the dialysis time of 2 hours were kept the same for all the synthesis experiments. After washing the final product, 10 µl of colloidal copper was taken as well as the same volume of initial solution (before dialysis) to measure the number of copper ions via inductively coupled plasma mass spectrometry (ICP-MS) and, consequently, calculate the efficiency of Cu nanocrystal production. According to the data summarized in Table 4.2, for the case of 60.0 mM, 6.0 mM, and 1.5 mM of $CuCl_2$, the final number of copper ions is almost the same, indicating that the number of Cu nanocrystals is the same. Therefore, 1.5 mM of $CuCl_2$ gives the higher Cu nanocrystals efficiency. However, by decreasing the $CuCl_2$ molarity to 1.0 mM, the production efficiency is reduced. This is probably because there are not enough copper ions inside the solution which can be reduced and form copper nanoparticles.

Table 4.3. Efficiency of Cu nanocrystals production based on the $CuCl_2$ molarity.

Molarity of $CuCl_2$ [mM]	**Concentration of Cu^{2+} [ppb]**		**Efficiency (%)**
	Initial	**Final**	
60.0	14641.24	203.75	1.39
6.0	2018.99	245.02	12.14
1.5	529.69	197.82	37.35
1.0	353.13	84.03	23.79

4.5.2. Concentration of NaOH

In section 4.2.2 it was mentioned that Cu nanocrystals were synthesized by employing 0.5 M of NaOH inside the reservoir. Here, to evaluate the effect of NaOH concentration on Cu nanocrystal formation, LDS experiments were conducted employing various NaOH concentration of 0.005 M, 0.05 M, and 0.1 M. TEM analysis shows that no Cu nanoparticles were formed by using reservoir of 0.005 M NaOH. The possible reason is that 0.005 M NaOH cannot make the pH of solution inside the dialysis bag high enough to reach the range of $pHR_r(Cu)$, so citrate ions cannot reduce the copper ions to copper atoms. However, Fig. 4.13 demonstrates that by employing both reservoir of 0.05 M and 0.1 M NaOH, Cu nanocrystals are formed. Comparing Figs. 4.13(a) and (b) shows that the mean size of Cu nanocrystals is not the same; 0.1 M NaOH creates larger Cu nanoparticles. The possible reason is that higher concentration of NaOH increases the rate of reactions inside the dialysis membrane, so the Cu nuclei grow faster before they are completely capped by citrate. Hence, higher concentration of NaOH inside the reservoir increases the mean size of copper nanocrystals.

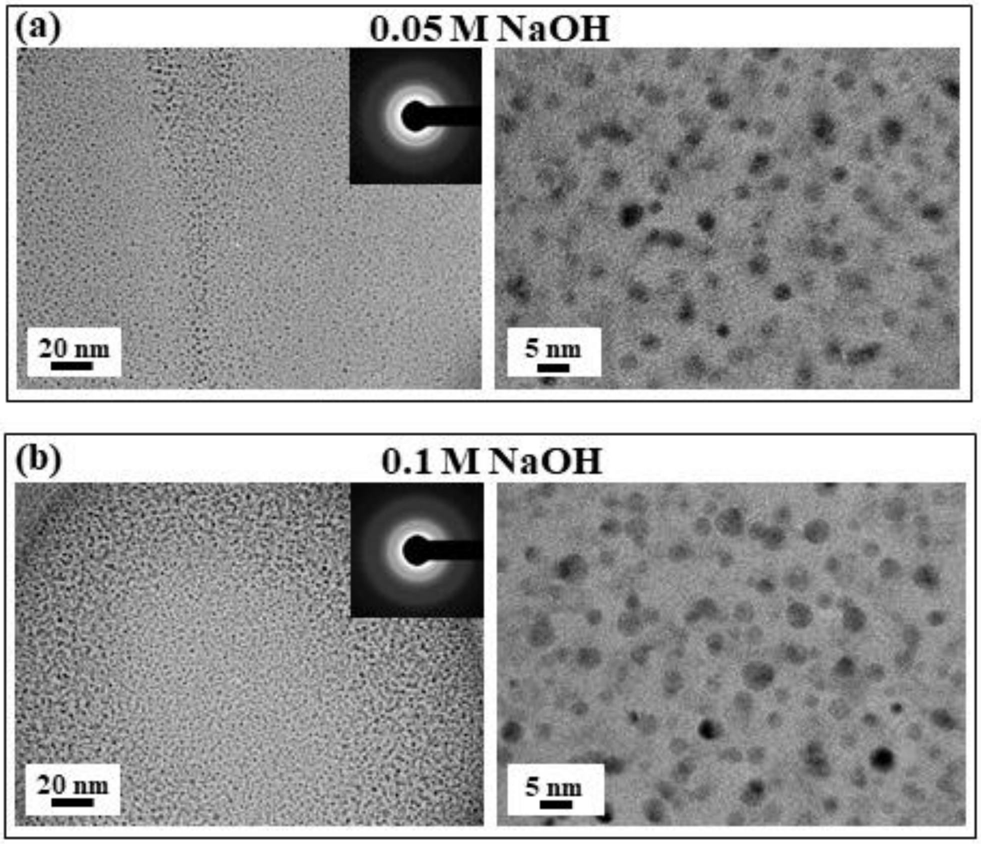

Fig. 4.13. HRTEM micrographs and the corresponding SAED patterns of CuNPs synthesized via LDS technique with NaOH concentration of (a) 0.05 M and (b) 0.1 M.

4.5.3. $CuCl_2$/citric acid molar ratio

The next parameter considered was the molar ratio of $CuCl_2$ to citric acid. Fig. 4.14 shows the TEM micrographs of sample processed by using the $CuCl_2$/citric acid molar ratio of 4/1. The resultant microstructure includes two distinctive parts: (1) well-separated Cu nanocrystals which are completely capped by citrate but have larger size comparing the size of Cu nanocrystals synthesized with $CuCl_2$/citric acid molar ratio of 1/1 (see Fig. 4.14(a)), and (2) some larger Cu oxide particles. It suggests that as the number of citrate ions is less than the Cu ions, a fraction of Cu ions are oxidized and form large aggregates.

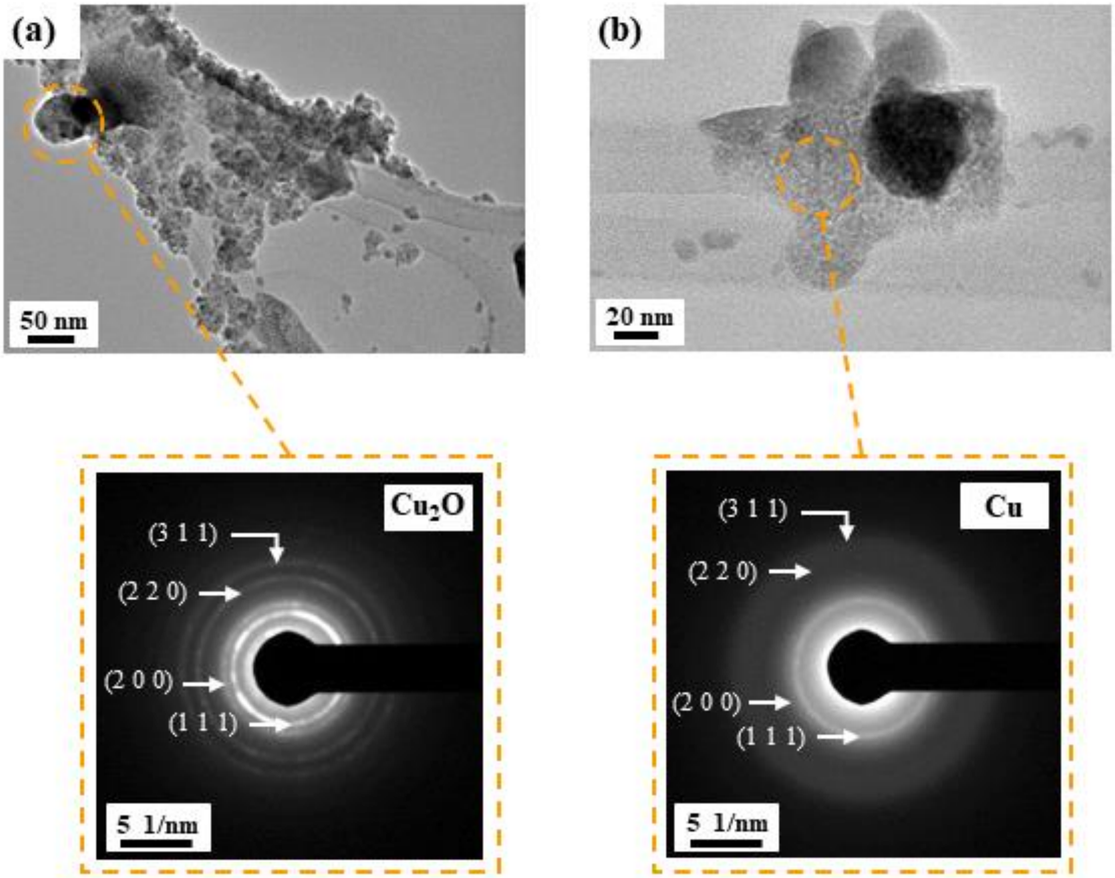

Fig. 4.14. HRTEM micrographs and the corresponding SAED patterns of CuNPs synthesized through LDS with $CuCl_2$/citric acid molar ratio of 4/1.

Fig. 4.15(a) demonstrates that by changing the $CuCl_2$/citric acid molar ratio to 1/4 and increasing the number of citrate ions comparing the copper ones, ultrasmall copper nanoparticles with the smaller size are formed. However, the resultant structure is not uniform and as it can be seen from Fig. 4.15(b), some tubular structures are formed which are carbon-based according to EDX analysis from excessive citric acid.

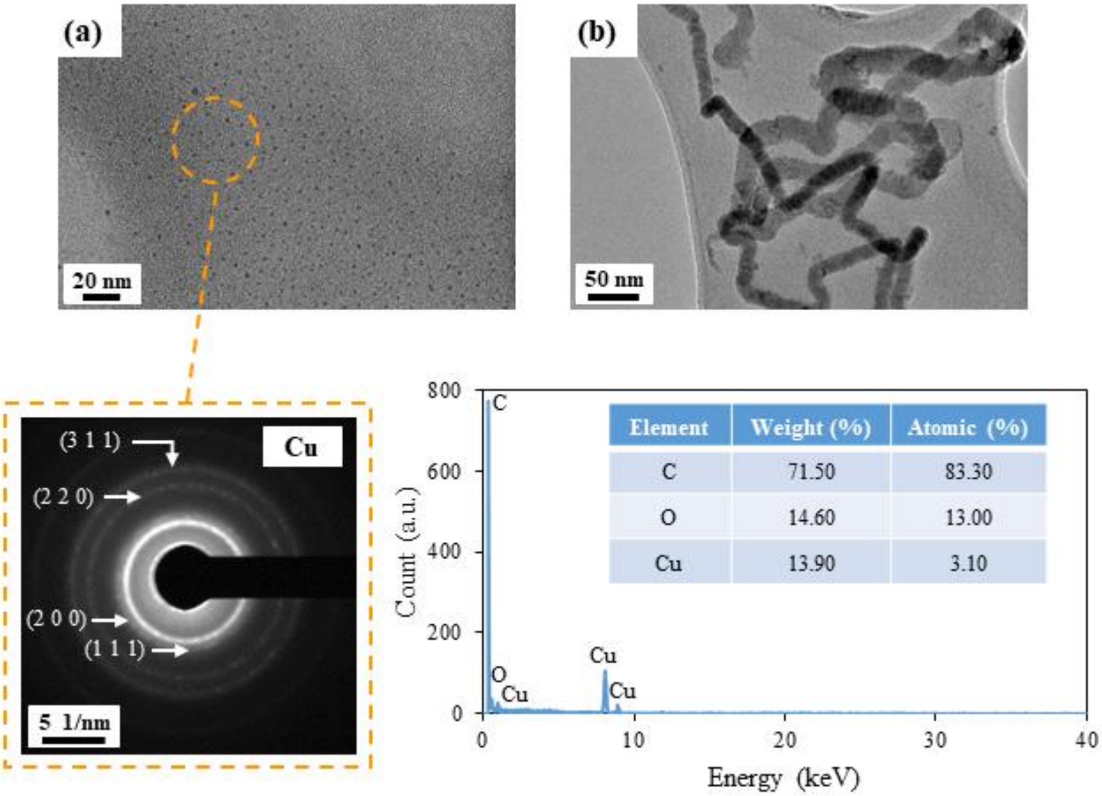

Element	Weight (%)	Atomic (%)
C	71.50	83.30
O	14.60	13.00
Cu	13.90	3.10

Fig. 4.15. HRTEM micrographs, SAED pattern, and EDX analysis of CuNPs synthesized through LDS method with $CuCl_2$/citric acid ratio of 1/4.

4.5.4. Dialysis time

The influence of synthesis time was studied by conducting LDS with different immersion time of 10 minutes, 20 minutes, 30 minutes, 60 minutes, and 600 minutes. Fig. 4.16 illustrates that the mean size of copper nanocrystals does not change by varying the dialysis time, indicating that the Cu nanocrystal size is insensitive to the dialysis time. This suggests the possibility of upscaling the production of nanocrystals using this method, in which a large dialysis bag is used to hold a large volume of solution which would require a prolonged diffusion process.

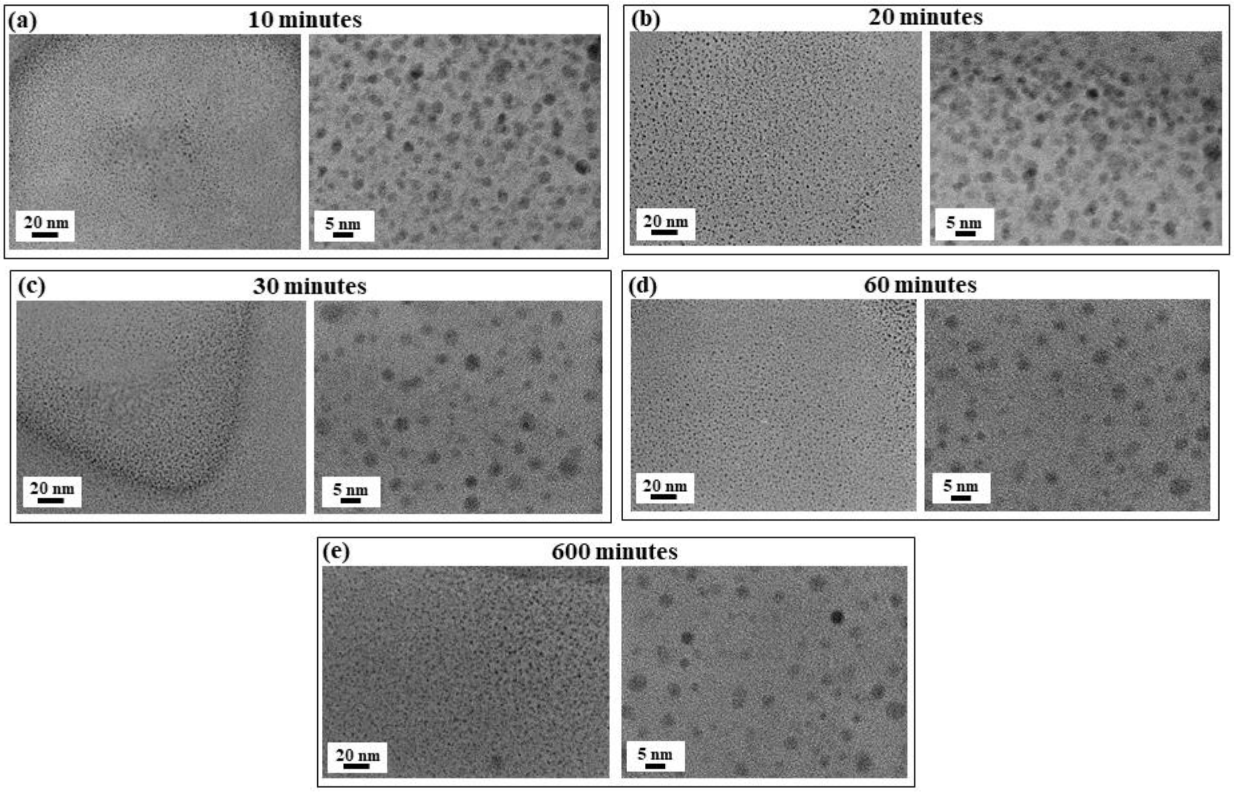

Fig. 4.16. HRTEM micrographs of Cu nanocrystals produced by various synthesis time of (a) 10 minutes, (b) 20 minutes, (c) 30 minutes, (d) 60 minutes, (e) 600 minutes.

4.5.5. Reducing agent

To evaluate the effect of reducing agent the same LDS process as mentioned in section 4.2.1 was conducted but with citric acid being replaced with sodium citrate and ascorbic acid. As it can be seen from Fig. 4.17, in addition to well-separated Cu nanocrystals, some of the Cu oxide aggregates exist in the final product. This probably due the temperature at which LDS was conducted. Previous experiments on synthesis of Au and Ag nanoparticles indicated that sodium citrate has the highest reducing power at elevated temperature [500, 472]. Therefore, as the LDS of Cu nanocrystals is conducted as room temperature, the reduction reaction rate is low, so some of them are oxidized. Furthermore, the main difference of citric acid and sodium citrate is that sodium citrate solution is basic. Therefore using sodium citrate narrows down the range of pHR_r(Cu), which results in the formation of higher fraction copper oxide nanoparticles.

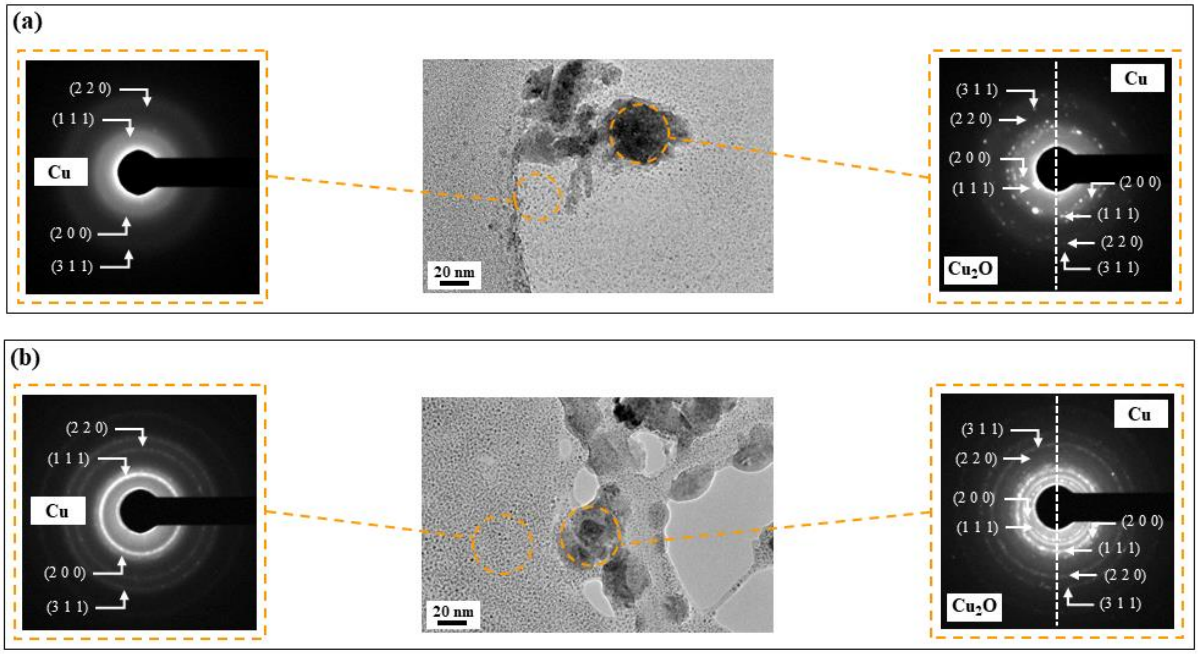

Fig. 4.17. HRTEM micrographs of SAED patterns of copper particles synthesized through LDS using (a) sodium citrate and (b) ascorbic acid as reducing agent.

Fig. 4.17(b) demonstrates that employing ascorbic acid creates microstructures similar to those from sodium citrate, but the explanation is different. Ascorbic acid becomes slightly unstable at temperatures higher than refrigeration temperature (4-5 °C) [501], which might lead to poor reducing power, resulting in the formation of copper oxide nanoparticles. Moreover, the previous investigations confirm that when ascorbic acid is used as the reducing agent, other chemicals such as sodium citrate should be used as the stabilizing agent. Therefore, as ascorbic acid cannot properly cap all the Cu nanocrystals, some of them stick together and form the big aggregates.

4.5.6. Diffusion rate of OH$^-$ ions

Two sets of experiments were conducted to examine the effect of OH$^-$ diffusion rate on Cu nanocrystals production via LDS. In the first experiment, two similar LDS setups were used to synthesize Cu nanoparticles. The only difference between these two setups is that the solution inside the one the dialysis membrane was vigorously stirred through the process. Without stirring, it was found that using 0.05 M NaOH could produce a large amount of smaller Cu nanoparticles with a uniform size distribution (Fig. 4.18(a)). Due to their further reduced size (~2 nm), these nanocrystals become fluorescent with an emission wavelength of 410 nm and an excitation wavelength of 570 nm. Stirring makes the diffusion process proceed at a much higher rate and a pH gradient cannot be established in the solution. With stirring, ultrasmall Cu_2O nanoparticles, rather than Cu nanoparticles, were generated (see Fig. 4.18(b)). UV-Vis absorption spectrum of the sample demonstrates an evident peak at 329 nm which is considered as the characteristic peak of cuprous oxide. Since $CuCl_2$ was used in the reactant solution, the formation of Cu_2O, instead of CuO, is attributed to the strong reduction capability of citrate ions at high pH. However, a weak, broad feature centered at 657 nm is also observed, which is attributed to the cupric oxide (CuO), possibly presents at the surface of the nanocrystals.

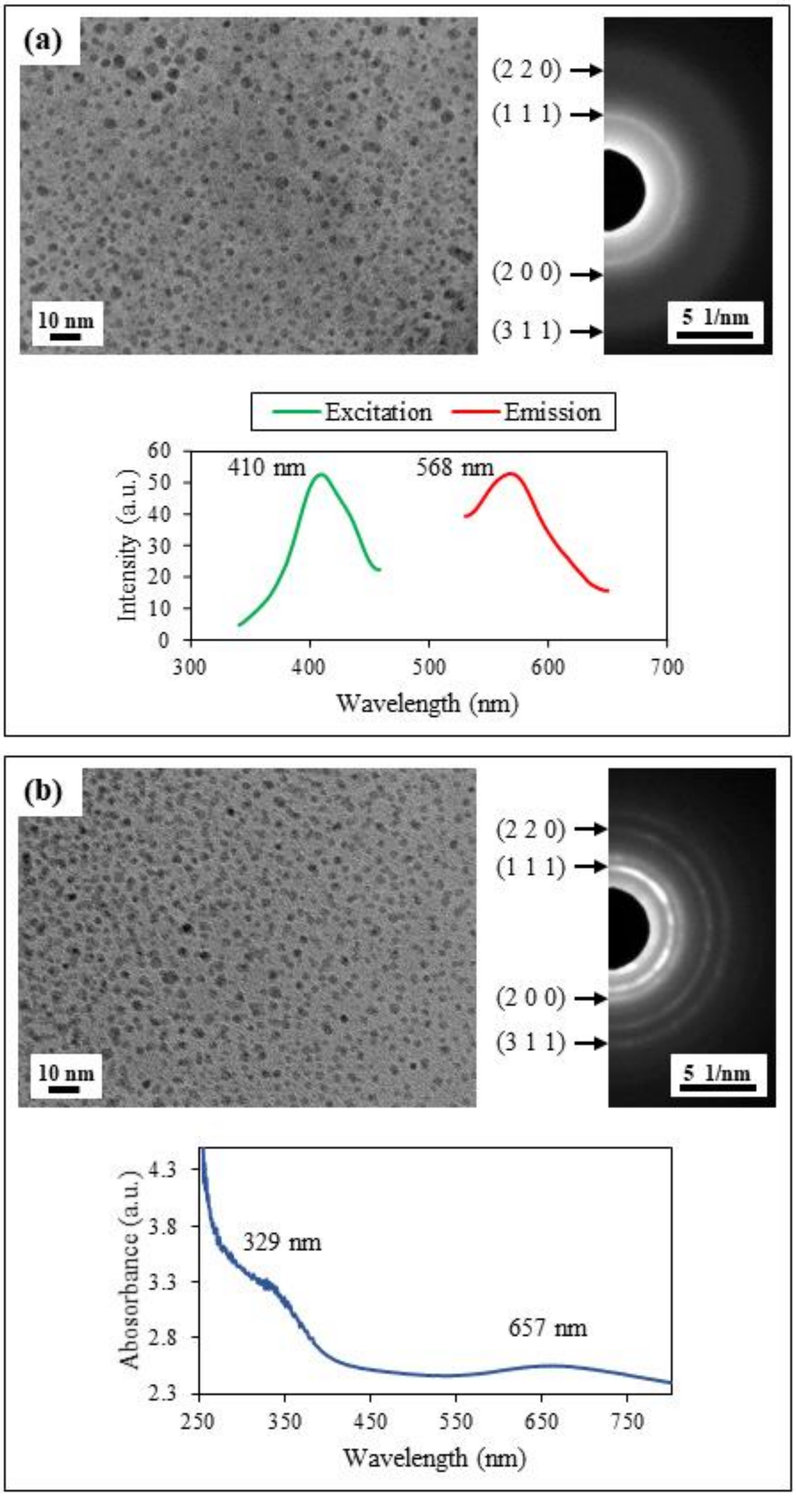

Fig. 4.18. HRTEM micrographs, SAED patterns and optical properties of CuNPs synthesized through LDS using 0.05 M NaOH (a) without stirring and (b) with stirring the solution inside the dialysis bag.

In the second experiment, a simple liquid diffusion tube was constructed, in which two ends of a plastic tube filled with the solution of 1.5 mM $CuCl_2$ and 1.5 mM citric acid were covered with the dialysis membrane and immersed in the NaOH solution reservoir. It was found that only ultrasmall Cu_2O nanoparticles were generated when 0.05 M NaOH solution was used in the reservoir regardless of the immersion time. The only difference between the tube setup and the dialysis bag setup is the ratio of the surface area of the membrane to the volume of the solution, r, which linearly affects the diffusion rate; the higher the ratio, the higher the reaction rate. r for the dialysis bag setup is much larger than the tube setup (about 15 times higher in our experiments). The result indicates that the synthesis product is also controlled by the diffusion rate of OH^- ions; a relatively high diffusion rate is another necessary condition for generation of metal nanocrystals. Another way to increase the diffusion rate is to use a higher concentration of NaOH solution inside the reservoir. When 0.5 M NaOH solution was used in the reservoir for the tube setup, Cu nanoparticles were indeed generated.

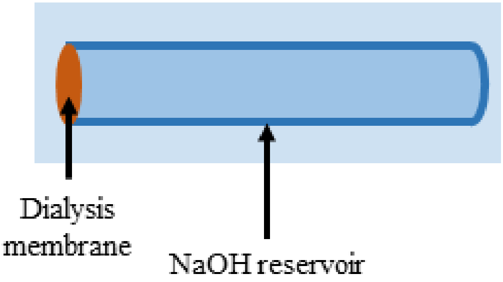

Fig. 4.19. Simple schematic of liquid diffusion tube.

Transport of hydroxide ions in aqueous medium is cause by two distinct mechanisms: (1) vehicular diffusion in which the center of charge moves together with the center of mass and (2) structural diffusion creating by movement of the center of charge regardless of the movement of the center of mass [502]. The structural diffusion of OH^- ions arises mainly from proton transfer (PT) between a solvated ion and a neighboring water molecule, which is known as Grotthuss diffusion, in which a covalent O-H bond breaks while another forms as the topological defect jumps to a neighboring site in the network [503, 504]. It is well known that the diffusion coefficients of hydroxide ions are anomalously large due to the added effect of structural diffusion [505].

The solvated structure is characterized by the coordination of water molecules and their distance around the central hydroxide oxygen, so based on their distance from the oxygen, they could be divided into different solvation layers. It was assumed that hydroxide exists in the form of $[HO^-\cdots H^+\cdots OH^-]^-$ complex with one water molecule [506]. Later, Botti at el. [507] employed neutron scattering and molecular modelling to correct the coordination number of OH^- to 3.9, referring to the classical Lewis acid evaluation of OH^- having three accepting hydrogen bonds (HBs) using the three lone atom pairs and one donating bond.

However, further investigations based on density functional theory (DFT) and molecular dynamics (MD) simulations on a single fully solvated hydroxide ion unveiled that these accepted HBs are non-localized where the HB electrons form a torus shapes orbital around the hydroxide oxygen [508]. Hence, OH^- can accept four HBs and donate a single weaker HB, causing hyper-coordination of OH^-. The latter mechanism predicted a diffusion coefficient closer to the experimental value.

This diffusion process of OH^- ions at the early stage in LDS can be modeled as the semi-infinite diffusion process with constant surface concentration, which has an error function analytical solution to the Fick's second law, with the concentration profile, $C(x,t)$, being expressed as:

$$C(x,t) = C_s - (C_s - C_0)\left[1 - erf\left(\frac{x}{2\sqrt{Dt}}\right)\right] \qquad \text{(Eq. 4.4)}$$

where x is the distance from the surface, t is the time, C_s the surface concentration, C_0 is the initial concentration in the solution, D is the diffusivity, and erf stands for error function [509]. By taking $C_0 = 0$, and $D = 5 \times 10^{-5}\, cm^2/s$ [510] the concentration profiles of OH^- ions in the solution from a reservoir containing 0.05 M (C_s) and 0.5 M (C_s) NaOH solution calculated using equation (4.4) are plotted in Fig. 4.20, respectively.

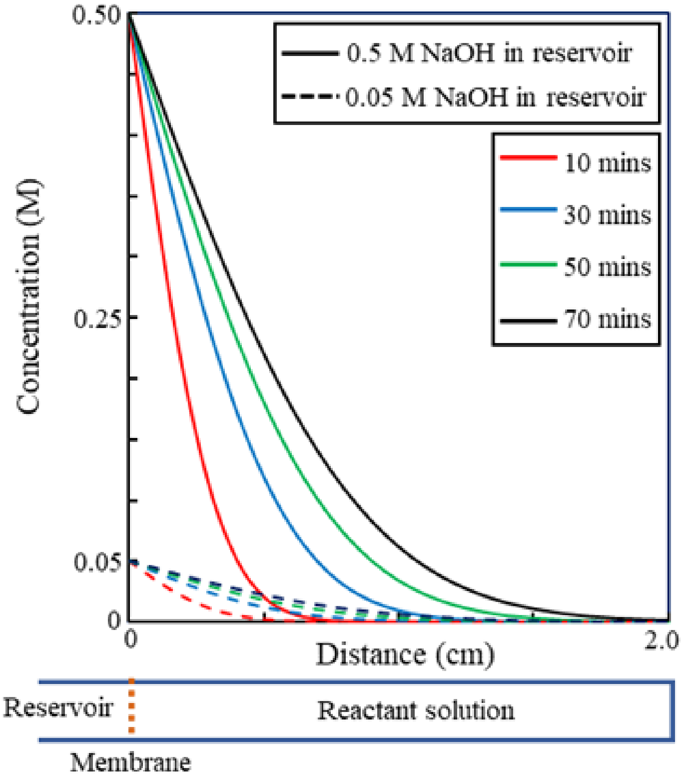

Fig. 4.20. The concentration profile of OH^- inside the dialysis bag in various synthesis time intervals, modeled as the semi-infinite diffusion process with constant surface concentration.

For better understanding, the concentration profile of OH^- inside the dialysis bag was plotted for both cases of 0.05 M and 0.5 M of NaOH for the case of 70 minutes dialysis (see Fig. 4.21). When 0.05 M NaOH solution is used, a gradual pH gradient makes the change of pH in the solution at much slower pace, so a large volume of the solution experiences a pH below $pHR_r(Cu)$ but above $pH_o(Cu)$ for a long time, in which only the oxide precipitation reaction takes place and ultrasmall oxide nanoparticles form. When 0.5 M NaOH solution is used, a steep pH gradient makes $pHR_r(Cu)$ quickly wipe through the whole solution and the solution experience a pH below $pHR_r(Cu)$ for a much shorter time, therefore metal nanoparticles form.

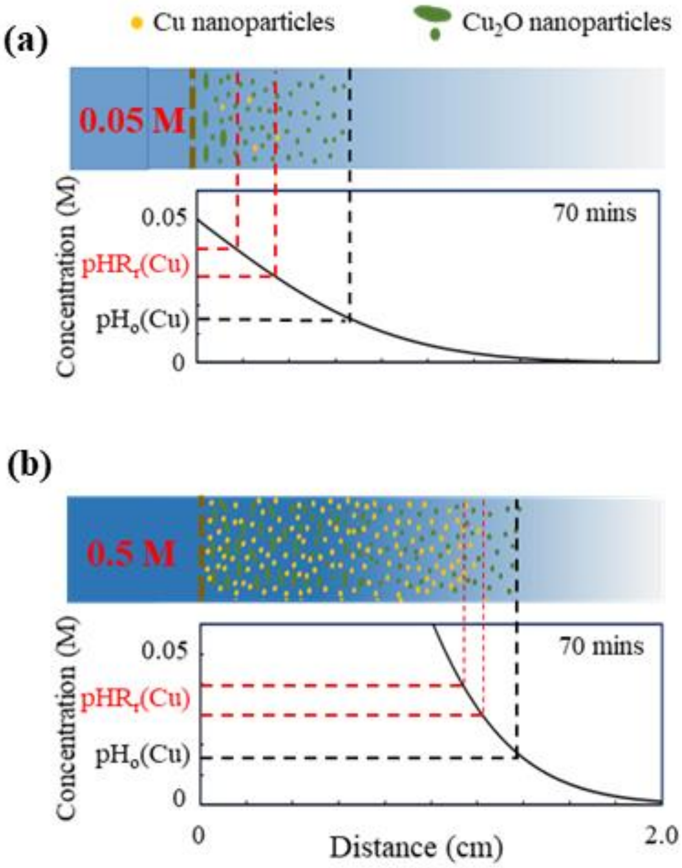

Fig. 4.21. Comparing the concentration profiles of OH^- ions employing (a) 0.05 M and (b) 0.5 M NaOH solution in the reservoir for synthesis time of 70 minutes.

4.6. Synthesis process of ultrasmall metal oxide nanoparticles

Based on the discussion mentioned in section 4.2.4, Cu_2O nanoparticles were synthesized by stirring the solution inside the dialysis bag. The detailed synthesis process is as follows. First, a mixture of 1.5 mM of citric acid and 1.5 mM of $CuCl_2$ is stir-mixed for 30 mins. Next, the mixture is transferred to a dialysis bag and the dialysis bag is immersed into a 0.05 M NaOH solution for 20 minutes at room temperature, keeping the solution inside the bag stirring with a magnetic stirring bar placed in a plastic cage.

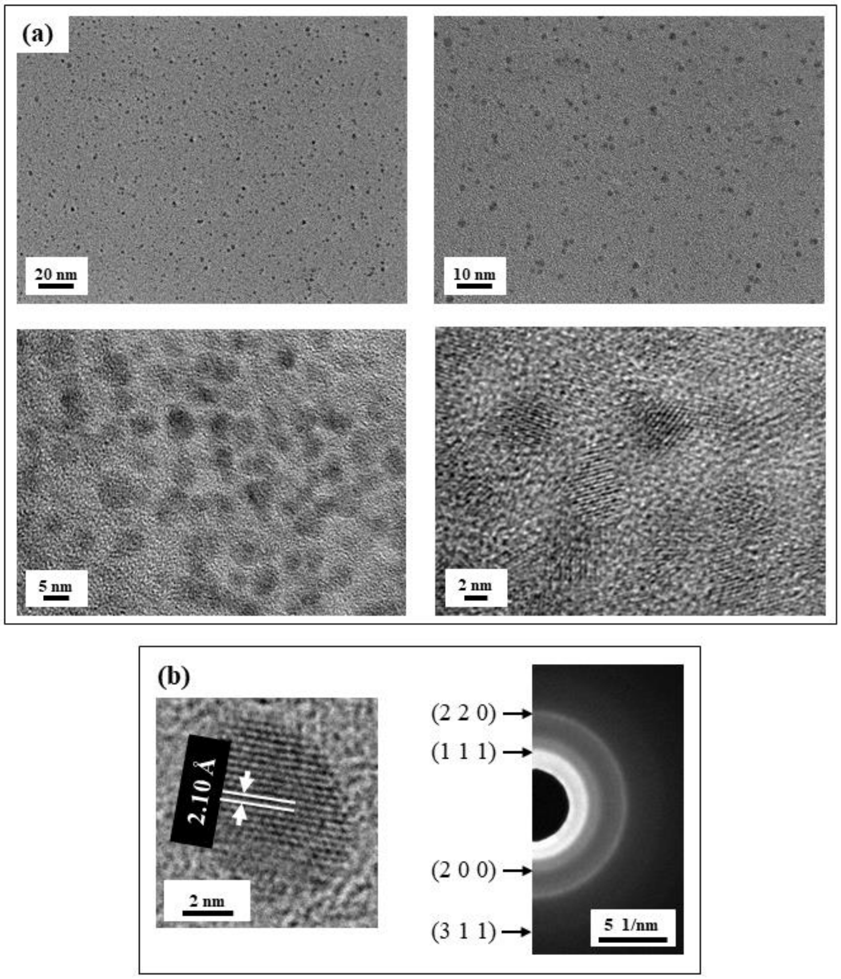

Fig. 4.22. (a) TEM micrographs of FeO nanoparticles produced via LDS process, and (b) corresponding SAED pattern and (1 1 1) lattice fringes of FeO nanoparticles.

Then, the collected solution is centrifuged at 14000 rpm for 20 minutes to separate large precipitates. Consequently, the resultant supernatant is mixed with acetone with a 4:1 (acetone: supernatant) ratio and centrifuged at 14000 rpm for 20 minutes. Finally, the precipitate is dialysis-washed in DI water for about 12 hours, while refreshing DI water every 2 hours.

Using this same process for synthesizing Cu_2O nanoparticles, other oxide nanoparticles including FeO, MnO, ZnO_2, and CeO_2 were produced (Figs. 4.22-4.25).

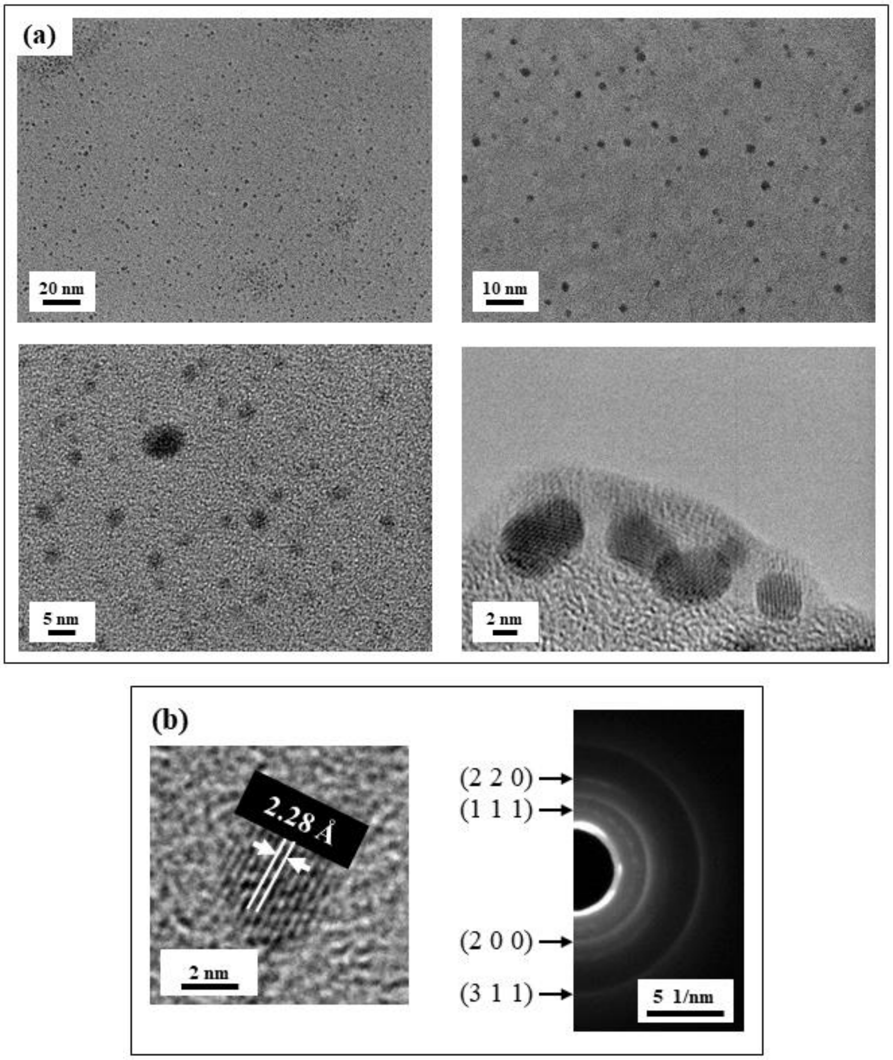

Fig. 4.23. (a) TEM micrographs of MnO nanoparticles produced via LDS process, and (b) corresponding SAED pattern and (1 1 1) lattice fringes of MnO nanoparticles.

These extremely small nanoparticles have a size ranging from 1 nm to 3 nm. Citrate cannot reduce these more reactive ions into metal, but for some ions with multiple valences such as Cu and Fe, citrate is still capable to reduce these ions to a lower valence state, as evidenced that Cu^{2+} to Cu^{1+} and Fe^{3+} to Fe^{2+}. However, in the case of Zn, the resultant nanoparticles were zinc peroxide (ZnO_2) instead of zinc oxide (ZnO). The reason is probably attributed to the decrease in reduction potential, resulting from citrate complexation.

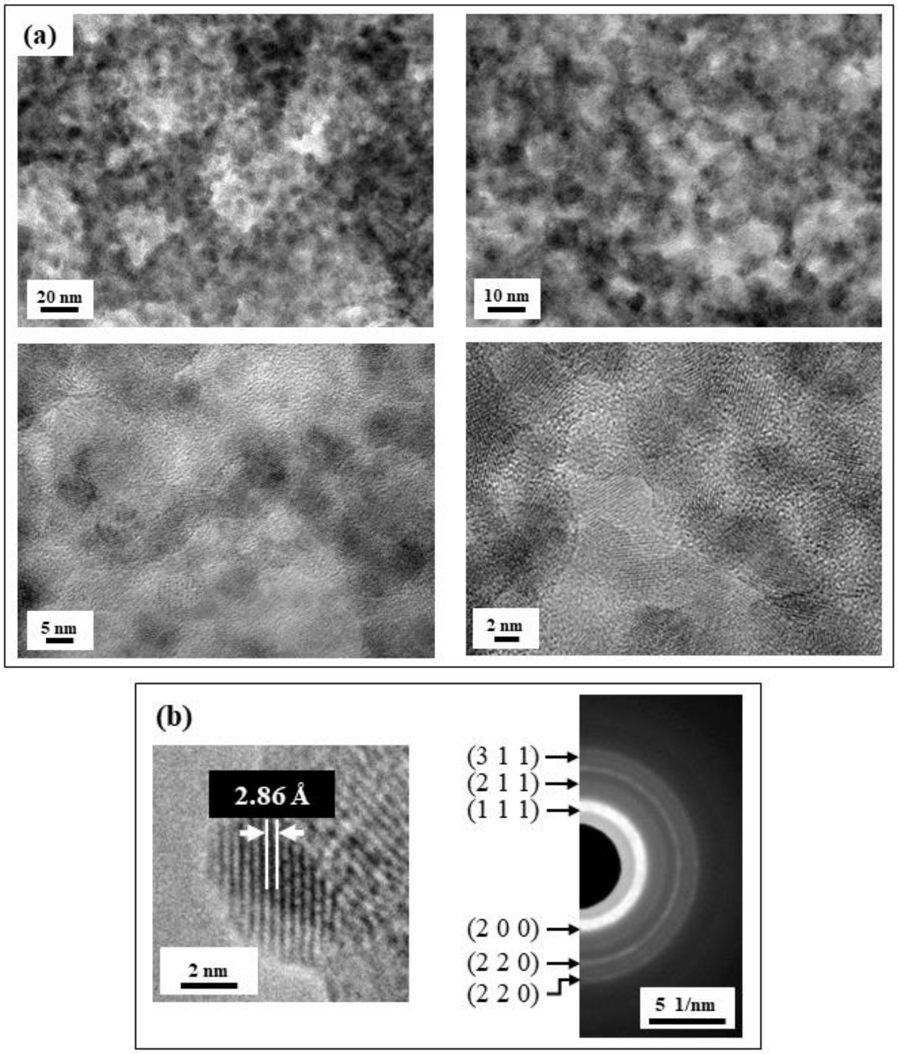

Fig. 4.24. (a) TEM micrographs of ZnO_2 nanoparticles produced via LDS process, and (b) corresponding SAED pattern and (1 1 1) lattice fringes of ZnO_2 nanoparticles.

For Ce which is more reactive than the mentioned metals, citrate is not capable of reducing Ce^{3+} to lower valence states and it was oxidized into Ce^{4+}, creating CeO_2 nanoparticles.

The chelating effect of citric acid play a critical role for oxide nanoparticle formation, which significantly slows down the precipitation reaction. After the nucleation of the precipitates is triggered, the growth process is so slow that the size of oxide nanoparticles is still few-nanometers large even after tens of minutes.

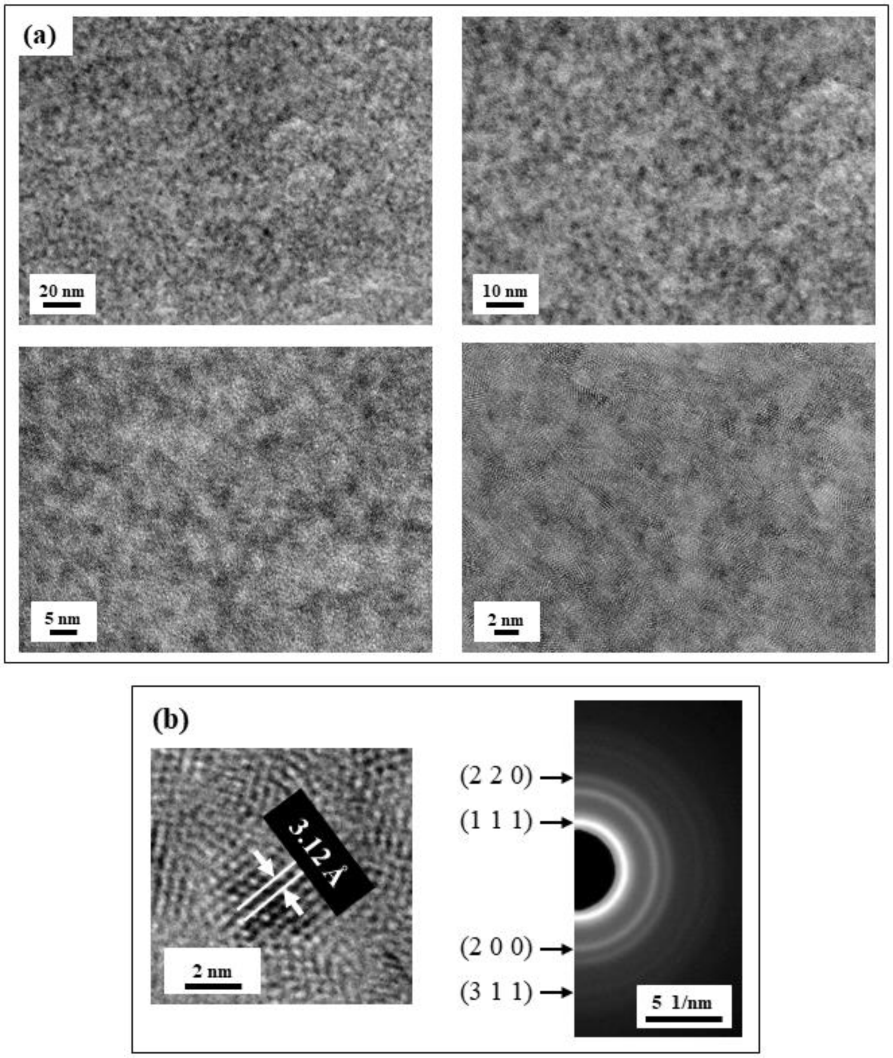

Fig. 4.25. (a) TEM micrographs of CeO_2 nanoparticles produced via LDS process, and (b) corresponding SAED pattern and (1 1 1) lattice fringes of CeO_2 nanoparticles.

4.7. Synthesis of lutetium nanoparticles

In an attempt to synthesize lutetium (Lu) oxide nanoparticles using LDS, to our surprise, metal Lu nanoparticles instead formed.

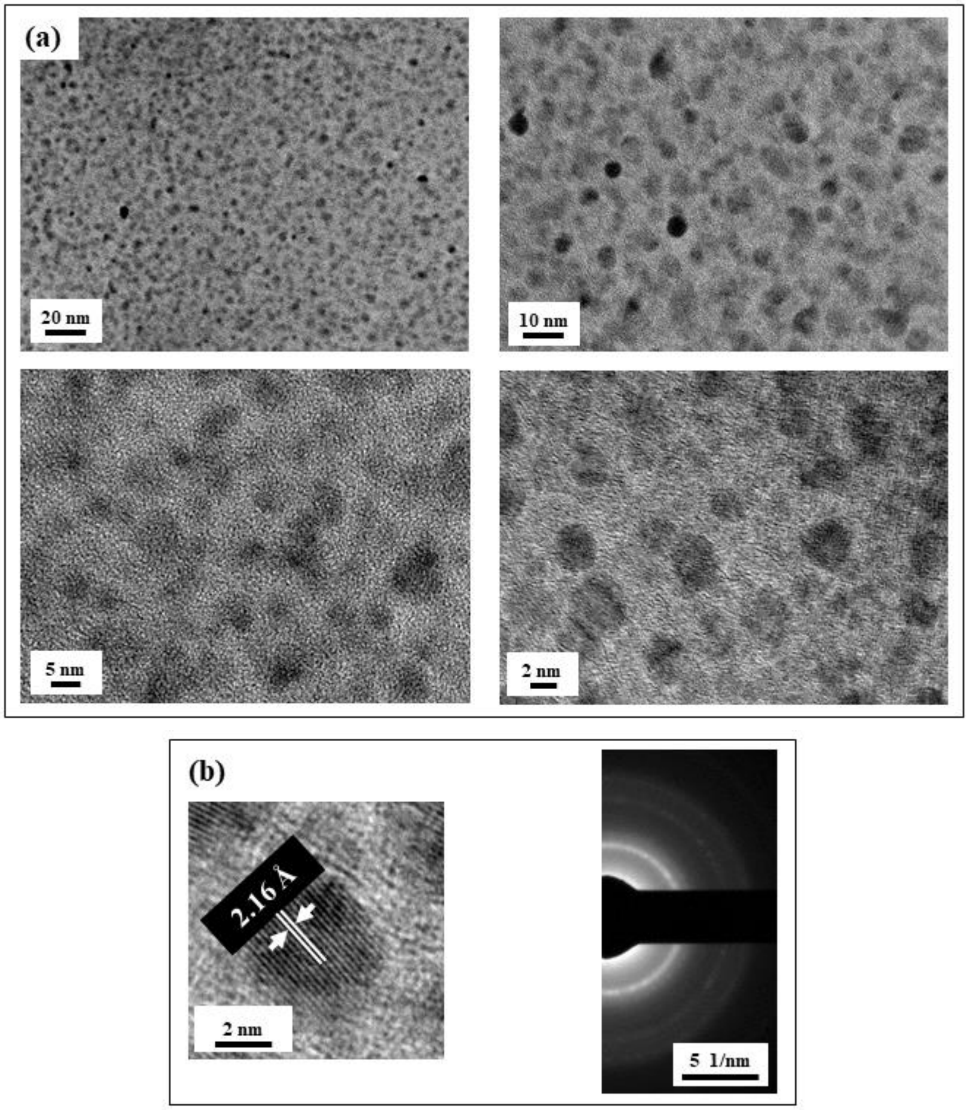

Fig. 4.26. (a) TEM micrographs of Lu nanocrystals produced via LDS process, and (b) corresponding SAED pattern and (1 1 1) lattice fringes of Lu nanocrystals.

Fig. 4.26 (b) shows lattice fringe and SAED pattern of these nanoparticles. Since Lu is relatively reactive metal, Lu oxide was expected. Based on the International Centre for Diffraction Data (ICDD) database, only two lutetium compounds exist including metal lutetium with hexagonal structure and lutetium oxide (Lu_2O_3) with cubic structure [511]. Recently, Kaminaga et al. [512] reported lutetium(II) oxide (LuO) with tetragonal structure. However, the SAED pattern from these nanoparticles does not match the patterns from these two oxides. Also, the EDX analysis, as shown in Fig. 4.27, exhibits the low content of oxygen for Lu nanoparticles, suggesting that the synthesized nanoparticles might be metal Lu nanoparticles.

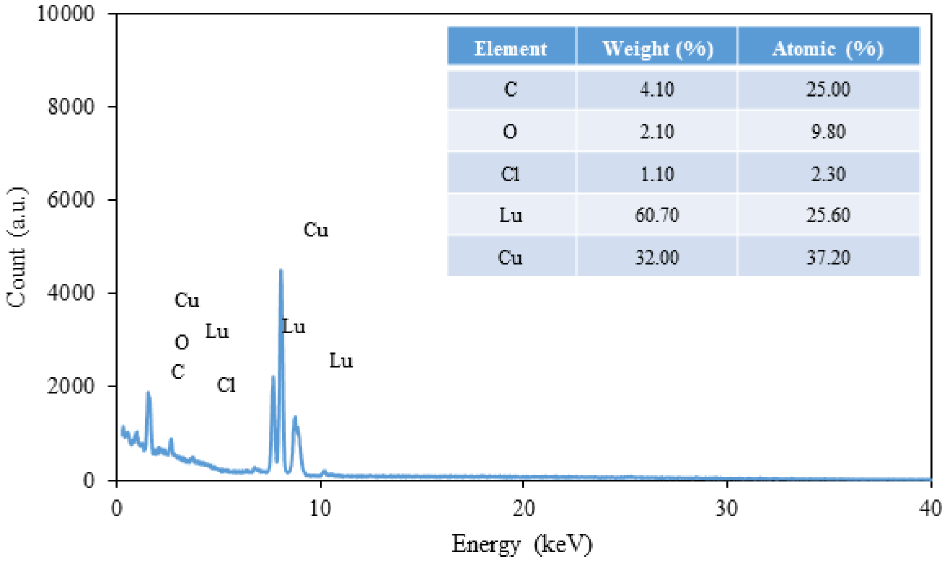

Element	Weight (%)	Atomic (%)
C	4.10	25.00
O	2.10	9.80
Cl	1.10	2.30
Lu	60.70	25.60
Cu	32.00	37.20

Fig. 4.27. EDX analysis of Lu nanocrystals synthesized via LDS.

The SAED analysis shown in Fig. 4.28 indicates that the diffraction rings of synthesized LuNPs completely match with the diffraction pattern of an FCC structure, shown in Table 4.4. Lu is a HCP metal; no FCC Lu has ever been reported. From the measured plane spacings, we calculated the lattice parameter (*a*) of LuNPs using the equation below:

$$d = \frac{a}{\sqrt{l^2+h^2+k^2}} \qquad \text{(Eq. 4.5)}$$

where d is d-spacing and h, k, and l are the Miller indices, and the lattice parameter was found to be about 3.73 Å.

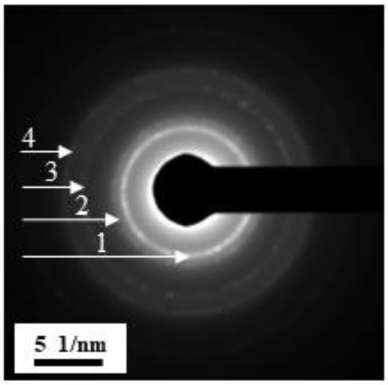

Fig. 4.28. SAED pattern of Lu nanocrystals synthesized through 3 minutes of LDS.

Table 4.4. The measured d-spacing and diffraction planes corresponding to Fig. 4.28.

Ring number	Measured 2R (1/nm)	Measured d-spacing (Å)	Plane
1	9.28	2.16	(1 1 1)
2	10.78	1.86	(2 0 0)
3	15.22	1.31	(2 2 0)
4	17.65	1.13	(3 1 1)

These results strongly suggest that when Lu particle size goes down to a few nanometers, FCC structure will be favored over HCP. This is also shown for Co nanoparticles, where synthesized ultrasmall Co nanoparticles by LDS have an FCC structure.

The size effect of nanoparticle crystal structure is displayed when increasing the synthesis time from 3 minutes to 6 minutes. For the sample with 6 minutes dialysis time, two bright points appear in the SAED pattern. These two points match with the diffraction pattern of plane (1 0 1) of Lu HCP structure (see Fig. 4.29). The possible reason is that with increase of synthesis time larger particles form, and these large particles have HCP structure.

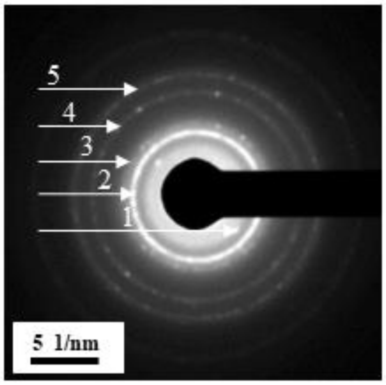

Fig. 4.29. SAED pattern of Lu nanocrystals synthesized through 6 minutes of LDS.

5. PRELIMINARY BIOMEDICAL STUDIES OF ULTRASMALL COPPER NANOPARTICLES

5.1. Introduction

The field of MNP research has been active as seen by the broad spectrum of extensive research each year since mid-1990s [513, 514]. They have covered various applications of MNPs especially the bio-related fields such as imaging and therapeutic capabilities of different MNPs [515-517]. One important biomedical application of MNPs is being used as nanocarriers for radioactive isotopes to construct imaging and radiation therapy agents. For imaging purpose, this approach provides a potential platform to generate multimodal imaging agents by combining molecular imaging techniques like single-photon emission computed tomography (SPECT) or positron emission tomography (PET) with other imaging modalities such as computed tomography (CT), magnetic resonance imaging (MRI), and optical imaging. For therapeutic purpose, the main driving force for the research is the high payload of radioisotopes, which is highly desired in radiation therapy.

For a theranostic application, the MNPs should display i) *in vivo* biocompatibility, ii) designed tissue distribution profile featuring high accumulation at their site of action but minimal uptake in non-target organs, iii) controlled release of the drugs or targeted delivery of therapeutic radiation at the intended sites of action, and finally, iv) desired *in vivo* stability. Moreover, if the MNPs undergo metabolism, their metabolites or fragments should not elicit acute or chronic toxicity and should be readily eliminated from the body. Design of a successful MNP nanoplatform for theranostic applications, which includes structural (MNP core and/or surface) modifications at multiple stages during the MNP synthesis, is essential to achieve a favorable balance of all these properties so as to accomplish the ultimate goal of diagnostic and/or therapeutic actions at the diseased sites with minimal toxicity. Hence, in this chapter we tried to evaluate stability and renal clearability of Cu nanocrystals prior to labeling with various radioisotopes for theranostic applications.

5.2. stability of Cu nanocrystals in phosphate-buffered saline and fatal bovine serum

Agglomeration and dissociation of MNPs within biological solutions is a major concern in their use in many biomedical applications [518]. To evaluate the stability of Cu nanoparticles, they are mixed with phosphate-buffered saline (PBS) which is considered as a buffer solution used in biological research, and also fatal bovine serum (FBS) which is the most commonly used serum-supplement for the *in vitro* cell culture. The mixture was analyzed using fast protein liquid chromatography (FPLC) with size exclusion column. In this technique, molecules are separated by differences in size as they pass through a resin packed in a column. The resin consists of a porous matrix of spherical particles (beads) that lack reactivity and adsorptive properties. After sample has entered the column, molecules larger than the pores are unable to diffuse into the beads, so they elute first. Molecules that range in size between the very big and very small can penetrate the pores to varying degrees based on their size. If a molecule is smaller than the smallest of the pores in the resin, it will be able to enter the total pore volume. Molecules that enter the total pore volume are eluted last.

About 100 µl of mixture of colloidal Cu and PBS passed through FPLC size exclusion column. As it can be seen from Fig. 5.1, there is a sharp peak at about 21 minutes which is related to Cu nanocrystals, only large size molecules (particles) present. Next, the same volume of copper nanoparticles was added to the PBS with 50% (v/v) of FBS to check the stability of Cu nanocrystal inside the cell culture medium. The result is demonstrated in Fig. 5.1(b). For comparison, analysis of FBS was conducted, as shown in Fig. 5.1(b), where the peak was related to the proteins inside FBS. Comparing Figs. 5.1(b) and (c) shows that there is a distinctive sharp peak at about 21 minutes which does not appear in the pure FBS sample. This peak is the same one appeared in Fig. 5.1(a), indicating that Cu nanoparticles did not disintegrated in FBS medium.

To confirm the existence of Cu nanoparticles inside PBS and FBS, the mixture of Cu nanoparticles with PBS and FBS was examined using HRTEM (Fig. 5.2). HRTEM micrographs clearly show Cu nanocrystals, confirming that Cu nanocrystals are stable inside PBS and FBS solutions.

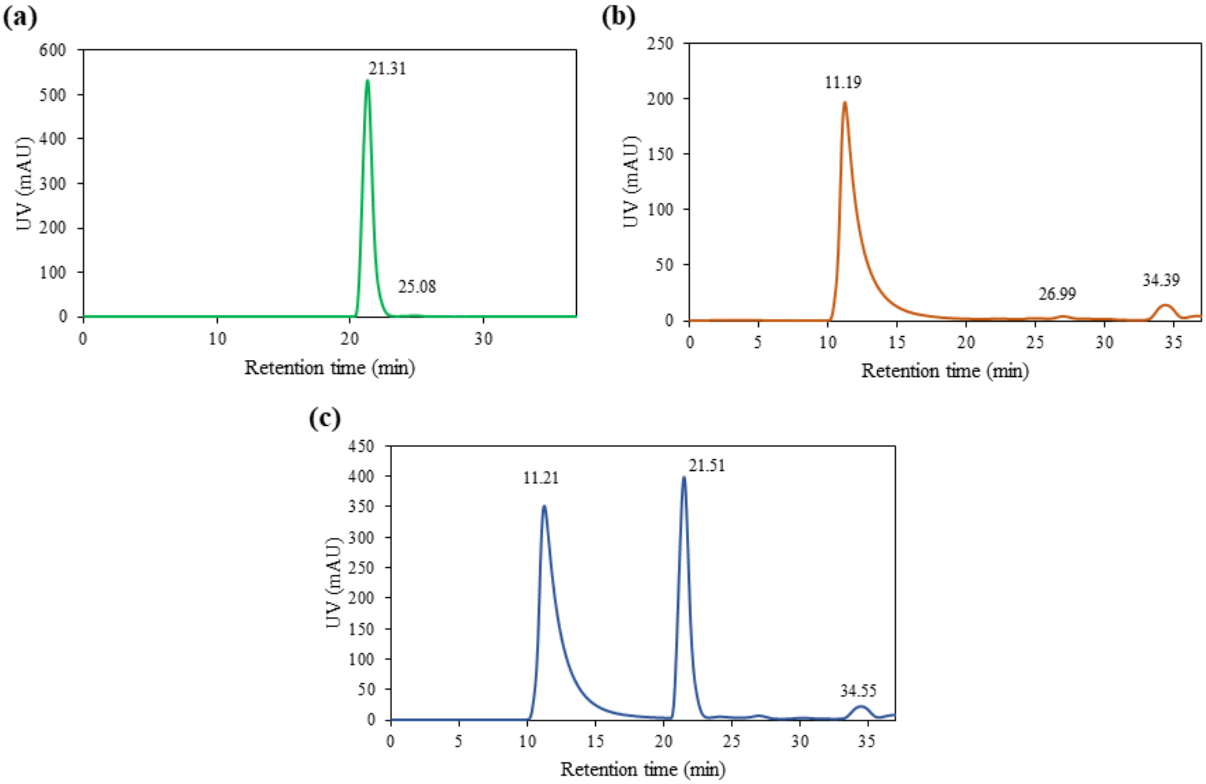

Fig. 5.1. FPLC analysis of (a) Cu nanocrystals incubated in PBS, (b) PBS with 50% (v/v) of FBS, and (c) Cu nanocrystals incubated in PBS with 50% (v/v) of FBS.

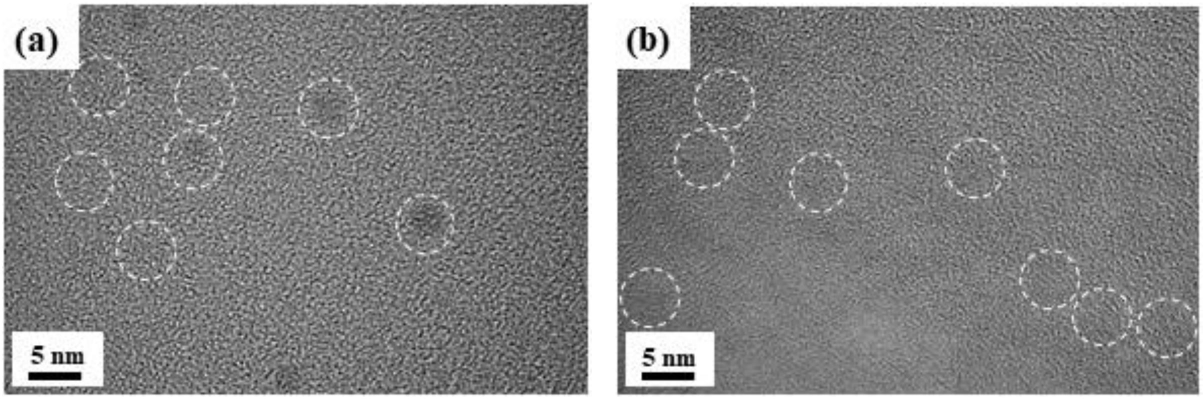

Fig. 5.2. TEM micrographs of Cu nanocrystals suspended in (a) PBS and (b) FBS.

5.3. Renal clearance of Cu nanocrystals

Renal clearance of Cu nanocrystals was evaluated by collecting and measuring Cu concentration in urines from three mice to which Cu nanocrystal suspension was intravenously injected. It is well established that the body rids itself of Cu ions by collecting them in the liver and excreting them through the liver's bile. However, Cu nanoparticles can only be eliminated through urine. Therefore, if there is the presence of Cu in urine, the only source is Cu nanoparticles.

First, three injection doses of colloidal copper were prepared by mixing 50 µl of Cu nanocrystals with Cu concentration of about 115 ppb with 100 µl of sodium chloride solution, making the total injection volume of 150 µl. Three 6-8 weeks old male mice (29.5 g, 31.7 g, and 36.6 g) were obtained from the University of Texas Southwestern Medical Center (UTSW) core breeding facility.

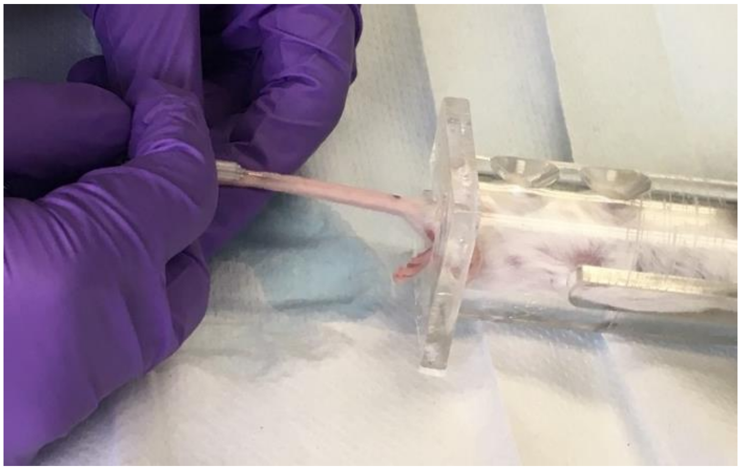

Fig. 5.3. Image of tail injection of 150 µl of Cu nanocrystals suspended sodium chloride solution.

All animal care and experimental procedures were approved by the University of Texas Southwestern Medical Center Institutional Animal Care and Use Committee in compliance with the United States Public Health Service Standards and National Institutes of Health guidelines. As it is demonstrated in Fig. 5.3, the prepared colloidal copper doses were intravenously injected into the mice and they were housed inside a metabolic cage at 22 ± 2 °C, 50-60% relative humidity, under a 12-hour light:12-hour dark cycle, for 48 hours. The mice were provided free access to tap water and commercialized food (Jae II Chow, Korea).

Their urine was collected at different time points of 3 hours, 7 hours, 10 hours, 20 hours, 26 hours, 30 hours, and 44 hours after injection. Each urine sample was separately heated at about 100 °C using a silicone oil bath, then dissolved by about 300 µl of aqua regia. Next, the acid concentration was decreased by adding 3.7 ml of 3% nitric acid to prepare the samples for ICP-MS analysis. Table 5.1 summarized the concentration of copper ions detected in collected urine sample. The cumulative number of Cu ions depicted in Fig. 5.4 indicates that after 48 hours after injection, about 67% of copper ions were excreted the body through urine, confirming the renal clearance property of Cu nanocrystals.

Table 5.1. ICP-MS data of urine samples collected at different time intervals.

Sample name	Concentration (ppb)	Mass of ions (g)	Mole (#)	Cu ions (#)
Injected dose	114.87	3.45E-06	5.42E-08	3.26E+16
3 h	112.20	4.49E-07	7.06E-09	4.25E+15
7 h	85.92	3.44E-07	5.41E-09	3.26E+15
10 h	44.86	1.79E-07	2.82E-09	1.70E+15
20 h	160.45	6.42E-07	1.01E-08	6.08E+15
26 h	35.09	1.40E-07	2.21E-09	1.33E+15
30 h	38.76	1.55E-07	2.44E-09	1.47E+15
44 h	103.21	4.13E-07	6.50E-09	3.91E+15

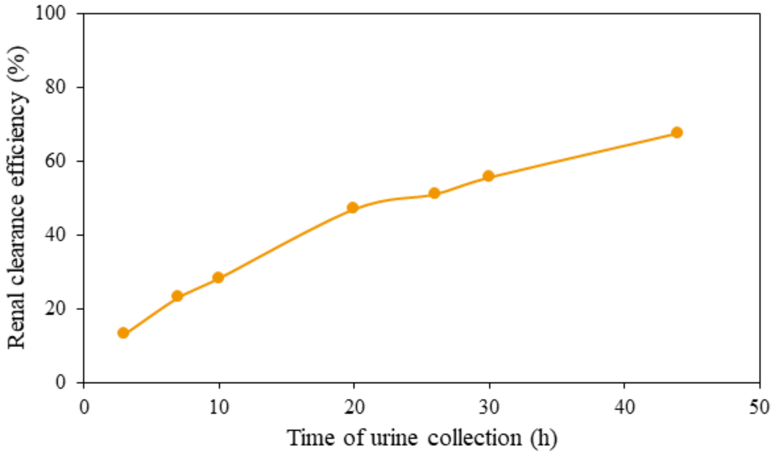

Fig. 5.4. Renal clearance efficiency of Cu nanocrystals injected into 3 mice after 48 hours.

The existence of copper nanoparticles in urine was further verified by HRTEM inspection. About 10 µl of collected urine sample was dropped on a 300-mesh Au TEM grid covered with a lacey carbon film and dried overnight. The EDX analysis (Fig. 5.5) spotted about 0.03 Wt% of copper in urine sample.

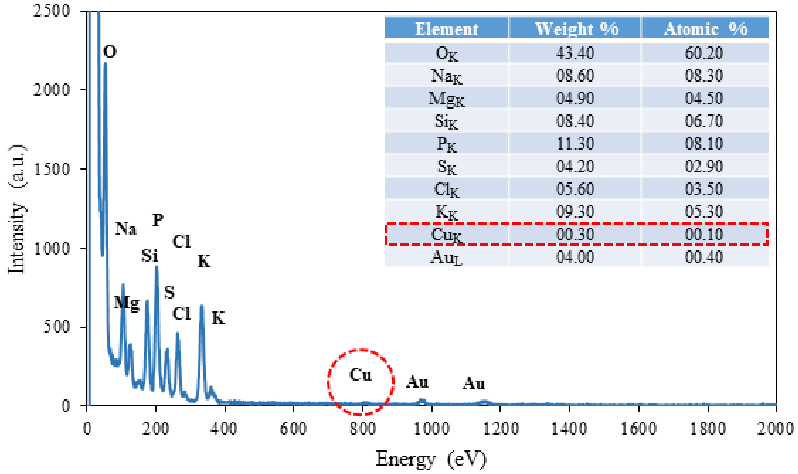

Element	Weight %	Atomic %
$\mathrm{O_K}$	43.40	60.20
$\mathrm{Na_K}$	08.60	08.30
$\mathrm{Mg_K}$	04.90	04.50
$\mathrm{Si_K}$	08.40	06.70
$\mathrm{P_K}$	11.30	08.10
$\mathrm{S_K}$	04.20	02.90
$\mathrm{Cl_K}$	05.60	03.50
$\mathrm{K_K}$	09.30	05.30
$\mathrm{Cu_K}$	00.30	00.10
$\mathrm{Au_L}$	04.00	00.40

Fig. 5.5. EDX analysis of urine sample collected from metabolic cage studies of Cu nanocrystals.

This trace amount of Cu detected in urine is a direct evidence of the existence of Cu which can only come from the injected Cu nanocrystals. TEM micrographs of urine sample, shown in Fig. 5.6, show nanocrystals which may be cleared Cu nanocrystals.

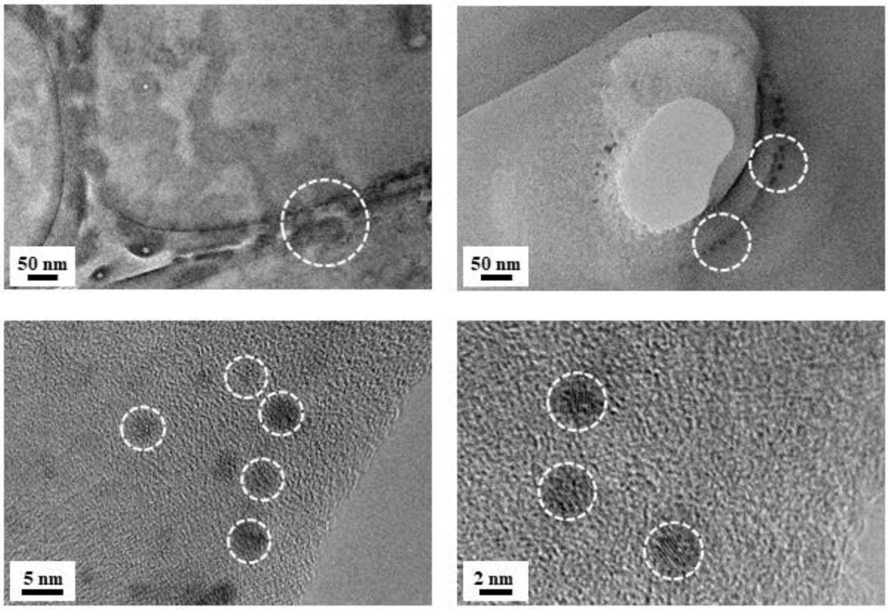

Fig. 5.6. TEM micrographs of urine samples collected from metabolic cage studies of Cu nanocrystals in different magnifications. The dashed circles indicate the copper nanocrystals existing inside urine.

6. CONCLUSIONS

We developed a general synthesis technique, called liquid diffusion synthesis (LDS), to produce transition metals and lanthanides nanocrystals with the mean size of 1-5 nm.

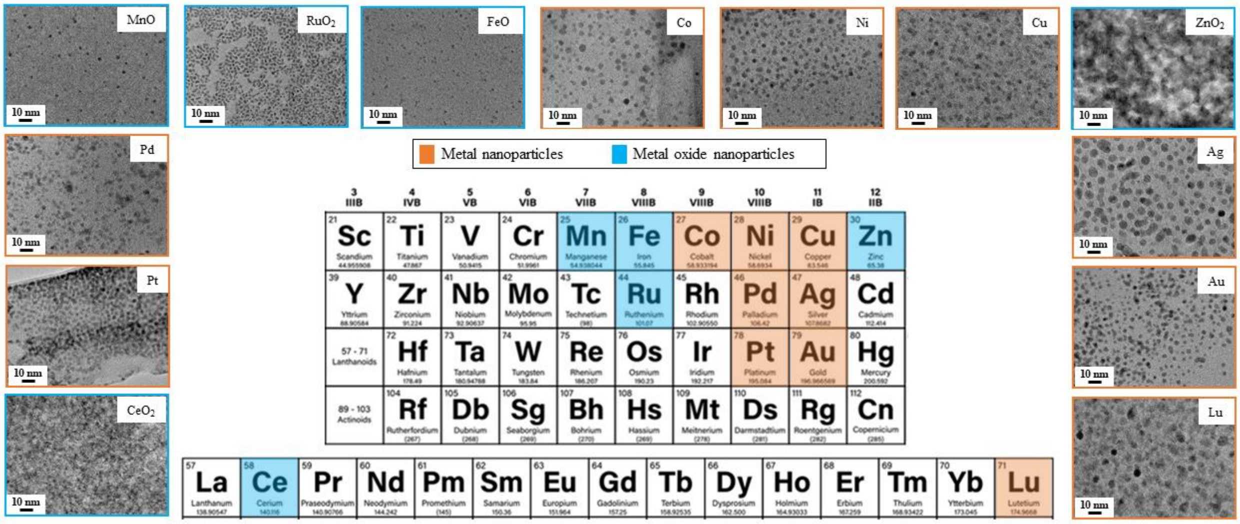

Fig. 6.1. Whole picture of transition metal and lanthanide nanocrystals synthesized via LDS.

In LDS, simply immersing a dialysis bag containing an aqueous solution of a metal salt mixed with citric acid in a NaOH solution reservoir for certain time, nanocrystals would form inside the dialysis bag. Ultrasmall nanocrystals of Co, Ni, Cu, Au, Ag, Pd, Pt, Lu, MnO, RuO_2, Cu_2O, FeO, ZnO_2, and CeO_2 have been synthesized using LDS.

The mechanistic study revealed the nanoparticle formation mechanism. The dialysis membrane forms a diffusion barrier for OH^- ions through membrane, creating a pH gradient inside the solution. There exists a pH range for each of these metal ions in which metal ions are reduced by citrate ions into metal atoms that nucleate and form ultrasmall nanocrystals. This pH range is referred as $pHR_r(i)$ where i represents different metal elements.

In case of Cu, Co, and Ni, during the synthesis process:

1. if $pH_0 < pH < pHR_r(i)$ → large metal oxide nanoparticles are created
2. if $pH = pHR_r(i)$ → ultrasmall metal nanoparticles are formed
3. If $pH > pHR_r(i)$ → combination of large metal oxide nanoparticles and ultrasmall metal nanoparticles are created

In case of Ag, Au, Pt, and Pd:

1. If $pH_0 < pH < pHR_r(i)$ → no reaction happens
2. If $pH = pHR_r(i)$ → ultrasmall metal nanoparticles are formed
3. If $pH > pHR_r(i)$ → large metal nanoparticles are created

Using Cu as a model system, a systematic investigation was conducted to obtain the effect of synthesis parameters on the nanocrystal formation. Higher concentration of NaOH in reservoir increases the mean size of nanocrystals. The average size of nanocrystals is independent of immersion time. Diffusion process of OH^- through dialysis determine whether Cu or Cu_2O are produced. Using stirring to drastically increase OH^- diffusion rate leads to the formation of Cu_2O. However, very slow diffusion rate caused by reducing NaOH concentration in the reservoir also leads to the formation of Cu_2O.

RuO_2, instead of metal Ru, nanocrystals are unexpectedly produced using the same LDS for synthesizing metal nanocrystals. The possible reason is that the reduction potential of citrate complex differs significantly from metal ions.

Also, metal Lu nanocrystals are surprisingly generated. Moreover, these Lu nanocrystals have a FCC crystal structure. Lu is a HCP metal, and FCC Lu has never been reported. The results strongly suggest that when Lu particle size goes down to a few nanometers, FCC structure will be favored over HCP. This is also shown for Co nanoparticles, where synthesized ultrasmall Co (a HCP metal) nanoparticles by LDS have an FCC structure.

Cu nanocrystals synthesized using LDS have preliminarily been tested for its *in vivo* biomedical applications. It was shown that Cu nanocrystals are stable inside phosphate-buffered saline (PBS) and fatal bovine serum (FBS). The renal clearance of Cu nanocrystals was tested by intravenously injecting nanocrystal suspension into normal mice and measuring the Cu concentration in collected urine. It was found that renal clearance efficiency of the nanocrystals was about 67% after 48 hours of the injection.

REFERENCES

1. Feynman RP. There's plenty of room at the bottom. California Institute of Technology, Engineering and Science magazine. 1960.

2. Khan I, Saeed K, Khan I. Nanoparticles: Properties, applications and toxicities. Arabian Journal of Chemistry. 2017.

3. Auffan M, Rose J, Bottero J-Y, Lowry GV, Jolivet J-P, Wiesner MR. Towards a definition of inorganic nanoparticles from an environmental, health and safety perspective. Nature nanotechnology. 2009;4(10):634.

4. Rastogi A, Zivcak M, Sytar O, Kalaji HM, He X, Mbarki S et al. Impact of metal and metal oxide nanoparticles on plant: a critical review. Frontiers in chemistry. 2017;5:78.

5. Maurer-Jones MA, Gunsolus IL, Murphy CJ, Haynes CL. Toxicity of engineered nanoparticles in the environment. Analytical chemistry. 2013;85(6):3036-49.

6. Jeevanandam J, Barhoum A, Chan YS, Dufresne A, Danquah MK. Review on nanoparticles and nanostructured materials: history, sources, toxicity and regulations. Beilstein journal of nanotechnology. 2018;9(1):1050-74.

7. Vinci G, Rapa M. Noble Metal Nanoparticles Applications: Recent Trends in Food Control. Bioengineering. 2019;6(1):10.

8. Neuschmelting V, Harmsen S, Beziere N, Lockau H, Hsu HT, Huang R et al. Dual-Modality Surface-Enhanced Resonance Raman Scattering and Multispectral Optoacoustic Tomography Nanoparticle Approach for Brain Tumor Delineation. Small. 2018;14(23):1800740.

9. Kvitek L, Prucek R, Panacek A, Soukupova J. Physicochemical Aspects of Metal Nanoparticle Preparation. Silver Nanoparticles-Health and Safety. IntechOpen; 2019.

10. Mbonyiryivuze A, Zongo S, Diallo A, Bertrand S, Minani E, Yadav LL et al. Titanium dioxide nanoparticles biosynthesis for dye sensitized solar cells application. 2015.

11. Stark WJ, Stoessel PR, Wohlleben W, Hafner A. Industrial applications of nanoparticles. Chemical Society Reviews. 2015;44(16):5793-805.

12. Schaming D, Remita H. Nanotechnology: from the ancient time to nowadays. Foundations of Chemistry. 2015;17(3):187-205.

13. Brun N, Mazerolles L, Pernot M. Microstructure of opaque red glass containing copper. Journal of Materials Science Letters. 1991;10(23):1418-20.

14. Leonhardt U. Optical metamaterials: Invisibility cup. Nature photonics. 2007;1(4):207.

15. Heiligtag FJ, Niederberger M. The fascinating world of nanoparticle research. Materials Today. 2013;16(7-8):262-71.

16. Nakai I, Numako C, Hosono H, Yamasaki K. Origin of the red color of Satsuma copper-ruby glass as determined by EXAFS and optical absorption spectroscopy. Journal of the American Ceramic Society. 1999;82(3):689-95.

17. Mie G. Beiträge zur Optik trüber Medien, speziell kolloidaler Metallösungen. Annalen der physik. 1908;330(3):377-445.

18. Grassian VH. When size really matters: size-dependent properties and surface chemistry of metal and metal oxide nanoparticles in gas and liquid phase environments. The Journal of Physical Chemistry C. 2008;112(47):18303-13.

19. Díez I, Ras RH. Few-atom silver clusters as fluorescent reporters. Advanced Fluorescence Reporters in Chemistry and Biology II. Springer; 2010. p. 307-32.

20. Zhang L, Wang E. Metal nanoclusters: new fluorescent probes for sensors and bioimaging. Nano Today. 2014;9(1):132-57.

21. Díez I, Ras RH. Fluorescent silver nanoclusters. Nanoscale. 2011;3(5):1963-70.

22. Bahadori SR, Dehghani K. Influence of intermediate annealing on the nanostructure and mechanical properties of pure copper processed by equal channel angular pressing and cold rolling. Metallurgical and Materials Transactions A. 2015;46(7):2796-802.

23. Bahadori SR, Mousavi SA. Examination of an aluminum alloy behavior under different routes of twist extrusion processing. Materials Science and Engineering: A. 2011;528(21):6527-34.

24. Mousavi SA, Bahadori SR. The effects of post annealing on the mechanical properties, microstructure and texture evolutions of pure copper deformed by twist extrusion process. Materials Science and Engineering: A. 2011;528(3):1242-6.

25. Bahadori SR, Mousavi SAAA. The evolution of homogeneity in a transverse cross section of aluminum alloy profile deformed by twist extrusion. JOM. 2012;64(5):593-9.

26. Kang H, Buchman JT, Rodriguez RS, Ring HL, He J, Bantz KC et al. Stabilization of silver and gold nanoparticles: Preservation and improvement of plasmonic functionalities. Chemical reviews. 2018;119(1):664-99.

27. Ghosh SK, Pal T. Interparticle coupling effect on the surface plasmon resonance of gold nanoparticles: from theory to applications. Chemical reviews. 2007;107(11):4797-862.

28. Konował E, Modrzejewska-Sikorska A, Motylenko M, Klapiszewski Ł, Wysokowski M, Bazhenov VV et al. Functionalization of organically modified silica with gold nanoparticles in the presence of lignosulfonate. International journal of biological macromolecules. 2016;85:74-81.

29. Tong Q, Wang W, Fan Y, Dong L. Recent progressive preparations and applications of silver-based SERS substrates. Trends Analyt Chem. 2018;106:246-58.

30. Jain PK, Huang X, El-Sayed IH, El-Sayed MA. Noble metals on the nanoscale: optical and photothermal properties and some applications in imaging, sensing, biology, and medicine. Accounts of chemical research. 2008;41(12):1578-86.

31. Hoffmann M, Hotze EM, Wiesner MR. Reactive oxygen species generation on nanoparticulate material. Environmental Nanotechnology Applications and Impacts of Nanomaterials. 2007:155-203.

32. Krajczewski J, Kołątaj K, Kudelski A. Plasmonic nanoparticles in chemical analysis. RSC Advances. 2017;7(28):17559-76.

33. Kelly KL, Coronado E, Zhao LL, Schatz GC. The optical properties of metal nanoparticles: the influence of size, shape, and dielectric environment. ACS Publications; 2003.

34. Kreibig U, Vollmer M. Optical properties of metal clusters. Springer Science & Business Media; 2013.

35. García MA. Surface plasmons in metallic nanoparticles: fundamentals and applications. Journal of Physics D: Applied Physics. 2011;44(28):283001.

36. Creighton JA, Eadon DG. Ultraviolet–visible absorption spectra of the colloidal metallic elements. Journal of the Chemical Society, Faraday Transactions. 1991;87(24):3881-91.

37. Dreaden EC, Alkilany AM, Huang X, Murphy CJ, El-Sayed MA. The golden age: gold nanoparticles for biomedicine. Chemical Society Reviews. 2012;41(7):2740-79.

38. Agnihotri S, Mukherji S, Mukherji S. Size-controlled silver nanoparticles synthesized over the range 5–100 nm using the same protocol and their antibacterial efficacy. Rsc Advances. 2014;4(8):3974-83.

39. Gans Rv. Form of ultramicroscopic particles of silver. Ann Phys. 1915;47(10):270-84.

40. Huang X, El-Sayed MA. Gold nanoparticles: Optical properties and implementations in cancer diagnosis and photothermal therapy. Journal of advanced research. 2010;1(1):13-28.

41. Oldenburg S, Averitt R, Westcott S, Halas N. Nanoengineering of optical resonances. Chemical Physics Letters. 1998;288(2-4):243-7.

42. Prodan E, Radloff C, Halas NJ, Nordlander P. A hybridization model for the plasmon response of complex nanostructures. science. 2003;302(5644):419-22.

43. Schmid G. Large clusters and colloids. Metals in the embryonic state. Chemical Reviews. 1992;92(8):1709-27.

44. Yu L, Zhang L, Ren G, Li S, Zhu B, Chai F et al. Multicolorful fluorescent-nanoprobe composed of Au nanocluster and carbon dots for colorimetric and fluorescent sensing Hg2+ and Cr6+. Sensors and Actuators B: Chemical. 2018;262:678-86.

45. Yu H, Rao B, Jiang W, Yang S, Zhu M. The photoluminescent metal nanoclusters with atomic precision. Coordination Chemistry Reviews. 2019;378:595-617.

46. Huang T, Murray RW. Visible luminescence of water-soluble monolayer-protected gold clusters. The Journal of Physical Chemistry B. 2001;105(50):12498-502.

47. Huang T, Murray RW. Luminescence of tiopronin monolayer-protected silver clusters changes to that of gold clusters upon galvanic core metal exchange. The Journal of Physical Chemistry B. 2003;107(30):7434-40.

48. Zhu M, Aikens CM, Hollander FJ, Schatz GC, Jin R. Correlating the crystal structure of a thiol-protected Au25 cluster and optical properties. Journal of the American Chemical Society. 2008;130(18):5883-5.

49. Liu L, Corma A. Metal catalysts for heterogeneous catalysis: from single atoms to nanoclusters and nanoparticles. Chemical reviews. 2018;118(10):4981-5079.

50. Zheng J, Zhou C, Yu M, Liu J. Different sized luminescent gold nanoparticles. Nanoscale. 2012;4(14):4073-83.

51. Zheng J, Zhang C, Dickson RM. Highly fluorescent, water-soluble, size-tunable gold quantum dots. Physical Review Letters. 2004;93(7):077402.

52. de Heer WA, Selby K, Kresin V, Masui J, Vollmer M, Chatelain A et al. Collective dipole oscillations in small sodium clusters. Physical review letters. 1987;59(16):1805.

53. Knight W, Clemenger K, de Heer WA, Saunders WA, Chou M, Cohen ML. Electronic shell structure and abundances of sodium clusters. Physical review letters. 1984;52(24):2141.

54. Zheng J, Nicovich PR, Dickson RM. Highly fluorescent noble-metal quantum dots. Annu Rev Phys Chem. 2007;58:409-31.

55. Kim BH, Hackett MJ, Park J, Hyeon T. Synthesis, characterization, and application of ultrasmall nanoparticles. Chemistry of Materials. 2013;26(1):59-71.

56. Corrigan JF, Fuhr O, Fenske D. Metal chalcogenide clusters on the border between molecules and materials. Advanced Materials. 2009;21(18):1867-71.

57. Nützenadel C, Züttel A, Chartouni D, Schmid G, Schlapbach L. Critical size and surface effect of the hydrogen interaction of palladium clusters. The European Physical Journal D. 2000;8(2):245-50.

58. Alivisatos AP. Semiconductor clusters, nanocrystals, and quantum dots. science. 1996;271(5251):933-7.

59. Schmid G, Liu Y-P, Schumann M, Raschke T, Radehaus C. Quasi one-dimensional arrangements of Au55 (PPh3) 12Cl6 clusters and their electrical properties at room temperature. Nano Letters. 2001;1(8):405-7.

60. Qian H, Zhu Y, Jin R. Atomically precise gold nanocrystal molecules with surface plasmon resonance. Proceedings of the National Academy of Sciences. 2012;109(3):696-700.

61. Wang G, Huang T, Murray RW, Menard L, Nuzzo RG. Near-IR luminescence of monolayer-protected metal clusters. Journal of the American Chemical Society. 2005;127(3):812-3.

62. Zhou C, Sun C, Yu M, Qin Y, Wang J, Kim M et al. Luminescent gold nanoparticles with mixed valence states generated from dissociation of polymeric Au (I) thiolates. The Journal of Physical Chemistry C. 2010;114(17):7727-32.

63. Tang Z, Robinson DA, Bokossa N, Xu B, Wang S, Wang G. Mixed dithiolate durene-DT and monothiolate phenylethanethiolate protected Au130 nanoparticles with discrete core and core-ligand energy states. Journal of the American Chemical Society. 2011;133(40):16037-44.

64. Huang CC, Yang Z, Lee KH, Chang HT. Synthesis of highly fluorescent gold nanoparticles for sensing mercury (II). Angewandte Chemie International Edition. 2007;46(36):6824-8.

65. Guo Y, Wang Z, Shao H, Jiang X. Stable fluorescent gold nanoparticles for detection of Cu 2+ with good sensitivity and selectivity. Analyst. 2012;137(2):301-4.

66. Higaki T, Zhou M, Lambright KJ, Kirschbaum K, Sfeir MY, Jin R. Sharp transition from nonmetallic Au246 to metallic Au279 with nascent surface Plasmon resonance. Journal of the American Chemical Society. 2018;140(17):5691-5.

67. Su Y, Xue T, Liu Y, Qi J, Jin R, Lin Z. Luminescent metal nanoclusters for biomedical applications. Nano Research. 2019:1-15.

68. Wu Z, Jin R. On the ligand’s role in the fluorescence of gold nanoclusters. Nano letters. 2010;10(7):2568-73.

69. Chang H-Y, Chang H-T, Hung Y-L, Hsiung T-M, Lin Y-W, Huang C-C. Ligand effect on the luminescence of gold nanodots and its application for detection of total mercury ions in biological samples. RSC Advances. 2013;3(14):4588-97.

70. Li G, Lei Z, Wang Q-M. Luminescent molecular Ag− S nanocluster [Ag62S13 (SBu t) 32](BF4) 4. Journal of the American Chemical Society. 2010;132(50):17678-9.

71. Jin S, Wang S, Song Y, Zhou M, Zhong J, Zhang J et al. Crystal structure and optical properties of the [Ag62S12 (SBut) 32] 2+ nanocluster with a complete face-centered cubic kernel. Journal of the American Chemical Society. 2014;136(44):15559-65.

72. Nguyen T-AD, Jones ZR, Leto DF, Wu G, Scott SL, Hayton TW. Ligand-exchange-induced growth of an atomically precise Cu29 nanocluster from a smaller cluster. Chemistry of Materials. 2016;28(22):8385-90.

73. Duan H, Nie S. Etching colloidal gold nanocrystals with hyperbranched and multivalent polymers: a new route to fluorescent and water-soluble atomic clusters. Journal of the American Chemical Society. 2007;129(9):2412-3.

74. Bootharaju MS, Joshi CP, Parida MR, Mohammed OF, Bakr OM. Templated atom-precise galvanic synthesis and structure elucidation of a [Ag24Au (SR) 18]− nanocluster. Angewandte Chemie International Edition. 2016;55(3):922-6.

75. Kang X, Xiong L, Wang S, Yu H, Jin S, Song Y et al. Shape-Controlled Synthesis of Trimetallic Nanoclusters: Structure Elucidation and Properties Investigation. Chemistry–A European Journal. 2016;22(48):17145-50.

76. Feng J, Chen Y, Han Y, Liu J, Ma S, Zhang H et al. pH-Regulated Synthesis of Trypsin-Templated Copper Nanoclusters with Blue and Yellow Fluorescent Emission. ACS omega. 2017;2(12):9109-17.

77. Jiang H, Zhang Y, Wang X. Single cytidine units-templated syntheses of multi-colored water-soluble Au nanoclusters. Nanoscale. 2014;6(17):10355-62.

78. Zhang Q, Yang M, Zhu Y, Mao C. Metallic nanoclusters for cancer imaging and therapy. Current medicinal chemistry. 2018;25(12):1379-96.

79. Chakraborty S, Babanova S, Rocha RC, Desireddy A, Artyushkova K, Boncella AE et al. A hybrid DNA-templated gold nanocluster for enhanced enzymatic reduction of oxygen. Journal of the American Chemical Society. 2015;137(36):11678-87.

80. Kawasaki H, Hamaguchi K, Osaka I, Arakawa R. ph-Dependent synthesis of pepsin-mediated gold nanoclusters with blue green and red fluorescent emission. Advanced Functional Materials. 2011;21(18):3508-15.

81. Le Guével X, Daum N, Schneider M. Synthesis and characterization of human transferrin-stabilized gold nanoclusters. Nanotechnology. 2011;22(27):275103.

82. Xie J, Zheng Y, Ying JY. Protein-directed synthesis of highly fluorescent gold nanoclusters. Journal of the American Chemical Society. 2009;131(3):888-9.

83. Jin R, Qian H, Wu Z, Zhu Y, Zhu M, Mohanty A et al. Size focusing: a methodology for synthesizing atomically precise gold nanoclusters. The Journal of Physical Chemistry Letters. 2010;1(19):2903-10.

84. Wilcoxon JP, Provencio P. Etching and aging effects in nanosize Au clusters investigated using high-resolution size-exclusion chromatography. The Journal of Physical Chemistry B. 2003;107(47):12949-57.

85. Bahadori SR, Dehghani K, Bakhshandeh F. Microstructure, texture and mechanical properties of pure copper processed by ECAP and subsequent cold rolling. Materials Science and Engineering: A. 2013;583:36-42.

86. Bahadori SR, Dehghani K, Mousavi SA. Comparison of microstructure and mechanical properties of pure copper processed by twist extrusion and equal channel angular pressing. Materials Letters. 2015;152:48-52.

87. Mousavi SA, Bahadori SR, Shahab A. Numerical and experimental studies of the plastic strains distribution using subsequent direct extrusion after three twist extrusion passes. Materials Science and Engineering: A. 2010;527(16-17):3967-74.

88. Bahadori SR, Dehghani K, Bakhshandeh F. Microstructural homogenization of ECAPed copper through post-rolling. Materials Science and Engineering: A. 2013;588:260-4.

89. Bahadori SR, Mousavi SA, Shahab A, editors. Sequence effects of twist extrusion and rolling on microstructure and mechanical properties of aluminum alloy 8112. Journal of Physics: Conference Series; 2010: IOP Publishing.

90. Huang X, Li Z, Yu Z, Deng X, Xin Y. Recent Advances in the Synthesis, Properties, and Biological Applications of Platinum Nanoclusters. Journal of Nanomaterials. 2019;2019.

91. Gedye R, Smith F, Westaway K, Ali H, Baldisera L, Laberge L et al. The use of microwave ovens for rapid organic synthesis. Tetrahedron letters. 1986;27(3):279-82.

92. Beeri A, Berman E, Vishkautsan R, Mazur Y. Reactions of hydrogen atoms produced by microwave discharge with olefins in acetone and toluene. Journal of the American Chemical Society. 1986;108(20):6413-4.

93. Liu S, Lu F, Zhu J-J. Highly fluorescent Ag nanoclusters: microwave-assisted green synthesis and Cr3+ sensing. Chemical Communications. 2011;47(9):2661-3.

94. Yue Y, Liu T-Y, Li H-W, Liu Z, Wu Y. Microwave-assisted synthesis of BSA-protected small gold nanoclusters and their fluorescence-enhanced sensing of silver (I) ions. Nanoscale. 2012;4(7):2251-4.

95. Suslick KS. Sonochemistry. science. 1990;247(4949):1439-45.

96. Mdleleni MM, Hyeon T, Suslick KS. Sonochemical synthesis of nanostructured molybdenum sulfide. Journal of the American chemical society. 1998;120(24):6189-90.

97. Suslick KS, Price GJ. Applications of ultrasound to materials chemistry. Annual Review of Materials Science. 1999;29(1):295-326.

98. Gedanken A. Using sonochemistry for the fabrication of nanomaterials. Ultrasonics sonochemistry. 2004;11(2):47-55.

99. Rana RK, Mastai Y, Gedanken A. Acoustic cavitation leading to the morphosynthesis of mesoporous silica vesicles. Advanced Materials. 2002;14(19):1414-8.

100. Ciawi E, Rae J, Ashokkumar M, Grieser F. Determination of temperatures within acoustically generated bubbles in aqueous solutions at different ultrasound frequencies. The Journal of Physical Chemistry B. 2006;110(27):13656-60.

101. Kondo T, Kodaira T, Kano E. Free radical formation induced by ultrasound and its effects on strand breaks in DNA of cultured FM3A cells. Free radical research communications. 1993;19(sup1):s193-s200.

102. Xu H, Suslick KS. Sonochemical synthesis of highly fluorescent Ag nanoclusters. ACS nano. 2010;4(6):3209-14.

103. Liu H, Zhang X, Wu X, Jiang L, Burda C, Zhu J-J. Rapid sonochemical synthesis of highly luminescent non-toxic AuNCs and Au@ AgNCs and Cu (II) sensing. Chemical Communications. 2011;47(14):4237-9.

104. Liu H, Yang G, Abdel-Halim E, Zhu J-J. Highly selective and ultrasensitive detection of nitrite based on fluorescent gold nanoclusters. Talanta. 2013;104:135-9.

105. Cui M, Zhao Y, Song Q. Synthesis, optical properties and applications of ultra-small luminescent gold nanoclusters. TrAC Trends in Analytical Chemistry. 2014;57:73-82.

106. Peyser LA, Vinson AE, Bartko AP, Dickson RM. Photoactivated fluorescence from individual silver nanoclusters. Science. 2001;291(5501):103-6.

107. Zhang J, Xu S, Kumacheva E. Photogeneration of fluorescent silver nanoclusters in polymer microgels. Advanced Materials. 2005;17(19):2336-40.

108. Soejima T, Tada H, Kawahara T, Ito S. Formation of Au nanoclusters on TiO2 surfaces by a two-step method consisting of Au (III)-complex chemisorption and its photoreduction. Langmuir. 2002;18(11):4191-4.

109. Adhikari B, Banerjee A. Short-Peptide-Based Hydrogel: A Template for the In Situ Synthesis of Fluorescent Silver Nanoclusters by Using Sunlight. Chemistry–A European Journal. 2010;16(46):13698-705.

110. Roy S, Banerjee A. Amino acid based smart hydrogel: formation, characterization and fluorescence properties of silver nanoclusters within the hydrogel matrix. Soft Matter. 2011;7(11):5300-8.

111. Díez I, Kanyuk MI, Demchenko AP, Walther A, Jiang H, Ikkala O et al. Blue, green and red emissive silver nanoclusters formed in organic solvents. Nanoscale. 2012;4(15):4434-7.

112. Liu Y-F, Wang G-Q, Zhao J-B, Jiang L, Fang S-M, Sun Y-A. Synthesis of chiral silver nanoclusters capped with small molecules. Colloids and Surfaces A: Physicochemical and Engineering Aspects. 2013;426:12-7.

113. Fujimura T, Yoshida Y, Inoue H, Shimada T, Takagi S. Dense Deposition of Gold Nanoclusters Utilizing a Porphyrin/Inorganic Layered Material Complex as the Template. Langmuir. 2015;31(33):9142-7.

114. Zhang C, Sun X, Li J, Liu Y-N. Synthesis of Ag nanoclusters by a pH-dependent etching method in aqueous solution. Nanoscale. 2013;5(14):6261-4.

115. Habeeb Muhammed MA, Verma PK, Pal SK, Retnakumari A, Koyakutty M, Nair S et al. Luminescent quantum clusters of gold in bulk by albumin-induced core etching of nanoparticles: metal ion sensing, metal-enhanced luminescence, and biolabeling. Chemistry–A European Journal. 2010;16(33):10103-12.

116. Habeeb Muhammed MA, Ramesh S, Sinha SS, Pal SK, Pradeep T. Two distinct fluorescent quantum clusters of gold starting from metallic nanoparticles by pH-dependent ligand etching. Nano Research. 2008;1(4):333-40.

117. Mrudula K, Rao TUB, Pradeep T. Interfacial synthesis of luminescent 7 kDa silver clusters. Journal of Materials Chemistry. 2009;19(25):4335-42.

118. Udaya Bhaskara Rao T, Pradeep T. Luminescent Ag7 and Ag8 clusters by interfacial synthesis. Angewandte Chemie International Edition. 2010;49(23):3925-9.

119. Reetz MT, Helbig W. Size-selective synthesis of nanostructured transition metal clusters. Journal of the American Chemical Society. 1994;116(16):7401-2.

120. Nielsch K, Müller F, Li AP, Gösele U. Uniform nickel deposition into ordered alumina pores by pulsed electrodeposition. Advanced Materials. 2000;12(8):582-6.

121. Peinetti AS, Herrera S, González GA, Battaglini F. Synthesis of atomic metal clusters on nanoporous alumina. Chemical Communications. 2013;49(96):11317-9.

122. Brust M, Walker M, Bethell D, Schiffrin DJ, Whyman R. Synthesis of thiol-derivatised gold nanoparticles in a two-phase liquid–liquid system. Journal of the Chemical Society, Chemical Communications. 1994(7):801-2.

123. Yu Y, Li J, Chen T, Tan YN, Xie J. Decoupling the CO-reduction protocol to generate luminescent Au22 (SR) 18 nanocluster. The Journal of Physical Chemistry C. 2015;119(20):10910-8.

124. Das A, Liu C, Byun HY, Nobusada K, Zhao S, Rosi N et al. Structure determination of [Au18 (SR) 14]. Angewandte Chemie International Edition. 2015;54(10):3140-4.

125. Higaki T, Liu C, Zeng C, Jin R, Chen Y, Rosi NL et al. Controlling the Atomic Structure of Au30 Nanoclusters by a Ligand-Based Strategy. Angewandte Chemie International Edition. 2016;55(23):6694-7.

126. Erickson JD, Mednikov EG, Ivanov SA, Dahl LF. Isolation and Structural Characterization of a Mackay 55-Metal-Atom Two-Shell Icosahedron of Pseudo-I h Symmetry, Pd55L12 (μ3-CO) 20 (L= PR3, R= Isopropyl): Comparative Analysis with Interior Two-Shell Icosahedral Geometries in Capped Three-Shell Pd145, Pt-Centered Four-Shell Pd–Pt M165, and Four-Shell Au133 Nanoclusters. Journal of the American Chemical Society. 2016;138(5):1502-5.

127. Wan X-K, Tang Q, Yuan S-F, Jiang D-e, Wang Q-M. Au19 nanocluster featuring a V-shaped alkynyl–gold motif. Journal of the American Chemical Society. 2015;137(2):652-5.

128. Wang Y, Su H, Xu C, Li G, Gell L, Lin S et al. An intermetallic Au24Ag20 superatom nanocluster stabilized by labile ligands. Journal of the American Chemical Society. 2015;137(13):4324-7.

129. Guo C, Irudayaraj J. Fluorescent Ag clusters via a protein-directed approach as a Hg (II) ion sensor. Analytical chemistry. 2011;83(8):2883-9.

130. Ghosh R, Sahoo AK, Ghosh SS, Paul A, Chattopadhyay A. Blue-emitting copper nanoclusters synthesized in the presence of lysozyme as candidates for cell labeling. ACS applied materials & interfaces. 2014;6(6):3822-8.

131. Garcia AR, Rahn I, Johnson S, Patel R, Guo J, Orbulescu J et al. Human insulin fibril-assisted synthesis of fluorescent gold nanoclusters in alkaline media under physiological temperature. Colloids and Surfaces B: Biointerfaces. 2013;105:167-72.

132. Liu J-M, Chen J-T, Yan X-P. Near infrared fluorescent trypsin stabilized gold nanoclusters as surface plasmon enhanced energy transfer biosensor and in vivo cancer imaging bioprobe. Analytical chemistry. 2013;85(6):3238-45.

133. Tao Y, Ju E, Li Z, Ren J, Qu X. Engineered CpG-antigen conjugates protected gold nanoclusters as smart self-vaccines for enhanced immune response and cell imaging. Advanced Functional Materials. 2014;24(7):1004-10.

134. Shao C, Yuan B, Wang H, Zhou Q, Li Y, Guan Y et al. Eggshell membrane as a multimodal solid state platform for generating fluorescent metal nanoclusters. Journal of Materials Chemistry. 2011;21(9):2863-6.

135. Morozov VA, Ogawa MY. Controlled formation of emissive silver nanoclusters using rationally designed metal-binding proteins. Inorganic chemistry. 2013;52(16):9166-8.

136. Luo Z, Yuan X, Yu Y, Zhang Q, Leong DT, Lee JY et al. From aggregation-induced emission of Au (I)–thiolate complexes to ultrabright Au (0)@ Au (I)–thiolate core–shell nanoclusters. Journal of the American Chemical Society. 2012;134(40):16662-70.

137. Aldeek F, Muhammed MH, Palui G, Zhan N, Mattoussi H. Growth of highly fluorescent polyethylene glycol-and zwitterion-functionalized gold nanoclusters. ACS nano. 2013;7(3):2509-21.

138. Pal NK, Kryschi C. A facile synthesis of highly stable and luminescent Ag clusters: a steady-state and time-resolved spectroscopy study. Physical Chemistry Chemical Physics. 2015;17(3):1957-65.

139. Zhang S, Zhao Y. Template synthesis of subnanometer gold clusters in interfacially cross-linked reverse micelles mediated by confined counterions. Langmuir. 2012;28(7):3606-13.

140. Petty JT, Zheng J, Hud NV, Dickson RM. DNA-templated Ag nanocluster formation. Journal of the American Chemical Society. 2004;126(16):5207-12.

141. Han B, Wang E. DNA-templated fluorescent silver nanoclusters. Analytical and bioanalytical chemistry. 2012;402(1):129-38.

142. Yang X, Gan L, Han L, Wang E, Wang J. High-Yield Synthesis of Silver Nanoclusters Protected by DNA Monomers and DFT Prediction of their Photoluminescence Properties. Angewandte Chemie International Edition. 2013;52(7):2022-6.

143. Díez I, Pusa M, Kulmala S, Jiang H, Walther A, Goldmann AS et al. Color tunability and electrochemiluminescence of silver nanoclusters. Angewandte Chemie International Edition. 2009;48(12):2122-5.

144. Shang L, Dong S. Facile preparation of water-soluble fluorescent silver nanoclusters using a polyelectrolyte template. Chemical Communications. 2008(9):1088-90.

145. Díez I, Jiang H, Ras RH. Enhanced emission of silver nanoclusters through quantitative phase transfer. ChemPhysChem. 2010;11(14):3100-4.

146. Richards CI, Choi S, Hsiang J-C, Antoku Y, Vosch T, Bongiorno A et al. Oligonucleotide-stabilized Ag nanocluster fluorophores. Journal of the American Chemical Society. 2008;130(15):5038-9.

147. Yeh Y-C, Creran B, Rotello VM. Gold nanoparticles: preparation, properties, and applications in bionanotechnology. Nanoscale. 2012;4(6):1871-80.

148. Hu M, Chen J, Li Z-Y, Au L, Hartland GV, Li X et al. Gold nanostructures: engineering their plasmonic properties for biomedical applications. Chemical Society Reviews. 2006;35(11):1084-94.

149. Shukla R, Bansal V, Chaudhary M, Basu A, Bhonde RR, Sastry M. Biocompatibility of Gold Nanoparticles and Their Endocytotic Fate Inside the Cellular Compartment: A Microscopic Overview. Langmuir. 2005;21(23):10644-54. doi:10.1021/la0513712.

150. Morales-Avila E, Ferro-Flores G, Ocampo-García BE, De León-Rodríguez LM, Santos-Cuevas CL, García-Becerra R et al. Multimeric system of 99mTc-labeled gold nanoparticles conjugated to c [RGDfK (C)] for molecular imaging of tumor α (v) β (3) expression. Bioconjugate chemistry. 2011;22(5):913-22.

151. Peltek OO, Muslimov AR, Zyuzin MV, Timin AS. Current outlook on radionuclide delivery systems: from design consideration to translation into clinics. Journal of nanobiotechnology. 2019;17(1):90.

152. Smith BR, Gambhir SS. Nanomaterials for in vivo imaging. Chemical reviews. 2017;117(3):901-86.

153. Chen D, Dougherty CA, Yang D, Wu H, Hong H. Radioactive nanomaterials for multimodality imaging. Tomography. 2016;2(1):3.

154. Koziorowski J, E Stanciu A, Gomez-Vallejo V, Llop J. Radiolabeled nanoparticles for cancer diagnosis and therapy. Anti-Cancer Agents in Medicinal Chemistry (Formerly Current Medicinal Chemistry-Anti-Cancer Agents). 2017;17(3):333-54.

155. Jeon J. Review of Therapeutic Applications of Radiolabeled Functional Nanomaterials. International journal of molecular sciences. 2019;20(9):2323.

156. Zhang Z. Radiolabeling of nanoparticles. Toxicology of Nanomaterials. 2016:69-94.

157. Brechbiel MW. Bifunctional chelates for metal nuclides. The quarterly journal of nuclear medicine and molecular imaging: official publication of the Italian Association of Nuclear Medicine (AIMN)[and] the International Association of Radiopharmacology (IAR),[and] Section of the Society of. 2008;52(2):166.

158. Lamb J, Holland JP. Advanced Methods for Radiolabeling Multimodality Nanomedicines for SPECT/MRI and PET/MRI. Journal of nuclear medicine : official publication, Society of Nuclear Medicine. 2018;59(3):382-9. doi:10.2967/jnumed.116.187419.

159. Jarrett BR, Gustafsson Br, Kukis DL, Louie AY. Synthesis of 64Cu-labeled magnetic nanoparticles for multimodal imaging. Bioconjugate chemistry. 2008;19(7):1496-504.

160. Lee H-Y, Li Z, Chen K, Hsu AR, Xu C, Xie J et al. PET/MRI dual-modality tumor imaging using arginine-glycine-aspartic (RGD)–conjugated radiolabeled iron oxide nanoparticles. Journal of Nuclear Medicine. 2008;49(8):1371-9.

161. Xie J, Chen K, Huang J, Lee S, Wang J, Gao J et al. PET/NIRF/MRI triple functional iron oxide nanoparticles. Biomaterials. 2010;31(11):3016-22.

162. Luna-Gutiérrez M, Ferro-Flores G, Ocampo-García BE, Santos-Cuevas CL, Jiménez-Mancilla N, León-Rodríguez D et al. A therapeutic system of 177Lu-labeled gold nanoparticles-RGD internalized in breast cancer cells. Journal of the Mexican Chemical Society. 2013;57(3):212-9.

163. Luna-Gutiérrez M, Ferro-Flores G, Ocampo-García B, Jiménez-Mancilla N, Morales-Avila E, De León-Rodríguez L et al. 177Lu-labeled monomeric, dimeric and multimeric RGD peptides for the therapy of tumors expressing α (ν) β (3) integrins. Journal of Labelled Compounds and Radiopharmaceuticals. 2012;55(4):140-8.

164. Moon S-H, Yang BY, Kim YJ, Hong MK, Lee Y-S, Lee DS et al. Development of a complementary PET/MR dual-modal imaging probe for targeting prostate-specific membrane antigen (PSMA). Nanomedicine: Nanotechnology, Biology and Medicine. 2016;12(4):871-9.

165. Polyak A, Nagy LN, Mihaly J, Görres S, Wittneben A, Leiter I et al. Preparation and 68Ga-radiolabeling of porous zirconia nanoparticle platform for PET/CT-imaging guided drug delivery. Journal of pharmaceutical and biomedical analysis. 2017;137:146-50.

166. Natarajan A, Gruettner C, Ivkov R, Denardo GL, Mirick G, Yuan A et al. NanoFerrite particle based radioimmunonanoparticles: binding affinity and in vivo pharmacokinetics. Bioconjugate chemistry. 2008;19(6):1211-8.

167. Natarajan A, Xiong C-Y, Gruettner C, DeNardo GL, DeNardo SJ. Development of multivalent radioimmunonanoparticles for cancer imaging and therapy. Cancer biotherapy & radiopharmaceuticals. 2008;23(1):82-91.

168. González-Ruíz A, Ferro-Flores G, Azorín-Vega E, Ocampo-García B, de Maria Ramírez F, Santos-Cuevas C et al. Synthesis and in vitro evaluation of an antiangiogenic cancer-specific dual-targeting 177 Lu-Au-nanoradiopharmaceutical. Journal of Radioanalytical and Nuclear Chemistry. 2017;314(2):1337-45.

169. Vilchis-Juárez A, Ferro-Flores G, Santos-Cuevas C, Morales-Avila E, Ocampo-García B, Díaz-Nieto L et al. Molecular targeting radiotherapy with cyclo-RGDFK (C) peptides conjugated to 177Lu-labeled gold nanoparticles in tumor-bearing mice. Journal of biomedical nanotechnology. 2014;10(3):393-404.

170. Mendoza-Nava H, Ferro-Flores G, Ramírez FdM, Ocampo-García B, Santos-Cuevas C, Azorín-Vega E et al. Fluorescent, plasmonic, and radiotherapeutic properties of the 177Lu–dendrimer-AuNP–folate–bombesin nanoprobe located inside cancer cells. Molecular imaging. 2017;16:1536012117704768.

171. Cai Z, Yook S, Lu Y, Bergstrom D, Winnik MA, Pignol J-P et al. Local radiation treatment of HER2-positive breast cancer using trastuzumab-modified gold nanoparticles labeled with 177 Lu. Pharmaceutical research. 2017;34(3):579-90.

172. Yook S, Cai Z, Lu Y, Winnik MA, Pignol J-P, Reilly RM. Radiation nanomedicine for EGFR-positive breast cancer: panitumumab-modified gold nanoparticles complexed to the β-particle-emitter, 177Lu. Molecular pharmaceutics. 2015;12(11):3963-72.

173. Yook S, Cai Z, Lu Y, Winnik MA, Pignol J-P, Reilly RM. Intratumorally injected 177Lu-labeled gold nanoparticles: gold nanoseed brachytherapy with application for neoadjuvant treatment of locally advanced breast cancer. Journal of Nuclear Medicine. 2016;57(6):936-42.

174. Yook S, Lu Y, Jeong JJ, Cai Z, Tong L, Alwarda R et al. Stability and biodistribution of thiol-functionalized and 177Lu-labeled metal chelating polymers bound to gold nanoparticles. Biomacromolecules. 2016;17(4):1292-302.

175. Xie H, Goins B, Bao A, Wang ZJ, Phillips WT. Effect of intratumoral administration on biodistribution of 64Cu-labeled nanoshells. International journal of nanomedicine. 2012;7:2227.

176. Xie H, Wang ZJ, Bao A, Goins B, Phillips WT. In vivo PET imaging and biodistribution of radiolabeled gold nanoshells in rats with tumor xenografts. International journal of pharmaceutics. 2010;395(1-2):324-30.

177. Bhatnagar P, Li Z, Choi Y, Guo J, Li F, Lee DY et al. Imaging of genetically engineered T cells by PET using gold nanoparticles complexed to Copper-64. Integrative Biology. 2013;5(1):231-8.

178. Zavaleta CL, Hartman KB, Miao Z, James ML, Kempen P, Thakor AS et al. Preclinical evaluation of Raman nanoparticle biodistribution for their potential use in clinical endoscopy imaging. Small. 2011;7(15):2232-40.

179. Wang Y, Liu Y, Luehmann H, Xia X, Brown P, Jarreau C et al. Evaluating the pharmacokinetics and in vivo cancer targeting capability of Au nanocages by positron emission tomography imaging. Acs Nano. 2012;6(7):5880-8.

180. Glaus C, Rossin R, Welch MJ, Bao G. In vivo evaluation of 64Cu-labeled magnetic nanoparticles as a dual-modality PET/MR imaging agent. Bioconjugate chemistry. 2010;21(4):715-22.

181. Hu H, Li D, Liu S, Wang M, Moats R, Conti PS et al. Integrin α2β1 targeted GdVO4: Eu ultrathin nanosheet for multimodal PET/MR imaging. Biomaterials. 2014;35(30):8649-58.

182. Tian M, Lu W, Zhang R, Xiong C, Ensor J, Nazario J et al. Tumor uptake of hollow gold nanospheres after intravenous and intra-arterial injection: PET/CT study in a rabbit VX2 liver cancer model. Molecular imaging and biology. 2013;15(5):614-24.

183. England CG, Im H-J, Feng L, Chen F, Graves SA, Hernandez R et al. Re-assessing the enhanced permeability and retention effect in peripheral arterial disease using radiolabeled long circulating nanoparticles. Biomaterials. 2016;100:101-9.

184. Kim S-m, Chae MK, Yim MS, Jeong IH, Cho J, Lee C et al. Hybrid PET/MR imaging of tumors using an oleanolic acid-conjugated nanoparticle. Biomaterials. 2013;34(33):8114-21.

185. Yang X, Hong H, Grailer JJ, Rowland IJ, Javadi A, Hurley SA et al. cRGD-functionalized, DOX-conjugated, and 64Cu-labeled superparamagnetic iron oxide nanoparticles for targeted anticancer drug delivery and PET/MR imaging. Biomaterials. 2011;32(17):4151-60.

186. Yang M, Cheng K, Qi S, Liu H, Jiang Y, Jiang H et al. Affibody modified and radiolabeled gold–iron oxide hetero-nanostructures for tumor PET, optical and MR imaging. Biomaterials. 2013;34(11):2796-806.

187. Cheng K, Kothapalli S-R, Liu H, Koh AL, Jokerst JV, Jiang H et al. Construction and validation of nano gold tripods for molecular imaging of living subjects. Journal of the American Chemical Society. 2014;136(9):3560-71.

188. Zhan Y, Shi S, Ehlerding EB, Graves SA, Goel S, Engle JW et al. Radiolabeled, antibody-conjugated manganese oxide nanoparticles for tumor vasculature targeted positron emission tomography and magnetic resonance imaging. ACS applied materials & interfaces. 2017;9(44):38304-12.

189. Zhu J, Li H, Xiong Z, Shen M, Conti PS, Shi X et al. Polyethyleneimine-coated manganese oxide nanoparticles for targeted tumor PET/MR imaging. ACS applied materials & interfaces. 2018;10(41):34954-64.

190. Yang BY, Moon S-H, Seelam SR, Jeon MJ, Lee Y-S, Lee DS et al. Development of a multimodal imaging probe by encapsulating iron oxide nanoparticles with functionalized amphiphiles for lymph node imaging. Nanomedicine. 2015;10(12):1899-910.

191. Frigell J, García I, Gómez-Vallejo V, Llop J, Penades S. 68Ga-labeled gold glyconanoparticles for exploring blood–brain barrier permeability: preparation, biodistribution studies, and improved brain uptake via neuropeptide conjugation. Journal of the American Chemical Society. 2014;136(1):449-57.

192. Sun Z, Cheng K, Wu F, Liu H, Ma X, Su X et al. Robust surface coating for a fast, facile fluorine-18 labeling of iron oxide nanoparticles for PET/MR dual-modality imaging. Nanoscale. 2016;8(47):19644-53.

193. Cheng D, Li X, Zhang C, Tan H, Wang C, Pang L et al. Detection of vulnerable atherosclerosis plaques with a dual-modal single-photon-emission computed tomography/magnetic resonance imaging probe targeting apoptotic macrophages. ACS applied materials & interfaces. 2015;7(4):2847-55.

194. Gao H, Liu X, Tang W, Niu D, Zhou B, Zhang H et al. 99m Tc-conjugated manganese-based mesoporous silica nanoparticles for SPECT, pH-responsive MRI and anti-cancer drug delivery. Nanoscale. 2016;8(47):19573-80.

195. Zhang G, Yang Z, Lu W, Zhang R, Huang Q, Tian M et al. Influence of anchoring ligands and particle size on the colloidal stability and in vivo biodistribution of polyethylene glycol-coated gold nanoparticles in tumor-xenografted mice. Biomaterials. 2009;30(10):1928-36.

196. de Souza Albernaz M, Toma SH, Clanton J, Araki K, Santos-Oliveira R. Decorated superparamagnetic iron oxide nanoparticles with monoclonal antibody and diethylene-triamine-pentaacetic acid labeled with thechnetium-99m and galium-68 for breast cancer imaging. Pharmaceutical research. 2018;35(1):24.

197. Shanehsazzadeh S, Oghabian MA, Lahooti A, Abdollahi M, Haeri SA, Amanlou M et al. Estimated background doses of [67Ga]-DTPA-USPIO in normal Balb/c mice as a potential therapeutic agent for liver and spleen cancers. Nuclear medicine communications. 2013;34(9):915-25.

198. Nosrati S, Shanehsazzadeh S, Yousefnia H, Gholami A, Grüttner C, Jalilian AR et al. Biodistribution evaluation of 166 Ho–DTPA–SPION in normal rats. Journal of Radioanalytical and Nuclear Chemistry. 2016;307(2):1559-66.

199. Silva F, Zambre A, Campello MPC, Gano L, Santos I, Ferraria AM et al. Interrogating the role of receptor-mediated mechanisms: biological fate of peptide-functionalized radiolabeled gold nanoparticles in tumor mice. Bioconjugate chemistry. 2016;27(4):1153-64.

200. Li X, Xiong Z, Xu X, Luo Y, Peng C, Shen M et al. 99mTc-labeled multifunctional low-generation dendrimer-entrapped gold nanoparticles for targeted SPECT/CT dual-mode imaging of tumors. ACS applied materials & interfaces. 2016;8(31):19883-91.

201. Zhao L, Wen S, Zhu M, Li D, Xing Y, Shen M et al. 99mTc-labelled multifunctional polyethylenimine-entrapped gold nanoparticles for dual mode SPECT and CT imaging. Artificial cells, nanomedicine, and biotechnology. 2018;46(sup1):488-98.

202. Song L, Falzone N, Vallis KA. EGF-coated gold nanoparticles provide an efficient nano-scale delivery system for the molecular radiotherapy of EGFR-positive cancer. International journal of radiation biology. 2016;92(11):716-23.

203. Bai J, Wang JT-W, Rubio N, Protti A, Heidari H, Elgogary R et al. Triple-modal imaging of magnetically-targeted nanocapsules in solid tumours in vivo. Theranostics. 2016;6(3):342.

204. Azadbakht B, Afarideh H, Ghannadi-Maragheh M, Bahrami-Samani A, Asgari M. Preparation and evaluation of APTES-PEG coated iron oxide nanoparticles conjugated to rhenium-188 labeled rituximab. Nuclear medicine and biology. 2017;48:26-30.

205. Azorín-Vega E, Zambrano-Ramírez O, Rojas-Calderón E, Ocampo-García B, Ferro-Flores G. Tumoral fibrosis effect on the radiation absorbed dose of 177Lu–Tyr3-octreotate and 177Lu–Tyr3-octreotate conjugated to gold nanoparticles. Applied Radiation and Isotopes. 2015;100:96-100.

206. Lee IJ, Park JY, Kim Y-i, Lee Y-S, Jeong JM, Kim J et al. Image-based analysis of tumor localization after intra-arterial delivery of technetium-99m-labeled SPIO using SPECT/CT and MRI. Molecular imaging. 2017;16:1536012116689001.

207. Radović M, Vranješ-Đurić S, Nikolić N, Janković D, Goya GF, Torres TE et al. Development and evaluation of 90Y-labeled albumin microspheres loaded with magnetite nanoparticles for possible applications in cancer therapy. Journal of Materials Chemistry. 2012;22(45):24017-25. doi:10.1039/C2JM35593K.

208. Radović M, Calatayud MP, Goya GF, Ibarra MR, Antić B, Spasojević V et al. Preparation and in vivo evaluation of multifunctional 90Y-labeled magnetic nanoparticles designed for cancer therapy. Journal of Biomedical Materials Research Part A. 2015;103(1):126-34.

209. Tang Q-S, Chen D-Z, Xue W-Q, Xiang J-Y, Gong Y-C, Zhang L et al. Preparation and biodistribution of 188Re-labeled folate conjugated human serum albumin magnetic cisplatin nanoparticles (188Re-folate-CDDP/HSA MNPs) in vivo. International journal of nanomedicine. 2011;6:3077.

210. Wang Y, Wu Y, Liu Y, Shen J, Lv L, Li L et al. BSA-mediated synthesis of bismuth sulfide nanotheranostic agents for tumor multimodal imaging and thermoradiotherapy. Advanced Functional Materials. 2016;26(29):5335-44.

211. Ocampo-García BE, Ramírez FdM, Ferro-Flores G, De León-Rodríguez LM, Santos-Cuevas CL, Morales-Avila E et al. 99mTc-labelled gold nanoparticles capped with HYNIC-

peptide/mannose for sentinel lymph node detection. Nuclear medicine and biology. 2011;38(1):1-11.

212. Mendoza-Sánchez AN, Ferro-Flores G, Ocampo-García BE, Morales-Avila E, Ramírez FdM, De León-Rodríguez LM et al. Lys3-Bombesin Conjugated to99mTc-Labelled Gold Nanoparticles for In Vivo Gastrin Releasing Peptide-Receptor Imaging. Journal of biomedical nanotechnology. 2010;6(4):375-84.

213. Zhang X, Yao M, Chen M, Li L, Dong C, Hou Y et al. Hyaluronic acid-coated silver nanoparticles as a nanoplatform for in vivo imaging applications. ACS applied materials & interfaces. 2016;8(39):25650-3.

214. Gao Z, Hou Y, Zeng J, Chen L, Liu C, Yang W et al. Tumor Microenvironment-Triggered Aggregation of Antiphagocytosis 99mTc-Labeled Fe3O4 Nanoprobes for Enhanced Tumor Imaging In Vivo. Advanced materials. 2017;29(24):1701095.

215. Qiu S, Zeng J, Hou Y, Chen L, Ge J, Wen L et al. Detection of lymph node metastasis with near-infrared upconversion luminescent nanoprobes. Nanoscale. 2018;10(46):21772-81.

216. Torres Martin de Rosales R, Tavaré R, Paul RL, Jauregui-Osoro M, Protti A, Glaria A et al. Synthesis of 64CuII–bis (dithiocarbamatebisphosphonate) and its conjugation with superparamagnetic iron oxide nanoparticles: in vivo evaluation as dual-modality PET–MRI agent. Angewandte Chemie International Edition. 2011;50(24):5509-13.

217. Sandiford L, Phinikaridou A, Protti A, Meszaros LK, Cui X, Yan Y et al. Bisphosphonate-anchored PEGylation and radiolabeling of superparamagnetic iron oxide: long-circulating nanoparticles for in vivo multimodal (T1 MRI-SPECT) imaging. Acs Nano. 2013;7(1):500-12.

218. Torres Martin de Rosales R, Tavaré R, Glaria A, Varma G, Protti A, Blower PJ. 99mTc-bisphosphonate-iron oxide nanoparticle conjugates for dual-modality biomedical imaging. Bioconjugate chemistry. 2011;22(3):455-65.

219. Abdollah MR, Carter TJ, Jones C, Kalber TL, Rajkumar V, Tolner B et al. Fucoidan prolongs the circulation time of dextran-coated iron oxide nanoparticles. ACS nano. 2018;12(2):1156-69.

220. Groult H, Ruiz-Cabello Js, Pellico J, Lechuga-Vieco AV, Bhavesh R, Zamai M et al. Parallel multifunctionalization of nanoparticles: a one-step modular approach for in vivo imaging. Bioconjugate chemistry. 2015;26(1):153-60.

221. Thorek DL, Ulmert D, Diop N-FM, Lupu ME, Doran MG, Huang R et al. Non-invasive mapping of deep-tissue lymph nodes in live animals using a multimodal PET/MRI nanoparticle. Nature communications. 2014;5(1):1-9.

222. Li X, Wang C, Tan H, Cheng L, Liu G, Yang Y et al. Gold nanoparticles-based SPECT/CT imaging probe targeting for vulnerable atherosclerosis plaques. Biomaterials. 2016;108:71-80.

223. Xu Z, Wang Y, Han J, Xu Q, Ren J, Xu J et al. Noninvasive multimodal imaging of osteosarcoma and lymph nodes using a 99mTc-labeled biomineralization nanoprobe. Analytical chemistry. 2018;90(7):4529-34.

224. Sharma R, Xu Y, Kim SW, Schueller MJ, Alexoff D, Smith SD et al. Carbon-11 radiolabeling of iron-oxide nanoparticles for dual-modality PET/MR imaging. Nanoscale. 2013;5(16):7476-83.

225. Nallathamby PD, Mortensen NP, Palko HA, Malfatti M, Smith C, Sonnett J et al. New surface radiolabeling schemes of super paramagnetic iron oxide nanoparticles (SPIONs) for biodistribution studies. Nanoscale. 2015;7(15):6545-55.

226. Rojas S, Gispert JD, Abad S, Buaki-Sogo M, Victor VM, Garcia H et al. In vivo biodistribution of amino-functionalized ceria nanoparticles in rats using positron emission tomography. Molecular pharmaceutics. 2012;9(12):3543-50.

227. Lee J, Lee TS, Ryu J, Hong S, Kang M, Im K et al. RGD peptide–conjugated multimodal NaGdF4: Yb3+/Er3+ nanophosphors for upconversion luminescence, MR, and PET imaging of tumor angiogenesis. Journal of Nuclear Medicine. 2013;54(1):96-103.

228. Jang B, Park S, Kang SH, Kim JK, Kim S-K, Kim I-H et al. Gold nanorods for target selective SPECT/CT imaging and photothermal therapy in vivo. Quantitative imaging in medicine and surgery. 2012;2(1):1.

229. Liu S, Jia B, Qiao R, Yang Z, Yu Z, Liu Z et al. A novel type of dual-modality molecular probe for MR and nuclear imaging of tumor: preparation, characterization and in vivo application. Molecular pharmaceutics. 2009;6(4):1074-82.

230. Tang Y, Zhang C, Wang J, Lin X, Zhang L, Yang Y et al. MRI/SPECT/fluorescent tri-modal probe for evaluating the homing and therapeutic efficacy of transplanted mesenchymal stem cells in a rat ischemic stroke model. Advanced functional materials. 2015;25(7):1024-34.

231. Liu LX, Li BX, Wang QY, Dong ZP, Li HM, Jin QM et al. An integrative folate-based metal complex nanotube as a potent antitumor nanomedicine as well as an efficient tumor-targeted drug carrier. Bioconjugate chemistry. 2016;27(12):2863-73.

232. Unak G, Ozkaya F, Medine EI, Kozgus O, Sakarya S, Bekis R et al. Gold nanoparticle probes: design and in vitro applications in cancer cell culture. Colloids and Surfaces B: Biointerfaces. 2012;90:217-26.

233. Zhu J, Chin J, Wängler C, Wängler B, Lennox RB, Schirrmacher R. Rapid 18F-labeling and loading of PEGylated gold nanoparticles for in vivo applications. Bioconjugate chemistry. 2014;25(6):1143-50.

234. Guerrero S, Herance JR, Rojas S, Mena JF, Gispert JD, Acosta GA et al. Synthesis and in vivo evaluation of the biodistribution of a 18F-labeled conjugate gold-nanoparticle-peptide with potential biomedical application. Bioconjugate chemistry. 2012;23(3):399-408.

235. Nahrendorf M, Keliher E, Marinelli B, Waterman P, Feruglio PF, Fexon L et al. Hybrid PET-optical imaging using targeted probes. Proceedings of the National Academy of Sciences. 2010;107(17):7910-5.

236. Deng S, Zhang W, Zhang B, Hong R, Chen Q, Dong J et al. Radiolabeled cyclic arginine-glycine-aspartic (RGD)-conjugated iron oxide nanoparticles as single-photon emission computed tomography (SPECT) and magnetic resonance imaging (MRI) dual-modality agents for imaging of breast cancer. Journal of Nanoparticle Research. 2015;17(1):19.

237. Su N, Dang Y, Liang G, Liu G. Iodine-125-labeled cRGD-gold nanoparticles as tumor-targeted radiosensitizer and imaging agent. Nanoscale research letters. 2015;10(1):160.

238. Wang J, Zhao H, Zhou Z, Zhou P, Yan Y, Wang M et al. MR/SPECT imaging guided photothermal therapy of tumor-targeting Fe@ Fe3O4 nanoparticles in vivo with low mononuclear phagocyte uptake. ACS applied materials & interfaces. 2016;8(31):19872-82.

239. Black KC, Akers WJ, Sudlow G, Xu B, Laforest R, Achilefu S. Dual-radiolabeled nanoparticle SPECT probes for bioimaging. Nanoscale. 2015;7(2):440-4.

240. Chen L, Chen J, Qiu S, Wen L, Wu Y, Hou Y et al. Biodegradable Nanoagents with Short Biological Half-Life for SPECT/PAI/MRI Multimodality Imaging and PTT Therapy of Tumors. Small. 2018;14(4):1702700.

241. Lattuada L, Barge A, Cravotto G, Giovenzana GB, Tei L. The synthesis and application of polyamino polycarboxylic bifunctional chelating agents. Chemical Society Reviews. 2011;40(5):3019-49.

242. Ge J, Zhang Q, Zeng J, Gu Z, Gao M. Radiolabeling nanomaterials for multimodality imaging: New insights into nuclear medicine and cancer diagnosis. Biomaterials. 2019:119553.

243. Enrique M-A, Mariana O-R, Mirshojaei SF, Ahmadi A. Multifunctional radiolabeled nanoparticles: strategies and novel classification of radiopharmaceuticals for cancer treatment. Journal of drug targeting. 2015;23(3):191-201.

244. Price EW, Orvig C. Matching chelators to radiometals for radiopharmaceuticals. Chemical Society Reviews. 2014;43(1):260-90.

245. Mei BC, Oh E, Susumu K, Farrell D, Mountziaris TJ, Mattoussi H. Effects of Ligand Coordination Number and Surface Curvature on the Stability of Gold Nanoparticles in Aqueous Solutions. Langmuir. 2009;25(18):10604-11. doi:10.1021/la901423z.

246. Ait-Mohand S, Fournier P, Dumulon-Perreault V, Kiefer GE, Jurek P, Ferreira CL et al. Evaluation of 64Cu-labeled bifunctional chelate–bombesin conjugates. Bioconjugate chemistry. 2011;22(8):1729-35.

247. Zhang Y, Hong H, Engle JW, Bean J, Yang Y, Leigh BR et al. Positron emission tomography imaging of CD105 expression with a 64Cu-labeled monoclonal antibody: NOTA is superior to DOTA. PloS one. 2011;6(12).

248. Zhan Y, Ai F, Chen F, Valdovinos HF, Orbay H, Sun H et al. Intrinsically zirconium-89 labeled Gd2O2S: Eu nanoprobes for in vivo positron emission tomography and gamma-ray-induced radioluminescence imaging. Small. 2016;12(21):2872-6.

249. Zhou B, Zheng L, Peng C, Li D, Li J, Wen S et al. Synthesis and characterization of PEGylated polyethylenimine-entrapped gold nanoparticles for blood pool and tumor CT imaging. ACS applied materials & interfaces. 2014;6(19):17190-9.

250. de Sá A, Prata MIM, Geraldes CF, André JP. Triaza-based amphiphilic chelators: synthetic route, in vitro characterization and in vivo studies of their Ga (III) and Al (III) chelates. Journal of inorganic biochemistry. 2010;104(10):1051-62.

251. Abstiens K, Gregoritza M, Goepferich AM. Ligand density and linker length are critical factors for multivalent nanoparticle–Receptor interactions. ACS applied materials & interfaces. 2018;11(1):1311-20.

252. McBride WJ, Sharkey RM, Karacay H, D'Souza CA, Rossi EA, Laverman P et al. A novel method of 18F radiolabeling for PET. Journal of nuclear medicine. 2009;50(6):991-8.

253. Kumar K, Ghosh A. 18F-AlF labeled peptide and protein conjugates as positron emission tomography imaging pharmaceuticals. Bioconjugate chemistry. 2018;29(4):953-75.

254. Cleeren F, Lecina J, Bridoux J, Devoogdt N, Tshibangu T, Xavier C et al. Direct fluorine-18 labeling of heat-sensitive biomolecules for positron emission tomography imaging using the Al 18 F-RESCA method. Nature protocols. 2018;13(10):2330-47.

255. Frullano L, Caravan P. Strategies for the preparation of bifunctional gadolinium (III) chelators. Current organic synthesis. 2011;8(4):535-65.

256. Brücher E. Kinetic stabilities of gadolinium (III) chelates used as MRI contrast agents. Contrast Agents I. Springer; 2002. p. 103-22.

257. Gabriel M, Decristoforo C, Donnemiller E, Ulmer H, Rychlinski CW, Mather SJ et al. An intrapatient comparison of 99mTc-EDDA/HYNIC-TOC with 111In-DTPA-octreotide for diagnosis of somatostatin receptor-expressing tumors. Journal of nuclear medicine. 2003;44(5):708-16.

258. Radioisotopes I, No RS. 1: Technetium 99m Radiopharmaceuticals: Status and Trends. Vienna; 2009.

259. Boschi A, Uccelli L, Martini P. A Picture of Modern Tc-99m Radiopharmaceuticals: Production, Chemistry, and Applications in Molecular Imaging. Applied Sciences. 2019;9(12):2526.

260. De Lima JJ. Nuclear medicine physics. CRC Press; 2016.

261. MacPherson DS, Fung K, Cook BE, Francesconi LC, Zeglis BM. A brief overview of metal complexes as nuclear imaging agents. Dalton Transactions. 2019;48(39):14547-65.

262. Holland JP, Divilov V, Bander NH, Smith-Jones PM, Larson SM, Lewis JS. 89Zr-DFO-J591 for immunoPET of prostate-specific membrane antigen expression in vivo. Journal of Nuclear Medicine. 2010;51(8):1293-300.

263. Bhatt NB, Pandya DN, Wadas TJ. Recent advances in zirconium-89 chelator development. Molecules. 2018;23(3):638.

264. Brandt M, Cardinale J, Aulsebrook ML, Gasser G, Mindt TL. An overview of PET radiochemistry, part 2: Radiometals. Journal of Nuclear Medicine. 2018;59(10):1500-6.

265. Oroujeni M, Garousi J, Andersson KG, Löfblom J, Mitran B, Orlova A et al. Preclinical Evaluation of [68Ga] Ga-DFO-ZEGFR: 2377: A Promising Affibody-Based Probe for Noninvasive PET Imaging of EGFR Expression in Tumors. Cells. 2018;7(9):141.

266. Gourni E, Del Pozzo L, Bartholomä M, Kiefer Y, T. Meyer P, Maecke HR et al. Radiochemistry and preclinical PET Imaging of 68Ga-desferrioxamine radiotracers targeting prostate-specific membrane antigen. Molecular imaging. 2017;16:1536012117737010.

267. Goel S, Chen F, Ehlerding EB, Cai W. Intrinsically radiolabeled nanoparticles: an emerging paradigm. Small. 2014;10(19):3825-30.

268. Salvanou EA, Bouziotis P, Tsoukalas C. Radiolabeled Nanoparticles in Nuclear Oncology. Advanced Nano Research. 2018;1(1):38-55.

269. Shi S, Xu C, Yang K, Goel S, Valdovinos HF, Luo H et al. Chelator-free radiolabeling of nanographene: Breaking the stereotype of chelation. Angewandte Chemie International Edition. 2017;56(11):2889-92.

270. Cheng L, Shen S, Shi S, Yi Y, Wang X, Song G et al. FeSe2-decorated Bi2Se3 nanosheets fabricated via cation exchange for chelator-free 64Cu-labeling and multimodal image-guided photothermal-radiation therapy. Advanced functional materials. 2016;26(13):2185-97.

271. Jauregui-Osoro M, Williamson PA, Glaria A, Sunassee K, Charoenphun P, Green MA et al. Biocompatible inorganic nanoparticles for [18F]-fluoride binding with applications in PET imaging. Dalton Transactions. 2011;40(23):6226-37.

272. Liu Q, Sun Y, Li C, Zhou J, Li C, Yang T et al. 18F-labeled magnetic-upconversion nanophosphors via rare-earth cation-assisted ligand assembly. Acs Nano. 2011;5(4):3146-57.

273. Zhou J, Yu M, Sun Y, Zhang X, Zhu X, Wu Z et al. Fluorine-18-labeled Gd3+/Yb3+/Er3+ co-doped NaYF4 nanophosphors for multimodality PET/MR/UCL imaging. Biomaterials. 2011;32(4):1148-56.

274. Chen M, Guo Z, Chen Q, Wei J, Li J, Shi C et al. Pd nanosheets with their surface coordinated by radioactive iodide as a high-performance theranostic nanoagent for orthotopic hepatocellular carcinoma imaging and cancer therapy. Chemical science. 2018;9(18):4268-74.

275. Chrastina A, Schnitzer JE. Iodine-125 radiolabeling of silver nanoparticles for in vivo SPECT imaging. International journal of nanomedicine. 2010;5:653.

276. Clanton R, Gonzalez A, Shankar S, Akabani G. Rapid synthesis of 125I integrated gold nanoparticles for use in combined neoplasm imaging and targeted radionuclide therapy. Applied Radiation and Isotopes. 2018;131:49-57.

277. Farrag NS, El-Sabagh HA, Al-mahallawi AM, Amin AM, AbdEl-Bary A, Mamdouh W. Comparative study on radiolabeling and biodistribution of core-shell silver/polymeric

nanoparticles-based theranostics for tumor targeting. International journal of pharmaceutics. 2017;529(1-2):123-33.

278. Shao X, Zhang H, Rajian JR, Chamberland DL, Sherman PS, Quesada CA et al. 125I-labeled gold nanorods for targeted imaging of inflammation. ACS nano. 2011;5(11):8967-73.

279. Cao X, Cao F, Xiong L, Yang Y, Cao T, Cai X et al. Cytotoxicity, tumor targeting and PET imaging of sub-5 nm KGdF 4 multifunctional rare earth nanoparticles. Nanoscale. 2015;7(32):13404-9.

280. Zhu J, Zhang B, Tian J, Wang J, Chong Y, Wang X et al. Synthesis of heterodimer radionuclide nanoparticles for magnetic resonance and single-photon emission computed tomography dual-modality imaging. Nanoscale. 2015;7(8):3392-5.

281. Cedrowska E, Łyczko M, Piotrowska A, Bilewicz A, Stolarz A, Trzcińska A et al. Silver impregnated nanoparticles of titanium dioxide as carriers for 211At. Radiochimica Acta. 2016;104(4):267-75.

282. Dziawer L, Koźmiński P, Męczyńska-Wielgosz S, Pruszyński M, Łyczko M, Wąs B et al. Gold nanoparticle bioconjugates labelled with 211At for targeted alpha therapy. RSC Advances. 2017;7(65):41024-32. doi:10.1039/C7RA06376H.

283. Dziawer Ł, Majkowska-Pilip A, Gaweł D, Godlewska M, Pruszyński M, Jastrzębski J et al. Trastuzumab-modified gold nanoparticles labeled with 211At as a prospective tool for local treatment of HER2-positive breast cancer. Nanomaterials. 2019;9(4):632.

284. Kučka J, Hrubý M, Koňák Č, Kozempel J, Lebeda O. Astatination of nanoparticles containing silver as possible carriers of 211At. Applied radiation and isotopes. 2006;64(2):201-6.

285. Gao F, Cai P, Yang W, Xue J, Gao L, Liu R et al. Ultrasmall [64Cu] Cu nanoclusters for targeting orthotopic lung tumors using accurate positron emission tomography imaging. ACS nano. 2015;9(5):4976-86.

286. Jin Q, Zhu W, Jiang D, Zhang R, Kutyreff CJ, Engle JW et al. Ultra-small iron-gallic acid coordination polymer nanoparticles for chelator-free labeling of 64 Cu and multimodal imaging-guided photothermal therapy. Nanoscale. 2017;9(34):12609-17.

287. Shen S, Jiang D, Cheng L, Chao Y, Nie K, Dong Z et al. Renal-clearable ultrasmall coordination polymer nanodots for chelator-free 64Cu-labeling and imaging-guided enhanced radiotherapy of cancer. ACS nano. 2017;11(9):9103-11.

288. Tong X, Wang Z, Sun X, Song J, Jacobson O, Niu G et al. Size dependent kinetics of gold nanorods in EPR mediated tumor delivery. Theranostics. 2016;6(12):2039.

289. Wang S, Lin J, Wang Z, Zhou Z, Bai R, Lu N et al. Core–Satellite Polydopamine–Gadolinium-Metallofullerene Nanotheranostics for Multimodal Imaging Guided Combination Cancer Therapy. Advanced Materials. 2017;29(35):1701013.

290. Burke BP, Baghdadi N, Clemente GS, Camus N, Guillou A, Kownacka AE et al. Final step gallium-68 radiolabelling of silica-coated iron oxide nanorods as potential PET/MR multimodal imaging agents. Faraday discussions. 2015;175:59-71.

291. Burke BP, Baghdadi N, Kownacka AE, Nigam S, Clemente GS, Al-Yassiry MM et al. Chelator free gallium-68 radiolabelling of silica coated iron oxide nanorods via surface interactions. Nanoscale. 2015;7(36):14889-96.

292. Ruiz-de-Angulo A, Zabaleta A, Gómez-Vallejo V, Llop J, Mareque-Rivas JC. Microdosed lipid-coated 67Ga-magnetite enhances antigen-specific immunity by image tracked delivery of antigen and CpG to lymph nodes. ACS nano. 2016;10(1):1602-18.

293. Wall MA, Shaffer TM, Harmsen S, Tschaharganeh D-F, Huang C-H, Lowe SW et al. Chelator-free radiolabeling of SERRS nanoparticles for whole-body PET and intraoperative Raman imaging. Theranostics. 2017;7(12):3068.

294. Boros E, Bowen AM, Josephson L, Vasdev N, Holland JP. Chelate-free metal ion binding and heat-induced radiolabeling of iron oxide nanoparticles. Chemical science. 2015;6(1):225-36.

295. Cheng L, Shen S, Jiang D, Jin Q, Ellison PA, Ehlerding EB et al. Chelator-free labeling of metal oxide nanostructures with zirconium-89 for positron emission tomography imaging. ACS nano. 2017;11(12):12193-201.

296. Ni D, Ferreira CA, Barnhart TE, Quach V, Yu B, Jiang D et al. Magnetic targeting of nanotheranostics enhances cerenkov radiation-induced photodynamic therapy. Journal of the American Chemical Society. 2018;140(44):14971-9.

297. Normandin MD, Yuan H, Wilks MQ, Chen HH, Kinsella JM, Cho H et al. Heat-Induced Radiolabeling of Nanoparticles for Monocyte Tracking by PET. Angewandte Chemie International Edition. 2015;54(44):13002-6.

298. Zhan Y, Ehlerding EB, Shi S, Graves SA, Goel S, Engle JW et al. Intrinsically zirconium-89-labeled manganese oxide nanoparticles for in vivo dual-modality positron emission tomography and magnetic resonance imaging. Journal of biomedical nanotechnology. 2018;14(5):900-9.

299. Adamiano A, Iafisco M, Sandri M, Basini M, Arosio P, Canu T et al. On the use of superparamagnetic hydroxyapatite nanoparticles as an agent for magnetic and nuclear in vivo imaging. Acta biomaterialia. 2018;73:458-69.

300. Jiang X, Han Y, Zhang H, Liu H, Huang Q, Wang T et al. Cu–Fe–Se Ternary Nanosheet-Based Drug Delivery Carrier for Multimodal Imaging and Combined Chemo/Photothermal Therapy of Cancer. ACS applied materials & interfaces. 2018;10(50):43396-404.

301. Tian L, Wang Y, Sun L, Xu J, Chao Y, Yang K et al. Cerenkov Luminescence-Induced NO Release from 32P-Labeled ZnFe (CN) 5NO Nanosheets to Enhance Radioisotope-Immunotherapy. Matter. 2019;1(4):1061-76.

302. Kamal R, Chadha VD, Dhawan D. Physiological uptake and retention of radiolabeled resveratrol loaded gold nanoparticles (99mTc-Res-AuNP) in colon cancer tissue. Nanomedicine: Nanotechnology, Biology and Medicine. 2018;14(3):1059-71.

303. Tian L, Yi X, Dong Z, Xu J, Liang C, Chao Y et al. Calcium Bisphosphonate Nanoparticles with Chelator-Free Radiolabeling to Deplete Tumor-Associated Macrophages for Enhanced Cancer Radioisotope Therapy. ACS nano. 2018;12(11):11541-51.

304. Kim YH, Jeon J, Hong SH, Rhim WK, Lee YS, Youn H et al. Tumor targeting and imaging using cyclic RGD-PEGylated gold nanoparticle probes with directly conjugated iodine-125. Small. 2011;7(14):2052-60.

305. Patrick PS, Bogart LK, Macdonald TJ, Southern P, Powell MJ, Zaw-Thin M et al. Surface radio-mineralisation mediates chelate-free radiolabelling of iron oxide nanoparticles. Chemical science. 2019;10(9):2592-7.

306. Chen F, Ellison PA, Lewis CM, Hong H, Zhang Y, Shi S et al. Chelator-free synthesis of a dual-modality PET/MRI agent. Angewandte Chemie International Edition. 2013;52(50):13319-23.

307. Chakravarty R, Valdovinos HF, Chen F, Lewis CM, Ellison PA, Luo H et al. Intrinsically germanium-69-labeled iron oxide nanoparticles: synthesis and in-vivo dual-modality PET/MR imaging. Advanced Materials. 2014;26(30):5119-23.

308. Mokhodoeva O, Vlk M, Málková E, Kukleva E, Mičolová P, Štamberg K et al. Study of 223 Ra uptake mechanism by Fe 3 O 4 nanoparticles: towards new prospective theranostic SPIONs. Journal of Nanoparticle Research. 2016;18(10):301.

309. Cui X, Mathe D, Kovács Nm, Horváth I, Jauregui-Osoro M, Torres Martin de Rosales R et al. Synthesis, characterization, and application of core–shell Co0. 16Fe2. 84O4@ NaYF4 (Yb, Er) and Fe3O4@ NaYF4 (Yb, Tm) nanoparticle as Trimodal (MRI, PET/SPECT, and optical) imaging agents. Bioconjugate chemistry. 2016;27(2):319-28.

310. Yuan H, Wilks MQ, Normandin MD, El Fakhri G, Kaittanis C, Josephson L. Heat-induced radiolabeling and fluorescence labeling of Feraheme nanoparticles for PET/SPECT imaging and flow cytometry. Nature protocols. 2018;13(2):392.

311. Riedinger A, Avellini T, Curcio A, Asti M, Xie Y, Tu R et al. Post-synthesis incorporation of 64Cu in CuS nanocrystals to radiolabel photothermal probes: a feasible approach for clinics. Journal of the American Chemical Society. 2015;137(48):15145-51.

312. Frellsen AF, Hansen AE, Jølck RI, Kempen PJ, Severin GW, Rasmussen PH et al. Mouse positron emission tomography study of the biodistribution of gold nanoparticles with different surface coatings using embedded copper-64. ACS nano. 2016;10(11):9887-98.

313. Hu H, Huang P, Weiss OJ, Yan X, Yue X, Zhang MG et al. PET and NIR optical imaging using self-illuminating 64Cu-doped chelator-free gold nanoclusters. Biomaterials. 2014;35(37):9868-76.

314. Zhao Y, Detering L, Sultan D, Cooper ML, You M, Cho S et al. Gold nanoclusters doped with 64Cu for CXCR4 positron emission tomography imaging of breast cancer and metastasis. ACS nano. 2016;10(6):5959-70.

315. Zhao Y, Sultan D, Detering L, Cho S, Sun G, Pierce R et al. Copper-64-alloyed gold nanoparticles for cancer imaging: Improved radiolabel stability and diagnostic accuracy. Angewandte Chemie International Edition. 2014;53(1):156-9.

316. Ng QK, Olariu CI, Yaffee M, Taelman VF, Marincek N, Krause T et al. Indium-111 labeled gold nanoparticles for in-vivo molecular targeting. Biomaterials. 2014;35(25):7050-7.

317. Sakr TM, Khowessah O, Motaleb M, El-Bary AA, El-Kolaly M, Swidan MM. I-131 doping of silver nanoparticles platform for tumor theranosis guided drug delivery. European Journal of Pharmaceutical Sciences. 2018;122:239-45.

318. Pellico J, Ruiz-Cabello J, Saiz-Alía M, del Rosario G, Caja S, Montoya M et al. Fast synthesis and bioconjugation of 68Ga core-doped extremely small iron oxide nanoparticles for PET/MR imaging. Contrast media & molecular imaging. 2016;11(3):203-10.

319. Paik T, Chacko A-M, Mikitsh JL, Friedberg JS, Pryma DA, Murray CB. Shape-controlled synthesis of isotopic yttrium-90-labeled rare earth fluoride nanocrystals for multimodal imaging. ACS nano. 2015;9(9):8718-28.

320. Zhou M, Zhao J, Tian M, Song S, Zhang R, Gupta S et al. Radio-photothermal therapy mediated by a single compartment nanoplatform depletes tumor initiating cells and reduces lung metastasis in the orthotopic 4T1 breast tumor model. Nanoscale. 2015;7(46):19438-47.

321. Chakravarty R, Chakraborty S, Ningthoujam RS, Vimalnath Nair K, Sharma KS, Ballal A et al. Industrial-scale synthesis of intrinsically radiolabeled 64cus nanoparticles for use in positron emission tomography (pet) imaging of cancer. Industrial & Engineering Chemistry Research. 2016;55(48):12407-19.

322. Cai H, Xie F, Mulgaonkar A, Chen L, Sun X, Hsieh J-T et al. Bombesin functionalized 64Cu-copper sulfide nanoparticles for targeted imaging of orthotopic prostate cancer. Nanomedicine. 2018;13(14):1695-705.

323. Ye D, Sultan D, Zhang X, Yue Y, Heo GS, Kothapalli SV et al. Focused ultrasound-enabled delivery of radiolabeled nanoclusters to the pons. Journal of Controlled Release. 2018;283:143-50.

324. Yang M, Huo D, Gilroy KD, Sun X, Sultan D, Luehmann H et al. Facile synthesis of 64Cu-doped Au nanocages for positron emission tomography imaging. ChemNanoMat. 2017;3(1):44-50.

325. Llop J, Jiang P, Marradi M, Gomez-Vallejo V, Echeverria M, Yu S et al. Visualisation of dual radiolabelled poly (lactide-co-glycolide) nanoparticle degradation in vivo using energy-discriminant SPECT. Journal of Materials Chemistry B. 2015;3(30):6293-300.

326. Wang H, Kumar R, Nagesha D, Duclos Jr RI, Sridhar S, Gatley SJ. Integrity of 111In-radiolabeled superparamagnetic iron oxide nanoparticles in the mouse. Nuclear medicine and biology. 2015;42(1):65-70.

327. Black KC, Wang Y, Luehmann HP, Cai X, Xing W, Pang B et al. Radioactive 198Au-doped nanostructures with different shapes for in vivo analyses of their biodistribution, tumor uptake, and intratumoral distribution. ACS nano. 2014;8(5):4385-94.

328. Chanda N, Kan P, Watkinson LD, Shukla R, Zambre A, Carmack TL et al. Radioactive gold nanoparticles in cancer therapy: therapeutic efficacy studies of GA-198AuNP nanoconstruct in

prostate tumor–bearing mice. Nanomedicine: Nanotechnology, Biology and Medicine. 2010;6(2):201-9.

329. Katti K, Khoobchandani M, Thipe V, Al-Yasiri A, Katti K, Loyalka S et al. Prostate tumor therapy advances in nuclear medicine: green nanotechnology toward the design of tumor specific radioactive gold nanoparticles. Journal of Radioanalytical and Nuclear Chemistry. 2018;318(3):1737-47.

330. Wang Y, Liu Y, Luehmann H, Xia X, Wan D, Cutler C et al. Radioluminescent gold nanocages with controlled radioactivity for real-time in vivo imaging. Nano letters. 2013;13(2):581-5.

331. Zhao Y, Pang B, Luehmann H, Detering L, Yang X, Sultan D et al. Gold Nanoparticles Doped with 199Au Atoms and Their Use for Targeted Cancer Imaging by SPECT. Advanced healthcare materials. 2016;5(8):928-35.

332. Zuykov M, Pelletier E, Demers S. Colloidal complexed silver and silver nanoparticles in extrapallial fluid of Mytilus edulis. Marine environmental research. 2011;71(1):17-21.

333. Zhang Z, He X, Zhang H, Ma Y, Zhang P, Ding Y et al. Uptake and distribution of ceria nanoparticles in cucumber plants. Metallomics. 2011;3(8):816-22.

334. Chakravarty R, Chakraborty S, Guleria A, Shukla R, Kumar C, Vimalnath Nair K et al. Facile one-pot synthesis of intrinsically radiolabeled and cyclic RGD conjugated 199Au nanoparticles for potential use in nanoscale brachytherapy. Industrial & Engineering Chemistry Research. 2018;57(43):14337-46.

335. Pang B, Zhao Y, Luehmann H, Yang X, Detering L, You M et al. 64Cu-Doped PdCu@ Au tripods: a multifunctional nanomaterial for positron emission tomography and image-guided photothermal cancer treatment. ACS nano. 2016;10(3):3121-31.

336. Woodward J, Kennel SJ, Stuckey A, Osborne D, Wall J, Rondinone AJ et al. LaPO4 nanoparticles doped with actinium-225 that partially sequester daughter radionuclides. Bioconjugate chemistry. 2011;22(4):766-76.

337. McLaughlin MF, Robertson D, Pevsner PH, Wall JS, Mirzadeh S, Kennel SJ. LnPO4 nanoparticles doped with Ac-225 and sequestered daughters for targeted alpha therapy. Cancer Biotherapy and Radiopharmaceuticals. 2014;29(1):34-41.

338. McLaughlin MF, Woodward J, Boll RA, Wall JS, Rondinone AJ, Kennel SJ et al. Gold coated lanthanide phosphate nanoparticles for targeted alpha generator radiotherapy. PLoS One. 2013;8(1).

339. Rojas J, Woodward J, Chen N, Rondinone A, Castano C, Mirzadeh S. Synthesis and characterization of lanthanum phosphate nanoparticles as carriers for 223Ra and 225Ra for targeted alpha therapy. Nuclear medicine and biology. 2015;42(7):614-20.

340. Cipreste MF, Peres AM, Cotta AA, Aragón FH, Antunes AdM, Leal AS et al. Synthesis and characterization of 159Gd-doped hydroxyapatite nanorods for bioapplications as theranostic systems. Materials Chemistry and Physics. 2016;181:301-11.

341. Lipka J, Semmler-Behnke M, Sperling RA, Wenk A, Takenaka S, Schleh C et al. Biodistribution of PEG-modified gold nanoparticles following intratracheal instillation and intravenous injection. Biomaterials. 2010;31(25):6574-81.

342. Munaweera I, Shi Y, Koneru B, Saez R, Aliev A, Di Pasqua AJ et al. Chemoradiotherapeutic magnetic nanoparticles for targeted treatment of nonsmall cell lung cancer. Molecular pharmaceutics. 2015;12(10):3588-96.

343. Soltani F, Samani AB, Sadeghi M, Arani SS, Yavari K. Production of cerium-141 using ceria and nanoceria powder: a potential radioisotope for simultaneous therapeutic and diagnostic applications. Journal of Radioanalytical and Nuclear Chemistry. 2015;303(1):385-91.

344. Hildebrand H, Schymura S, Holzwarth U, Gibson N, Dalmiglio M, Franke K. Strategies for radiolabeling of commercial TiO 2 nanopowder as a tool for sensitive nanoparticle detection in complex matrices. Journal of Nanoparticle Research. 2015;17(6):278.

345. Simonelli F, Marmorato P, Abbas K, Ponti J, Kozempel J, Holzwarth U et al. Cyclotron Production of Radioactive ${\hbox {CeO}} _ {2} $ Nanoparticles and Their Application for In Vitro Uptake Studies. IEEE transactions on nanobioscience. 2011;10(1):44-50.

346. Kreyling WG, Abdelmonem AM, Ali Z, Alves F, Geiser M, Haberl N et al. In vivo integrity of polymer-coated gold nanoparticles. Nature nanotechnology. 2015;10(7):619.

347. Rambanapasi C, Barnard N, Grobler A, Buntting H, Sonopo M, Jansen D et al. Dual radiolabeling as a technique to track nanocarriers: the case of gold nanoparticles. Molecules. 2015;20(7):12863-79.

348. Hirn S, Semmler-Behnke M, Schleh C, Wenk A, Lipka J, Schäffler M et al. Particle size-dependent and surface charge-dependent biodistribution of gold nanoparticles after intravenous administration. European journal of pharmaceutics and biopharmaceutics. 2011;77(3):407-16.

349. Schleh C, Holzwarth U, Hirn S, Wenk A, Simonelli F, Schäffler M et al. Biodistribution of inhaled gold nanoparticles in mice and the influence of surfactant protein D. Journal of aerosol medicine and pulmonary drug delivery. 2013;26(1):24-30.

350. Schleh C, Semmler-Behnke M, Lipka J, Wenk A, Hirn S, Schäffler M et al. Size and surface charge of gold nanoparticles determine absorption across intestinal barriers and accumulation in secondary target organs after oral administration. Nanotoxicology. 2012;6(1):36-46.

351. Melnik E, Demin V, Demin V, Gmoshinski I, Tyshko N, Tutelyan V. Transfer of silver nanoparticles through the placenta and breast milk during in vivo experiments on rats. Acta Naturae (англоязычная версия). 2013;5(3 (18)).

352. Oughton DH, Hertel-Aas T, Pellicer E, Mendoza E, Joner EJ. Neutron activation of engineered nanoparticles as a tool for tracing their environmental fate and uptake in organisms. Environmental Toxicology and Chemistry: An International Journal. 2008;27(9):1883-7.

353. Cohen JM, Derk R, Wang L, Godleski J, Kobzik L, Brain J et al. Tracking translocation of industrially relevant engineered nanomaterials (ENMs) across alveolar epithelial monolayers in vitro. Nanotoxicology. 2014;8(sup1):216-25.

354. He X, Zhang H, Ma Y, Bai W, Zhang Z, Lu K et al. Lung deposition and extrapulmonary translocation of nano-ceria after intratracheal instillation. Nanotechnology. 2010;21(28):285103.

355. Zhang P, He X, Ma Y, Lu K, Zhao Y, Zhang Z. Distribution and bioavailability of ceria nanoparticles in an aquatic ecosystem model. Chemosphere. 2012;89(5):530-5.

356. Yeh T-K, Chen J-K, Lin C-H, Yang M-H, Yang CS, Chou F-I et al. Kinetics and tissue distribution of neutron-activated zinc oxide nanoparticles and zinc nitrate in mice: effects of size and particulate nature. Nanotechnology. 2012;23(8):085102.

357. Pérez-Campaña C, Gómez-Vallejo V, Puigivila M, Martín A, Calvo-Fernández T, Moya SE et al. Biodistribution of different sized nanoparticles assessed by positron emission tomography: a general strategy for direct activation of metal oxide particles. ACS nano. 2013;7(4):3498-505.

358. Pérez-Campaña C, Sansaloni F, Gómez-Vallejo V, Baz Z, Martin A, Moya SE et al. Production of 18F-labeled titanium dioxide nanoparticles by proton irradiation for biodistribution

and biological fate studies in rats. Particle & Particle Systems Characterization. 2014;31(1):134-42.

359. Hildebrand H, Franke K. A new radiolabeling method for commercial Ag 0 nanopowder with 110m Ag for sensitive nanoparticle detection in complex media. Journal of Nanoparticle Research. 2012;14(10):1142.

360. Hoffman D, Sun M, Yang L, McDonagh PR, Corwin F, Sundaresan G et al. Intrinsically radiolabelled [59Fe]-SPIONs for dual MRI/radionuclide detection. American journal of nuclear medicine and molecular imaging. 2014;4(6):548.

361. Freund B, Tromsdorf UI, Bruns OT, Heine M, Giemsa A, Bartelt A et al. A simple and widely applicable method to 59Fe-radiolabel monodisperse superparamagnetic iron oxide nanoparticles for in vivo quantification studies. ACS nano. 2012;6(8):7318-25.

362. Pospisilova M, Zapotocky V, Nesporova K, Laznicek M, Laznickova A, Zidek O et al. Preparation and biodistribution of 59 Fe-radiolabelled iron oxide nanoparticles. Journal of Nanoparticle Research. 2017;19(2):80.

363. Liu Y, Sun Y, Cao C, Yang Y, Wu Y, Ju D et al. Long-term biodistribution in vivo and toxicity of radioactive/magnetic hydroxyapatite nanorods. Biomaterials. 2014;35(10):3348-55.

364. Shi S, Fliss BC, Gu Z, Zhu Y, Hong H, Valdovinos HF et al. Chelator-free labeling of layered double hydroxide nanoparticles for in vivo PET imaging. Scientific reports. 2015;5:16930.

365. Cędrowska E, Pruszynski M, Majkowska-Pilip A, Męczyńska-Wielgosz S, Bruchertseifer F, Morgenstern A et al. Functionalized TiO2 nanoparticles labelled with 225Ac for targeted alpha radionuclide therapy. Journal of Nanoparticle Research. 2018;20(3):83. doi:10.1007/s11051-018-4181-y.

366. Lee SB, Ahn SB, Lee S-W, Jeong SY, Ghilsuk Y, Ahn B-C et al. Radionuclide-embedded gold nanoparticles for enhanced dendritic cell-based cancer immunotherapy, sensitive and quantitative tracking of dendritic cells with PET and Cerenkov luminescence. NPG Asia Materials. 2016;8(6):e281-e.

367. Lee SB, Lee S-W, Jeong SY, Yoon G, Cho SJ, Kim SK et al. Engineering of radioiodine-labeled gold core–shell nanoparticles as efficient nuclear medicine imaging agents for trafficking of dendritic cells. ACS applied materials & interfaces. 2017;9(10):8480-9.

368. Liu T, Shi S, Liang C, Shen S, Cheng L, Wang C et al. Iron oxide decorated MoS2 nanosheets with double PEGylation for chelator-free radiolabeling and multimodal imaging guided photothermal therapy. ACS nano. 2015;9(1):950-60.

369. Rosenblum D, Joshi N, Tao W, Karp JM, Peer D. Progress and challenges towards targeted delivery of cancer therapeutics. Nat Commun. 2018;9(1):1410. doi:10.1038/s41467-018-03705-y.

370. Choi MH, Shim H-E, Yun S-J, Park S-H, Choi DS, Jang B-S et al. Gold-Nanoparticle-Immobilized Desalting Columns for Highly Efficient and Specific Removal of Radioactive Iodine in Aqueous Media. ACS Applied Materials & Interfaces. 2016;8(43):29227-31. doi:10.1021/acsami.6b11136.

371. Choi MH, Jeong S-W, Shim HE, Yun S-J, Mushtaq S, Choi DS et al. Efficient bioremediation of radioactive iodine using biogenic gold nanomaterial-containing radiation-resistant bacterium, Deinococcus radiodurans R1. Chemical Communications. 2017;53(28):3937-40. doi:10.1039/C7CC00720E.

372. Mushtaq S, Yun S-J, Yang JE, Jeong S-W, Shim HE, Choi MH et al. Efficient and selective removal of radioactive iodine anions using engineered nanocomposite membranes. Environmental Science: Nano. 2017;4(11):2157-63. doi:10.1039/C7EN00759K.

373. Ho TL. 1 - Introduction. In: Ho T-L, editor. Hard and soft acids and bases principle in organic chemistry. Academic Press; 1977. p. 1-3.

374. Chakravarty R, Ashutosh D, Weibo C. Radiolabeled inorganic nanoparticles for positron emission tomography imaging of cancer: an overview. The quarterly journal of nuclear medicine and molecular imaging: official publication of the Italian Association of Nuclear Medicine (AIMN)[and] the International Association of Radiopharmacology (IAR),[and] Section of the Society of. 2017;61(2):181.

375. Kalantar-zadeh K, Ou JZ, Daeneke T, Strano MS, Pumera M, Gras SL. Two-dimensional transition metal dichalcogenides in biosystems. Advanced Functional Materials. 2015;25(32):5086-99.

376. Sun X, Cai W, Chen X. Positron emission tomography imaging using radiolabeled inorganic nanomaterials. Accounts of chemical research. 2015;48(2):286-94.

377. Zhou M, Zhang R, Huang M, Lu W, Song S, Melancon MP et al. A chelator-free multifunctional [64Cu] CuS nanoparticle platform for simultaneous micro-PET/CT imaging and

photothermal ablation therapy. Journal of the American Chemical Society. 2010;132(43):15351-8.

378. Jelley NA. Fundamentals of nuclear physics. Cambridge University Press; 1990.

379. Gibson N, Holzwarth U, Abbas K, Simonelli F, Kozempel J, Cydzik I et al. Radiolabelling of engineered nanoparticles for in vitro and in vivo tracing applications using cyclotron accelerators. Archives of toxicology. 2011;85(7):751.

380. Adeyemi JA, Machado ART, Ogunjimi AT, Alberici LC, Antunes LMG, Barbosa F, Jr. Cytotoxicity, mutagenicity, oxidative stress and mitochondrial impairment in human hepatoma (HepG2) cells exposed to copper oxide, copper-iron oxide and carbon nanoparticles. Ecotoxicol Environ Saf. 2020;189:109982. doi:10.1016/j.ecoenv.2019.109982.

381. Travis LB, Hauptmann M, Gaul LK, Storm HH, Goldman MB, Nyberg U et al. Site-specific cancer incidence and mortality after cerebral angiography with radioactive thorotrast. Radiat Res. 2003;160(6):691-706. doi:10.1667/rr3095.

382. Nguyen VH, Lee BJ. Protein corona: a new approach for nanomedicine design. Int J Nanomedicine. 2017;12:3137-51. doi:10.2147/IJN.S129300.

383. Wilhelm S, Tavares AJ, Dai Q, Ohta S, Audet J, Dvorak HF et al. Analysis of nanoparticle delivery to tumours. Nat Rev Mater. 2016;1(5). doi:10.1038/natrevmats.2016.14.

384. Tenzer S, Docter D, Kuharev J, Musyanovych A, Fetz V, Hecht R et al. Rapid formation of plasma protein corona critically affects nanoparticle pathophysiology. Nat Nanotechnol. 2013;8(10):772-81. doi:10.1038/nnano.2013.181.

385. Ashby J, Pan S, Zhong W. Size and surface functionalization of iron oxide nanoparticles influence the composition and dynamic nature of their protein corona. ACS Appl Mater Interfaces. 2014;6(17):15412-9. doi:10.1021/am503909q.

386. Mahmoudi M, Sheibani S, Milani AS, Rezaee F, Gauberti M, Dinarvand R et al. Crucial role of the protein corona for the specific targeting of nanoparticles. Nanomedicine (Lond). 2015;10(2):215-26. doi:10.2217/nnm.14.69.

387. Boselli L, Polo E, Castagnola V, Dawson KA. Regimes of Biomolecular Ultrasmall Nanoparticle Interactions. Angew Chem Int Ed Engl. 2017;56(15):4215-8. doi:10.1002/anie.201700343.

388. Bastus NG, Casals E, Ojea I, Varon M, Puntes V. The Reactivity of Colloidal Inorganic Nanoparticles. Delivery of Nanoparticles. 2012:377-400. doi:Book_Doi 10.5772/2647.

389. Choi HS, Liu W, Misra P, Tanaka E, Zimmer JP, Itty Ipe B et al. Renal clearance of quantum dots. Nat Biotechnol. 2007;25(10):1165-70. doi:10.1038/nbt1340.

390. Wong OA, Hansen RJ, Ni TW, Heinecke CL, Compel WS, Gustafson DL et al. Structure-activity relationships for biodistribution, pharmacokinetics, and excretion of atomically precise nanoclusters in a murine model. Nanoscale. 2013;5(21):10525-33. doi:10.1039/c3nr03121g.

391. Julien DC, Behnke S, Wang G, Murdoch GK, Hill RA. Utilization of monoclonal antibody-targeted nanomaterials in the treatment of cancer. MAbs. 2011;3(5):467-78. doi:10.4161/mabs.3.5.16089.

392. Hoshyar N, Gray S, Han H, Bao G. The effect of nanoparticle size on in vivo pharmacokinetics and cellular interaction. Nanomedicine (Lond). 2016;11(6):673-92. doi:10.2217/nnm.16.5.

393. Yang G, Phua SZF, Bindra AK, Zhao Y. Degradability and Clearance of Inorganic Nanoparticles for Biomedical Applications. Adv Mater. 2019;31(10):e1805730. doi:10.1002/adma.201805730.

394. Shreffler JW, Pullan JE, Dailey KM, Mallik S, Brooks AE. Overcoming Hurdles in Nanoparticle Clinical Translation: The Influence of Experimental Design and Surface Modification. Int J Mol Sci. 2019;20(23). doi:10.3390/ijms20236056.

395. Luehmann HP, Pressly ED, Detering L, Wang C, Pierce R, Woodard PK et al. PET/CT imaging of chemokine receptor CCR5 in vascular injury model using targeted nanoparticle. Journal of nuclear medicine. 2014;55(4):629-34.

396. Peer D, Karp JM, Hong S, Farokhzad OC, Margalit R, Langer R. Nanocarriers as an emerging platform for cancer therapy. Nature Nanotechnology. 2007;2(12):751-60. doi:10.1038/nnano.2007.387.

397. Suk JS, Xu Q, Kim N, Hanes J, Ensign LM. PEGylation as a strategy for improving nanoparticle-based drug and gene delivery. Advanced Drug Delivery Reviews. 2016;99(Pt A):28-51. doi:10.1016/j.addr.2015.09.012.

398. Zhao Y, Detering L, Sultan D, Cooper ML, You M, Cho S et al. Gold Nanoclusters Doped with (64)Cu for CXCR4 Positron Emission Tomography Imaging of Breast Cancer and Metastasis. ACS Nano. 2016;10(6):5959-70. doi:10.1021/acsnano.6b01326.

399. Heo GS, Zhao Y, Sultan D, Zhang X, Detering L, Luehmann HP et al. Assessment of Copper Nanoclusters for Accurate in Vivo Tumor Imaging and Potential for Translation. ACS Appl Mater Interfaces. 2019;11(22):19669-78. doi:10.1021/acsami.8b22752.

400. Zhou C, Hao G, Thomas P, Liu J, Yu M, Sun S et al. Near-infrared emitting radioactive gold nanoparticles with molecular pharmacokinetics. Angewandte Chemie International Edition. 2012;51(40):10118-22.

401. Chen X, Qiu X, Hou M, Wu X, Dong Y, Ma Y et al. Differences in zwitterionic sulfobetaine and carboxybetaine dextran-based hydrogels. Langmuir. 2018;35(5):1475-82.

402. Moyano DF, Saha K, Prakash G, Yan B, Kong H, Yazdani M et al. Fabrication of corona-free nanoparticles with tunable hydrophobicity. ACS Nano. 2014;8(7):6748-55. doi:10.1021/nn5006478.

403. Jiang X, Du B, Huang Y, Zheng J. Ultrasmall noble metal nanoparticles: Breakthroughs and biomedical implications. Nano today. 2018;21:106-25.

404. Safavi-Sohi R, Maghari S, Raoufi M, Jalali SA, Hajipour MJ, Ghassempour A et al. Bypassing Protein Corona Issue on Active Targeting: Zwitterionic Coatings Dictate Specific Interactions of Targeting Moieties and Cell Receptors. ACS Appl Mater Interfaces. 2016;8(35):22808-18. doi:10.1021/acsami.6b05099.

405. Hao G, Zhou J, Guo Y, Long MA, Anthony T, Stanfield J et al. A cell permeable peptide analog as a potential-specific PET imaging probe for prostate cancer detection. Amino Acids. 2011;41(5):1093-101.

406. Yang S, Sun S, Zhou C, Hao G, Liu J, Ramezani S et al. Renal clearance and degradation of glutathione-coated copper nanoparticles. Bioconjug Chem. 2015;26(3):511-9. doi:10.1021/acs.bioconjchem.5b00003.

407. Oh JY, Kim HS, Palanikumar L, Go EM, Jana B, Park SA et al. Cloaking nanoparticles with protein corona shield for targeted drug delivery. Nature Communications. 2018;9(1):4548. doi:10.1038/s41467-018-06979-4.

408. Cagliani R, Gatto F, Bardi G. Protein Adsorption: A Feasible Method for Nanoparticle Functionalization? Materials (Basel). 2019;12(12):1991. doi:10.3390/ma12121991.

409. Schaffler M, Sousa F, Wenk A, Sitia L, Hirn S, Schleh C et al. Blood protein coating of gold nanoparticles as potential tool for organ targeting. Biomaterials. 2014;35(10):3455-66. doi:10.1016/j.biomaterials.2013.12.100.

410. Homayun B, Lin X, Choi H-J. Challenges and recent progress in oral drug delivery systems for biopharmaceuticals. Pharmaceutics. 2019;11(3):129. doi:10.3390/pharmaceutics11030129.
411. Paudel KS, Milewski M, Swadley CL, Brogden NK, Ghosh P, Stinchcomb AL. Challenges and opportunities in dermal/transdermal delivery. Therapeutic Delivery. 2010;1(1):109-31. doi:10.4155/tde.10.16.
412. Moeendarbari S, Tekade R, Mulgaonkar A, Christensen P, Ramezani S, Hassan G et al. Theranostic Nanoseeds for Efficacious Internal Radiation Therapy of Unresectable Solid Tumors. Sci Rep. 2016;6:20614. doi:10.1038/srep20614.
413. Howell M, Wang C, Mahmoud A, Hellermann G, Mohapatra SS, Mohapatra S. Dual-function theranostic nanoparticles for drug delivery and medical imaging contrast: perspectives and challenges for use in lung diseases. Drug Delivery and Translational Research. 2013;3(4):352-63. doi:10.1007/s13346-013-0132-4.
414. Ramanathan S, Archunan G, Sivakumar M, Tamil Selvan S, Fred AL, Kumar S et al. Theranostic applications of nanoparticles in neurodegenerative disorders. International Journal of Nanomedicine. 2018;13:5561-76. doi:10.2147/IJN.S149022.
415. Zhang S, Gao H, Bao G. Physical Principles of Nanoparticle Cellular Endocytosis. ACS Nano. 2015;9(9):8655-71. doi:10.1021/acsnano.5b03184.
416. Nam J, Won N, Bang J, Jin H, Park J, Jung S et al. Surface engineering of inorganic nanoparticles for imaging and therapy. Adv Drug Deliv Rev. 2013;65(5):622-48. doi:10.1016/j.addr.2012.08.015.
417. Bertrand N, Wu J, Xu X, Kamaly N, Farokhzad OC. Cancer nanotechnology: the impact of passive and active targeting in the era of modern cancer biology. Adv Drug Deliv Rev. 2014;66:2-25. doi:10.1016/j.addr.2013.11.009.
418. Matsumura Y, Maeda H. A new concept for macromolecular therapeutics in cancer chemotherapy: mechanism of tumoritropic accumulation of proteins and the antitumor agent smancs. Cancer Res. 1986;46(12 Pt 1):6387-92.
419. De Jong WH, Hagens WI, Krystek P, Burger MC, Sips AJ, Geertsma RE. Particle size-dependent organ distribution of gold nanoparticles after intravenous administration. Biomaterials. 2008;29(12):1912-9. doi:10.1016/j.biomaterials.2007.12.037.

420. Du B, Jiang X, Das A, Zhou Q, Yu M, Jin R et al. Glomerular barrier behaves as an atomically precise bandpass filter in a sub-nanometre regime. Nat Nanotechnol. 2017;12(11):1096-102. doi:10.1038/nnano.2017.170.

421. Kettler K, Veltman K, van de Meent D, van Wezel A, Hendriks AJ. Cellular uptake of nanoparticles as determined by particle properties, experimental conditions, and cell type. Environ Toxicol Chem. 2014;33(3):481-92. doi:10.1002/etc.2470.

422. Overchuk M, Zheng G. Overcoming obstacles in the tumor microenvironment: Recent advancements in nanoparticle delivery for cancer theranostics. Biomaterials. 2018;156:217-37. doi:10.1016/j.biomaterials.2017.10.024.

423. Haute DV, Berlin JM. Challenges in realizing selectivity for nanoparticle biodistribution and clearance: lessons from gold nanoparticles. Ther Deliv. 2017;8(9):763-74. doi:10.4155/tde-2017-0057.

424. Cornelissen B. Imaging the inside of a tumour: a review of radionuclide imaging and theranostics targeting intracellular epitopes. J Labelled Comp Radiopharm. 2014;57(4):310-6. doi:10.1002/jlcr.3152.

425. Zarschler K, Rocks L, Licciardello N, Boselli L, Polo E, Garcia KP et al. Ultrasmall inorganic nanoparticles: State-of-the-art and perspectives for biomedical applications. Nanomedicine. 2016;12(6):1663-701. doi:10.1016/j.nano.2016.02.019.

426. Albanese A, Tang PS, Chan WC. The effect of nanoparticle size, shape, and surface chemistry on biological systems. Annu Rev Biomed Eng. 2012;14:1-16. doi:10.1146/annurev-bioeng-071811-150124.

427. Pearce AK, O’Reilly RK. Insights into active targeting of nanoparticles in drug delivery: advances in clinical studies and design considerations for cancer nanomedicine. Bioconjugate chemistry. 2019;30(9):2300-11.

428. Huang H-C, Barua S, Sharma G, Dey SK, Rege K. Inorganic nanoparticles for cancer imaging and therapy. Journal of controlled Release. 2011;155(3):344-57.

429. Attia MF, Anton N, Wallyn J, Omran Z, Vandamme TF. An overview of active and passive targeting strategies to improve the nanocarriers efficiency to tumour sites. Journal of Pharmacy and Pharmacology. 2019;71(8):1185-98.

430. Li P-C, Wang C-RC, Shieh D-B, Wei C-W, Liao C-K, Poe C et al. In vivo photoacoustic molecular imaging with simultaneous multiple selective targeting using antibody-conjugated gold nanorods. Optics Express. 2008;16(23):18605-15.

431. Kim C, Cho EC, Chen J, Song KH, Au L, Favazza C et al. In vivo molecular photoacoustic tomography of melanomas targeted by bioconjugated gold nanocages. ACS nano. 2010;4(8):4559-64.

432. Pellico J, Lechuga-Vieco AV, Almarza E, Hidalgo A, Mesa-Nunez C, Fernandez-Barahona I et al. In vivo imaging of lung inflammation with neutrophil-specific (68)Ga nano-radiotracer. Sci Rep. 2017;7(1):13242. doi:10.1038/s41598-017-12829-y.

433. Pellico J, Fernández-Barahona I, Benito M, Gaitán-Simón Á, Gutiérrez L, Ruiz-Cabello J et al. Unambiguous detection of atherosclerosis using bioorthogonal nanomaterials. Nanomedicine: Nanotechnology, Biology and Medicine. 2019;17:26-35.

434. Ruggiero A, Villa CH, Bander E, Rey DA, Bergkvist M, Batt CA et al. Paradoxical glomerular filtration of carbon nanotubes. Proceedings of the National Academy of Sciences. 2010;107(27):12369-74.

435. Xu J, Peng C, Yu M, Zheng J. Renal clearable noble metal nanoparticles: photoluminescence, elimination, and biomedical applications. Wiley Interdisciplinary Reviews: Nanomedicine and Nanobiotechnology. 2017;9(5):e1453.

436. Venkatachalam MA, Rennke HG. The structural and molecular basis of glomerular filtration. Circ Res. 1978;43(3):337-47. doi:10.1161/01.res.43.3.337.

437. Liang X, Wang H, Zhu Y, Zhang R, Cogger VC, Liu X et al. Short- and Long-Term Tracking of Anionic Ultrasmall Nanoparticles in Kidney. ACS Nano. 2016;10(1):387-95. doi:10.1021/acsnano.5b05066.

438. Yu M, Zheng J. Clearance Pathways and Tumor Targeting of Imaging Nanoparticles. ACS Nano. 2015;9(7):6655-74. doi:10.1021/acsnano.5b01320.

439. Lin F-S, Chen C-H, Tseng F-G, Hwu Y, Chen J-K, Lin S-Y et al. Radiotherapy of the Excretable Radioactive Gold Nanocomposite with Intratumoral Injection. International Journal of Materials, Mechanics and Manufacturing. 2013:265-8. doi:10.7763/ijmmm.2013.V1.56.

440. Lasser A. The mononuclear phagocytic system: a review. Human pathology. 1983;14(2):108-26.

441. Nelson PJ, Rees AJ, Griffin MD, Hughes J, Kurts C, Duffield J. The renal mononuclear phagocytic system. Journal of the American Society of Nephrology. 2012;23(2):194-203.

442. Bronte V, Pittet MJ. The spleen in local and systemic regulation of immunity. Immunity. 2013;39(5):806-18.

443. Blanco E, Shen H, Ferrari M. Principles of nanoparticle design for overcoming biological barriers to drug delivery. Nature biotechnology. 2015;33(9):941.

444. Patra JK, Das G, Fraceto LF, Campos EVR, del Pilar Rodriguez-Torres M, Acosta-Torres LS et al. Nano based drug delivery systems: recent developments and future prospects. Journal of nanobiotechnology. 2018;16(1):71.

445. Hoshyar N, Gray S, Han H, Bao G. The effect of nanoparticle size on in vivo pharmacokinetics and cellular interaction. Nanomedicine. 2016;11(6):673-92.

446. Harris JM, Chess RB. Effect of pegylation on pharmaceuticals. Nature reviews Drug discovery. 2003;2(3):214-21.

447. Li S-D, Huang L. Nanoparticles evading the reticuloendothelial system: role of the supported bilayer. Biochimica et Biophysica Acta (BBA)-Biomembranes. 2009;1788(10):2259-66.

448. Bartlett DW, Su H, Hildebrandt IJ, Weber WA, Davis ME. Impact of tumor-specific targeting on the biodistribution and efficacy of siRNA nanoparticles measured by multimodality in vivo imaging. Proceedings of the National Academy of Sciences. 2007;104(39):15549-54.

449. Zhang YN, Poon W, Tavares AJ, McGilvray ID, Chan WCW. Nanoparticle-liver interactions: Cellular uptake and hepatobiliary elimination. J Control Release. 2016;240:332-48. doi:10.1016/j.jconrel.2016.01.020.

450. Soenen SJ, Parak WJ, Rejman J, Manshian B. (Intra)cellular stability of inorganic nanoparticles: effects on cytotoxicity, particle functionality, and biomedical applications. Chem Rev. 2015;115(5):2109-35. doi:10.1021/cr400714j.

451. Speisky H, López-Alarcón C, Olea-Azar C, Sandoval-Acuña C, Aliaga ME. Role of superoxide anions in the redox changes affecting the physiologically occurring Cu(II)-glutathione complex. Bioinorganic Chemistry and Applications. 2011;2011:674149. doi:10.1155/2011/674149.

452. Kim B-E, Nevitt T, Thiele DJ. Mechanisms for copper acquisition, distribution and regulation. Nature chemical biology. 2008;4(3):176.

453. Gaetke LM, Chow-Johnson HS, Chow CK. Copper: toxicological relevance and mechanisms. Archives of toxicology. 2014;88(11):1929-38.

454. Abbaspour N, Hurrell R, Kelishadi R. Review on iron and its importance for human health. Journal of research in medical sciences: the official journal of Isfahan University of Medical Sciences. 2014;19(2):164.

455. Wallace DF. The regulation of iron absorption and homeostasis. The Clinical Biochemist Reviews. 2016;37(2):51.

456. Kanwar P, Kowdley KV. Metal storage disorders: Wilson disease and hemochromatosis. Medical Clinics. 2014;98(1):87-102.

457. Engwa GA, Ferdinand PU, Nwalo FN, Unachukwu MN. Mechanism and health effects of heavy metal toxicity in humans. Poisoning in the Modern World-New Tricks for an Old Dog? : IntechOpen; 2019.

458. Ajdary M, Moosavi MA, Rahmati M, Falahati M, Mahboubi M, Mandegary A et al. Health concerns of various nanoparticles: A review of their in vitro and in vivo toxicity. Nanomaterials. 2018;8(9):634.

459. Ferreira CR, Gahl WA. Disorders of metal metabolism. Translational science of rare diseases. 2017;2(3-4):101-39.

460. Schieda N, Blaichman JI, Costa AF, Glikstein R, Hurrell C, James M et al. Gadolinium-based contrast agents in kidney disease: a comprehensive review and clinical practice guideline issued by the Canadian Association of Radiologists. Canadian journal of kidney health and disease. 2018;5:2054358118778573.

461. Boyd AS, Zic JA, Abraham JL. Gadolinium deposition in nephrogenic fibrosing dermopathy. Journal of the American Academy of Dermatology. 2007;56(1):27-30.

462. Marckmann P, Skov L, Rossen K, Dupont A, Damholt MB, Heaf JG et al. Nephrogenic systemic fibrosis: suspected causative role of gadodiamide used for contrast-enhanced magnetic resonance imaging. Journal of the American Society of Nephrology. 2006;17(9):2359-62.

463. Sharapa DI, Doronkin DE, Studt F, Grunwaldt JD, Behrens S. Moving Frontiers in Transition Metal Catalysis: Synthesis, Characterization and Modeling. Advanced Materials. 2019;31(26):1807381.

464. Cargnello M. Colloidal Nanocrystals as Building Blocks for Well-Defined Heterogeneous Catalysts. Chemistry of Materials. 2019;31(3):576-96.

465. Ranjbar Bahadori S, Mulgaonkar A, Hart R, Wu CY, Zhang D, Pillai A et al. Radiolabeling strategies and pharmacokinetic studies for metal based nanotheranostics. Wiley Interdisciplinary Reviews: Nanomedicine and Nanobiotechnology. 2020:e1671.

466. Liang M, Yan X. Nanozymes: from new concepts, mechanisms, and standards to applications. Accounts of chemical research. 2019;52(8):2190-200.

467. Huang Y, Ren J, Qu X. Nanozymes: classification, catalytic mechanisms, activity regulation, and applications. Chemical reviews. 2019;119(6):4357-412.

468. Losch P, Huang W, Goodman ED, Wrasman CJ, Holm A, Riscoe AR et al. Colloidal nanocrystals for heterogeneous catalysis. Nano Today. 2019;24:15-47.

469. Ranjbar Bahadori S, Hart R, Hao Y-W. Synthesis of cobalt, palladium, and rhenium nanoparticles. Tungsten. 2020;2(3):261-88. doi:10.1007/s42864-020-00057-3.

470. Cushing BL, Kolesnichenko VL, O'connor CJ. Recent advances in the liquid-phase syntheses of inorganic nanoparticles. Chemical reviews. 2004;104(9):3893-946.

471. Turkevich J, Kim G. Palladium: preparation and catalytic properties of particles of uniform size. Science. 1970;169(3948):873-9.

472. Turkevich J, Stevenson PC, Hillier J. A study of the nucleation and growth processes in the synthesis of colloidal gold. Discussions of the Faraday Society. 1951;11:55-75.

473. Ji X, Song X, Li J, Bai Y, Yang W, Peng X. Size control of gold nanocrystals in citrate reduction: the third role of citrate. Journal of the American Chemical Society. 2007;129(45):13939-48.

474. Piella J, Bastús NG, Puntes V. Size-Controlled Synthesis of Sub-10-nanometer Citrate-Stabilized Gold Nanoparticles and Related Optical Properties. Chemistry of Materials. 2016;28(4):1066-75.

475. Bastús NG, Comenge J, Puntes V. Kinetically controlled seeded growth synthesis of citrate-stabilized gold nanoparticles of up to 200 nm: size focusing versus Ostwald ripening. Langmuir. 2011;27(17):11098-105.

476. Bastús NG, Merkoçi F, Piella J, Puntes V. Synthesis of highly monodisperse citrate-stabilized silver nanoparticles of up to 200 nm: kinetic control and catalytic properties. Chemistry of Materials. 2014;26(9):2836-46.

477. Sun S, Murray C. Synthesis of monodisperse cobalt nanocrystals and their assembly into magnetic superlattices. Journal of applied Physics. 1999;85(8):4325-30.

478. van Embden J, Chesman AS, Jasieniak JJ. The heat-up synthesis of colloidal nanocrystals. Chemistry of Materials. 2015;27(7):2246-85.

479. Sun S, Murray CB, Weller D, Folks L, Moser A. Monodisperse FePt nanoparticles and ferromagnetic FePt nanocrystal superlattices. science. 2000;287(5460):1989-92.

480. Park J, An K, Hwang Y, Park J-G, Noh H-J, Kim J-Y et al. Ultra-large-scale syntheses of monodisperse nanocrystals. Nature materials. 2004;3(12):891-5.

481. Cargnello M, Doan-Nguyen VV, Murray CB. Engineering uniform nanocrystals: Mechanism of formation and self-assembly into bimetallic nanocrystal superlattices. AIChE Journal. 2016;62(2):392-8.

482. Rossotti FJ, Rossotti H. The determination of stability constants: and other equilibrium constants in solution: McGraw-Hill1961.

483. Eivazihollagh A. Metal-Chelate Complexes in Alkaline Solution: On Recovery Techniques and Cellulose-based Hybrid Material Synthesis: Mid Sweden University; 2018.

484. Dwyer F. Chelating agents and metal chelates. Elsevier; 2012.

485. Morgan GT, Drew HDK. CLXII.—Researches on residual affinity and co-ordination. Part II. Acetylacetones of selenium and tellurium. Journal of the Chemical Society, Transactions. 1920;117:1456-65.

486. Flora SJ, Pachauri V. Chelation in metal intoxication. International journal of environmental research and public health. 2010;7(7):2745-88.

487. Nowack B, Schulin R, Robinson BH. Critical assessment of chelant-enhanced metal phytoextraction. Environmental Science & Technology. 2006;40(17):5225-32.

488. Eivazihollagh A, Svanedal I, Edlund H, Norgren M. On chelating surfactants: molecular perspectives and application prospects. Journal of Molecular Liquids. 2019;278:688-705.

489. Perrin DD. Stability constants of metal-ion complexes: organic ligands. vol 22. Pergamon; 1979.

490. Martell AE, Smith RM. Critical Stability Constants 5. First Supplement. Springer; 1982.

491. Martell AE, Smith RM. Critical stability constants. Springer; 1974.

492. Gao Y, Torrente-Murciano L. Mechanistic insights of the reduction of gold salts in the Turkevich protocol. Nanoscale. 2020;12(4):2740-51.

493. Kimling J, Maier M, Okenve B, Kotaidis V, Ballot H, Plech A. Turkevich method for gold nanoparticle synthesis revisited. The Journal of Physical Chemistry B. 2006;110(32):15700-7.

494. Tyagi H, Kushwaha A, Kumar A, Aslam M. A facile pH controlled citrate-based reduction method for gold nanoparticle synthesis at room temperature. Nanoscale research letters. 2016;11(1):362.

495. Ojea-Jiménez I, Campanera JM. Molecular modeling of the reduction mechanism in the citrate-mediated synthesis of gold nanoparticles. The Journal of Physical Chemistry C. 2012;116(44):23682-91.

496. Agunloye E, Panariello L, Gavriilidis A, Mazzei L. A model for the formation of gold nanoparticles in the citrate synthesis method. Chemical Engineering Science. 2018;191:318-31.

497. Lide DR. CRC handbook of chemistry and physics. CRC press; 2004.

498. Greenwood NN, Earnshaw A. Chemistry of the Elements. Elsevier; 2012.

499. Vanysek P. Electrochemical series. CRC handbook of chemistry and physics. 2000;8.

500. Qin Y, Ji X, Jing J, Liu H, Wu H, Yang W. Size control over spherical silver nanoparticles by ascorbic acid reduction. Colloids and Surfaces A: Physicochemical and Engineering Aspects. 2010;372(1-3):172-6.

501. Oyetade O, Oyeleke G, Adegoke B, Akintunde A. Stability studies on ascorbic acid (Vitamin C) from different sources. Journal of Applied Chemistry. 2012;2(4):20-4.

502. Zadok I, Dekel DR, Srebnik S. Unexpected water-hydroxide ion structure and diffusion behavior in low hydration media. arXiv preprint arXiv:181206961. 2018.

503. Chen M, Zheng L, Santra B, Ko H-Y, DiStasio Jr RA, Klein ML et al. Hydroxide diffuses slower than hydronium in water because its solvated structure inhibits correlated proton transfer. Nature chemistry. 2018;10(4):413-9.

504. Agmon N, Bakker HJ, Campen RK, Henchman RH, Pohl P, Roke S et al. Protons and hydroxide ions in aqueous systems. Chemical reviews. 2016;116(13):7642-72.

505. Lee SH, Rasaiah JC. Proton transfer and the mobilities of the H+ and OH− ions from studies of a dissociating model for water. The Journal of chemical physics. 2011;135(12):124505.

506. Zatsepina G. State of the hydroxide ion in water and aqueous solutions. Journal of Structural Chemistry. 1972;12(6):894-8.

507. Botti A, Bruni F, Imberti S, Ricci M, Soper A. Ions in water: The microscopic structure of concentrated NaOH solutions. The Journal of chemical physics. 2004;120(21):10154-62.

508. Tuckerman ME, Marx D, Parrinello M. The nature and transport mechanism of hydrated hydroxide ions in aqueous solution. Nature. 2002;417(6892):925-9.

509. Porter DA, Easterling KE. Phase Transformations in Metals and Alloys. CRC Press; 2009.

510. Lee SH, Rasaiah JC. Proton transfer and the mobilities of the H+ and OH- ions from studies of a dissociating model for water. J Chem Phys. 2011;135(12). doi:10.1063/1.3632990.

511. Gates-Rector S, Blanton T. The Powder Diffraction File: a quality materials characterization database. Powder Diffraction. 2019;34(4):352-60.

512. Kaminaga K, Oka D, Hasegawa T, Fukumura T. New Lutetium Oxide: Electrically Conducting Rock-Salt LuO Epitaxial Thin Film. ACS omega. 2018;3(10):12501-4.

513. Campelo JM, Luna D, Luque R, Marinas JM, Romero AA. Sustainable preparation of supported metal nanoparticles and their applications in catalysis. ChemSusChem: Chemistry & Sustainability Energy & Materials. 2009;2(1):18-45.

514. Murphy CJ. Sustainability as an emerging design criterion in nanoparticle synthesis and applications. Journal of Materials Chemistry. 2008;18(19):2173-6.

515. Same S, Aghanejad A, Akbari Nakhjavani S, Barar J, Omidi Y. Radiolabeled theranostics: magnetic and gold nanoparticles. Bioimpacts. 2016;6(3):169-81. doi:10.15171/bi.2016.23.

516. Liu Y, Ji M, Wang P. Recent advances in small copper sulfide nanoparticles for molecular imaging and tumor therapy. Molecular pharmaceutics. 2019;16(8):3322-32.

517. Abou D, Pickett J, Thorek D. Nuclear molecular imaging with nanoparticles: radiochemistry, applications and translation. The British journal of radiology. 2015;88(1054):20150185.

518. Anders CB, Chess JJ, Wingett DG, Punnoose A. Serum proteins enhance dispersion stability and influence the cytotoxicity and dosimetry of ZnO nanoparticles in suspension and adherent cancer cell models. Nanoscale research letters. 2015;10(1):448.

Biographical Information

Shahab Ranjbar Bahadori received his B.Sc. in Materials Science and Engineering from University of Tehran, Tehran, Iran in 2007. He Also earned his M.Sc. Materials Science and Engineering from University of Tehran, Tehran, Iran in 2010. He received his first Ph.D. from Amirkabir University of Technology, Tehran, Iran in 2015. From 2007 to 2015, he studies on different sever plastic deformation techniques including twist extrusion and equal channel angular pressing and their combination with conventional forming methods. Then he joined Department of Materials Science and Engineering of University of Texas at Arlington to pursue his studies toward the second Ph.D. in 2016. Under Prof. Hao's supervision, he developed a simple general synthesis technique called liquid diffusion synthesis which can be used for a wide variety of ultrasmall transition metal and lanthanide nanocrystals. In addition to fabricating and characterizing ultrasmall metals, he tried to radiolabel inorganic nanoparticles for theranostic applications. Yttrium-doping of iron oxide nanoparticles and synthesizing silver dendrites for SERS-based applications were other are the other projects conducted by him Through his doctoral research.